

Coordination Polymers of Ligands Based on Imine Functional Groups: Analysis of their Structure and Property Relationship

THESIS

Submitted in partial fulfillment of the requirements for the degree of

DOCTOR OF PHILOSOPHY

by

Fayaz Baig

(2012PHXF0410P)

Under the supervision of

Prof. Madhushree Sarkar

Associate Professor, Department of Chemistry

Birla Institute of Technology and Science Pilani, Pilani Campus

Rajasthan-333031 (Rajasthan)



BITS Pilani
Pilani | Dubai | Goa | Hyderabad

**BIRLA INSTITUTE OF TECHNOLOGY AND SCIENCE, PILANI
PILANI-CAMPUS, RAJASTHAN, INDIA**

2019

*Dedicated to My Beloved
Family Members*

TABLE OF CONTENTS

Certificate	i
Acknowledgments	iii
Abstract	vii
List of Abbreviations and Symbols	ix
List of Tables	xiii
List of Schemes	xv
List of Figures	xvii

Chapter 1: Introduction

1.1 Supramolecular Chemistry and Crystal Engineering	3
1.1.1 Supramolecular Chemistry	3
1.1.2 Crystal Engineering	3
1.2 Intermolecular Interactions in Supramolecular Chemistry	4
1.2.1 Hydrogen Bonding Interaction	5
1.2.2 $\pi\cdots\pi$ Interactions	8
1.2.3 Co-ordinate Bond Interactions	9
1.3 Co-ordination Polymers (CPs) and Metal Organic Frameworks (MOFs)	10
1.3.1 One Dimensional (1D) Co-ordination Polymers	12
1.3.2 Two Dimensional (2D) Co-ordination Polymers	15
1.3.3 Three Dimensional (3D) Co-ordination Polymers	18
1.4 Co-ordination Polymers Containing Imine Functionalities	18
1.4.1 Coordination Polymers of Monoimine Ligands	18
1.4.2 Coordination Polymers of Diimine Ligands	21
1.4.2.1 Coordination Polymers of <i>Bis</i> -pyridyl-diimine Ligands	22
1.5 Post Synthetic Properties of Coordination Polymers	24
1.5.1 Anion Exchange of Coordination Polymers	24
1.5.2 Adsorption Studies of Coordination Polymers	25
1.6 Aim of the Present Study	26
1.7 References	27

Chapter 2: Materials and Experimental Techniques	35
2.1 Introduction	35
2.1.1 Chemicals and Reagents	35
2.2 Synthesis of Schiff Base Ligands or Schiff Base Linkers	37
2.3 Synthesis of Co-ordination Polymers (CPs)	37
2.3.1 Solvent Diffusion Technique	38
2.3.2 Vapour Diffusion Technique	39
2.3.3 Solvothermal or Hydrothermal Synthesis	40
2.4 Characterization Techniques	41
2.4.1 Infrared (IR) Spectroscopy	41
2.4.2 Elemental Analysis	42
2.4.3 Nuclear Magnetic Resonance (NMR) Spectroscopy	43
2.4.4 Structural Determination of CPs by X-ray Crystallography	44
2.4.4.1 Single Crystal X-ray Diffraction (SXRd)	44
2.4.4.2 Powder X-ray Diffraction (PXRd)	45
2.4.5 Ultraviolet (UV) – visible Spectroscopy	47
2.4.6 Fluorescence Spectroscopy	48
2.4.7 Thermo Gravimetric Analysis (TGA)	49
2.5 References	50
Chapter 3: Synthesis, Characterization and Photophysical Studies of Bis-pyridyl-diimines	53
3.1 Introduction	53
3.2 Experimental Section	56
3.2.1 General	56
3.2.2 Synthesis of Schiff bases (L1-L6)	56
3.2.3 X-Ray Crystallography	63
3.3 Results and Discussion	63
3.3.1 Structural Description of the Compounds	63
3.3.1.1 Crystal Structural Analysis of L1c	64
3.3.1.2 Crystal Structural Analysis of L2a	64
3.3.1.3 Crystal Structural Analysis of L2b	66

3.3.1.4 Crystal Structural Description of L3c	66
3.3.1.5 Crystal Structural Description of L5c and L5d	67
3.3.1.6 Crystal Structural Description of L6c and L6d	69
3.3.2 Powder XRD Spectra	69
3.3.3 UV-visible Absorption Spectra of the Ligands L1a-L2c	69
3.3.4 Excitation Spectra and Photoluminescence Spectra of L2a	69
3.3.5 Photophysical Properties of L2b, L3c, L5c, L5d, L6c and L6d	76
3.3.5.1 Excitation Spectra and Photoluminescence spectra of L2b	76
3.3.5.2 Excitation Spectra and Photoluminescence spectra of L3c	76
3.3.5.3 Excitation Spectra and Photoluminescence spectra of L5c	79
3.3.5.4 Excitation Spectra and Photoluminescence spectra of L5d	80
3.3.5.5 Excitation Spectra and Photoluminescence spectra of L6c	82
3.3.5.6 Excitation Spectra and Photoluminescence spectra of L6d	83
3.3.6 Correlating the Photophysical Properties of L2b, L3c, L5c, L5d, L6c and L6d with their Structure	86
3.3.7 Excitation Spectra and Photoluminescence Spectra of L1c	87
3.3.8 NMR assay for Detecting the Aggregation in L1c	90
3.4 Conclusions	92
3.5 References	92
Chapter 4: 1D Zn(II) Coordination Polymers of Bis-pyridyl-diimines: Anion Exchange and Methyl Orange Adsorption Studies	99
4.1 Introduction	99
4.2 Experimental Section	102
4.2.1 Synthesis of Ligands	102
4.2.1.1 Synthesis of 1,2-Bis-(pyridine-3-ylmethylene)hydrazine (L3a)	102
4.2.1.2 Synthesis of 1,2-Bis-(1-(pyridine-3-yl)ethylidene)hydrazine (L4a)	102
4.2.1.3 Synthesis of 1,2-Bis-(1-(pyridine-4-yl)ethylidene)hydrazine (L6a)	102
4.2.2 Synthesis of [C ₁₂ H ₁₀ N ₄ I ₂ Zn] _n , (CP1)	103
4.2.3 Synthesis of [C ₁₄ H ₁₄ N ₄ I ₂ Zn] _n , (CP2)	103
4.2.4 Synthesis of [C ₁₄ H ₁₄ N ₄ I ₂ Zn] _n , (CP3)	103
4.2.5 Anion Exchange Reactions	103

4.2.5.1 Anion Exchange Reaction of CP1 with Cl^-	104
4.2.5.2 Anion Exchange Reaction of CP1 with SCN^-	104
4.2.5.3 Anion Exchange Reaction of CP1 with N_3^-	104
4.2.5.4 Anion Exchange Reaction of CP1 with CO_3^{2-}	104
4.2.5.5 Anion Exchange Reaction of CP2 with Cl^-	104
4.2.5.6 Anion Exchange Reaction of CP2 with SCN^-	105
4.2.5.7 Anion Exchange Reaction of CP2 with N_3^-	105
4.2.5.8 Anion Exchange Reaction of CP2 with CO_3^{2-}	105
4.2.5.9 Anion Exchange Reaction of CP3 with Cl^-	105
4.2.5.10 Anion Exchange Reaction of CP3 with SCN^-	105
4.2.5.11 Anion Exchange Reaction of CP3 with N_3^-	106
4.2.5.12 Anion Exchange Reaction of CP3 with CO_3^{2-}	106
4.2.6 Single Crystal X-ray Diffraction	107
4.3 Results and Discussion	107
4.3.1 Structural Description of L4a and the Coordination Polymers CP1 , CP2 and CP3	107
4.3.1.1 Structural Features of L4a	108
4.3.1.2 Structural Features of CP1	108
4.3.1.3 Structural Features of CP2	109
4.3.1.4 Structural Features of CP3	110
4.3.2 Anion Exchange Reactions	111
4.3.2.1 Anion Exchange Reactions of CP1 with Cl^- , SCN^- , N_3^- and CO_3^{2-}	111
4.3.2.2 Anion Exchange Reactions of CP2 with Cl^- , SCN^- , N_3^- and CO_3^{2-}	113
4.3.2.3 Anion Exchange Reactions of CP3 with Cl^- , SCN^- , N_3^- and CO_3^{2-}	114
4.3.3 Consequences of Anion Exchange on the Geometry of CPs	115
4.3.4 Thermo Gravimetric Analysis of CPs	119
4.3.5 Dye Adsorption Study of CPs	119
4.4 Conclusions	120
4.5 References	121

Chapter 5: Influence of Reaction Conditions on Construction of 2D and 3D Cd(II) Coordination Polymers	125
5.1 Introduction	125
5.2 Experimental Section	127
5.2.1 Synthesis of 2,5-Bis-(3-pyridyl)-3,4-diaza-2,4-hexadiene (L4a)	127
5.2.2 Synthesis of $\{[\text{Cd}_2(\text{L1b})(\text{C}_4\text{H}_4\text{O}_4)_2] \cdot 5\text{H}_2\text{O}\}_n$, (CP4)	128
5.2.3 Single-Crystal X-ray Diffraction	128
5.3 Results and Discussion	129
5.3.1 Crystal Structure Description of CP4	129
5.3.2 Analysis of Structural Features in CP4 , CP5 and CP6	131
5.3.2.1 Coordination Environment Around Cd(II)	131
5.3.2.2 Geometry of L4a in CP4 , CP5 and CP6	132
5.3.2.3 Geometry of Succinate in CP4 , CP5 and CP6	132
5.3.2.4 Network Differences in CP4 , CP5 and CP6	134
5.3.2.5 Effect of Reaction Conditions on the Geometry of CPs	136
5.3.3 Thermogravimetric Analysis	137
5.3.4 Photophysical Properties of CPs	138
5.4 Conclusions	141
5.5 References	142
Chapter 6: Porous 3D Cd(II) Coordination Polymer of Bis-pyridyl-diimine and Benzene-1,3-disulfonate ligands: Iodine and Methyl Orange Adsorption Studies	147
6.1 Introduction	147
6.2 Experimental	150
6.2.1 General	150
6.2.2 Single-Crystal X-ray Diffraction	150
6.2.3 Synthesis of 2,5-Bis-(4-pyridyl)-3,4-diaza-2,4-hexadiene (L6a)	151
6.2.4 Synthesis of $[\text{Cd}(\text{L6a})_2 (\text{L7})]_n$, (CP7)	152
6.2.5 Iodine Adsorption and Desorption	152
6.2.6 Dye Adsorption Studies	152
6.3 Results and Discussion	153

6.3.1 Crystal Structural Description of L6a	153
6.3.2 Crystal Structural Description of CP7	154
6.3.3 Adsorption and Desorption of Iodine in CP7	155
6.3.4 Adsorption and Separation of Dyes by CP7	158
6.4 Conclusions	160
6.5 References	160
Chapter 7: Rationalization of Results and Conclusions	167
7.1 Influence of Non-covalent Interactions to Enhance Emission of Ligands L2b-L6d	167
7.2 Construction of Zn(II) Coordination Polymers with Single Ligand System: Effect of Change in Coordination Site on the Structure, their Anion Exchange and Photo Degradation Studies	167
7.3 Effect of Reaction Conditions on the Structural Features of Coordination Polymers	168
7.4 3D Interpenetrated Coordination Network of Cd(II) with <i>Bis</i> -pyridyl-diimine and Disulfonate Ligands and its Adsorption Studies	168
7.5 Future Scope of Present Work	169
Appendix Figures	173
FT-IR, ¹ H NMR, ¹³ C NMR, PXRD and ORTEP of Ligands and CPs	173
List of Publications	A1
List of Papers Presented in Conferences	A3
Brief Biography of the Supervisor	A5
Brief Biography of the Candidate	A7

**BIRLA INSTITUTE OF TECHNOLOGY AND SCIENCE, PILANI
PILANI CAMPUS, RAJASTHAN, INDIA**

CERTIFICATE

This is to certify that the thesis entitled “**Coordination Polymers of Ligands Based on Imine Functional Groups: Analysis of their Structure and Property Relationship**” and submitted by **Mr. Fayaz Baig** ID No **2012PHXF0410P** for award of Ph.D. Degree of the Institute embodies the original work done by him under my supervision.

Signature in full of the Supervisor: *Madhushree Sarkar*

Name : **Prof. Madhushree Sarkar**

Designation: Associate Professor

Birla Institute of Technology & Science Pilani, Pilani Campus
Pilani-333031 (Rajasthan)

Date: 24.7.2019

Chapter-1

Introduction

Chapter 1

Introduction

1.1 Supramolecular Chemistry and Crystal Engineering

1.1.1 Supramolecular Chemistry

Jean-Marie Lehn defined the term supramolecular chemistry as ‘Chemistry beyond molecules’ and ‘chemistry of molecular assemblies and the intermolecular bond’. In 1987, Jean-Marie Lehn was awarded Nobel Prize along with Donald J. Cram and Charles J. Pedersen for establishing their work in this field.^[1-5] Supramolecular chemistry focuses on the design and development of novel systems by assembling of molecular components *via* non-covalent interactions (Figure 1.1). The non-covalent interactions responsible for the molecular assembly in supramolecular chemistry include hydrogen bond interaction, coordinate bond interaction, $\pi\cdots\pi$ interactions and van der Waals interaction. Supramolecular chemistry has emerged as an interdisciplinary science having wide range of areas with important applications. The studies on crown-ethers, particularly in the selective "host-guest" complexes development, where recognition and selective binding certain guest by a host, is a significant milestone in this area.^[6-8] Even Supramolecular chemistry is an important, interdisciplinary branch of science which has been extended to solid-state chemistry,^[9] liquid-crystal^[10] and polymer science.^[11] Researchers from the areas of chemical, physical, computational, biological and biochemical sciences have been benefitted by the knowledge and resources from this area. Thus supramolecular chemistry involves the investigation of molecular systems in which the molecular components are detained together with interesting intermolecular interactions instead covalent bonds.^[12]

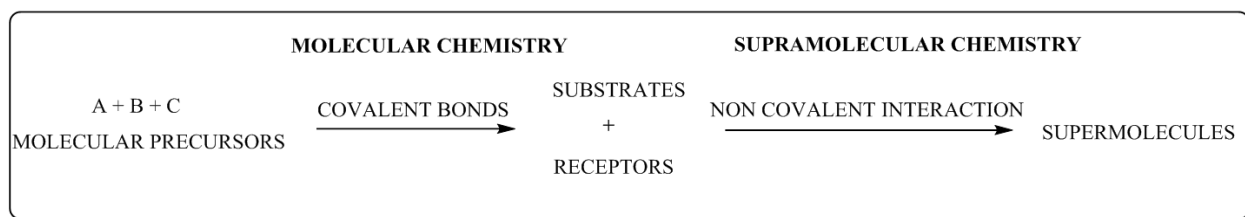


Figure 1.1: An analogy between supramolecular and molecular chemistry according to Lehn.^[5]

1.1.2 Crystal Engineering

The term ‘crystal engineering’ was used by Schmidt in 1971, while studying the photodimerization of cinnamic acids.^[12] Later on, in 1988, Desiraju^[13] defined ‘crystal

engineering' as "the understanding of intermolecular interactions in the circumstance of crystal packing and the exploitation of such understanding in the design of new solids with desired physical and chemical properties". The perceptions of crystal engineering are used in tailor-made the materials according to our requirement. The materials designed using the concepts of crystal engineering have potential applications in the areas of storage of gases,^[14] sensors,^[15,16] separation and catalysis,^[17] host-guest chemistry,^[18,19] photovoltaic cells,^[20] luminescence^[21] and semiconductors.^[22] Designing different building blocks to construct desired network architectures is the primary task in crystal engineering.

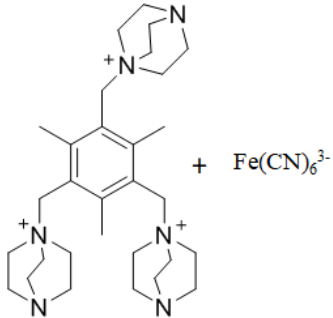
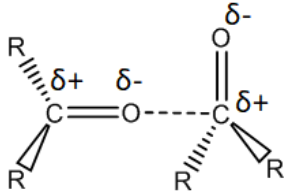
Supramolecular synthons,^[23] is defined as "a structural unit of a supramolecule, which can be formed by the assembled intermolecular interactions between the molecules by known or conceivable synthetic operations". These supramolecular synthons are the tools to identify the persistent intermolecular interaction patterns between different functional groups. The important research tool which gives us the survey of all previous reports on various compounds is the Cambridge Structural Database (CSD).^[24] In CSD, the information available includes compound name, unit-cell parameters, molecular formula, symmetry operators and space-group, atomic coordinates, R-factors and journal reference. This data is useful to identify structure-property relationship, to understand the supramolecular synthons of various functional groups and geometrical constraints in the occurrence of any intermolecular interactions. The information gained from CSD along with other databases can navigate to design new materials with predefined properties.

1.2 Intermolecular Interactions in Supramolecular Chemistry

The most important part of crystal engineering is the understanding of intermolecular interactions for predicting and designing the structures to construct new materials. It is also important for the knowledge of non-covalent interactions in supramolecular chemistry is required to understand the effect of non-covalent interactions in directing the overall supramolecular architecture. The higher complexities and the molecular aggregates are the outcomes of all the intermolecular interactions. During the formation of supramolecular assemblies, the contributing molecules may be polar or permanently charged species resulting in electrostatic interaction between the molecules. In case of non-polar molecules non-bonded interactions may result due to induced dipoles, however the strength is less when compared to

that of permanently charged species. Some of the non-covalent interactions include: Hydrogen bonding, $\pi\cdots\pi$ interactions, Ion-Ion, Ion-Dipole, Dipole-Dipole, Hydrophobic and van der Waals interactions (Table 1.1).

Table 1.1: Types of non-covalent interactions

Interaction	Strength (kJ mole ⁻¹) (in general)	Examples in Supramolecular chemistry
Ion \cdots Ion ^[25]	100 – 350	
Ion \cdots Dipole ^[26]	50 – 200	Crown ether – Metal cation (host) – (guest)
Dipole \cdots Dipole	5 – 50	
Hydrogen Bonding	4 – 120	Base pairing in DNA
$\pi\cdots\pi$ interactions	0.05 – 50	Aromatic moieties
van der Waals	< 5	Attractive dispersion forces causing by multipoles
Hydrophobic effects	Depends on solvent-solvent interactions energy	Cyclodextrin – Organic molecule guest

1.2.1 Hydrogen Bonding Interaction

The most commonly occurring interaction is hydrogen bond interaction in small molecules and also in large biological systems such as polysaccharides, proteins and in nucleic acids.^[27] Hydrogen bond interaction is electrostatic interaction results when a hydrogen atom, which is

covalently bonded to an electronegative atom F, O, N etc. (Donor) interacts with another electronegative atom (Acceptor). Thus the hydrogen atom has interaction simultaneously with two electronegative atoms, i.e. the covalently bonded atom (hydrogen donor) and the other electronegative atom (hydrogen acceptor) (Figure 1.2).

Four parameters can be used to characterize Hydrogen bond namely d , D , θ and ϕ (Figure 1.2). d and D are the $H\cdots A$ and $X\cdots A$ distances respectively, whereas θ and ϕ are the $X-H\cdots A$ and $B-A\cdots H$ angles respectively. The angle ϕ represents the linearity of the hydrogen bond. The angle ϕ related to the directionality of the hydrogen bond. The D and d should be less than sum of the van der Waals radii of the atoms for the formation of a hydrogen bond.^[28]

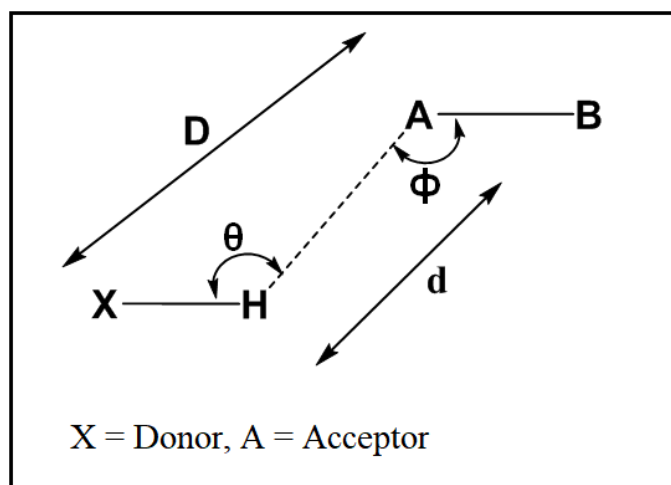


Figure 1.2: Schematic representation of hydrogen bond.

In 1920s, Rodebush and Latimer^[29] suggested that “a free pair of electrons on one water molecule might be able to exert enough force on hydrogen held by a pair of electrons on another water molecule to bind the two water molecules together”. Pauling^[30] defined hydrogen bond as largely ionic in character and formed only between the most electronegative atom. In 1960, about 2000 cases were examined the existed hydrogen bonding by McClellan and Pimentel.^[31] They defined hydrogen bonding based on their study, as “a hydrogen bond exists if (1) there is evidence of a bond and (2) there is evidence that this bond sterically involves a hydrogen atom already bonded to another atom”. This definition didn’t identify the chemical nature of the atoms, such as their polarities, electro-negativities, net charges and hence it can comprise various weak hydrogen bonds such as $C-H\cdots N$, $C-H\cdots O$ and so on. In 1989, Atkins^[32] defined hydrogen bond as a link formed by a hydrogen atom lying between two strongly electronegative atoms.

Steiner^[28] in 2002 modified the definition of the hydrogen bond as: “X-H•••A interaction is called a hydrogen bond if: (1) it comprises a local bond, and (2) X-H acts as proton donor to A and A is called the acceptor”.

Hydrogen bonding interactions can be categorized into three types based on their strength as: (1) very strong (2) strong and (3) weak hydrogen bonds^[33] (Table 1.2). Due to the reproducibility in occurrence, the strong hydrogen bonds are structure directing and structure prediction with the help of their known supramolecular synthons are quite reliable (Figure 1.3). CPs containing hydrogen bonding functionalities play a crucial role in assembling and directing the networks into higher dimensions.^[34-41] Many researchers widely reported the hydrogen bonding assemblies of co-ordination complexes and co-ordination polymers (CPs).

Table 1.2: Classification of hydrogen bonds based on strength.^[33]

Types of hydrogen bonds	Bond Energy (kcal/mol)	Examples	D (X•••A) (Å)	d (H•••A) (Å)	θ range (°)	Lengthening of X-H bond (Å)	Effect on crystal packing
Very Strong	15-40	[F•••H•••F], [N•••H•••N] + P-OH•••O=P	2.2-2.5	1.2-1.5	170-180	0.08-0.25	High
Strong	4-15	O-H•••O=C N-H•••O=C O-H•••O-H	2.5-3.2	1.5-2.2	130-170	0.02-0.08	Distinctive
Weak	< 4	C-H•••O O-H•••π	3.2-4.0	2.2-3.2	90-130	<0.02	Variable

The pyridyl-based ligands with certain functional groups e.g. carboxylic acids, oximes, and amides were used by Aakeroy *et al.*^[34-36] where the functional groups help in the formation of hydrogen bonded networks in co-ordination complexes. They have reported the role of self-complementary oxime•••oxime hydrogen-bond interactions in the propagation of Ag(I) complex.^[36] Important results have introduced by Desiraju *et al.*^[33] and Braga *et al.*^[37,40,41] in the perspective of assembling the organometallic complexes *via* hydrogen bonds.

Bazzicalupi *et al.*^[38] reported the hydrogen bond assembled transition metal macrocycle complexes where Thymine and Uracil based di-zinc macrocyclic complexes assembled by inter and intra-molecular hydrogen bonding. Goldberg *et al.*^[39] have studied the metal-porphyrin building blocks arrangements *via* various hydrogen bonded interactions.

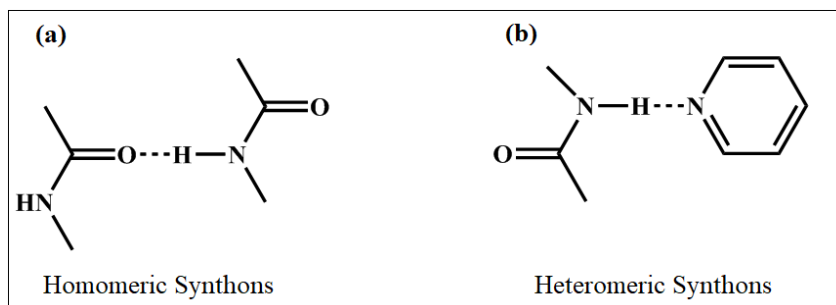


Figure 1.3: Supramolecular synthons with NH...O and NH...N hydrogen bond functionalities

1.2.2 $\pi\cdots\pi$ Interactions

In the molecules containing π -bonds or compounds with aromatic rings, one of the important non-covalent interactions are “ $\pi\cdots\pi$ interactions”. The presence of an ‘electron deficient’ aromatic center in close proximity with an electron-rich aromatic moiety will result in face-to-face stacking. This is also called ‘aromatic donor–acceptor interaction’ as it involves a state in which relatively electron-rich and electron-deficient aromatic molecules stack in an alternate fashion.^[42,43]

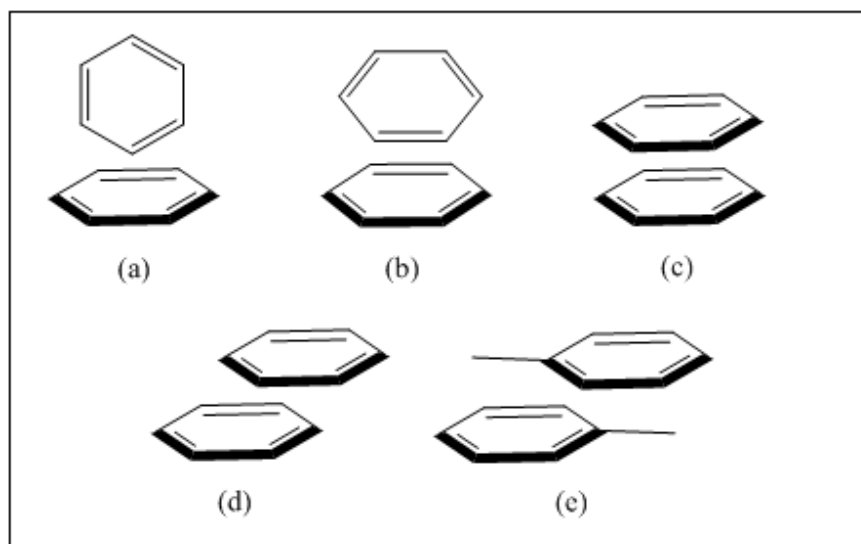


Figure 1.4: Aromatic stacking: (a) Perpendicular T-shaped (b) Perpendicular Y-shaped (c) Parallel face-centered (d) Parallel-offset for benzene (e) Parallel-offset for toluene^[44]

Benzene and toluene neutron diffraction spectroscopic studies have given information about aromatic $\pi\cdots\pi$ stacking.^[45] Benzene molecules in solid state, interact and arrange predominantly in perpendicular edge-to-face arrangement. These edge-to-face arrangements are of two types: T-shaped and Y-shaped in which more stability is observed in Y-shaped arrangement. In solid state toluene molecules the methyl group of the adjacent molecule interacts with π -orbitals of the aromatic ring, resulting molecules stack in an off-center parallel manner. For benzene, Sinnokrot and Sherrill^[44] carried out a comprehensive set of calculations and reported, parallel-offset dimmers and T-shaped edge-to-face arrangement are nearly isoenergetic (Figure 1.4). Cockroft *et al.*^[46] used double mutant to study the aromatic interactions in di-amides and observed T-shaped edge-to-face arrangement. They also studied the substituent effect on $\pi\cdots\pi$ stacking interaction. Cai *et al.*^[47] reported Cu(II) co-ordination polymer with $\pi\cdots\pi$ interactions between aromatic rings of pyrazole.

1.2.3 Co-ordinate Bond Interactions

The strength of coordinate bond interaction is in the range of 30-70 kcal/mol which offers greater directionality and stability that results in varied structures of CPs. As the name suggests Co-ordination polymers are polymeric networks containing organic ligands and metal ions.

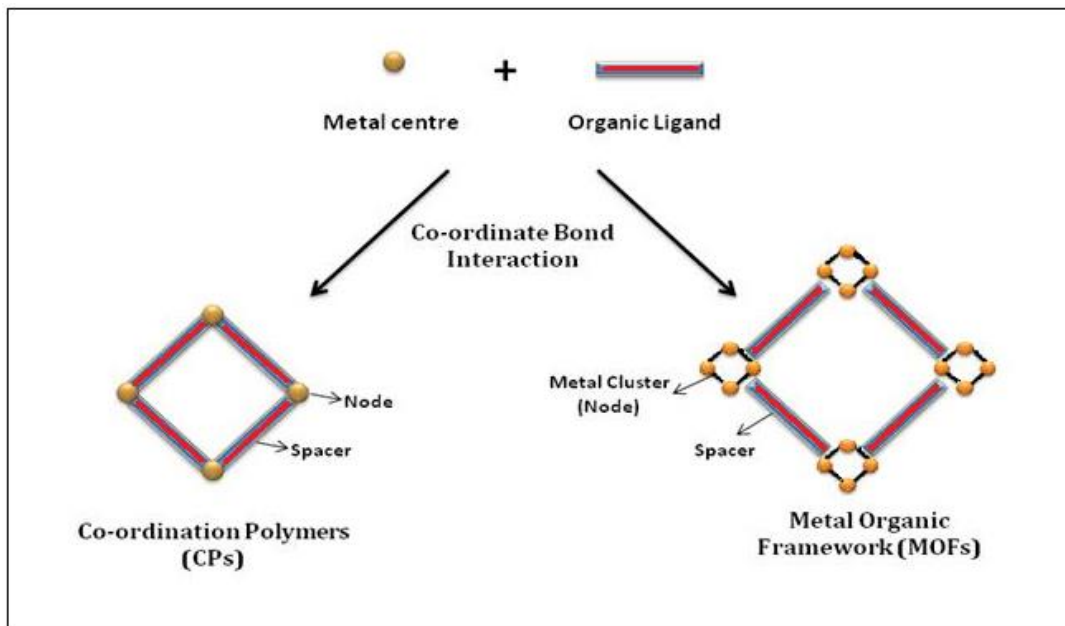


Figure 1.5: Co-ordinate bond between metal ions and organic ligands in co-ordination polymers (CPs) and between metal clusters and organic ligands in Metal Organic Frameworks (MOFs)^[43,45]

R. Robson and co-workers^[42] in the early 1990s, for designing the porous co-ordination polymers ‘node and spacer’ approach was described. The metal ions were replaced with inorganic clusters, known as the secondary building units (SBUs) by O. M. Yaghi’s research group^[43,45] and introduced reticular chemistry in around 2000. Thus a special class of co-ordination polymers, the Metal Organic Frameworks (MOFs) aroused where the metal clusters are connected by organic linkers (usually carboxylates) (Figure 1.5).

The structural networks and properties of the materials resulting from co-ordinate bond interactions get further diversified with the addition of versatile hydrogen bond interactions. The construction of co-ordination polymers primarily depends on the co-ordination preferences of the metal center and the ligand functionalities. Several other factors such as ligand to metal ratio, guest or solvent molecules, counter anions and reaction conditions, also play the structure directing roles.

1.3 Co-ordination Polymers (CPs) and Metal Organic Frameworks (MOFs)

Although there are reports on CPs from late 1950s^[48,49] and early 1960s,^[50–53] the area of research on CP was boosted by the pioneering works of Robson and co-workers^[42,54] followed by Kitagawa *et al.*^[55,56] and Ferey *et al.*^[57] Later on Yaghi *et al.*^[43,45,58,59] explored MOFs widely in the area of gas storage, best known example published in 1999 in Nature, is the structure of MOF-5. Giving the term CP or MOF for a polymeric solid structure is often confusing and showed a competition CPs verses MOFs. The term CP is defined as “the coordination compound where a ligand bridges between metal centres, where metal centre binds to more than one ligand to create an infinitive array of metal centres” and the MOF is defined as “crystalline compound consisting of metal ions or clusters coordinated to often rigid organic molecules to form one-, two-, or three dimensional structures that can be porous”. O. M. Yaghi differentiated the CP and MOFs based on porosity. According to him CPs are non porous and MOFs are porous coordination networks. In solid state science a framework structure defined as “a crystalline structure in which there are strong interatomic bonds which are not confined to a single plane in contrast to layer structure”. This will define that the one-, and two dimensional networks are considered as coordination polymers and three dimensional networks are considered as MOFs irrespective of porosity.^[60,61] Due to the porous nature, the CPs and MOFs are exploited widely.

Their porosity is greater than 50% of the MOF crystal volume and the surface area value ranges from 1000 to 10,000 m²/g.^[62]

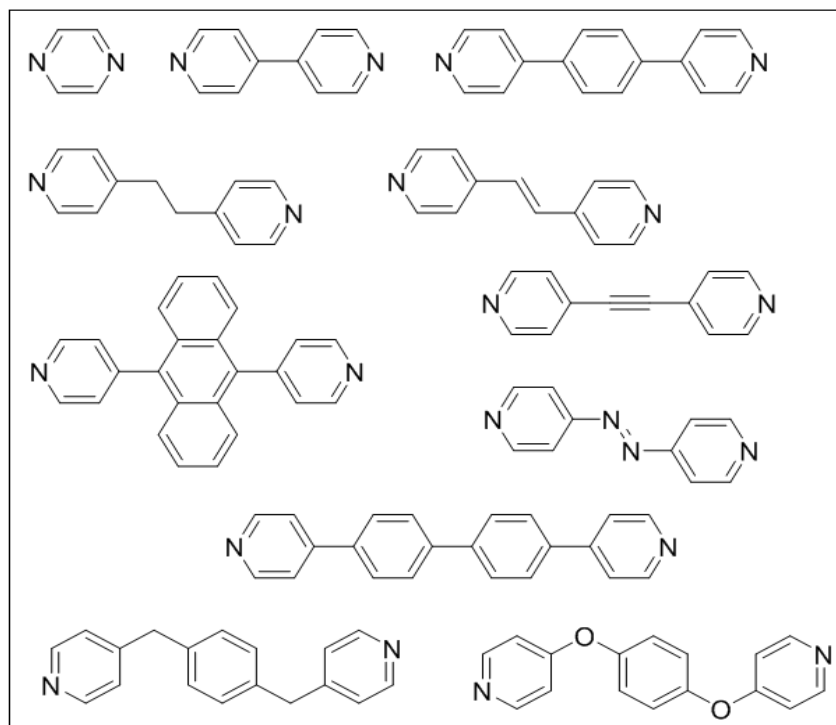


Figure 1.6: Representation of "rod-like" *bis*-pyridyl ligands with diverse spacers.

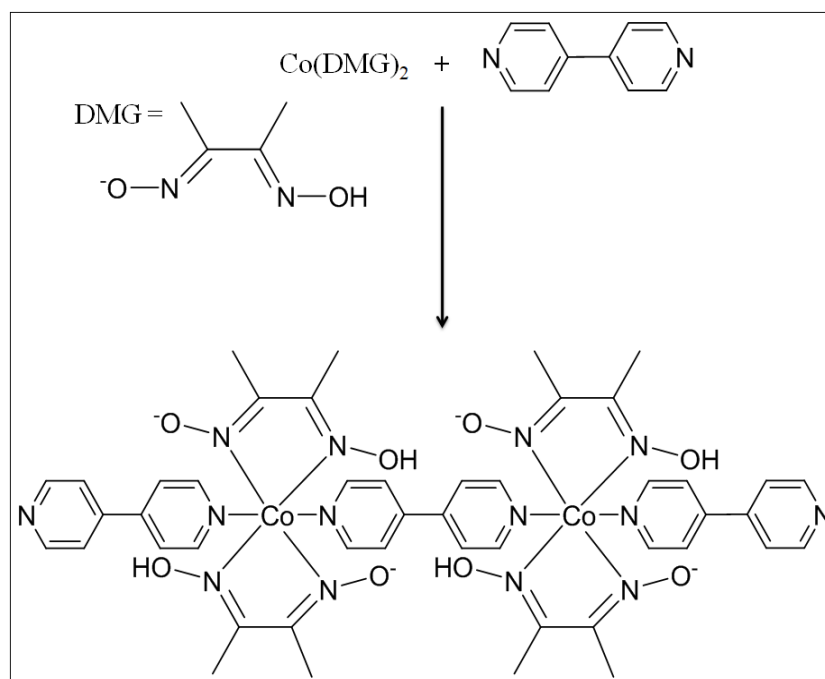


Figure 1.7: 1D-linear chain co-ordination polymer of 4,4'-bipy.^[63]

For the construction of robust CPs, 4,4'-bipyridine is one of the most widely used ligands. The synthesis of one-, two-, and three dimensional (1D, 2D, and 3D) networks using the derivatives of 4,4'-bipyridine with various spacer units between two pyridine rings (Figure 1.6) are also reported widely. There are many reports on co-ordination polymers of these ligands with different Cu(I) and Cu(II), Ag(I), Cd(II), Zn(II), Co(II) and Ni(II) ions.^[60-86]

1.3.1 One Dimensional (1D) Co-ordination Polymers (CPs)

The reaction conditions such as the solvent, temperature, pressure, solubility of the product formed, influence the dimensionality and the geometry of the network of CPs. The 1D CPs of transition metal atoms with 4,4'-bipyridine obtained mainly due to the competition between 4,4'-bipyridine with other ligands and anions, solvent *etc.* to co-ordinate the metal center.

Kubel *et al.*^[63] reported X-ray structure of the first co-ordination polymer of 4,4'-bipyridine in 1982 where the reaction of Co(dimethylglyoximate)₂ with 4,4'-bipyridine resulted in a 1D-linear chain. In this 1D network, Co(II) attains octahedral geometry and 4,4'-bipyridine occupy the two co-ordination sites *trans* to each other while the remaining sites co-ordinated by dimethylglyoximates (Figure 1.7). It was also reported that the 4,4'-bipyridine ligand competes with bi-dentate chelating ligands such as 2,2'-bipyridine or ethylene-diamine and results in the formation of 1D-zigzag chain network.

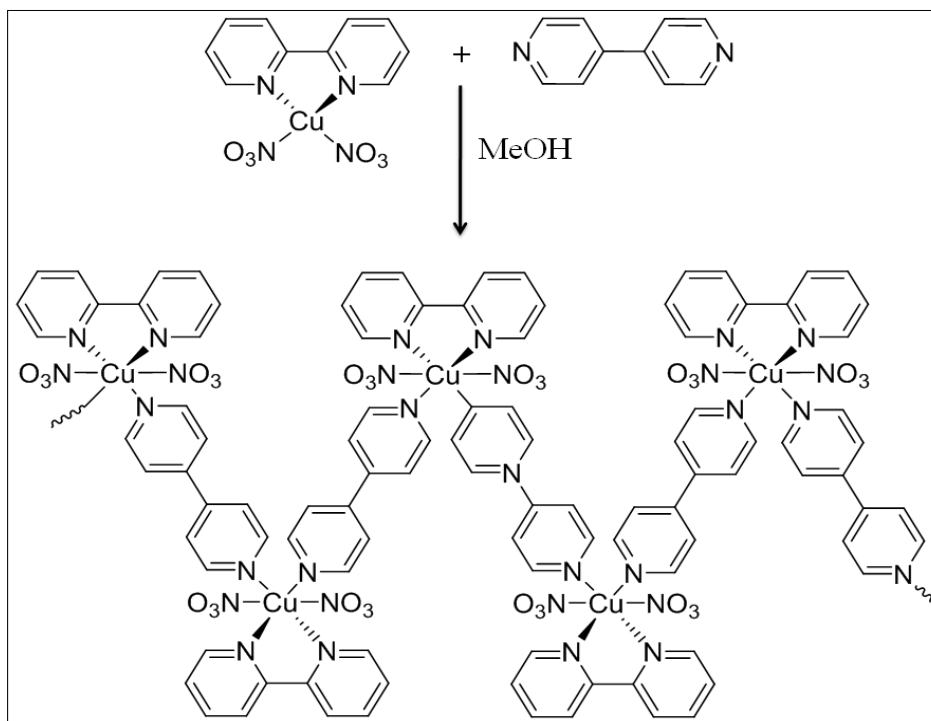


Figure 1.8: 1D-zigzag chain co-ordination polymer of 4,4'-bipy.^[64]

For the construction of robust CPs, 4,4'-bipyridine is one of the most widely used ligands. The synthesis of one-, two-, and three dimensional (1D, 2D, and 3D) networks using the derivatives of 4,4'-bipyridine with various spacer units between two pyridine rings (Figure 1.6) are also reported widely. There are many reports on co-ordination polymers of these ligands with different Cu(I) and Cu(II), Ag(I), Cd(II), Zn(II), Co(II) and Ni(II) ions.^[60-86] Though the metal to ligand ratio of linear, zigzag and helical chains is same, the metal center to ligands arrangement is different. When the ligands are *trans* to each other the linear chain is formed but when the ligands are *cis* to each other zigzag and helical chains are formed (Figure 1.8).

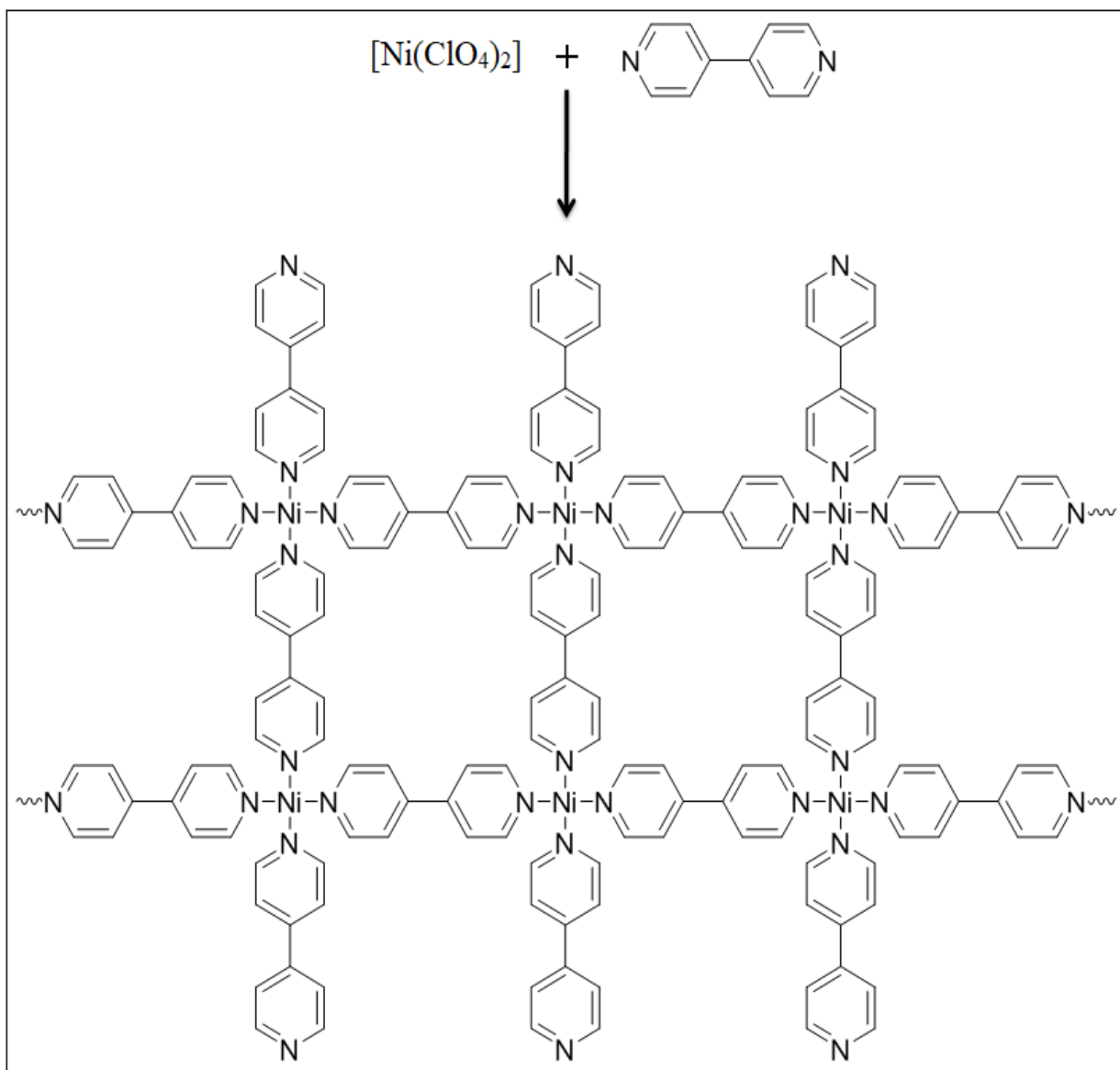


Figure 1.9: 1D-railroad co-ordination polymer of 4,4'-bipy.^[65]

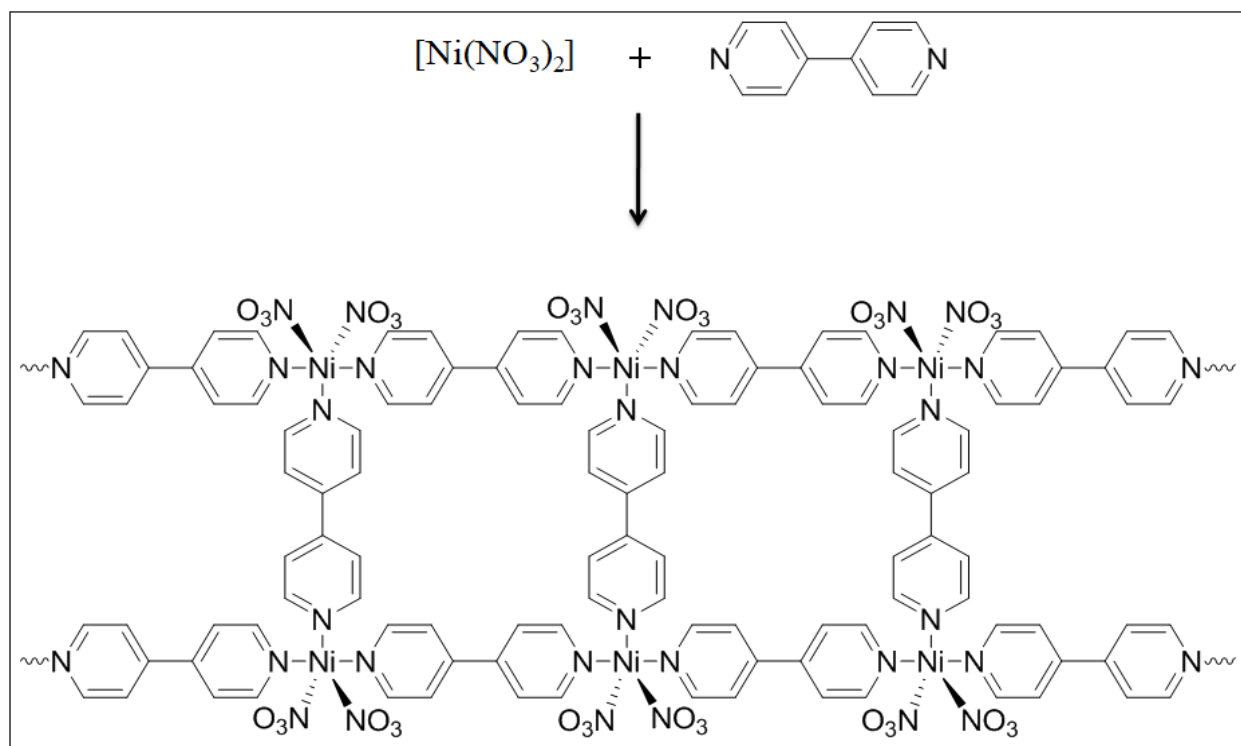


Figure 1.10: 1D-molecular ladder co-ordination polymer of 4,4'-bipy.^[66]

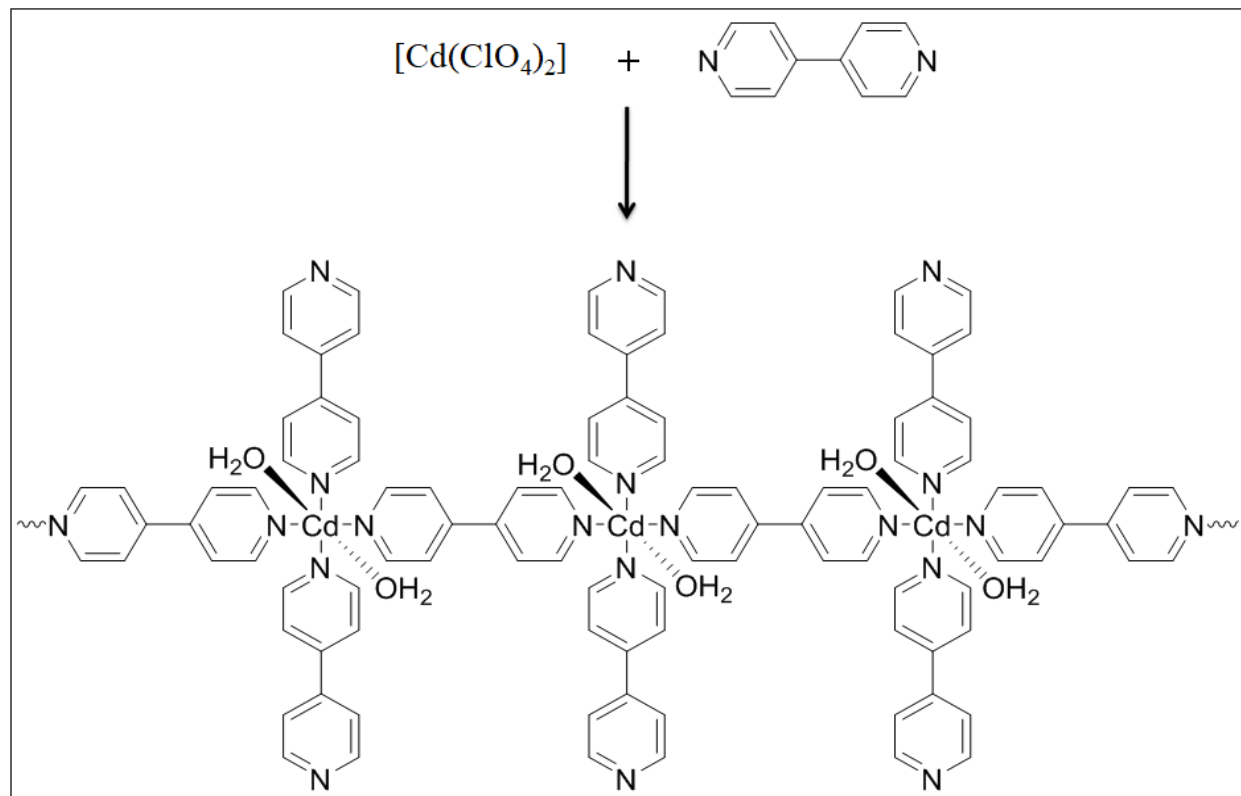


Figure 1.11: 1D-molecular antenna co-ordination polymer of 4,4'-bipy.^[67]

The T-shaped coordination environment of metal, where ligands occupy three co-ordinating sites of the metal ion, results in the formation of 1D railroad (Figure 1.9) and 1D-ladder (Figure 1.10) networks. The square planar coordination environment of metal center results in 1D-molecular antenna provided 4,4'-bipyridine ligands are present in excess amount and 4,4'-bipyridine acts as bidentate as well as monodentate ligand (Figure 1.11).

1.3.2 Two Dimensional (2D) Co-ordination Polymers (CPs)

4,4'-bipyridine and its analogue form different 2D geometries include bilayer^[68,69], brick wall^[70], herringbone^[71], honeycomb^[72,73], square grids^[74–77] and rectangular grids^[78,79]. The bilayer, brick wall, herringbone and honeycomb networks are three-connected networks (Figure 1.12) whereas the square grids (Figure 1.13) and rectangular grids are four-connected networks.

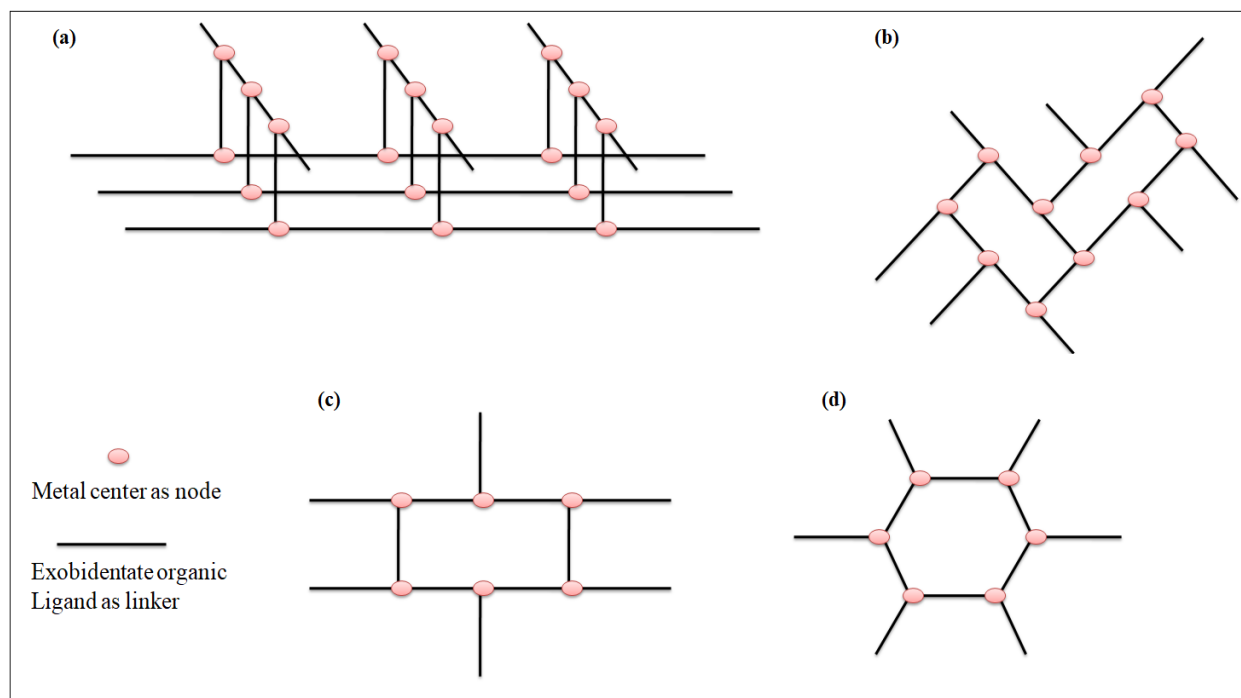


Figure 1.12: (a) 2D-bilayer,^[68,69] (b) herringbone,^[71] (c) brick wall^[70] and (d) 2D-honeycomb^[72,73] networks.

The first bilayer co-ordination polymer was reported by Zaworotko *et al.*^[68,69] with $\text{Co}(\text{NO}_3)_2$. Using 1,2-*bis*-(4-pyridyl)ethane. The bilayer network observed in CPs is different from the conventional bilayers of the lyotropic liquid crystals. In the conventional bilayers, the hydrophilic and hydrophobic layers are arranged in alternate fashion. In the bilayer networks of CPs, the two layers are identical and are separated by a spacer ligand. In the bilayer networks,

both the layers contain a set of 1D chains arranged parallelly and the chains in one layer make an approximate angle of 90° with those of the other layer (Figure 1.12a). Lin *et al.*^[71] have reported the herringbone network where Zn(II) was reacted hydrothermally with pyridine-2,4,6-tricarboxylic acid and 4,4'-bipy (Figure 1.12b). An example of the brick wall network is reported with Cd(NO₃)₂ coordinated with imidazole-4,5-dicarboxylic acid and 4,4'-bipy (Figure 1.12c).^[70] The brick wall and herringbone networks are propagated by T-shaped metal geometry.

The trigonal geometry of the metal center results in the honeycomb network. The occurrence of honeycomb networks is rare due to the requirement of less occurring trigonal-bipyramidal or trigonal co-ordination geometries of transition metal center (Figure 1.12d). Yaghi *et al.*^[72] and Zaworotko *et al.*^[73] reported honeycomb network of Cu(II) with 4,4'-bipyridine and pyrazine respectively.

Square grids contain huge voids to include various guest molecules are well explored and are achieved upon 1:2 metals to ligand ratio. The metal center in the square grid network adopts octahedral co-ordination geometry with four ligands at the equatorial positions and two H₂O/solvent/counter anions at the axial positions. Robson *et al.*^[80] reported the first square grid CP using 4,4'-bipyridine in the crystal structure of $\{(Zn(4,4'-bipy)_2(H_2O)_2)(SiF_6)\}_n$, in which the 2D networks are doubly interpenetrated (Figure 1.13). Later on open or non-interpenetrated square grid network was reported by Fujita *et al.*^[74] with 4,4'-bipyridine in the crystal structure of $\{(Cd(4,4'-bipy)_2(NO_3)_2) \cdot 2(o\text{-dibromobenzene})\}_n$ (Figure 1.13) in which the guest molecules were included in the pores of the network.

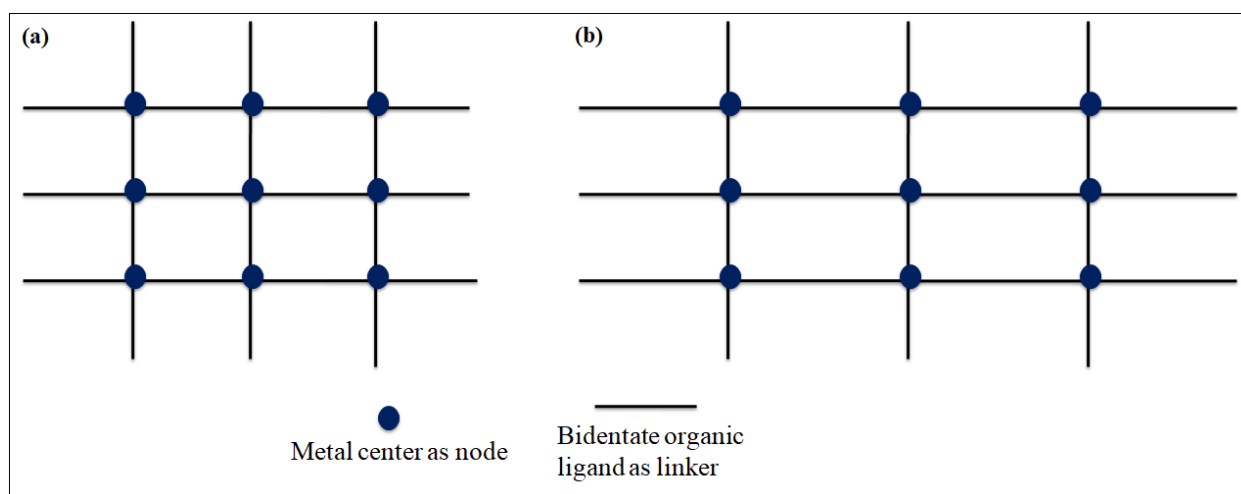


Figure 1.13: (a) 2D-square grid^[74] and (b) 2D-rectangular grid networks^[82]

Subsequently, Biradha *et al.*^[75-77] have reported the square grid networks of 4,4'-bipyridine in the presence of different guest molecules such as benzene, naphthalene, nitrobenzene, pyrene, veratrole and anisole. The use of 4,4'-bipyridine longer analogue resulted in square grid networks containing larger cavities of dimensions $11 \times 11 \text{ \AA}^2$, $15 \times 15 \text{ \AA}^2$, $20 \times 20 \text{ \AA}^2$ and $25 \times 25 \text{ \AA}^2$. Gong *et al.*^[81] reported interpenetrated CPs of Zn(II) and Cd(II) with *bis*-pyridyl-*bis*-amide ligand contained phenyl spacer along with aromatic polycarboxylate. Biradha *et al.*^[82] studied interpenetrated network in Cu(II) CP of *bis*-pyridyl-*bis*-amide ligand, where the layers were parallel interpenetrated. Wang *et al.*^[83] reported interpenetrated CPs of Cu(II) with flexible *bis*-pyridyl-*bis*-amide ligand, *meta*- position of pyridyl-N and different length alkyl spacer.

Rectangular grid networks obtained by taking two different ligands (Figure 1.13). The formation of rectangular grids with neutral ligands are rare. Tong *et al.*^[78] have shown the formation of rectangular grid network of Cu(II) with dimensions $6.8 \times 11.1 \text{ \AA}^2$ with 4,4'-bipyridine and pyrazine. Further Fujita *et al.*^[79] reported rectangular grid networks using bipyridine and longer analogues of 4,4'-bipyridine.

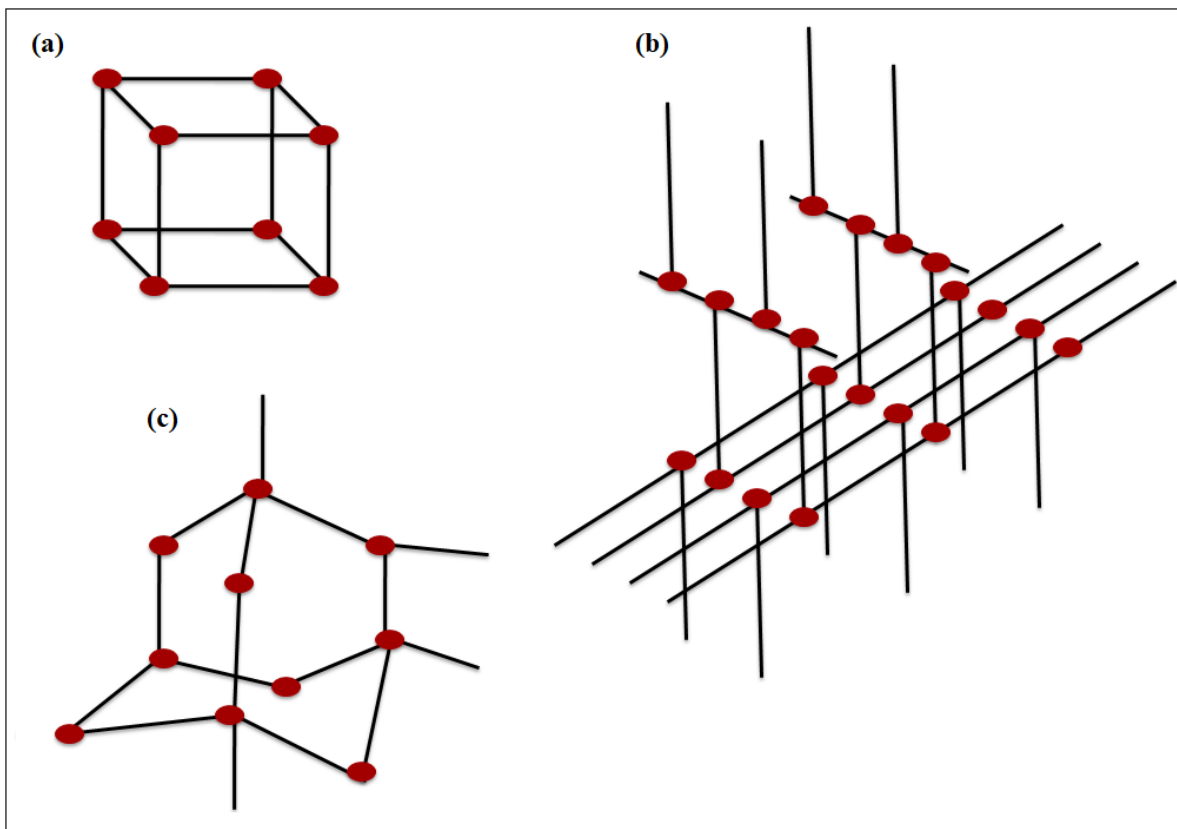


Figure 1.14: (a) 3D-cubic,^[85] (b) lincoln logs^[86-88] and (c) diamondoid^[73,89] co-ordination polymers.

1.3.3 Three Dimensional (3D) Co-ordination Polymers (CPs)

The 3D networks formed using bidentate ligands can be extensively classified as

- (i) Linking of the 2D layers *via* anions ^[84,85]
- (ii) Propagation by three-connected nodes, ^[86–88]
- (ii) Propagation by four-connected nodes, ^[73,89]

Anions play an important role in linking of the two-dimensional metal-organic layers to form 3D networks. Kitagawa *et al.*^[85] and Zaworotko *et al.*^[84] have reported the role of SiF_6^- ions in the formation of 3D networks by linking the square grid networks of M(II) and 4,4'-bipyridine. In the 3D networks that are propagated by three-connected nodes, the metal center can adopt either trigonal or T-shaped co-ordination geometry. Out of the various possible networks, the T-shaped geometry can lead to the formation of Lincoln Log networks which are reported with Ag(I) and 4,4'-bipyridine (Figure 1.14).^[86–88] Diamondoid network is the most common network that is propagated by four-connected node (Figure 1.14). Ciani *et al.*^[89] and Zaworotko *et al.*^[73] reported the diamondoid network with Ag(I) and Cu(I) along with 4,4'-bipyridine respectively.

1.4 Co-ordination Polymers (CPs) containing imine Functionalities

CPs of metal ions and ligands containing imine functionalities such as: monoimines, diimines, alkyl or aryl diimines, *etc.* (Figure 1.15) result in the formation of novel networks due to the participation of imine function either in non-covalent interactions or in direct coordination with the metal atoms. The coordination polymers containing only imine functional ligands are relatively less due to the stability and low tendency of imine function alone to form intermolecular interactions.

To overcome this problem, a wide range of reports obtained based on mixed functional coordination polymers where dicarboxylic acid ligands were used along with the imine functional ligands and obtained novel networks with desired properties.^[90–93]

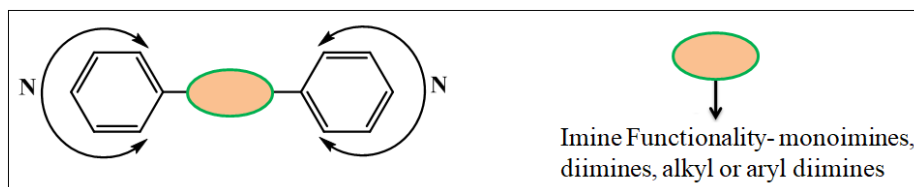


Figure 1.15: Bis-pyridyl ligands with imine functionality in the spacer

1.4.1 Coordination polymers of monoimine ligands

Notash *et al.*^[94] reported the *bis*-3-pyridyl-*mono*-imine ligand to synthesize co-ordination polymers of Hg(II) halides where the halides are Cl⁻, Br⁻ and I⁻. They investigated structures and observed the effect of halide ions in directing the structure of CP by the formation of non-covalent interactions (Figure 1.16). The CP of the ligand with Cl⁻ and Br⁻ resulted in zigzag networks by the formation of C–H...Cl–Hg hydrogen bonds, Hg–Cl... π , π ... π interactions and Hg–Br... π , π ... π interactions respectively but the CP of the ligand with I⁻ forms C–H...Cl–Hg hydrogen bonds where iodide acted as bifurcated hydrogen bond acceptor along with π ... π interactions regulate to fold into helical structure.

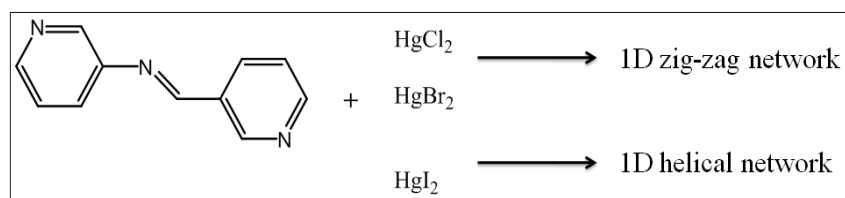


Figure 1.16: Synthesis of 1D CPs of *bis*-3-pyridyl-*mono*-imine with Hg(II) halides.^[94]

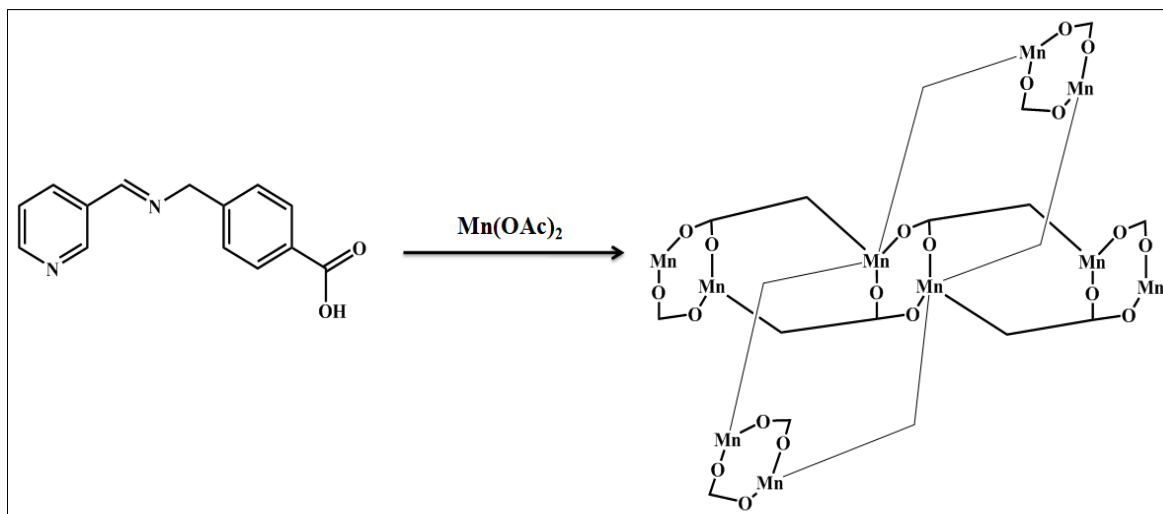


Figure 1.17: 2D CP formed from Mn(II) and pyridyl-carboxylate functional Schiff base ligand.^[95]

Han *et al.*^[95] reported Ag, Mn and Cd CPs using imine based ligands containing pyridyl-carboxylate terminals. Ag(I) forms a 3D CP but Mn(II) and Cd(II) form 2D coordination networks. They studied the variation in the coordination modes of the ligand with the metals. In the Ag CP all the hetero atoms including imine N coordinate to Ag(I) center and results in the

formation of 3D network structure but in Cd CPs and Mn CPs the imine N remain uncoordinated. The carboxylate functionality in the Cd CP resulted in chelating as well as bridging coordination modes whereas in Ag and Mn CPs only chelating coordination mode of carboxylate was observed (Figure 1.17).

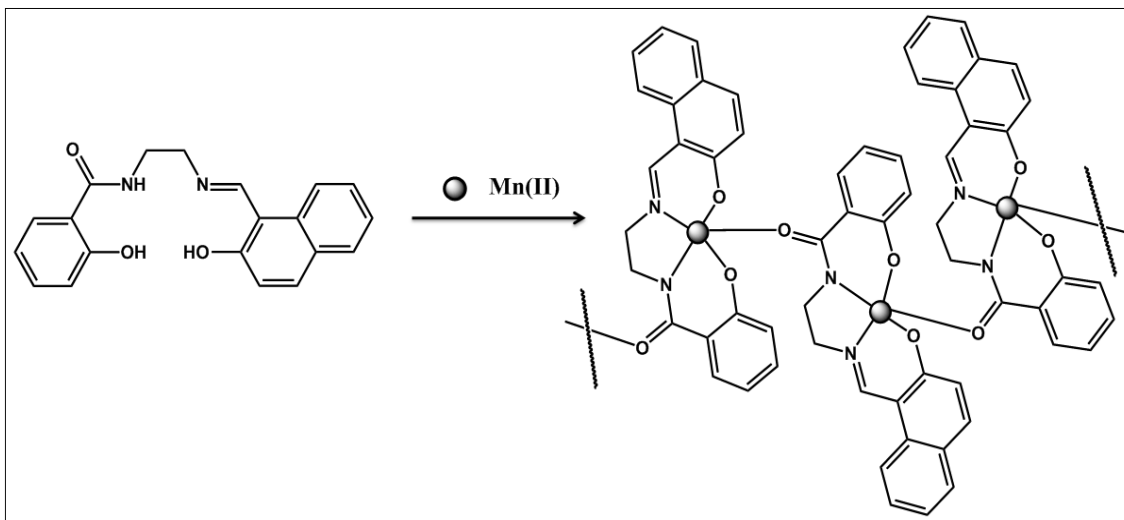


Figure 1.18: 1D chain network of Mn(II) with 2-hydroxy-N-(2-(((3-hydroxynaphthalen-2-yl)methylene)amino)-ethyl)benzamide ligand^[96]

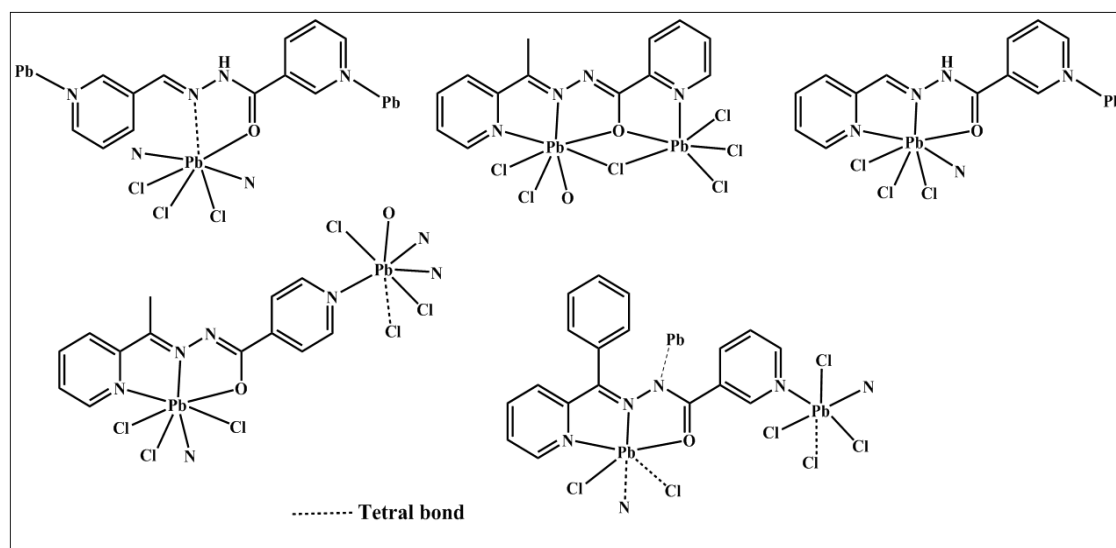


Figure 1.19: Coordination environment of amide-imine functional *bis*-pyridyl ligands with Pb(II)^[97]

Liu *et al.*^[96] synthesized a 1D Mn(II) coordination polymer with a ligand containing amide and imine functions (Figure 1.18). They also studied the magnetic properties of the coordination

where the CP exhibits weak anti-ferromagnetic property throughout the chain through amide function. Mahmoudi *et al.*^[97] recently reported various *bis*-pyridyl ligands contained mixed amide and imine functional groups used to construct Pb CPs. They employed different ligands by changing the position of N in the pyridyl rings and the substituent on imine carbon to assemble different CPs (Figure 1.19). Pb(II) center coordinates with imine N, 2-pyridyl rings and the network is propagated by coordination with 3pyridyl or 4pyridyl rings and also by the formation of tetra bonds. But when *bis*-2pyridyl ligand was used the network propagated *via* the formation of dimeric tetranuclear blocks linked in a zigzag chain. They also explored the effect of ligand geometry on the topology of the network obtained.

1.4.2 Coordination polymers of diimine ligands

Introducing two imine functions between two phenyl groups may increase the chelation effect of metal atoms to form metal salen type coordination complexes as well as dimensionality of the coordination polymers based on the type of primary functional group used and the length of spacer between two imine functions. The most widely used diimine coordination complexes are metal-Salen/Salophane Schiff's base complexes. The homogeneous catalysis was well studied with metal-salen complexes formed with various transition metals.^[98-101] Introducing functional groups at the terminals of metal-Salen complexes results in the construction of novel polymer networks of higher dimensions for desired properties. Song *et al.*^[102] investigated the potential of generating heterogeneous catalysts by incorporating homogeneous metal-Salen catalyst into the frameworks. They reported isoreticular chiral MOFs constructed using Zn_4 secondary building units (SBU) and three different Mn-salen dicarboxylate linkers. These were (i) interpenetrated, (ii) non-interpenetrated and (iii) threefold interpenetrated MOF structures with different pore size due to the length of Mn-Salen dicarboxylates and the steric effect of solvent molecules. They explored the asymmetric epoxidation of various unsymmetrical alkenes with up to 92% enantiomeric excess (ee). Xi *et al.*^[103] synthesized Zn(II) and Cd(II) chiral porous MOFs using VO (Salen) derived dicarboxylate and bipyridyl ligands for heterogeneous catalysis of asymmetric cyanosilylation of aldehydes with up to 95% ee. They further post synthetically introduced Cr(Salen) and Al(Salen) derived bipyridyl linkers to form mixed linker MOFs for obtaining asymmetric epoxide ring opening reaction. Liu *et al.*^[104] assembled the chiral Cu(salen) dicarboxylates with the Cd SBUs to get the efficient chiral heterogeneous catalyst for aziridination and amination of olefins.

1.4.2.1 Coordination polymers of *bis*-pyridyl-diimine ligands

Dong *et al.*^[105] initiated the synthesis of CPs of *bis*-pyridyl-diimine ligands with Co, Ni, Cu, Zn and Cd metals since 2000. They obtained isostructural $\text{Co}(\text{NO}_3)_2$ and $\text{Cd}(\text{NO}_3)_2$ CPs of 1,4-*bis*-(3-pyridyl)-2,3-diaza-1,3-butadiene (**L3a**) which exhibits non-interpenetrated poly cyclohexane structural motifs. The non-interpenetrated open frameworks showed large cavities and channels with adequate pore size for guest inclusion. They used Cd CP for the solvation and desolvation of CH_2Cl_2 guest molecules. Loye and group^[106] also reported the Co and Ni CPs of 1,4-*bis*-(4-pyridyl)-2,3-diaza-1,3-butadiene (**L5a**) and Co CPs of 2,5-*bis*-(4-pyridyl)-3,4-diaza-2,4-hexadiene (**L6a**) where the CPs of **L5a** with Co and Ni exhibit 2D non-interpenetrated brick wall structure and interpenetrated 3D rhombus grid structure respectively and the CPs of Co with **L6a** exhibits 2D square grid when benzene incorporated as solvent and 1D ladder structure obtained with CH_2Cl_2 solvent molecules (Figure 1.20).

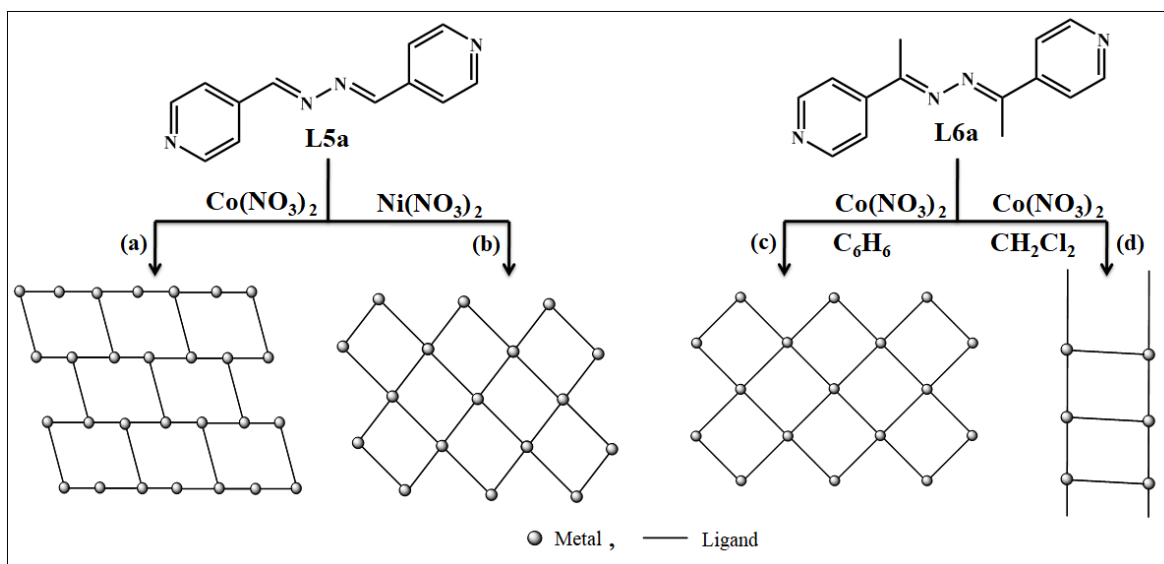


Figure 1.20: Construction of (a) 2D brick wall Co CP, (b) 3D rhombus grid Ni CP, (c) 2D square grid CP and (d) 1D ladder Co CPs using *bis*-pyridyl-diimine ligands^[106]

Ali Morsali *et al.*^[107–111] explored the CPs of *bis*-pyridyl-diimine ligands with various metal salts of Zn, Cd, Pb and Hg and investigated the structural and thermal studies, adsorption of CO_2 , iodine adsorption, catalytic Knoevenagel condensation, dye degradation and the catalytic synthesis of tetrahydrochromones. Ghoshal *et al.*^[112–115] reported several CPs with transition metals with *bis*-pyridyl-diimine ligands along with dicarboxylates and achieved various network architectures. They reported Cu MOFs with 4,4'-azo-*bis*-pyridine and 1,4-*bis*-(4-pyridyl)-2,3-diaza-1,3-butadiene

ligands with 2-nitroterephthalic acid where the MOFs furnished with functional pores with free nitro functional groups embedded in the side walls of the pore channels which were used to capture the CO₂ gas (Figure 1.21). They also reported the Zn CPs of 1,4-*bis*-(4-pyridyl)-2,3-diaza-1,3-butadiene and 2,5-*bis*-(4-pyridyl)-3,4-diaza-2,4-hexadiene ligands with 5-amino-1,3-benzenedicarboxylate and showed the decreased pore size with the presence methyl group results in decreasing the uptake of CO₂.

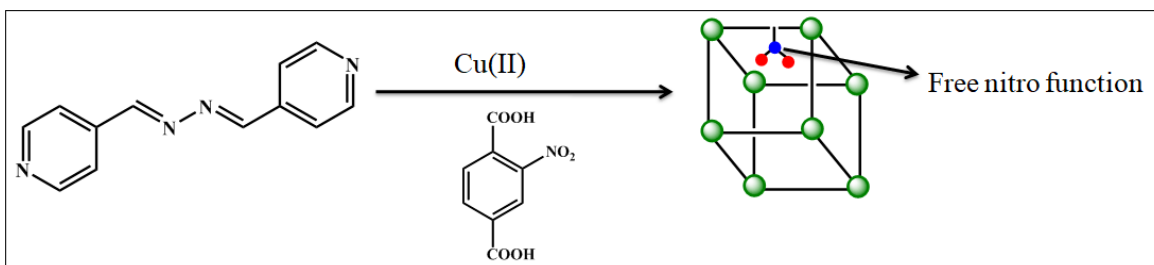


Figure 1.21: Construction of 3D MOFs with functional pores^[115]

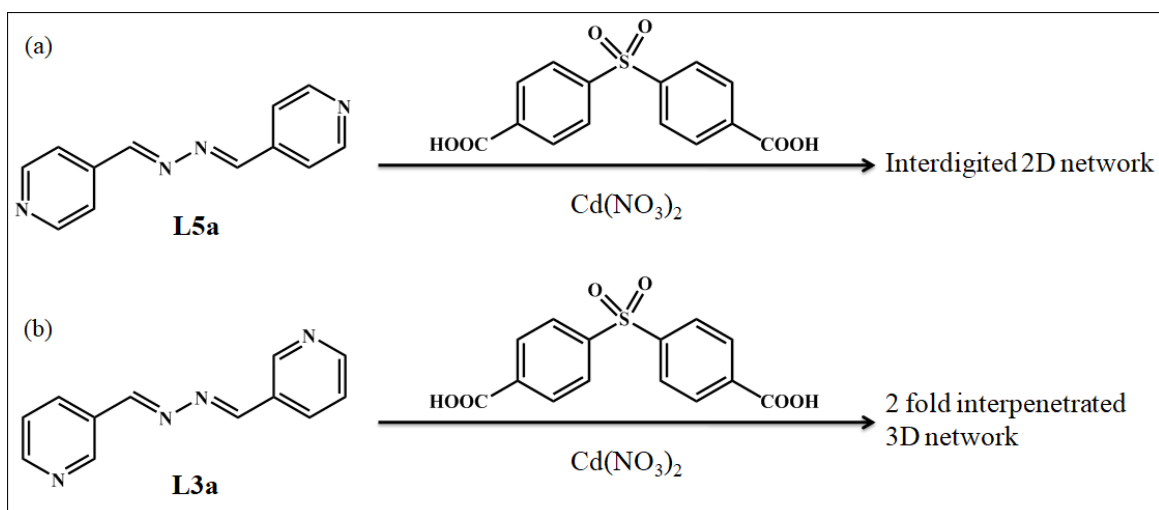


Figure 1.22: Controlled synthesis of CPs by shifting coordination sites^[116]

Parshamoni *et al.*^[116] reported two Cd MOFs of 4,4'-sulfonyl dibenzoic acid with 1,4-*bis*-(4-pyridyl)-2,3-diaza-1,3-butadiene (**L5a**) and with 1,4-*bis*-(3-pyridyl)-2,3-diaza-1,3-butadiene (**L3a**). They investigated the regulation of pore size on shifting the coordination sites by ligand modification where both the MOFs form secondary building units of same kind but formed 2D interdigitated and 3D porous networks respectively. They observed high selectivity of CO₂ over CH₄ uptake where the 3D MOF showed CO₂ uptake almost double the amount than 2D MOF. Further they examined the solvent effect on the luminescence property of MOFs emulsions of

organic solvents and studied the selective sensing of nitrobenzene even at low concentrations (Figure 1.22).

1.5 Post synthetic properties of coordination polymers

1.5.1 Anion exchange of coordination polymers

Anion exchange of coordination polymers is a type of post synthetic modification,^[117] which is a controlled path to construct various network architectures with pre designed properties. In general, neutral ligands and metal atoms form cationic CPs where the charge can be balanced by the void filling anions or weakly coordinated anions. The anion exchange of CPs is a great deal of interest because anions play a crucial role in many chemical processes. Ghosh *et al.*^[118] reported water stable Ni-MOF with a tripodal neutral ligand and uncoordinated SO_4^{2-} anions occupied the channels. They successfully exchanged the free SO_4^{2-} anions with the $\text{Cr}_2\text{O}_7^{2-}$ anions, a common industrial waste product and with MnO_4^- anions an analog of TcO_4^- which is a radioactive waste product. The anion exchange is rapid, selective and obtained by visible color change that can be used as a real time sensor. They examined the selectivity of $\text{Cr}_2\text{O}_7^{2-}$ or MnO_4^- ions from the binary mixtures of salts of ClO_4^- , NO_3^- , BF_4^- or CF_3SO_3^- ions where the exchange of $\text{Cr}_2\text{O}_7^{2-}$ or MnO_4^- ions were selective over other anions. Li *et al.*^[119] explored the dual structural evolution of a Ag(II) CP prompted by anion exchange. They harvested a Ag CP with a neutral ligand which acts as a tridentate linker and the NO_3^- ions reside freely in the voids results a threefold interpenetrated network. Anion exchange reactions were performed with NO_2^- and CF_3COO^- ions where single-crystal-to-single-crystal (SC-SC) transformations occurred. The anion exchanged CP with NO_2^- exhibited similar structure but the NO_2^- ions are coordinated to the Ag atoms in a chelating mode but when the NO_3^- ions exchanged with CF_3COO^- ions, the cationic network changes to neutral and the threefold interpenetrated network turns to twofold inter penetrated network without change in topology. Roy *et al.*^[120] synthesized intriguing Ag CPs with *bis*-(cyanobenzyl)- biperidine ligands in presence of different anions, guest molecules and at different ligand to metal ratios. The ligand forms two different topological 3D CPs at 1:1 and 1:2 ligand to metal ratios in presence NO_3^- anion. The same components formed 2D networks in presence of aromatic guest molecules perylene and pyrene. The components also formed a 3D CP in presence of ClO_4^- anions but the CF_3SO_3^- and BF_4^- anions directs the components to form 2D and 1D networks, respectively. While the PF_6^- anions restrict the

propagation of CP by forming coordination complex. They performed the anion exchange and observed that only the NO_3^- and BF_4^- anion exchange was reversible and the remaining anion exchange studies were irreversible (Figure 1.23).

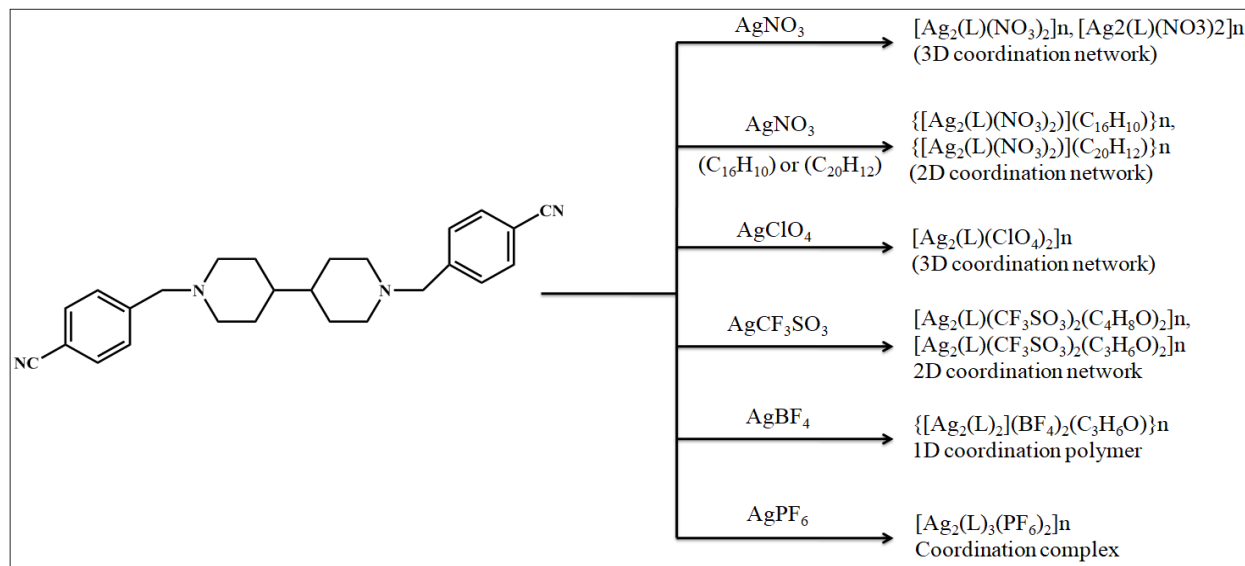


Figure 1.23: Structural variations with different counter anions^[120]

1.5.2 Adsorption studies of coordination polymers

Coordination polymers and metal organic frameworks are widely used materials due to the porosity to accommodate guest molecules for storage, separation, sensing etc.^[121–123] The flexibility of porous CPs recommends control of pore shape and size. The chemical functionality of the ligands result in electronic interactions such as hydrogen-bonding, π -electronic moieties, polar groups, and organic acid/base sites, leading to structural transformations shrinking, and expansion of the overall network, which is exhibited by the unusual sorption and reaction properties. Liu *et al.*^[124] reported a Cd MOF with a triazole based ligand for the enrichment of iodine using molecular sorption and ion exchange processes. In the molecular sorption process the crystals of MOF were dipped in closed atmosphere of hexane solution of I_2 . The adsorption of iodine was observed by color change and the encapsulation of iodine was due to the formation of $\text{ClO}_4^- \cdots \text{I}_2$, $\pi \cdots \text{I}$ and $\text{N-H} \cdots \text{I}_2$ interactions. Further the execution of iodine achieved by immersing the iodine enriched crystals into ethanol solution. In ion exchange process, dilute solution of MOF was taken and the ClO_4^- ions were exchanged by the aqueous solution of NaIO_3 where the anion exchange is reversible which further identified using luminescence study of MOF. Sava *et al.*^[125] reported a Cu-BTC MOF and identified the preferential adsorption of I_2

from a mixture of steam of iodine and water vapor using a comprehensive structural and modeling analysis. They described that the adsorption of iodine occurs in two cages of the MOF. The triangular smaller cage in which I₂ strongly bound by the carbonyl O and the larger pores in which I₂ interacts with the metal clusters and organic linkers with slightly longer contacts. The adsorption of I₂ at the junction of both the pores result a hydrophobic barrier that prevents water adsorption. Under the tested conditions, I₂ is adsorbed preferentially over water. That MOF represented as the highest reported I₂ adsorbed MOF(175 wt % I₂ or 3 I/Cu).^[125]

The intensity of water pollution is a serious problem as a result of industrial development and pollution due to organic dyes is one of the most abundant and frequently observed water pollutants. Hasan *et al.*^[126] reviewed the possible mechanisms for the adsorption of organic dyes which includes electrostatic interactions, hydrogen bonding, acid-base interactions, $\pi\cdots\pi$ interactions/stacking, hydrophobic interactions, pore/size selective adsorption etc. Du *et al.*^[127] reported a 1D Holmium CP with 3,3',5,5'-azobenzene-tetracarboxylic acid and explored its cationic dye adsorption studies where they observed the adsorption of Crystal Violet, Rhodamine B, Safranin T and Methylene Blue. The binary mixtures of these dye showed the selective adsorption of methylene blue over other cationic dyes. Further they explored the enhanced adsorption of all these cationic dyes with temperature in less period of time when the adsorption performed at 50 °C. Moreover, they also optimized the MB adsorption study at different pH range from 2-12 where MB was shown maximum adsorption at pH 3. They mentioned the adsorption was occurred due to the exchange of dimethyl amine of CP with the cationic dyes and the adsorption is size and charge selective due to which different dyes adsorbed at different rates.

1.6 Aim of the present study

Construction of functional coordination polymers with various novel robust or flexible architectures with desired properties has always been a major challenge. This can be achieved by designing various coordination building units which include different types of ligands (neutral, anionic or mixed functional of ligands), metals with various coordination abilities (transition metals, lanthanides or actinides), counter anions used with the metal salts, type of solvents used (polar, non-polar or mixture of solvents), presence of guest molecules (aliphatic or aromatic) and the conditions under which the reactions have been performed (temperature, pressure, microwave, mechano-chemical etc.).

The main objective of the present thesis is to obtain various 1D, 2D or 3D coordination polymers constructing with ligands in combination of different functional groups. Synthesizing varieties of networks lead us to the following achievements: (i) Construction of diverse network CPs with different topologies where the assembling of networks *via* different functional ligands at different reaction conditions, (ii) post synthetic transformations of CPs by exchange of counter ions, (iii) Guest inclusion studies inside the framework *via* adsorption through non-covalent interactions, whereas the designs of CPs leads to identify the structure property relationship will be explored.

1.7 References

- 1 J. M. Lehn, *Pure Appl. Chem.*, 1978, **50**, 871–892.
- 2 J. M. Lehn, *Angew. Chem. Int. Ed.*, 1988, **27**, 89–112.
- 3 D. J. Cram, *Angew. Chem. Int. Ed.*, 1988, **27**, 1009–1020.
- 4 C. J. Pedersen, *Angew. Chem. Int. Ed.*, 1988, **27**, 1021–1027.
- 5 J. M. Lehn, *Supramolecular chemistry*, Vch, Weinheim Germany, 1995, vol. 1.
- 6 D. J. Cram, *Angew. Chem. Int. Ed.*, 1986, **25**, 1039–1057.
- 7 T. R. Cook, Y. R. Zheng and P. J. Stang, *Chem. Rev.*, 2012, **113**, 734–777.
- 8 D. H. Qu, Q. C. Wang, Q. W. Zhang, X. Ma and H. Tian, *Chem. Rev.*, 2015, **115**, 7543–7588.
- 9 M. D. Hollingsworth, *Science*, 2002, **295**, 2410–2413.
- 10 T. Kato, *Science*, 2002, **295**, 2414–2418.
- 11 O. Ikkala and G. ten Brinke, *Science*, 2002, **295**, 2407–2409.
- 12 G. M. J. Schmidt, *Pure Appl. Chem.*, 1971, **27**, 647–678.
- 13 G. R. Desiraju and G. W. Parshall, *Crystal Engineering: The Design of Organic Solids*, Elsevier, Amsterdam 1989.
- 14 J. Liu, P. K. Thallapally, B. P. McGrail, D. R. Brown and J. Liu, *Chem. Soc. Rev.*, 2012, **41**, 2308–2322.
- 15 B. Chen, L. Wang, F. Zapata, G. Qian and E. B. Lobkovsky, *J. Am. Chem. Soc.*, 2008, **130**, 6718–6719.
- 16 B. Chen, L. Wang, Y. Xiao, F. R. Fronczek, M. Xue, Y. Cui and G. Qian, *Angew. Chem. Int. Ed.*, 2009, **121**, 508–511.

- 17 S. Hasegawa, S. Horike, R. Matsuda, S. Furukawa, K. Mochizuki, Y. Kinoshita and S. Kitagawa, *J. Am. Chem. Soc.*, 2007, **129**, 2607–2614.
- 18 C. V McGuire and R. S. Forgan, *Chem. Commun.*, 2015, **51**, 5199–5217.
- 19 T. Devic, P. Horcajada, C. Serre, F. Salles, G. Maurin, B. Moulin, D. Heurtaux, G. Clet, A. Vimont, J. M. Greneche and others, *J. Am. Chem. Soc.*, 2009, **132**, 1127–1136.
- 20 D. Y. Lee, E. K. Kim, C. Y. Shin, D. V Shinde, W. Lee, N. K. Shrestha, J. K. Lee and S. H. Han, *RSC Adv.*, 2014, **4**, 12037–12042.
- 21 C. A. Bauer, T. V Timofeeva, T. B. Settersten, B. D. Patterson, V. H. Liu, B. A. Simmons and M. D. Allendorf, *J. Am. Chem. Soc.*, 2007, **129**, 7136–7144.
- 22 C. G. Silva, A. Corma and H. Garcia, *J. Mater. Chem.*, 2010, **20**, 3141–3156.
- 23 G. R. Desiraju, *Angew. Chem. Int. Ed.*, 1995, **34**, 2311–2327.
- 24 F. H. Allen and O. Kennard, *Chem. Des. Autom. News*, 1993, **8**, 31–37.
- 25 A. M. Christofi, P. J. Garratt, G. Hogarth, A. J. Ibbett, Y. F. Ng and J. W. Steed, *Tetrahedron*, 2002, **58**, 4543–4549.
- 26 R. Hilgenfeld and W. Saenger, *Angew. Chem. Int. Ed.*, 1981, **20**, 1045–1046.
- 27 R. Taylor and O. Kennard, *Acc. Chem. Res.*, 1984, **17**, 320–326.
- 28 T. Steiner, *Angew. Chem. Int. Ed.*, 2002, **41**, 48–76.
- 29 W. M. Latimer and W. H. Rodebush, *J. Am. Chem. Soc.*, 1920, **42**, 1419–1433.
- 30 L. Pauling, *The nature of the chemical bond: and the structure of molecules and crystals; an introduction to modern structural chemistry*, 1940.
- 31 G. C. Pimentel and A. L. McClellan, *The Hydrogen Bond*, Freeman, San Francisco, 1960.
- 32 P. W. Atkins and J. A. Beran, *General chemistry*, Scientific american books, 1992.
- 33 G. R. Desiraju and T. Steiner, *The weak hydrogen bond: in structural chemistry and biology*, International Union of Crystal, 2001, vol. 9.
- 34 C. B. Aakeroy, *Chem. Commun.*, 1998, 1067–1068.
- 35 C. B. Aakeroy, A. M. Beatty and D. S. Leinen, *Angew. Chem. Int. Ed.*, 1999, **38**, 1815–1819.
- 36 C. B. Aakeroy, A. M. Beatty and D. S. Leinen, *CrystEngComm*, 2002, **4**, 310–314.
- 37 D. Braga and F. Grepioni, *Acc. Chem. Res.*, 2000, **33**, 601–608.
- 38 C. Bazzicalupi, A. Bencini, E. Berni, A. Bianchi, S. Ciattini, C. Giorgi, P. Paoletti and B. Valtancoli, *Eur. J. Inorg. Chem.*, 2001, **2001**, 629–632.

- 39 I. Goldberg, *Chem. Commun.*, 2005, 1243–1254.
- 40 D. Braga, F. Grepioni, K. Biradha, V. R. Pedireddi and G. R. Desiraju, *J. Am. Chem. Soc.*, 1995, **117**, 3156–3166.
- 41 D. Braga, F. Grepioni and G. R. Desiraju, *Chem. Rev.*, 1998, **98**, 1375–1406.
- 42 B. F. Hoskins and R. Robson, *J. Am. Chem. Soc.*, 1990, **112**, 1546–1554.
- 43 M. Eddaoudi, H. Li and O. M. Yaghi, *J. Am. Chem. Soc.*, 2000, **122**, 1391–1397.
- 44 M. O. Sinnokrot and C. D. Sherrill, *J. Phys. Chem. A*, 2006, **110**, 10656–10668.
- 45 O. M. Yaghi, M. O’keeffe, N. W. Ockwig, H. K. Chae, M. Eddaoudi and J. Kim, *Nature*, 2003, **423**, 705.
- 46 S. L. Cockroft, C. A. Hunter, K. R. Lawson, J. Perkins and C. J. Urch, *J. Am. Chem. Soc.*, 2005, **127**, 8594–8595.
- 47 H. Cai, Y. Guo and J. G. Li, *Acta Crystallogr. Sect. C*, 2013, **69**, 8–10.
- 48 Y. Kinoshita, I. Matsubara, T. Higuchi and Y. Saito, *Bull. Chem. Soc. Jpn.*, 1959, **32**, 1221–1226.
- 49 F. W. Knobloch and W. H. Rauscher, *J. Polym. Sci.*, 1959, **38**, 261–262.
- 50 A. A. Berlin and N. G. Matveeva, *Russ. Chem. Rev.*, 1960, **29**, 119–128.
- 51 B. P. Block, S. H. Rose, Cw. Schaumann, E. S. Roth and J. Simkin, *J. Am. Chem. Soc.*, 1962, **84**, 3200–3201.
- 52 M. Kubo, M. Kishita and Y. Kuroda, *J. Polym. Sci.*, 1960, **48**, 467–471.
- 53 E. A. Tomic, *J. Appl. Polym. Sci.*, 1965, **9**, 3745–3752.
- 54 S. R. Batten, B. F. Hoskins and R. Robson, *J. Am. Chem. Soc.*, 1995, **117**, 5385–5386.
- 55 S. Kitagawa, S. Matsuyama, M. Munakata and T. Emori, *Dalt. Trans.*, 1991, 2869–2874.
- 56 S. Kitagawa, S. Kawata, Y. Nozaka and M. Munakata, *Dalt. Trans.*, 1993, 1399–1404.
- 57 D. Riou and G. Ferey, *J. Mater. Chem.*, 1998, **8**, 2733–2735.
- 58 H. Li, M. Eddaoudi, M. O’Keeffe and O. M. Yaghi, *Nature*, 1999, **402**, 276.
- 59 J. R. Long and O. M. Yaghi, *Chem. Soc. Rev.*, 2009, **38**, 1213–1214.
- 60 K. Biradha, A. Ramanan and J. J. Vittal, *Cryst. Growth Des.*, 2009, **9**, 2969–2970.
- 61 S. R. Batten, N. R. Champness, X. M. Chen, J. Garcia Martinez, S. Kitagawa, L. Ohrström, M. O’Keeffe, M. P. Suh and J. Reedijk, *CrystEngComm*, 2012, **14**, 3001–3004.
- 62 G. Ferey, *Chem. Soc. Rev.*, 2008, **37**, 191–214.
- 63 F. Kubel and J. Strahle, *Zeitschrift für Naturforsch. B*, 1982, **37**, 272–275.
-

-
- 64 S. K. Chawla, M. S. Hundal, J. Kaur and S. Obrai, *Polyhedron*, 2001, **20**, 2105–2111.
- 65 O. M. Yaghi, H. Li and T. L. Groy, *Inorg. Chem.*, 1997, **36**, 4292–4293.
- 66 A. J. Fletcher, E. J. Cussen, D. Bradshaw, M. J. Rosseinsky and K. M. Thomas, *J. Am. Chem. Soc.*, 2004, **126**, 9750–9759.
- 67 R. W. Seidel, R. Goddard, B. Zibrowius and I. M. Oppel, *Polymers*, 2011, **3**, 1458–1474.
- 68 T. L. Hennigar, D. C. MacQuarrie, P. Losier, R. D. Rogers and M. J. Zaworotko, *Angew. Chem. Int. Ed.*, 1997, **36**, 972–973.
- 69 R. Atencio, K. Biradha, T. L. Hennigar, K. M. Poirier, K. N. Power, C. M. Seward, N. S. White and M. J. Zaworotko, *CrystEngComm*, 1998, **1**, 203–212.
- 70 W. G. Lu, L. Jiang, X. L. Feng and T. B. Lu, *Cryst. Growth Des.*, 2006, **6**, 564–571.
- 71 J. Lin, L. Wen, S. Zang, Y. Su, Z. Lu, H. Zhu and Q. Meng, *Inorg. Chem. Commun.*, 2007, **10**, 74–76.
- 72 O. M. Yaghi and G. Li, *Angew. Chem. Int. Ed.*, 1995, **34**, 207–209.
- 73 L. R. MacGillivray, S. Subramanian and M. J. Zaworotko, *J. Chem. Soc. Chem. Commun.*, 1994, 1325–1326.
- 74 M. Fujita, Y. J. Kwon, S. Washizu and K. Ogura, *J. Am. Chem. Soc.*, 1994, **116**, 1151–1152.
- 75 K. Biradha and M. Fujita, *Dalt. Trans.*, 2000, 3805–3810.
- 76 K. Biradha, Y. Hongo and M. Fujita, *Angew. Chem. Int. Ed.*, 2000, **39**, 3843–3845.
- 77 K. Biradha, M. Aoyagi and M. Fujita, *J. Am. Chem. Soc.*, 2000, **122**, 2397–2398.
- 78 M. L. Tong, J. W. Cai, X. L. Yu, X. M. Chen, S. W. Ng and T. C. W. Mak, *Aust. J. Chem.*, 1998, **51**, 637–641.
- 79 K. Biradha and M. Fujita, *Chem. Commun.*, 2001, 15–16.
- 80 R. W. Gable, B. F. Hoskins and R. Robson, *J. Chem. Soc. Chem. Commun.*, 1990, 1677–1678.
- 81 Y. Gong, J. Li, J. Qin, T. Wu, R. Cao and J. Li, *Cryst. Growth Des.*, 2011, **11**, 1662–1674.
- 82 M. Sarkar and K. Biradha, *Cryst. Growth Des.*, 2007, **7**, 1318–1331.
- 83 X. L. Wang, J. Luan, F. F. Sui, H.-Y. Lin, G. C. Liu and C. Xu, *Cryst. Growth Des.*, 2013, **13**, 3561–3576.
- 84 S. Subramanian and M. J. Zaworotko, *Angew. Chem. Int. Ed.*, 1995, **34**, 2127–2129.
- 85 S. Noro, S. Kitagawa, M. Kondo and K. Seki, *Angew. Chem. Int. Ed.*, 2000, **39**, 2081–
-

- 2084.
- 86 F. Robinson and M. J. Zaworotko, *Chem. Commun.*, 1995, 2413–2414.
- 87 O. M. Yaghi and H. Li, *J. Am. Chem. Soc.*, 1995, **117**, 10401–10402.
- 88 O. M. Yaghi and H. Li, *J. Am. Chem. Soc.*, 1996, **118**, 295–296.
- 89 L. Carlucci, G. Ciani, D. M. Proserpio and A. Sironi, *Chem. Commun.*, 1994, 2755–2756.
- 90 A. Azhdari Tehrani, H. Ghasempour, A. Morsali, G. Makhloufi and C. Janiak, *Cryst. Growth Des.*, 2015, **15**, 5543–5547.
- 91 A. Pal, S. Chand, S. Senthilkumar, S. Neogi and M. C. Das, *CrystEngComm*, 2016, **18**, 4323–4335.
- 92 Y. Aono, H. Yoshida, K. Katoh, B. K. Breedlove, K. Kagesawa and M. Yamashita, *Inorg. Chem.*, 2015, **54**, 7096–7102.
- 93 S. Pal, T. K. Pal and P. K. Bharadwaj, *CrystEngComm*, 2016, **18**, 1825–1831.
- 94 B. Notash, N. Safari and H. R. Khavasi, *CrystEngComm*, 2012, **14**, 6788–6796.
- 95 S. H. Han and S. W. Lee, *Polyhedron*, 2012, **31**, 255–264.
- 96 P. P. Liu, L. Sheng, X. Q. Song, W. Y. Xu and Y. A. Liu, *Inorganica Chim. Acta*, 2015, **434**, 252–257.
- 97 G. Mahmoudi, A. V. Gurbanov, S. Rodriguez-Hermida, R. Carballo, M. Amini, A. Bacchi, M. P. Mitoraj, F. Sagan, M. Kukułka and D. A. Safin, *Inorg. Chem.*, 2017, **56**, 9698–9709.
- 98 T. Katsuki, *Coord. Chem. Rev.*, 1995, **140**, 189–214.
- 99 E. N. Jacobsen, *Acc. Chem. Res.*, 2000, **33**, 421–431.
- 100 P. G. Cozzi, *Chem. Soc. Rev.*, 2004, **33**, 410–421.
- 101 E. M. McGarrigle and D. G. Gilheany, *Chem. Rev.*, 2005, **105**, 1563–1602.
- 102 F. Song, C. Wang, J. M. Falkowski, L. Ma and W. Lin, *J. Am. Chem. Soc.*, 2010, **132**, 15390–15398.
- 103 W. Xi, Y. Liu, Q. Xia, Z. Li and Y. Cui, *Chem. Eur. J.*, 2015, **21**, 12581–12585.
- 104 Y. Liu, Z. Li, G. Yuan, Q. Xia, C. Yuan and Y. Cui, *Inorg. Chem.*, 2016, **55**, 12500–12503.
- 105 Y.-B. Dong, M. D. Smith, R. C. Layland and H. C. Zur Loye, *Chem. Mater.*, 2000, **12**, 1156–1161.
- 106 D. M. Ciurtin, Y. B. Dong, M. D. Smith, T. Barclay and H. C. Zur Loye, *Inorg. Chem.*, 2001, **40**, 2825–2834.

- 107 L. Hashemi and A. Morsali, *CrystEngComm*, 2014, **16**, 4955–4958.
- 108 M. Y. Masoomi, K. C. Stylianou, A. Morsali, P. Retailleau and D. Maspoch, *Cryst. Growth Des.*, 2014, **14**, 2092–2096.
- 109 V. Safarifard, S. Beheshti and A. Morsali, *CrystEngComm*, 2015, **17**, 1680–1685.
- 110 M. Y. Masoomi, A. Morsali and P. C. Junk, *CrystEngComm*, 2015, **17**, 686–692.
- 111 M. Y. Masoomi, S. Beheshti and A. Morsali, *J. Mater. Chem. A*, 2014, **2**, 16863–16866.
- 112 B. Bhattacharya, R. Haldar, D. K. Maity, T. K. Maji and D. Ghoshal, *CrystEngComm*, 2015, **17**, 3478–3486.
- 113 A. Das, B. Bhattacharya, D. K. Maity, A. Halder and D. Ghoshal, *Polyhedron*, 2016, **117**, 585–591.
- 114 A. Halder, B. Bhattacharya, F. Haque and D. Ghoshal, *Cryst. Growth Des.*, 2017, **17**, 6613–6624.
- 115 D. K. Maity, A. Halder, B. Bhattacharya, A. Das and D. Ghoshal, *Cryst. Growth Des.*, 2016, **16**, 1162–1167.
- 116 S. Parshamoni, J. Telangae and S. Konar, *Dalton. Trans.*, 2015, **44**, 20926–20935.
- 117 L. Hashemi and A. Morsali, *CrystEngComm*, 2013, **15**, 8894–8897.
- 118 A. V Desai, B. Manna, A. Karmakar, A. Sahu and S. K. Ghosh, *Angew. Chem. Int. Ed.*, 2016, **128**, 7942–7946.
- 119 C. P. Li, S. Wang, W. Guo, Y. Yan and M. Du, *Chem. Commun.*, 2016, **52**, 11060–11063.
- 120 S. Roy, H. M. Titi, B. K. Tripuramallu, N. Bhunia, R. Verma and I. Goldberg, *Cryst. Growth Des.*, 2016, **16**, 2814–2825.
- 121 Z. Chang, D. H. Yang, J. Xu, T. L. Hu and X. H. Bu, *Adv. Mater.*, 2015, **27**, 5432–5441.
- 122 S. Y. Liu, J. P. Zhang and X. M. Chen, *Cryst. Growth Des.*, 2017, **17**, 1441–1449.
- 123 D. Banerjee, A. J. Cairns, J. Liu, R. K. Motkuri, S. K. Nune, C. A. Fernandez, R. Krishna, D. M. Strachan and P. K. Thallapally, *Acc. Chem. Res.*, 2014, **48**, 211–219.
- 124 Q. K. Liu, J. P. Ma and Y. B. Dong, *Chem. Commun.*, 2011, **47**, 7185–7187.
- 125 D. F. Sava, K. W. Chapman, M. A. Rodriguez, J. A. Greathouse, P. S. Crozier, H. Zhao, P. J. Chupas and T. M. Nenoff, *Chem. Mater.*, 2013, **25**, 2591–2596.
- 126 Z. Hasan and S. H. Jung, *J. Hazard. Mater.*, 2015, **283**, 329–339.
- 127 P. Y. Du, H. Li, X. Fu, W. Gu and X. Liu, *Dalton. Trans.*, 2015, **44**, 13752–13759.

Chapter-2

Materials and Experimental Methods

Materials and Experimental Techniques

2.1 Introduction:

This chapter deals with the chemicals used and the experimental methods utilized to accomplish the objectives of the current thesis. The experimental methods include synthesis and characterization of organic Schiff's base ligands and their coordination polymers. Suitable crystallization techniques employed to achieve good quality crystals of ligands and CPs, their characterization, and property studies. The characterization techniques employed here include IR, NMR, Elemental analysis, UV-visible Spectroscopy, Spectrofluorometry, Single crystal XRD and powder XRD. Photo-physical studies, thermal analysis and adsorption properties of organic molecules and CPs were studied using UV-visible Spectrophotometer, Spectrofluorometer and Thermo Gravimetric Analysis instruments. Details of instrumentation of various experimental techniques are discussed in this chapter.

2.1.1 Chemicals and Reagents:

The following chemicals and reagents used for the synthesis of ligands and CPs were obtained from Sigma-Aldrich Chemicals Pvt. Ltd.

- 2-Pyridinecarboxaldehyde
- 3-Pyridinecarboxaldehyde
- 4-Pyridinecarboxaldehyde
- 2-Acetylpyridine
- 3-Acetylpyridine
- 4-Acetylpyridine
- Hydrazine hydrate
- Ethylenediamine
- Diamino butane
- Hexamethylene-diamine
- 1,2,4,5-Benzenetetracarboxylic acid
- Disodium succinate
- Disodium-1,3benzene-disulfonate
- Potassium bromide
- Barium sulfate

The following chemicals used for the synthesis of ligands and CPs were obtained from Spectrochem Pvt. Ltd.

- Cobalt nitrate hexahydrate
- Nickel nitrate hexahydrate
- Cupric nitrate trihydrate
- Zinc nitrate hexahydrate
- Cadmium nitrate tetrahydrate
- Silver nitrate
- Copper iodide
- Cupric bromide

-
- Nickel chloride hexahydrate
 - Cobalt chloride hexahydrate
 - Zinc chloride
 - Mercuric chloride
 - Cupric acetate hydrate
 - Cobalt acetate tetrahydrate
 - Cadmium acetate
 - Mercuric acetate
 - Copper carbonate
 - Nickel carbonate
 - Zinc carbonate
 - Cadmium carbonate
 - Perchloric acid
 - Malonic acid
 - Succinic acid
 - Glutaric acid
 - Adipic acid
 - Naphthalene
 - Anthracene
 - Pyrene, Iodine
 - Methylene blue
 - Methyl orange
 - Malachite green
 - Rhodamine-B

The following metal salts used for the anion exchange studies of CPs were obtained from Spectrochem Pvt. Ltd.

- Sodium chloride
- Sodium perchlorate
- Sodium sulphate
- Sodium carbonate
- Sodium tetrafluoro borate
- Silicon hexafluoro phosphate
- Ammonium thiocyanate
- Ammonium hexafluoro phosphate

The following metal salts were prepared by using simple anion exchange reaction between the corresponding metal carbonates with perchloric acid for the anion exchange studies of CPs

- Cadmium perchlorate hexahydrate
- Zinc perchlorate hexahydrate
- Copper perchlorate hexahydrate
- Nickel perchlorate hexahydrate
- Silver perchlorate

The following reagents used for the guest inclusion/exchange studies were obtained from Merck Pvt. Ltd.

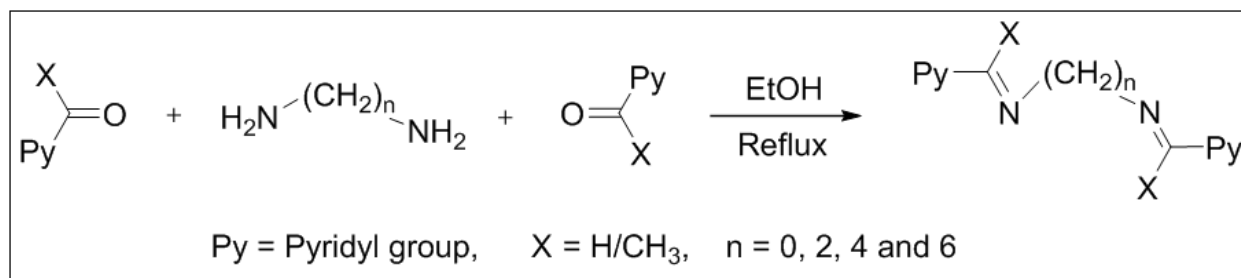
- Benzene
- Toluene
- Xylene
- Phenol
- Nitrobenzene
- Benzonitrile

The following UV-visible grade solvents used for photophysical studies were obtained from Merck Pvt. Ltd.

- Methanol
- Chloroform
- Tetrahydrofuran (THF)
- Dichloromethane (DCM)
- Hexane
- Ethylacetate
- Ethanol
- 1,4-dioxane
- Acetonitrile
- Acetone
- Dimethylsulfoxide (DMSO)
- Dimethylformamide (DMF)

2.2 Synthesis of Schiff base ligands or Schiff base linkers

The ligands were synthesized according to the literature procedure by the usual condensation reaction between carbonyl compounds with diamines where the components are mixed in ethanol and stirred under reflux condition for about 6-8 hours.^[1,2] After the reaction was complete, the solution was concentrated by evaporating ethanol and the resulting compound was recrystallized using hexane.



Scheme 2.1: Synthesis of pyridyl based exobidentate compounds having imine spacer^[1,2]

The compounds are soluble in organic solvents such as EtOH, MeOH, DCM, THF, CHCl₃, DMF and DMSO but partially soluble in hexane and insoluble in water. All the compounds have been recrystallized from hexane and the percentage yield was calculated. Using thin capillary tube, the melting point was recorded. The compounds were characterized by elemental analysis, IR, ¹H NMR and ¹³C NMR.

2.3 Synthesis of co-ordination polymers (CPs)

Usual synthesis of coordination polymers includes pre-designing and synthesis ligands or organic linkers followed by polymerization using various techniques. The exobidentate linkers

bis-pyridyl-*bis*-imine were designed and synthesized using commercially available or prior synthesized compounds. Various methods employed to construct the CPs for reacting ligands with metal salts, where the main goal is to obtain the CPs by using synthesized ligands in complete crystalline form for analyzing them using Single Crystal X-Ray Diffraction (SXRD). Most of the cases direct mixing results in precipitation of product during polymerization reactions between ligands and metal salts. The precipitate can be crystallized by dissolving both by heating or adding various solvents or solvent mixtures and by slow evaporation.

Three methods were engaged for the synthesis of CPs in perfect crystalline form. (i) Solvent diffusion technique, (ii) Vapor diffusion technique and (iii) Solvothermal or Hydrothermal synthesis.

2.3.1 Solvent diffusion technique^[3]

CPs mostly reported has been synthesized using solvent diffusion technique to achieve the CPs in perfectly crystalline form. This method includes very slow diffusion of two solvents contained different components. For this purpose solvents of various densities were taken. Higher density solvent contained organic ligand was poured at the bottom and lower density solvent contained metal salt slowly layered on the top in glass vials or in test tubes and allowed for slow diffusion (Figure 2.1).

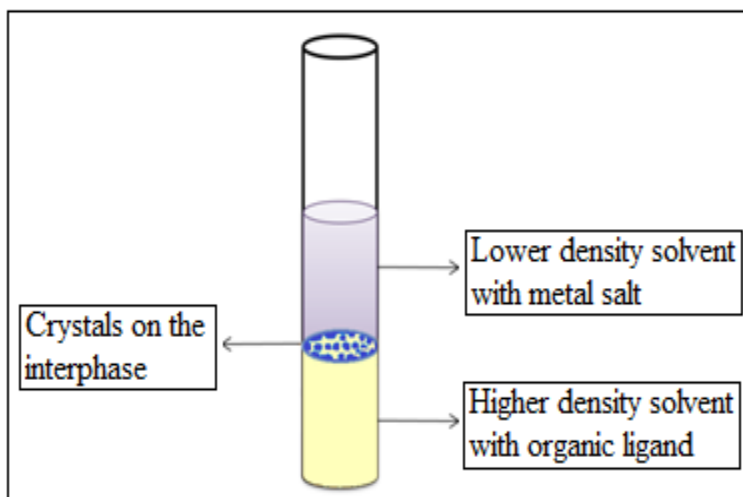


Figure 2.1: Synthesis of coordination polymers (CPs) using layering technique.

Solvents used in the present thesis for layering technique are as follows:

(i) Protic solvents

- ❖ Water, Ethanol, Methanol

(ii) Non-aromatic organic solvents

- ❖ Chloroform (CHCl_3), Dichloromethane (DCM), Acetonitrile (CH_3CN), Carbon tetrachloride (CCl_4), Tetrahydrofuran (THF), Acetone, Dimethylformamide (DMF), Dimethylsulfoxide (DMSO)

(iii) Aromatic organic solvents

- ❖ Benzene, Xylene, Toluene, Nitrobenzene, Benzonitrile, Acetophenone

(iv) Solvents used to dissolve the solid aromatic compounds: CHCl_3 , CCl_4 etc. used to dissolve Dihydroxy benzenes, Naphthalene, Anthracene etc.

2.3.2 Vapor diffusion technique^[4]

Vapor diffusion technique includes diffusion of vapors of high volatile solvent into the low volatile solvent containing the different components to synthesize CPs. In this technique, two vials are used where the two vials arranged in such a way that components are dissolved low volatile solvent contained narrow vial accommodate inside the high volatile solvent contained wider vial. The wider vial should be closed and the solvents allowed for diffusing with time which leads precipitating the compounds in the form of crystals (Figure 2.2).

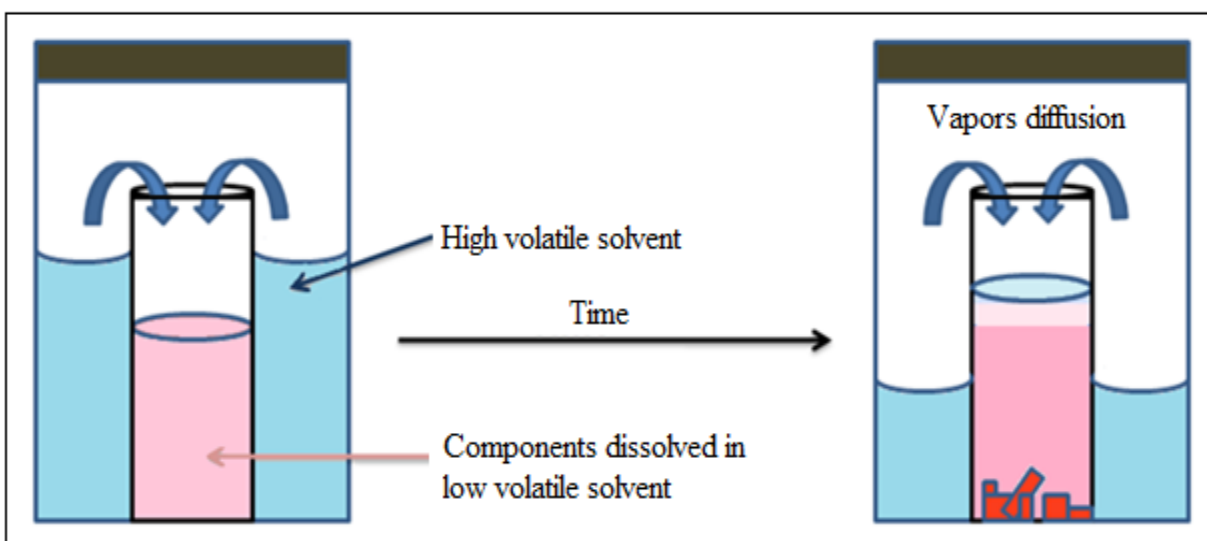


Figure 2.2: Crystallization of coordination polymers (CPs) using vapor diffusion technique.

In general high boiling point solvents such as Benzene, Toluene, Methanol, Tetrahydrofuran (THF), Acetonitrile or Dichloromethane (DCM) are used in narrow vial with dissolved sample and low boiling point solvents such as Hexane, Diethyl-ether or Pentane are used in wider vial.

2.3.3 Solvothermal or Hydrothermal synthesis^[5]

Solvothermal synthesis is applied by using sealed Teflon-lined autoclaves. In this method, all the components of the reaction including ligand, metal salt and solvent should be kept under a particular temperature in Teflon coated sealed autoclave tube. While all the parameters such as composition of components, solubility, concentration, pH value, temperature, pressure, reaction time etc should be set prior to the reaction^[6].

In hydrothermal synthesis as solvent selection is most important usually water is used as the priority solvent. As most of the organic ligands have poor solubility in water, solvents other than water are also used. For maintaining solubility either mono or mixture of solvents can also be useful, some cases ultrasonic pretreatment for solubility can also be helpful.

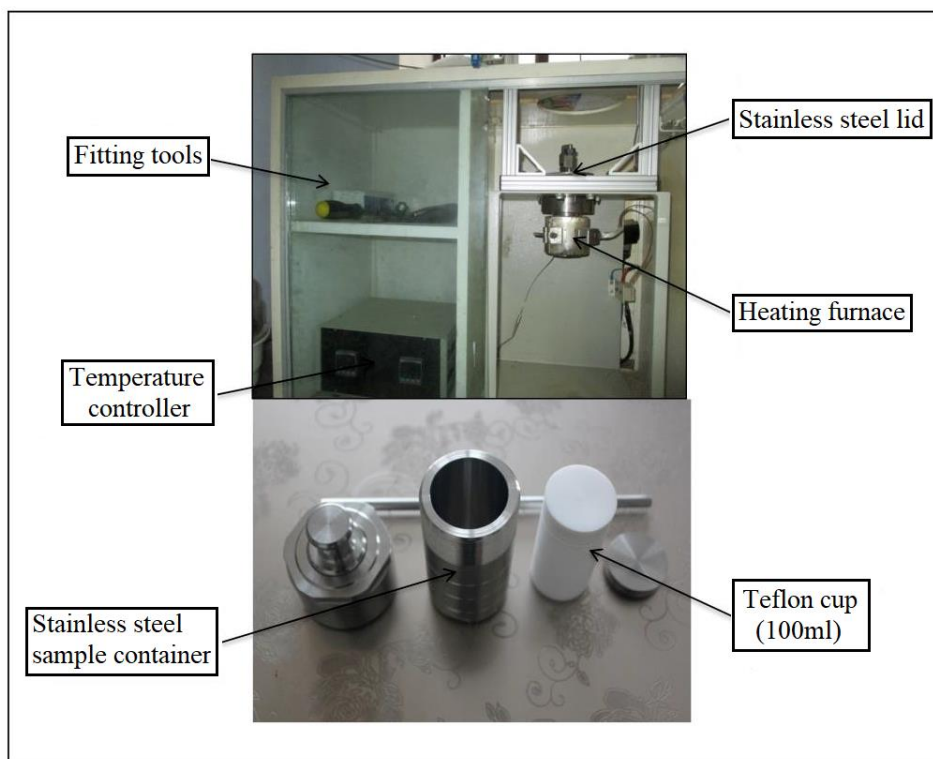


Figure 2.3: Photograph of autoclave used for solvothermal synthesis.

During the formation of CPs, solvent molecules play a key role as structure directing, pores filling and templating agents. Slow cooling and cooling speed is essential parameter to get good quality crystals. As the solubility of reactants enhances with temperature, the hydrothermal synthesis plays an important role to generate stable and robust CPs compared with solution reactions^[7].

2.4 Characterization Techniques

The instrumental analytical techniques used for characterization and property analysis of the organic compounds and CPs are summarized below.

The instruments used for the characterization are as follows

- Infrared (IR) spectroscopy
- Elemental Analyzer
- Nuclear Magnetic Resonance (NMR) Spectroscopy
- Single Crystal X-ray Diffraction (SXRD)
- Powder X-ray Diffraction (PXRD)

The instruments used for studying the properties are as follows

- Ultraviolet (UV) – visible Spectroscopy
- Fluorescence spectroscopy
- Thermo Gravimetric Analysis (TGA)

2.4.1 Infrared (IR) Spectroscopy

IR spectrum is a graph of wave number on the x-axis vs. absorbance or transmittance of infrared radiation on the y-axis. IR radiation is associated with photon energies ranges from 1-15 kcal.mol⁻¹ which induce vibrations in any molecule in many ways. According to Gross selection rule, only those vibrations are IR active in which there is a change in the dipole moment during vibration. Each fundamental vibration does not display individual signal separately for individual molecules but a combined spectrum of all possible vibrations could display at a time. Various factors especially the increased or decreased intermolecular interactions lead to variations in the number of observed signals.

IR spectroscopy used in the present thesis work to analyze the synthesized molecules qualitatively. For the synthesized *bis*-pyridyl-*bis*-imine Schiff base ligands and their CPs, IR spectra were recorded with KBr pellets using ABB Bomen MB-3000 and Shimadzu IRAffinity-1S Fourier transform infrared (FT-IR) spectrometer (Figure 2.4). The details of the molecules were analyzed by the intensity, position and shape of the peaks obtained in the IR spectrum. The intensities of IR signals indicated by the abbreviations: s (strong), m (medium), w (weak). The broad shaped signal sometimes indicated by br. and approximate peak value (\approx) was given rather a range for such broad signals.



Figure 2.4: Photographs of (a) ABB Bomen MB-3000 and (b) Shimadzu IR Affinity-1S IR instruments

2.4.2 Elemental Analysis

This technique is used to determine the elements especially carbon, hydrogen and nitrogen quantitatively. CHN analysis is accomplished by combusting the sample in excess of oxygen and the combustion products: CO_2 , H_2O , and NO_x (nitric/nitrous oxides) are collected. To calculate the composition of the unknown sample, the masses of these combustion products are used. A staircase type signal is registered whose step height is proportional to the substance amount in the mixture. The detection limit for carbon, hydrogen and nitrogen at sample amounts of 2 to 5 mg was found to be 0.05 weight % (500 ppm).



Figure 2.5: Photograph of Vario Micro V2.20 Elemental analyzer

The elemental analyzer used in the present work is Thermo Finnigan, Italy, Model FLASH EA 1112 series and Vario Micro V2.20 CHN analyzers (Figure 2.5) of the system unit, a MAS 200 auto sampler for solid samples, and a Windows compatible computer with Eager 300 software.

2.4.3 Nuclear Magnetic Resonance (NMR) Spectroscopy

NMR analysis is relevant to any type of molecule which possesses spinning nuclei e.g. ^1H and ^{13}C . The sample is placed in magnetic field to absorb electromagnetic radiation at a particular frequency characteristic to the isotope. The absorption energy, resonance frequency and the signal intensity are directly proportional to the strength of the magnetic field.

The ^1H and ^{13}C NMR of all synthesized Schiff's base ligands were measured with Bruker AVANCE III 400 MHz NMR spectrometer equipped with BBFO probe and auto-sampler, using CDCl_3 or DMSO as solvents (Figure 2.6).



Figure 2.6: Photograph of 400 MHz NMR spectrometer (Bruker AVANCE III)

Using deuterated solvent peak as reference the chemical shift (δ) values were reported in parts per million (ppm). In the present thesis NMR data reported as follows: chemical shifts, multiplicity (s = singlet, d = doublet, t = triplet, q = quartet, dd = doublet of doublets, m = multiplet), and coupling constants (J).

2.4.4 Structural Determination of CPs by X-ray crystallography

Max von Laue in 1912, discovered that in a crystal lattice, similar to the spacing of planes the crystalline substances act as three-dimensional diffraction gratings for X-ray wavelengths^[8]. X-ray crystallography is the most popular and universal technique for determining the crystalline solid structures to the atomic and molecular levels. In this technique, X-rays are passed through the crystalline solids which diffract the incident X-rays into many specific directions similar to the formation of rainbow from the diffracted light of water droplets. Depending on the atomic arrangement and crystal lattice different crystals exhibits different X-ray diffraction patterns. A crystallographer can produce a three-dimensional (3D) picture of the density of electrons by measuring the angles and intensities of the diffracted beams within the crystalline solids by which various other information; chemical bonds between the atoms and their disorder, positions of the atoms in the crystal can be determined. To analyze the structures of our CPs we used two types of X-ray diffraction spectroscopy:

1. Single Crystal X-ray Diffraction (SXRD)
2. Powder X-ray Diffraction (PXRD)

In both the techniques X-rays are generated by a cathode ray tube and the interaction of the incident rays with the sample produces constructive interference and resulted diffracted ray.

$$\text{According to Bragg's Law}^{[9,10]} n\lambda = 2d \sin\theta$$

Where n = order of diffraction

θ = Bragg's angle

d = interplanar spacing

2θ = diffraction angle

λ = wavelength

This relates the diffraction angle with wavelength of electromagnetic radiation and lattice spacing in crystalline solids. These diffracted X-rays are then detected, processed and counted.

2.4.4.1 Single Crystal X-ray Diffraction (SXRD)

This analytical technique provides complete information about the internal lattice structure of crystalline solids which includes unit cell, cell parameters etc. For analysis, the sample should be selected from optically clear, unfractured crystals using a petro graphic microscope. Crystals can be broken off a larger sample and the best fragment selected. Sample crystals should be between 30 and 300 microns with ideal average of 150-250 microns in size. X-ray diffractometers consist of three basic elements - a sample holder, X-ray tube, and X-ray detector. X-rays are generated by heating a filament in a cathode ray tube to produce and accelerating the electrons toward a

target. Molybdenum is the most common target material for single-crystal diffraction, Mo $K\alpha$ radiation = 0.7107\AA .

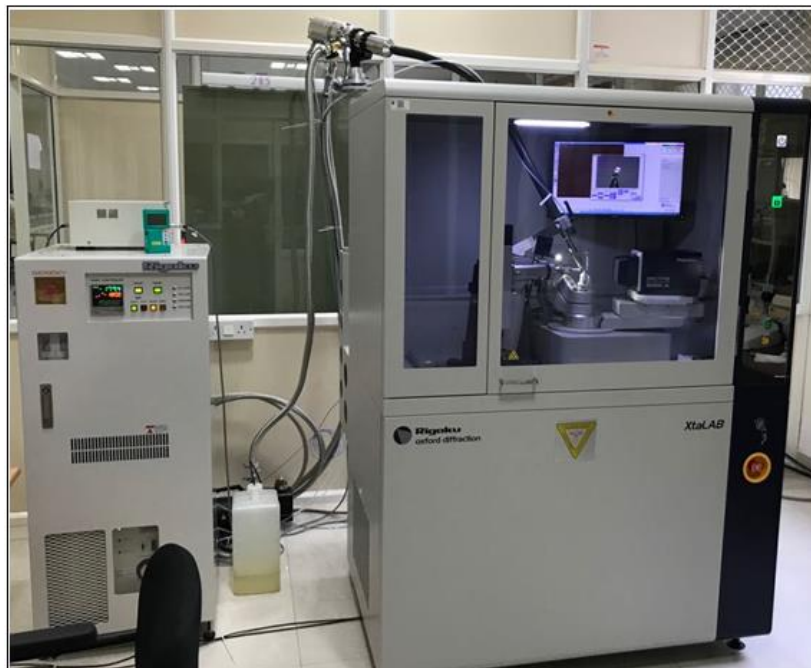


Figure 2.7: Photograph of Rigaku Xta LAB Pro single crystal X-Ray diffractometer

The data have been collected and phase problem must be solved to find the unique set of phases that can be combined with the structure factors to determine the electron density and therefore, the crystal structure. Once the initial crystal structure is solved, various steps can be done to attain the best possible fit between the observed and calculated crystal structure. With an R value the final structure solution will be presented which gives the percentage variation between the observed and calculated structures. In the present study the single crystal X-ray diffractometer were used (1) Xcalibur, Sapphire 3 X-ray diffractometer (University of Jammu, Jammu Tawi) (2) Bruker Kappa APEX II diffractometer (Indian Institute of Science Education and Research, (IISER) Mohali) (3) Rigaku Xta LAB Pro: Kappa dual offset/far diffractometer (Birla Institute of Technology and Science-Pilani, Hyderabad) (Figure 2.7).

2.4.4.2 Powder X-ray Diffraction (PXRD)

In this technique X-rays are generated within a sealed tube under vacuum; for heating the filaments current is applied where the number of electrons emission from the filament depends on the current supplied. A high voltage, 15-60 kilovolts is applied within the tube. This high voltage accelerates the electrons to hit a target, commonly made of Cu and X-rays are produced.

These X-rays are collimated and directed on-to the sample. The sample is powdered to produce particle sizes of less than 10 microns. A detector detects the X-ray signal; the signal is then processed either by a microprocessor or electronically, converting the signal to a count rate. In a powder X-ray diffractogram; the peaks represent positions where the X-ray beam has been diffracted by the crystal lattice. The diffraction pattern is represented as intensity vs. 2θ . Bragg's law is used to convert observed 2θ positions to d_{hkl} . The characteristic set of d-spacings generated in a typical X-ray scan provides a unique "fingerprint" of the mineral present in the sample. After proper interpretation, by comparison with standard patterns and measurements, this "fingerprint" allows for identification of the material. In case of crystalline/polycrystalline solids, well-defined sharp peak pattern is usually obtained and for amorphous/glassy solids, which doesn't have long-range periodic structure, halo patterns are observed.



Figure 2.8: Photograph of Rigaku Mini Flex II powder X-ray diffractometer.

In the PXRD pattern of a crystalline sample, (i) intensity of the peaks correspond to the planar density, (ii) position of the peaks refers to particular sets of planes, (iii) any shift with broadening in peak position may correspond to the lattice strain, (iv) full width at half maximum (β) of the peak deduce the crystalline size (Debye-Scherrer Formula). In the present study, the powder X-ray diffractometer used of Rigaku Mini Flex II (Figure 2.8) with a typical $\text{Cu K}\alpha$ radiation ($\lambda =$

1.54 Å) at room temperature, operated at 30 kV with the filament current of 30 mA. In the present thesis, finely powdered form samples of organic molecules, CPs with different anions and CPs with guest molecules X-ray powder diffraction were compared.

2.4.5 Ultraviolet – visible Spectroscopy (UV-Vis)

The UV-visible spectroscopy can be utilized in the analytical chemistry for calculating different analytes quantitatively such as highly conjugated organic molecules, transition metal ions and biological macromolecules. The UV-visible absorption spectroscopy contains UV, 190-380 nm and Visible, 380-800 nm regions with overall 190-800 nm. When molecules subjected to UV or visible light the π -electrons and non-bonding electrons (n-electrons) present in the highest occupied molecular orbitals (HOMO) excited to the higher energy lowest unoccupied molecular orbitals (LUMO). Since the transition is between electronic energy levels this is also called electronic spectroscopy. UV-visible spectroscopy works based on Lambert-Beer's Law.

$$A = \log (I_0/I) = \varepsilon.c.l$$

Where A = absorbance, c = concentration, ε = molar extinction coefficient, l = path length and I_0 and I are intensity of incident and transmitted light.

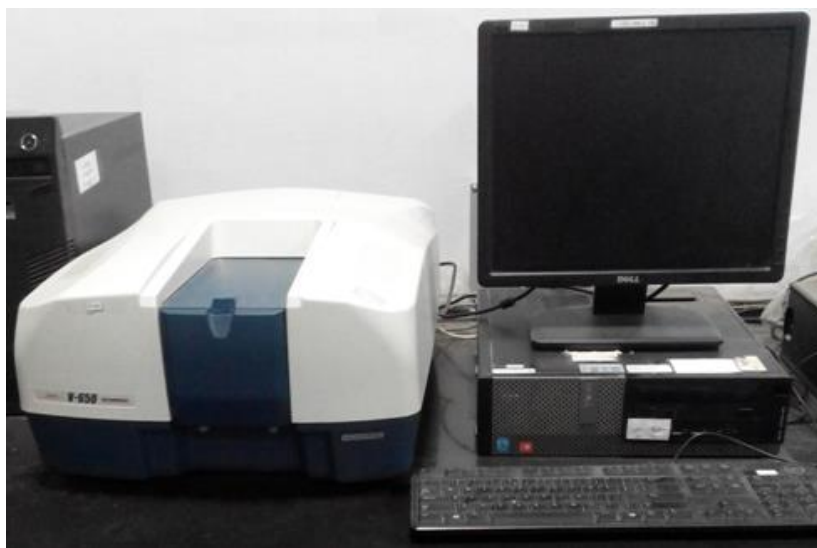


Figure 2.9: Photograph of the JASCO V-650 UV-Vis spectrophotometer

UV-visible spectrum was measured using two separate instruments: (i) JASCO V-650 spectrophotometer for recording solution phase UV-visible spectra and (ii) Shimadzu UV-2450 spectrophotometer for recording solid phase UV-visible spectrum (Figure 2.9). 190-900 nm wavelength range was used in both spectrophotometers. Tungsten (W)-lamp and deuterium (D₂)-

lamp were used as light source for the corresponding 1100-350 nm and 400-190 nm regions and silicon photodiodes are used as light detectors. 0.2 nm is the minimum resolution wavelength used for both the spectrophotometers.

2.4.6 Fluorescence spectroscopy

In this technique, a sample is irradiated by the spectrofluorometer with excitation light and measures the fluorescence from the irradiated sample. The spectrofluorometer equipped with 150W Xenon lamp as the light source. The light passes through the excitation monochromator which isolates a band of a particular wavelength and to collect the largest possible amount of light it incorporates a diffraction grating with a large aperture. The monochromator is of blazed holographic concave diffraction grating (F/2.5 for both excitation and emission sides) with the measurable scan range of 220-750 nm. When the sample emits selective fluorescence was received by the emission monochromator and the intensity of fluorescence measures by the photomultiplier tube

A light beam from the xenon lamp is incident upon the excitation monochromator. From the excitation monochromator through the beam splitter, part of the beam is directed to the monitor detector. All the drive components including slit control motor and the wavelength motor are operated from the internal computer according to signals. Output signals from fluorescence measurement detector (photomultiplier) and the monitor detector are fed to the A/D converter and the internal computer for processing, and then output data is sent to the personal computer.



Figure 2.10: Photograph of (a) Horiba Jobin Yvon Fluoromax-4 and (b) Shimadzu RF-5301PC Spectrofluorimeters

The Xenon lamp characterized by non-uniformity in the radiation spectrum and the spectral sensitivity characteristics of the photomultiplier tube causes distortion in the spectrum. To

overcome these factors, the photomultiplier tube monitors a portion of excitation light and feeds the resultant signal back to photomultiplier tube for fluorescence scanning. It is called the light-source compensation system. It also has variable slit width facility (1.5/3/5/10/15/20 nm) with the wavelength accuracy of 1.5 nm.

In the present work, Fluorescence measurements were performed using a Horiba Jobin Yvon Fluoromax-4 scanning spectrofluorimeter and Simadzu spectrofluorimeter with model RF-5301PC (Figure 2.10).

2.4.7 Thermo Gravimetric Analysis (TGA)

Thermo gravimetric Analysis (TGA) explains the changes in chemical and physical properties of the materials with respect to the temperature. A known amount of a starting material between 3 to 50 mg should be placed in the sample pan. Knowing the initial weight of the starting material and the total weight of inclusions which are decomposed upon heating and the stoichiometric ratio can be used to calculate the % weight loss of the substance in a sample. The TGA results can be presented by –

1. Weight loss (or %weight loss) versus temperature (or time) curve, called the thermogravimetry (TG)
2. Rate of weight loss versus temperature curve, called the differential thermogravimetry (DTG).



Figure 2.11: Photograph of (a) Shimadzu TGA-50 and (b) Perkin Elmer TGA-4000 TGA analyzers

TGA can be used to evaluate the thermal stability of CPs, over a temperature range. During heating of CPs following processes takes place - chemical reactions, releasing adsorbed species and at the end thermal decomposition which indicates that the material is no longer thermally

stable. The TGA instruments used in the present thesis are Shimadzu TGA-50 and Perkin Elmer Thermo Gravimetric Analyzer of model TGA – 4000 (Figure 2.11).

2.5 References

- 1 Y. B. Dong, M. D. Smith and H. C. Zur Loye, *Inorg. Chem.*, 2000, **39**, 4927–4935.
- 2 Y. B. Dong, M. D. Smith, R. C. Layland and H. C. Zur Loye, *Chem. Mater.*, 2000, **12**, 1156–1161.
- 3 C. Bridle and T. R. Lomer, *Acta Crystallogr.*, 1965, **19**, 483–484.
- 4 W. P. Dreaper, *J. Soc. Chem. Ind.*, 1913, **32**, 678–684.
- 5 J. L. C. Rowsell and O. M. Yaghi, *Microporous Mesoporous Mater.*, 2004, **73**, 3–14.
- 6 G. Demazeau, *J. Mater. Sci.*, 2008, **43**, 2104–2114.
- 7 X. X. Zhao, J. P. Ma, Y. B. Dong, R. Q. Huang and T. Lai, *Cryst. Growth Des.*, 2007, **7**, 1058–1068.
- 8 M. Eckert, *Ann. Phys.*, 2012, **524**, A83-A85.
- 9 W. H. Bragg, W. L. Bragg, *Proc. R. Soc. Lond. A*, 1913, **88**, 428–438.
- 10 W. L. Bragg, *Proc. R. Soc. Lond. A*, 1913, **89**, 248–277.

Chapter-3

Synthesis, Characterization and Photophysical Studies of *Bis*-pyridyl- diimines

Synthesis, Characterization and Photophysical Studies of *Bis*-pyridyl-diimines

3.1 Introduction

There has been a widespread increase in designing and synthesizing organic materials for optoelectronic applications such as organic light-emitting diodes (OLEDs),^[1-4] bio-imaging, organic lasers, fluorescence probes, optical data storage media and so on.^[5-11] Research in these areas is focused on synthesizing organic molecules, which can function as light emitters, and tuning the photophysical properties of the molecules by incorporating various functional groups. The chromaticity, morphological and thermal stabilities, charge transporting abilities of luminescence materials and simplifying the device structures are the key factor to be taken into account in the construction of optoelectronic devices. Along with these, an ideal luminescent material must possess high luminescence efficiency in the solid state.

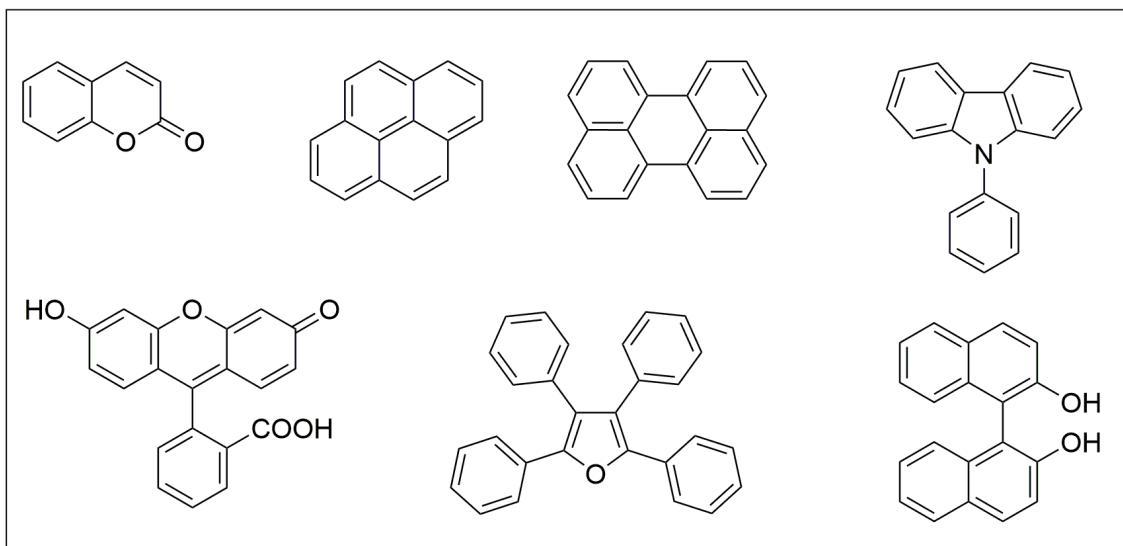


Figure 3.1: Highly conjugated organic molecules exhibiting aggregation caused quenching (ACQ).^[12-15]

In general, a fluorescent organic molecule involves large π -conjugated system of polycyclic aromatic rings, which are promising candidates for providing intense emission bands of higher quantum yield. Although the major drawback in designing organic materials based on polycyclic

aromatic system is the Aggregation Caused Quenching (ACQ).^[12–15] The ACQ will limit the practical applications such as OLED, where the materials are required in the solid state. Figure 3.1 shows the molecules exhibiting ACQ property.^[12–15]

In 2001, Tang and co-workers observed the property of Aggregation Induced Emission (AIE)^[16–19] in silole-based organic compounds, where no emission was observed in CHCl_3 solution, but the aggregates and solid states showed very strong emissions. Since then, there has been an enormous increase in the research focus on the materials based on AIE properties.^[20–24] Many explanations are provided to decode the AIE effect, which includes restriction of intramolecular rotation in the aggregates/solid states, formation of J-aggregates, intramolecular planarization, restriction of intramolecular charge transfer and twisted intramolecular charge transfer.^[25–30]

Figure 3.2 illustrates some examples of AIE molecules.

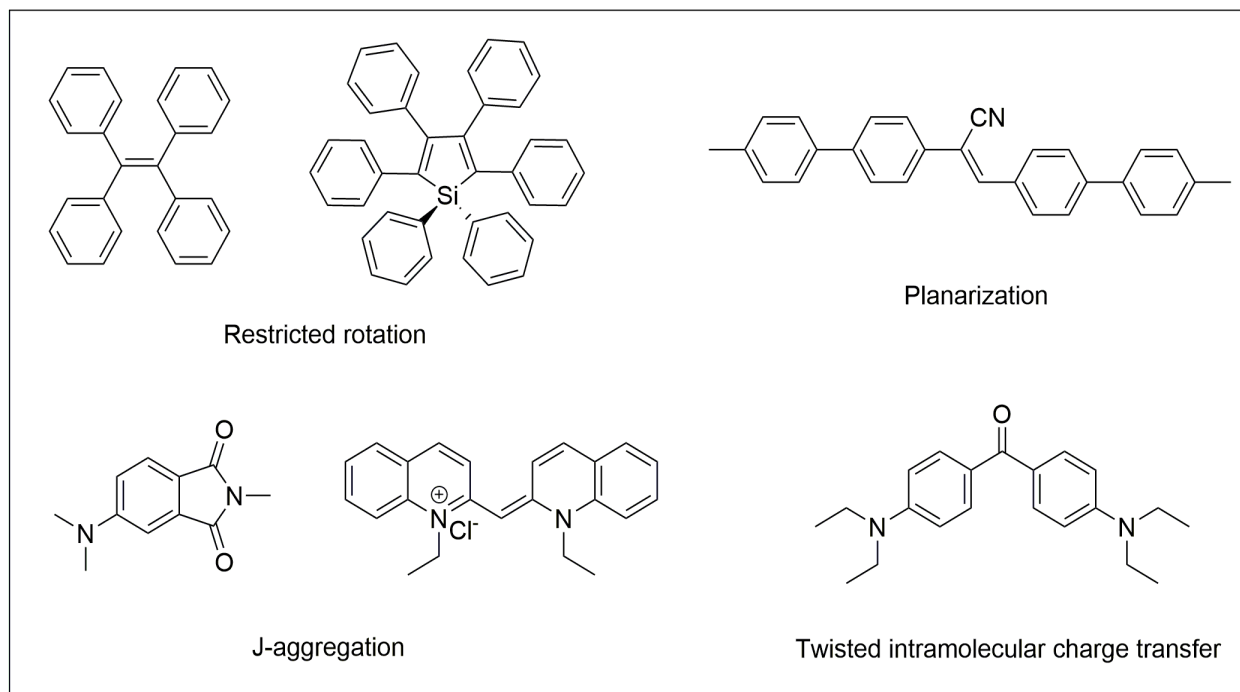
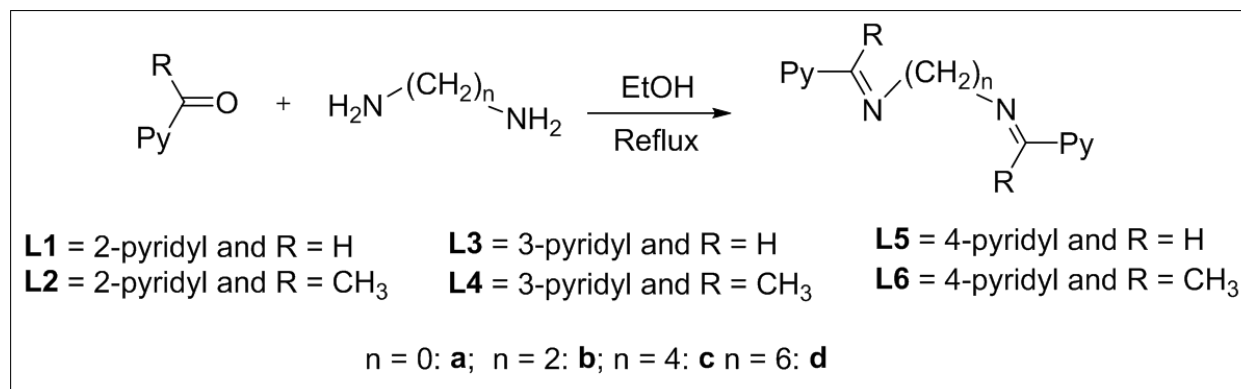


Figure 3.2: Organic molecules displaying Aggregation Induced Emission (AIE).^[25–30]

The light-emitting property of a compound in solid state is dictated by the arrangement of the entire array of molecules rather than by an individual molecule. Studying crystal structures of the compounds provides essential information on how molecules are arranged with respect to their neighbors, what are the non-covalent interactions binding them together and what are their conformational preferences. The knowledge of relating various properties with the

supramolecular arrangement of the molecules in the solid state, the sensitivity of these properties with respect to the packing in the solids could lead to derive new strategies to tailor made the compounds according to our requirement. Supramolecular synthesis, which involves non-covalent interactions, has emerged as an efficient route to synthesize a wide range of solid forms. It is also a versatile approach to tune solid-state luminescence by controlling the molecular organization *via* intermolecular interactions. Draper and co-workers have observed that the solid state luminescence of 2-cyano-3(4-diphenylamino)phenyl)acrylic acid can be tuned by co-crystallization with substituted pyridines and amines, which results in effective control in the non-covalent interactions.^[31] Das *et al.*^[32–35] have highlighted the reports on non-covalent methods and their utility in attaining switchable solid state emitting molecular materials. In order to obtain structural correlations to solid state optoelectronic properties of molecular materials, it is necessary to obtain and analyze the crystal structure along with the spectroscopic results.

The photophysical properties of Salen^[36–40] based compounds were studied by many groups. The relationship of the solid state PL spectra and length of the alkyl bridges were observed by Kawasaki *et al.*^[41] The AIE property in salicylaldehydeazine was reported by Tang *et al.* while Tang *et al.*^[42] and Cheng *et al.*^[37] reported the AIE properties in functionalized Salens. In all these reports, the AIE active compounds have non-conjugated alkyl bridges and leading to very small chromophore. The role of the alkyl chain in AIE properties require a systematic analysis of related compounds.



Scheme 3.1: Schiff bases studied in the present work

This chapter discusses the structure-photophysical property study of a series of 18 Schiff Base compounds, which differs in alkyl spacer length and positioning of N in the pyridyl group (Scheme 3.1). The analysis on the effect of different arrangements of the molecules in solid state

on their photophysical properties will be discussed. The solid state structure of **L2a**, **L1a** and **L2b** are reported by various research groups. The crystal structure of compound **L2a** is reported by Qing-Jin and co-workers.^[43] while the structure of **L1a** is reported by Rudolph and co-workers & also by Foxman and co-workers.^[44,45] Buyukgungor and coworkers^[46] have reported the crystal structure of **L2b**.

3.2 Experimental Section

3.2.1 General

Melting points of Schiff base compounds were measured using capillary tubes on a MPA120-Automated Melting Point apparatus. Infra-red (IR) spectrum was recorded in FT-IR ABB Bomen MB-3000 using KBr pellets. Elemental analyses were obtained with a Thermo Finnigan, Italy, Model FLASH EA 1112 series. Proton and carbon-13 nuclear magnetic resonance (¹H-NMR and ¹³C-NMR) spectra of all ligands are measured on a 400 MHz Bruker NMR spectrometer; using CDCl₃ as solvent and the chemical shifts are expressed in ppm. Data are reported as follows: chemical shifts, multiplicity (s = singlet, d = doublet, t = triplet, q = quartet, dd = doublet of doublets, m = multiplet), coupling constants (Hz), and integration. UV-visible absorption spectra were recorded in Shimadzu Spectrophotometer with model UV-2450. Fluorescence spectra were recorded in Horiba JobinYvon Fluoromax-4 scanning spectrofluorimeter and Shimadzu Spectrofluorophotometer with model RF-5301PC. Powder X-ray diffraction (PXRD) data were recorded with a Rigaku Miniflex II, $\lambda = 1.54$, Cu K α .

2, 3 and 4-pyridyl aldehydes and ketones were purchased from Sigma-Aldrich Chemicals Pvt. Ltd. All other reagents and solvents were purchased from Merck Speciality Pvt. Ltd. and used without further purification unless otherwise specified.

3.2.2 Synthesis of Schiff bases (L1-L6)

The compounds **L1-L6** were synthesized by the usual method of preparation of Schiff bases, which involved the condensation reaction of primary diamines (0.25 ml, 5 mmol) with an aldehyde/ketone precursor (0.95 ml, 10 mmol) in alcoholic solution (20 mL) under reflux conditions. For the synthesized compounds, percentage yield and melting point were noted. The compounds were characterized using FT-IR, Elemental analysis and ¹H-NMR and ¹³C-NMR.

1,4-Bis-(2pyridyl)-2,3diaz-1,3-butadiene (L1a): **L1a** was prepared by taking hydrazine hydrate and 2-pyridine carboxaldehyde. Yield: 45%. Melting point: 148 °C. IR (cm⁻¹): 3047 (w),

3001 (w), 2955 (w), 1628 (vs), 1582 (vs), 1466 (vs), 1427 (vs), 1288 (w), 1250 (w), 1219 (s), 1142 (w), 1080 (w), 957 (s), 864 (s), 779 (vs), 687 (vs), 617 (vs), 494 (vs). ^1H NMR (400 MHz, CDCl_3) δ (ppm): 8.70 (m, $J = 4.8, 1.7, 0.9$ Hz, 2H), 8.67 (s, 2H), 8.10 (dt, $J = 7.9, 1.0$ Hz, 2H), 7.78 (td, $J = 7.7, 1.6$ Hz, 2H), 7.34 (m, $J = 7.5, 4.8, 1.2$ Hz, 2H). ^{13}C NMR (101 MHz, CDCl_3) δ (ppm): 162.14, 152.74, 149.94, 136.54, 125.09, 122.49. Elemental analysis (found %): C 68.64, H 4.75, N 26.61; calculated: C, 68.56; H, 4.79; N, 26.65.

1,6-Bis-(2-pyridyl)-2,5-diaza-1,5-hexadiene (L1b): L1b was prepared by taking 2-pyridine carboxaldehyde and ethylene-diamine. Yield: 42%. Melting point: 66 °C. IR (cm^{-1}): 3047 (s), 3009 (w), 2916 (s), 2885 (vs), 2831 (s), 1643 (vs), 1566 (vs), 1466 (vs), 1427 (vs), 1335 (vs), 1296 (s), 1219 (s), 1041 (vs), 972 (vs), 918 (vs), 864 (vs), 771 (vs). ^1H NMR (400 MHz, CDCl_3) δ (ppm): 8.60 (m, $J = 4.8, 1.7, 0.9$ Hz, 2H), 8.40 (s, 2H), 7.96 (dt, $J = 7.9, 1.0$ Hz, 2H), 7.73-7.68 (m, 2H), 7.28 (m, $J = 6.3, 4.2, 1.0$ Hz, 2H), 4.04 (s, 4H). ^{13}C NMR (101 MHz, CDCl_3) δ (ppm): 163.37, 154.27, 149.33, 136.49, 124.71, 121.29, 61.26; Elemental analysis (found %): C 70.62, H 5.90, N 23.48; calculated: C, 70.57; H, 5.92; N, 23.51.

1,8-Bis-(2-pyridyl)-2,7-diaza-1,7-octadiene (L1c): L1c was prepared by taking 2-pyridine carboxaldehyde and 1,4-diaminobutane. Yield: 43%. Melting point: 73.5 °C. IR (cm^{-1}): 3055 (w), 3009 (w), 2916 (s), 2839 (s), 1636 (vs), 1566 (s), 1466 (vs), 1435 (vs), 1366 (m), 1335 (s), 1288 (w), 1211 (w), 1188 (w), 1142 (w), 1088 (w), 1041 (s), 987 (vs) (Appendix figure A1). ^1H NMR (400 MHz, CDCl_3) δ (ppm): 8.61 (m, $J = 4.8, 1.7, 0.9$ Hz, 2H), 8.36 (s, 2H), 7.95 (dt, $J = 7.9, 1.0$ Hz, 2H), 7.73-7.69 (m, 2H), 7.28 (m, $J = 7.5, 4.9, 1.2$ Hz, 2H), 3.71 (td, $J = 5.2, 1.4$ Hz, 4H), 1.83-1.78 (m, 4H) (Appendix figure A2). ^{13}C NMR (101 MHz, CDCl_3) δ (ppm): 161.88, 154.46, 149.35, 136.47, 124.58, 121.18, 61.18, 28.38 (Appendix figure A3); elemental analysis (found %): C 72.21, H 6.78, N 21.01; calculated: C, 72.15; H, 6.81; N, 21.04.

2,5-Bis-(2-pyridyl)-3,4-diaza-2,4-hexadiene (L2a): L2a was prepared by taking 2-acetylpyridine and hydrazine hydrate. Yield: 39%. Melting point: 52 °C. IR (cm^{-1}): 3055 (m), 3009 (w), 2924 (w), 1612 (m), 1566 (vs), 1466 (vs), 1435 (vs), 1358 (vs), 1304 (s), 1242 (s), 1149 (w), 1095 (s), 1041 (s), 987 (s) (Appendix figure A4). ^1H NMR (400 MHz, CDCl_3) δ (ppm): 8.63 (m, $J = 4.9, 1.8, 0.9$ Hz, 2H), 8.22 (dt, $J = 8.0, 1.0$ Hz, 2H), 7.74 (m, $J = 8.0, 7.5, 1.8$ Hz, 2H), 7.30 (m, $J = 7.5, 4.9, 1.2$ Hz, 2H), 2.36 (s, 6H) (Appendix figure A5). ^{13}C NMR (101 MHz, CDCl_3) δ (ppm): 157.42, 155.58, 148.64, 136.20, 124.03, 121.14, 13.87 (Appendix figure A6); Elemental analysis (found%): C 70.63, H 5.89, N 23.48; calculated: C, 70.57; H, 5.92; N, 23.51.

2,5-Bis-(2-pyridyl)-3,4-diaza-2,4-octadiene (L2b): L2b was prepared by taking 2-acetylpyridine and ethylene diamine. Yield: 45%. Melting point: 103-106 °C. IR (cm⁻¹): 3055 (w), 3009 (w), 2893 (s), 2831 (m), 1636 (vs), 1558 (vs), 1466 (vs), 1435 (vs), 1358 (s), 1281 (s), 1242 (s), 1180 (w), 1103 (w), 1041 (s), 987 (s), 787 (s) (Appendix figure A7). ¹H NMR (400 MHz, CDCl₃) δ(ppm): 8.58 (m, J = 4.8, 1.8, 0.9 Hz, 2H), 8.06 (dt, J = 8.0, 1.0 Hz, 2H), 7.71-7.66 (m, 2H), 7.26 (m, J = 7.4, 4.8, 1.2 Hz, 2H), 3.96 (s, 4H), 2.42 (s, 6H) (Appendix figure A8). ¹³C NMR (101 MHz, CDCl₃) δ(ppm): 167.50, 157.68, 148.21, 136.26, 124.03, 120.86, 53.49, 14.39 (Appendix figure A9); Elemental analysis (found %): C 72.23, H 6.79, N 20.98; calculated: C, 72.15; H, 6.81; N, 21.04.

2,9-Bis-(2-pyridyl)-3,8-diaza-2,8-decadiene (L2c): L2c was prepared by taking 2-acetylpyridine and 1,4-diaminobutane. Yield: 38%. Melting point: 74 °C. IR (cm⁻¹): 3047 (w), 3009 (w), 2932 (vs), 2878 (vs), 1628 (vs), 1566 (vs), 1466 (vs), 1435 (vs), 1358 (vs), 1304 (s), 1227 (w), 1103 (s), 1072 (w), 1041 (w), 987 (w), 787 (vs), 741 (s). ¹H NMR (400 MHz, CDCl₃) δ(ppm): 8.57 (m, J = 4.8, 1.8, 0.9 Hz, 2H), 8.07 (dt, J = 8.0, 1.0 Hz, 2H), 7.68 (m, J = 8.0, 7.5, 1.8 Hz, 2H), 7.26 (m, J = 7.5, 5.0, 1.2 Hz, 2H), 3.59 (dd, J = 6.3, 5.6 Hz, 4H), 2.36 (s, 6H), 1.93-1.89 (m, 4H). ¹³C NMR (101 MHz, CDCl₃) δ(ppm): 166.35, 157.83, 148.16, 136.22, 123.93, 120.82, 77.32, 77.00, 76.68, 52.33, 28.93, 13.96; Elemental analysis (Found %): C 73.50, H 7.50, N 19.00; calculated: C, 73.44; H, 7.53; N, 19.03.

N,N'-(ethane-1,2-diyl)-bis-(1-(pyridin-3-yl)methanimine) (L3b): L3b was prepared by using 3-pyridine carboxaldehyde and 2-pyridine carboxaldehyde. Yield: 83%. Melting point: 91 °C. IR (cm⁻¹): 3086 (w), 3024 (w), 2885 (m), 2847 (m), 2754 (w), 1642 (s), 1582 (m), 1481 (m), 1420 (m), 1373 (m), 1228 (m), 1188 (w), 980 (w), 864 (m), 702 (s), 617 (m). ¹H NMR (400 MHz, CDCl₃) δ (ppm): 8.68 (d, J = 1.5 Hz, 2H), 8.44 (dd, J = 4.8, 1.7 Hz, 2H), 8.15 (s, 2H), 7.88 (dt, J = 7.9, 1.9 Hz, 2H), 7.13 (dd, J = 7.9, 4.8 Hz, 2H), 3.83 (s, 4H). ¹³C NMR (101 MHz, CDCl₃) δ (ppm): 159.74, 151.48, 150.07, 134.43, 131.46, 123.59, 61.53.

N,N'-(butane-1,4-diyl)-bis-(1-(pyridin-3-yl)methanimine) (L3c): L3c was prepared by taking 3-pyridine carboxaldehyde and 1,4-diaminobutane. Yield: 92%. Melting point: 55 °C. IR (cm⁻¹): 3032 (w), 2939 (w), 2908 (w), 2878 (m), 2839 (m), 1643 (s), 1582 (s), 1474 (w), 1420 (s), 1373 (m), 1311 (s), 1227 (m), 1188 (m), 1088 (w), 1049 (w), 1018 (m), 972 (m), 918 (w), 849 (w), 818 (s), 710 (s), 617 (w). (Appendix figure A10). ¹H NMR (400 MHz, CDCl₃) δ (ppm): 8.69 (d, J = 1.5 Hz, 2H), 8.45 (dd, J = 4.8, 1.7 Hz, 2H), 8.14 (s, 2H), 7.91 (dt, J = 7.9, 2.0 Hz, 2H), 7.15

(m, $J = 7.9, 4.8, 0.8$ Hz, 2H), 3.52 (t, $J = 5.6$ Hz, 4H), 1.63 (t, $J = 3.0$ Hz, 4H) (Appendix figure A11). ^{13}C NMR (101 MHz, CDCl_3) δ (ppm): 157.91, 151.20, 149.94, 134.28, 131.57, 123.47, 61.46, 28.45 (Appendix figure A12).

N,N'-(hexane-1,6-diyl)-bis-(1-(pyridin-3-yl)methanimine) (L3d): L3d was prepared by taking 3-pyridine carboxaldehyde and 1,6-diaminohexane. Yield: 53%. Melting point: 47-48 °C. IR (cm^{-1}): 3279 (w), 3024 (w), 2924 (m), 1643 (s), 1582 (m), 1420 (m), 1378 (m), 1250 (w), 1188 (m), 1026 (m), 980 (m), 949 (w), 818 (m), 710 (m), 702 (m). ^1H NMR (400 MHz, CDCl_3) δ (ppm): 8.69 (d, $J = 1.5$ Hz, 2H), 8.45 (dd, $J = 4.8, 1.7$ Hz, 2H), 8.13 (s, 2H), 7.92 (dt, $J = 7.9, 1.9$ Hz, 2H), 7.16 (dd, $J = 7.9, 4.8$ Hz, 2H), 3.53-3.38 (m, 4H), 1.66-1.49 (m, 4H), 1.26 (p, $J = 3.7$ Hz, 4H). ^{13}C NMR (101 MHz, CDCl_3) δ (ppm): 157.82, 151.23, 150.02, 134.36, 131.72, 123.59, 61.79, 30.64, 27.06.

N,N'-(ethane-1,2-diyl)-bis-(1-(pyridin-3-yl)ethan-1-imine) (L4b): L4b was prepared by taking 3-acetyl pyridine and ethylene diamine. Yield: 55%. Melting point: 95-96 °C. IR (cm^{-1}): 3086 (m), 3032 (w), 2955 (w), 2824 (m), 1628 (s), 1582 (m), 1474 (w), 1420 (m), 1366 (m), 1327 (m), 1273 (m), 1996 (w), 1088 (m), 1049 (m), 1018 (m), 818 (m), 702 (s), 617 (m). ^1H NMR (400 MHz, CDCl_3) δ (ppm): 8.97-8.85 (m, 2H), 8.53 (dd, $J = 4.8, 1.7$ Hz, 2H), 8.01 (dt, $J = 8.0, 1.9$ Hz, 2H), 7.23 (m, $J = 8.0, 4.8, 0.8$ Hz, 2H), 3.87 (s, 4H), 2.25 (s, 7H). ^{13}C NMR (101 MHz, CDCl_3) δ (ppm): 164.02, 150.25, 148.06, 136.23, 133.95, 123.11, 53.15, 15.84.

N,N'-(butane-1,4-diyl)-bis-(1-(pyridin-3-yl)ethan-1-imine) (L4c): L4c was prepared by taking 3-acetyl pyridine and 1,4-diaminobutane. Yield: 51%. Melting point: 72-73 °C. IR (cm^{-1}): 3387 (w), 3240 (w), 3086 (w), 3032 (w), 2932 (m), 2870 (m), 2816 (w), 1628 (s), 1582 (m), 1481 (m), 1412 (m), 1381 (m), 1288 (m), 1227 (m), 1196 (m), 1118 (w), 1018 (w), 810 (m), 710 (s), 609 (m), 532 (w). ^1H NMR (400 MHz, CDCl_3) δ (ppm): 8.84-8.76 (m, 2H), 8.41 (dd, $J = 4.8, 1.7$ Hz, 2H), 7.92 (dt, $J = 8.0, 1.9$ Hz, 2H), 7.10 (m, $J = 8.0, 4.8, 0.9$ Hz, 2H), 3.39 (s, 4H), 2.07 (s, 6H), 1.74 (s, 4H). ^{13}C NMR (101 MHz, CDCl_3) δ (ppm): 162.62, 150.25, 148.13, 136.38, 133.88, 123.06, 77.23, 52.08, 28.96, 15.30.

N,N'-(hexane-1,6-diyl)-bis-(1-(pyridin-3-yl)ethan-1-imine) (L4d): L4d was prepared by taking 3-acetyl pyridine and 1,6-diaminohexane. Yield: 55%. Melting point: 46-48 °C. IR (cm^{-1}): 3387 (m), 3047 (w), 2932 (m), 2885 (w), 2854 (w), 1636 (s), 1582 (m), 1474 (m), 1420 (m), 1366 (m), 1288 (m), 1196 (w), 1126 (w), 1018 (m), 818 (m), 710 (s), 617 (m). ^1H NMR (400 MHz, CDCl_3) δ (ppm): 8.79 (d, $J = 2.1$ Hz, 2H), 8.40 (dd, $J = 4.7, 1.5$ Hz, 2H), 7.89 (d, $J = 7.9$

Hz, 2H), 7.07 (d, $J = 4.8$ Hz, 2H), 3.31 (t, $J = 6.9$ Hz, 4H), 2.04 (s, 6H), 1.61 (s, 4H), 1.34 (s, 4H). ^{13}C NMR (101 MHz, CDCl_3) δ (ppm): 162.49, 150.17, 148.07, 136.41, 133.86, 123.06, 52.16, 30.80, 27.51, 15.28.

N,N'-(ethane-1,2-diyl)-bis-(1-(pyridin-4-yl)methanimine) (L5b): L5b was prepared by taking 4-pyridine carboxaldehyde and ethylene diamine. Yield: 63%. Melting point: 135 °C. IR (cm^{-1}): 3032 (w), 3024 (w), 2908 (w), 2847 (s), 1643 (s), 1597 (m), 1551 (m), 1412 (s), 1319 (m), 1227 (m), 957 (s), 818 (s), 640 (m), 532 (m). ^1H NMR (400 MHz, CDCl_3) δ (ppm): 8.72–8.36 (m, 4H), 8.12 (s, 2H), 7.57–7.24 (m, 4H), 3.89 (s, 4H). ^{13}C NMR (101 MHz, CDCl_3) δ (ppm): 160.78, 150.38, 142.60, 121.81, 61.25.

N,N'-(butane-1,4-diyl)-bis-(1-(pyridin-4-yl)methanimine) (L5c): L5c was prepared by taking 4-pyridine carboxaldehyde and 1,4-diaminobutane. Yield: 92%. Melting point: 103-105 °C. IR (cm^{-1}): 3024 (w), 2939 (s), 2854 (s), 2746 (w), 1643 (s), 1597 (s), 1551 (s), 1489 (w), 1458 (w), 1420 (s), 1373 (w), 1227 (s), 1049 (m), 987 (m), 818 (s), 633 (m), 517 (m) (Appendix figure A13). ^1H NMR (400 MHz, CDCl_3) δ (ppm): 8.71–8.68 (m, 4H), 8.29 (s, 2H), 7.61–7.59 (m, 4H), 3.73 (m, 4H), 1.83 (m, 4H) (Appendix figure A14). ^{13}C NMR (101 MHz, CDCl_3) δ (ppm): 159.13, 150.40, 142.91, 121.88, 61.56, 28.46 (Appendix figure A15).

N,N'-(butane-1,4-diyl)-bis-(1-(pyridin-4-yl)methanimine) (L5d): L5d was prepared by taking 4-pyridine carboxaldehyde and 1,6-diaminohexane. Yield: 80%. Melting point: 103 °C. IR (cm^{-1}): 3024 (w), 2932 (s), 2854 (s), 1975 (m), 1643 (s), 1589 (s), 1551 (m), 1489 (w), 1420 (s), 1358 (w), 1311 (m), 1227 (m), 1057 (m), 987 (m), 941 (m), 825 (s), 640 (m), 525 (m) (Appendix figure A16). ^1H NMR (400 MHz, CDCl_3) δ (ppm): 8.71–8.68 (m, 4H), 8.27 (s, 2H), 7.61–7.58 (m, 4H), 3.67 (m, 4H), 1.78–1.72 (m, 4H), 1.44 (m, 4H) (Appendix figure A17). ^{13}C NMR (101 MHz, CDCl_3) δ (ppm): 158.60, 150.15, 142.80, 121.66, 61.53, 30.37, 26.91 (Appendix figure A18).

N,N'-(ethane-1,2-diyl)-bis-(1-(pyridin-4-yl)ethan-1-imine) (L6b): L6b was prepared by taking 4-acetyl pyridine and ethylene diamine. Yield: 52%. Melting point: 174 °C. IR (cm^{-1}): 3387 (w), 2970 (w), 2893 (m), 2824 (w), 2361 (w), 1697 (w), 1628 (s), 1597 (m), 1543 (m), 1412 (s), 1366 (m), 1273 (m), 1219 (m), 825 (s), 756 (w), 633 (w), 579 (m). ^1H NMR (400 MHz, CDCl_3) δ (ppm): 8.64–8.53 (m, 1H), 7.62–7.50 (m, 1H), 3.89 (s, 1H), 2.22 (s, 2H). ^{13}C NMR (101 MHz, CDCl_3) δ (ppm): 164.50, 150.12, 147.70, 120.77, 77.23, 53.34, 15.64.

N,N'-(butane-1,4-diyl)-bis-(1-(pyridin-4-yl)ethan-1-imine) (L6c): L6c was prepared by taking 4-acetyl pyridine and 1,4-diaminobutane. Yield: 42%. Melting point: 107-109 °C. IR (cm⁻¹): 3070 (w), 3024 (w), 2939 (s), 2885 (s), 1643 (s), 1589 (s), 1543 (s), 1458 (m), 1412 (s), 1358 (s), 1288 (s), 1227 (w), 1065 (m), 987 (m), 825 (s), 764 (m), 617 (m), 579 (s) (Appendix figure A19). ¹H NMR (400 MHz, CDCl₃) δ (ppm): 8.40 (dd, *J* = 4.5, 1.6 Hz, 4H), 7.42 (dd, *J* = 4.6, 1.6 Hz, 4H), 3.35 (s, 4H), 1.98 (s, 6H), 1.73-1.67 (m, 4H) (Appendix figure A20). ¹³C NMR (101 MHz, CDCl₃) δ (ppm): 163.01, 149.93, 147.72, 120.69, 52.21, 28.78, 15.05 (Appendix figure A21).

N,N'-(hexane-1,6-diyl)-bis-(1-(pyridin-4-yl)ethan-1-imine) (L6d): L6d was prepared by taking 4-acetyl pyridine and 1,6-diaminohexane. Yield: 47%. Melting point: 80-81 °C. IR (cm⁻¹): 3070 (w), 3024 (w), 2932 (s), 2878 (w), 1628 (s), 1597 (s), 1543 (s), 1497 (w), 1466 (w), 1412 (m), 1366 (m), 1319 (m), 1281 (s), 1227 (w), 1142 (w), 1088 (w), 1026 (w), 987 (w), 825 (s), 756 (m), 725 (m), 617 (m), 579 (s) (Appendix figure A22). ¹H NMR (400 MHz, CDCl₃) δ (ppm): 8.40–8.36 (m, 4H), 7.40–7.37 (m, 4H), 3.26 (t, *J* = 7.0 Hz, 4H), 1.94 (s, 6H), 1.60–1.52 (m, 4H), 1.29 (m, 4H) (Appendix figure A23). ¹³C NMR (101 MHz, CDCl₃) δ (ppm): 162.80, 149.92, 147.78, 120.68, 52.31, 30.64, 27.43, 14.97 (Appendix figure A24).

Table 3.1: Crystallographic data and refinement parameters of L1c, L2a, L2b and L3c

Compound	L1c	L2a	L2b	L3c
Empirical formula	C ₁₆ H ₁₈ N ₄	C ₁₄ H ₁₄ N ₄	C ₁₆ H ₁₈ N ₄	C ₁₆ H ₁₈ N ₄
Formula Wt.	266.34	238.29	266.34	266.34
Crystal system	Monoclinic	Monoclinic	Orthorhombic	Monoclinic
Space group	<i>P</i> 2 ₁ / <i>c</i>	<i>P</i> 2 ₁	<i>P</i> <i>c</i> <i>a</i> <i>b</i>	<i>P</i> 2 ₁ / <i>c</i>
<i>a</i> /Å	9.2157(5)	8.6694(4)	19.379(5)	13.476(2)
<i>b</i> /Å	8.9944(5)	17.8009(8)	24.584(5)	4.6771(8)
<i>c</i> /Å	9.3471(5)	12.8064(6)	12.300(5)	11.5023(19)
<i>α</i> /°	90.00	90.00	90.00	90.00
<i>β</i> /°	107.344(6)	98.394(4)	90.00	102.811(16)
<i>γ</i> /°	90.00	90.00	90.00	90.00
<i>V</i> /Å ³	739.55(7)	1955.15(16)	5860(3)	706.9(2)

Z	2	6	16	2
D _{calcd} /g cm ⁻³	1.196	1.214	1.208	1.251
T/K	293(2)	293(2)	293(2)	93(2)
Theta (°) range for data used	3.51 to 25.99	3.65 to 26.00	3.54 to 26.00	10.19 to 49.996
R _{int}	0.0418	0.0690	0.0441	0.0325
Reflections With $I > 2\sigma(I)$	4636	2710	993	3797
No. of parameters refined	493	366	91	91
Final R (With $I > 2\sigma(I)$)	R ₁ = 0.0445, wR ₂ = 0.1085	R ₁ = 0.0637, wR ₂ = 0.1609	R ₁ = 0.0813, wR ₂ = 0.1901	R ₁ = 0.0539, wR ₂ = 0.1393
GOF on F^2	1.001	1.038	1.042	1.093

Table 3.2: Crystal structure data of ligands **L5c**, **L5d**, **L6c** and **L6b**

Compound	L5c	L5d	L6c	L6d
Empirical formula	C ₁₆ H ₁₈ N ₄	C ₉ H ₁₁ N ₂	C ₁₈ H ₂₂ N ₄	C ₁₀ H ₁₃ N ₂
Formula Wt.	266.34	147.20	294.40	161.22
Crystal system	Monoclinic	Monoclinic	Triclinic	Triclinic
Space group	$P2_1/c$	$P2_1/c$	$P-1$	$P-1$
a/Å	8.2748(13)	10.0279(8)	6.5255(7)	6.5117(4)
b/Å	9.9426(14)	9.5564(7)	7.3778(9)	8.3222(6)
c/Å	8.7346(12)	8.5907(7)	8.5279(10)	8.5049(6)
α /°	90.00	90.00	88.498(10)	78.006(6)
β /°	90.300(11)	103.997(8)	75.415(10)	76.549(6)
γ /°	90.00	90.00	78.317(10)	87.692(6)
V/Å ³	718.61(18)	798.80(11)	388.97(8)	438.45(5)
Z	2	4	1	2
D _{calcd} /g cm ⁻³	1.231	1.224	1.257	1.221
T/K	296(2)	103(2)	93(2)	293(2)

Theta (°) range for data used	2.46 to 25.06	9.782 to 49.992	9.982 to 50	10.072 to 49.996
R _{int}	0.0292	0.0172	0.0227	0.0139
Reflections	5487	4781	3796	4722
With $I > 2\sigma(I)$				
No. of parameters refined	91	100	101	110
Final R (With $I > 2\sigma(I)$)	R ₁ = 0.0497, wR ₂ = 0.1363	R ₁ = 0.0465, wR ₂ = 0.1203	R ₁ = 0.0891, wR ₂ = 0.2946	R ₁ = 0.0705, wR ₂ = 0.2149
GOF on F^2	0.971	1.036	1.178	1.096

3.2.3 X-Ray Crystallography

The single crystal XRD of **L1c**, **L2a**, **L2b** and **L5c** were done at IISER Mohali, where the single crystal data were collected on a Xcalibur, Sapphire 3 X-ray diffractometer that uses graphite monochromated Mo K α radiation ($\lambda = 0.71073 \text{ \AA}$) by the ω -scan method. The structures were solved by direct methods and refined by least square methods on F^2 using SHELX-97.^[47] Non-hydrogen atoms were refined anisotropically and hydrogen atoms were fixed at calculated positions and refined using a riding model.

The single crystal XRD of **L3c**, **L5d**, **L6c** and **L6d** were done at BITS, Pilani, Hyderabad Campus, where the single crystal data were collected on Rigaku XtaLAB Pro: Kappa dual offset/far diffractometer. The crystal was kept at 93(2) K during data collection. Using Olex2^[48], the structure was solved with the ShelXT^[49] structure solution program using Intrinsic Phasing and refined with the ShelXL refinement package using Least Squares minimization.^[50]

The crystal data and structure refinements of **L1c**, **L2a**, **L2b** and **L3c** are summarized in Table 3.1 and that of **L5c**, **L5d**, **L6c** and **L6d** are summarized in Table 3.2. The ORTEP are shown in Appendix figures A25-A32.

3.3 Results and Discussion

3.3.1 Structural description of the compounds: Crystal structures were obtained for the compounds **L1c**, **L2a**, **L2b**, **L3c**, **L5c**, **L5d**, **L6c** and **L6d**. The structural descriptions of the

compounds are studied to analyze its relation with the photophysical properties of the compounds.

3.3.1.1 Crystal structural analysis of L1c: The compound **L1c** crystallizes in monoclinic $P2_1/c$ space group with half of the molecule present in the asymmetric unit (Figure 3.3a). The molecules are held together by $\text{CH}\cdots\text{N}$ hydrogen bond interactions (2.781 Å; 3.709 Å; 176.02°) (Figure 3.3b). The butyl chain in the spacer of **L1c** adopts *gauche-anti-gauche* conformation, which give “S”-shaped geometry to the molecule. The “S”-shaped molecules of **L1c** are further assembled *via* $\text{CH}\cdots\text{N}$ hydrogen bond to form corrugated layers. The corrugated layers are packed in an offset manner (Figure 3.3c). The aromatic $\text{CH}\cdots\pi$ interactions are holding the layers together to pack them in 3D (Figure 3.3d).

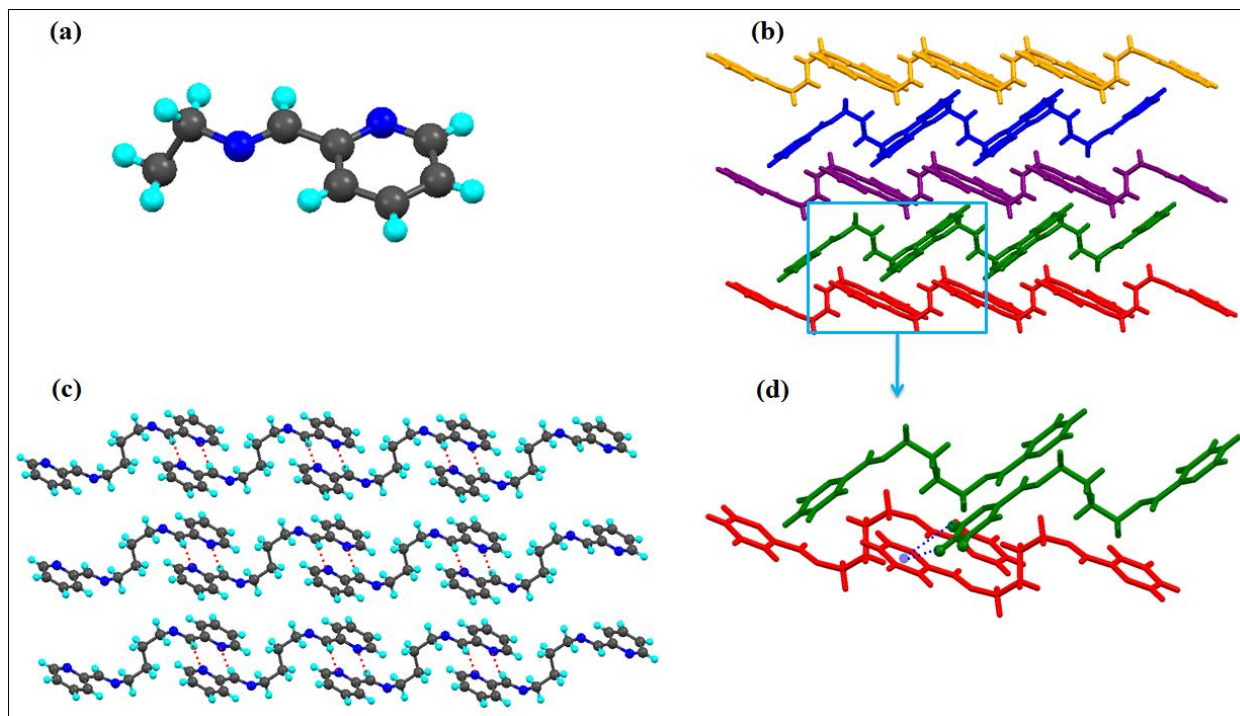


Figure 3.3: Illustration of the crystal structure of **L1c**: (a) asymmetric unit; (b) $\text{CH}\cdots\text{N}$ interactions leading to the formation of corrugated 2D layers; (c) offset packing of corrugated layers; (d) aromatic $\text{CH}\cdots\pi$ interactions between the **L1c** molecules of two adjacent layers

3.3.1.2 Crystal structural analysis of L2a: The crystal structure analysis of the compound **L2a** shows that it has crystallized in $P2_1$ and has three molecules in the asymmetric unit. The three molecules (molecule I, II and III) differ in the orientation of the pyridyl and imine moieties (Figure 3.4a). On further analyzing the structure, it can be observed that the molecule I and

molecule II are arranged in parallel manner; such that pyridyl rings and C=N moieties of the two molecules are overlapping over one another. The distance between the C=N of the two molecules are 3.906 and 3.943 Å, while the centroid-to-centroid distance between the two pyridyl rings are 3.888 Å and 4.009 Å.

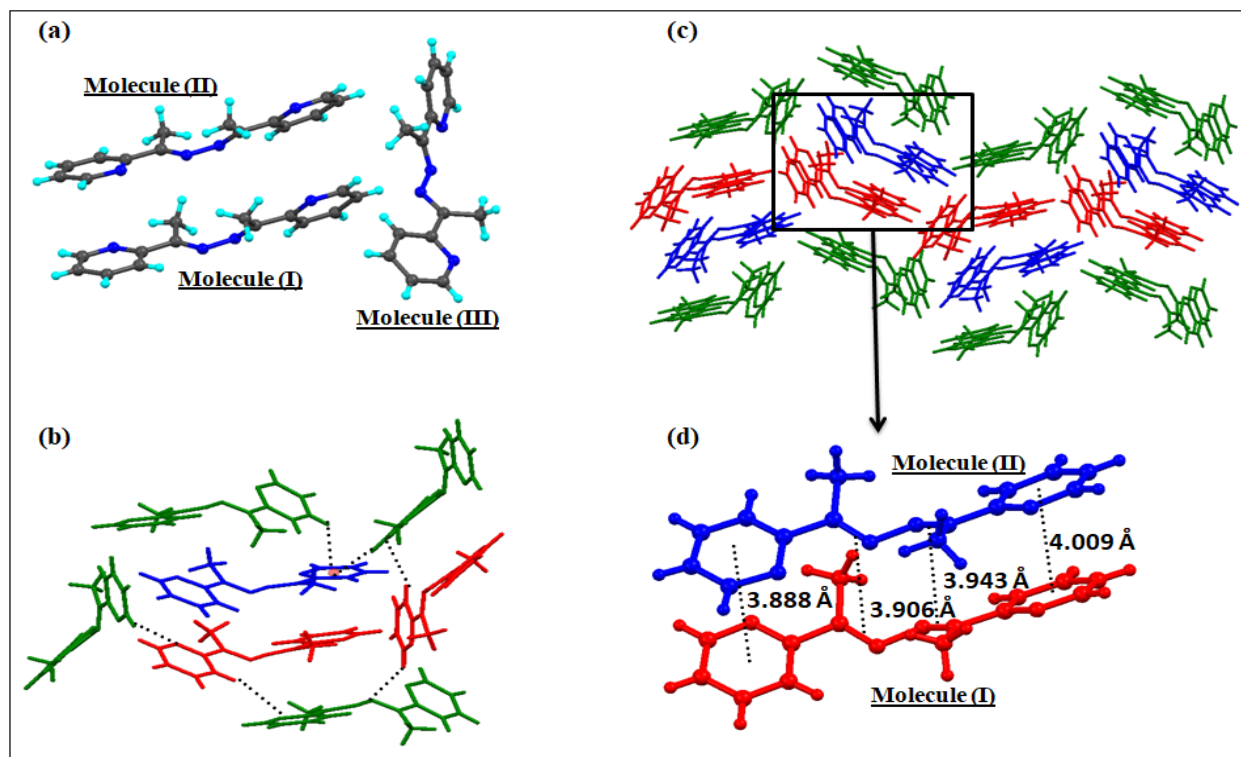


Figure 3.4: Illustration of the crystal structure of **L2a**: (a) asymmetric unit. The three molecules are labeled as molecule I, II & III; (b) non-covalent interaction between the molecules; (c) packing of the molecules; (d) parallel arrangement of molecule I & II

Aromatic $\pi\cdots\pi$ interactions are present between the molecule I and molecule II. The non-covalent interactions present in molecule III are rather significant. There are C–H \cdots N and aromatic $\pi\cdots\pi$ interactions present between molecule III & molecule I and molecule III & molecule II (Figure 3.4b). In fact, molecule III is sewing the molecule I and molecule II in a way such that they form dimers (Figure 3.4c and 3.4d). The crystal structure of a polymorph of **L2a** was reported by Qing-Jin and co-workers^[43] where it has crystallized in $P2_1/c$ space group. In that structure, there are three molecules in the asymmetric unit and the molecules adopt transoid geometry. In the present structure, the **L2a** molecules are crystallized in non-centrosymmetric space group.

3.3.1.3 Crystal structural analysis of L2b: The crystal structure analysis of **L2b** shows that it has crystallized in orthorhombic $Pcab$ space group with two molecules present in the asymmetric unit (Figure 3.5a). The two molecules differ in the orientations of the pyridyl and imine groups. The ethyl spacer of **L2b** is arranged in *anti* conformation, which gives it a linear geometry; flexible ethyl spacer, the arrangement of the molecules in the solid state gives it a “rigid” planar-like geometry. The molecules are further assembled via aromatic interactions to form zigzag layers which are stacked further in 3D (Figure 3.5b and 3.5c).

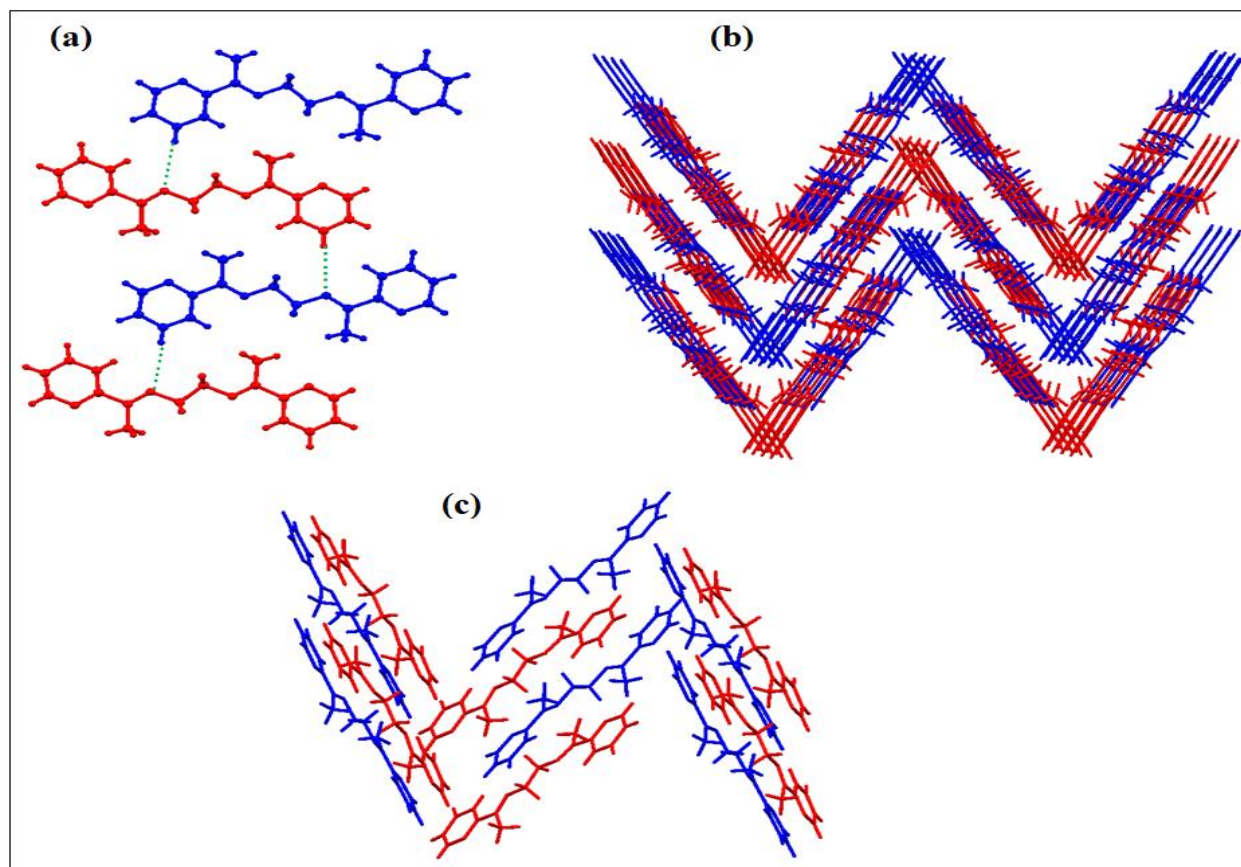


Figure 3.5: Illustration of the crystal structure of **L2b**: (a) asymmetric unit contains two molecules; the two types of molecules are shown in different colors; (b) packing of the zigzag layers; (c) aromatic interactions leading to zigzag layers.

3.3.1.4 Crystal structural description of L3c: The crystal structural analysis of compound **L3c** crystallizes into monoclinic $P2_1/c$ space group with half molecule present in the asymmetric unit. The molecules are held together by two types of $CH\cdots N$ hydrogen bond interactions one between aromatic CH and pyridyl ‘N’ (2.739 Å, 3.620 Å, 158.36°) and the other between

aromatic CH and 'N' of imine function (2.971 Å, 3.864 Å, 161.26°). Similar to **L1c**, the butyl chain in the spacer of **L3c** also adopts *gauche-anti-gauche* conformation. This conformation of alkyl chain attains S-shaped geometry to the molecule which further assembled *via* CH•••N hydrogen bonding interactions and forms criss-cross network. The molecules are further forms aromatic head to tail CH••• π interactions lead to pack into the 3D network (Figure 3.6).

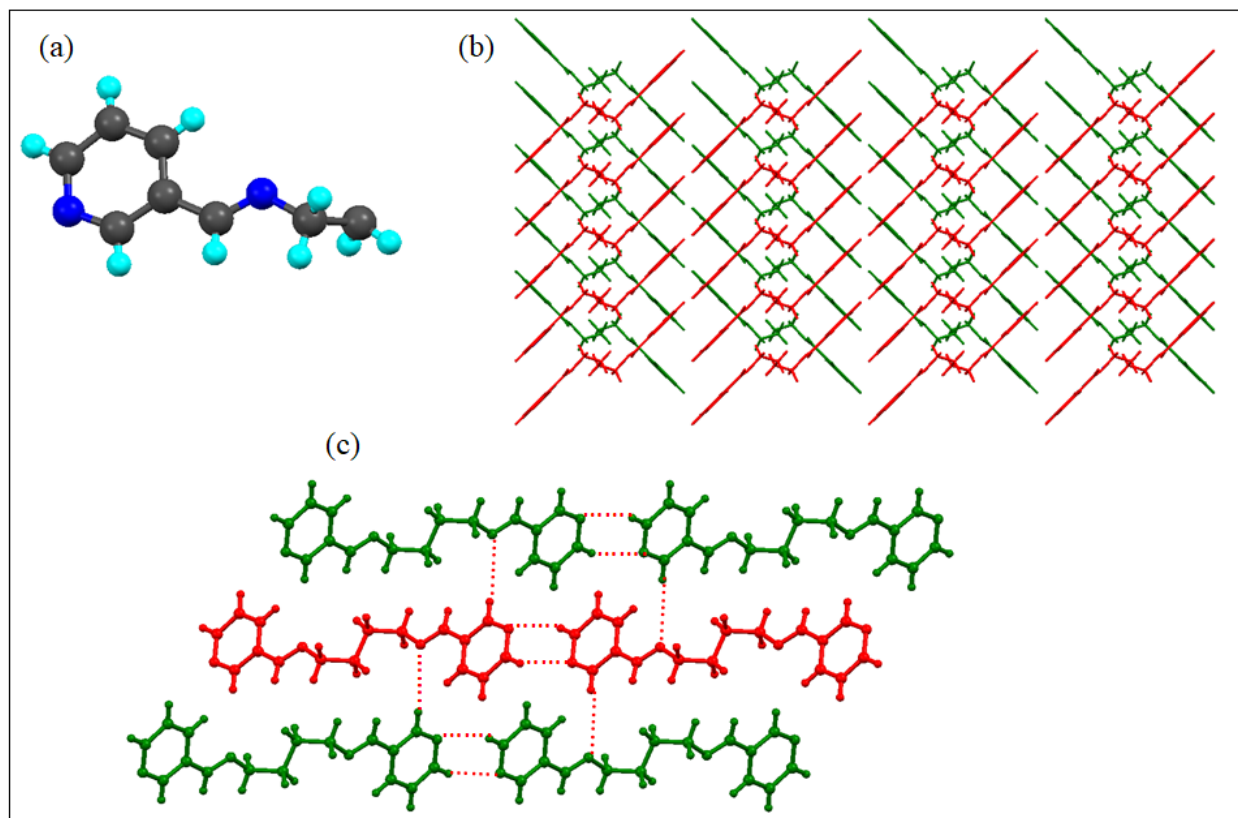


Figure 3.6: Illustration of the crystal structure of **L3c**: (a) asymmetric unit, (b) packing of the molecules; (c) hydrogen bonding interaction between the molecules

3.3.1.5 Crystal structural description of L5c and L5d: The compound **L5c** crystallizes in monoclinic $P2_1/c$ space group with half of the molecule present in the asymmetric unit. The molecules are held together by CH•••N hydrogen bond interactions between pyridyl-H and imine 'N' (2.708 Å, 3.630 Å, 170.89°). The butyl chain in the spacer adopts all *anti* conformation presents planar geometry to the molecule. The CH•••N hydrogen bonding interactions between aromatic CH and N of imine atoms extend the molecules into the 3D network (Figure 3.7a and 3.7b). The structure of compound **L5d** is similar to **L5c**, which is monoclinic $P2_1/c$ space group with half of the molecule present in the asymmetric unit.

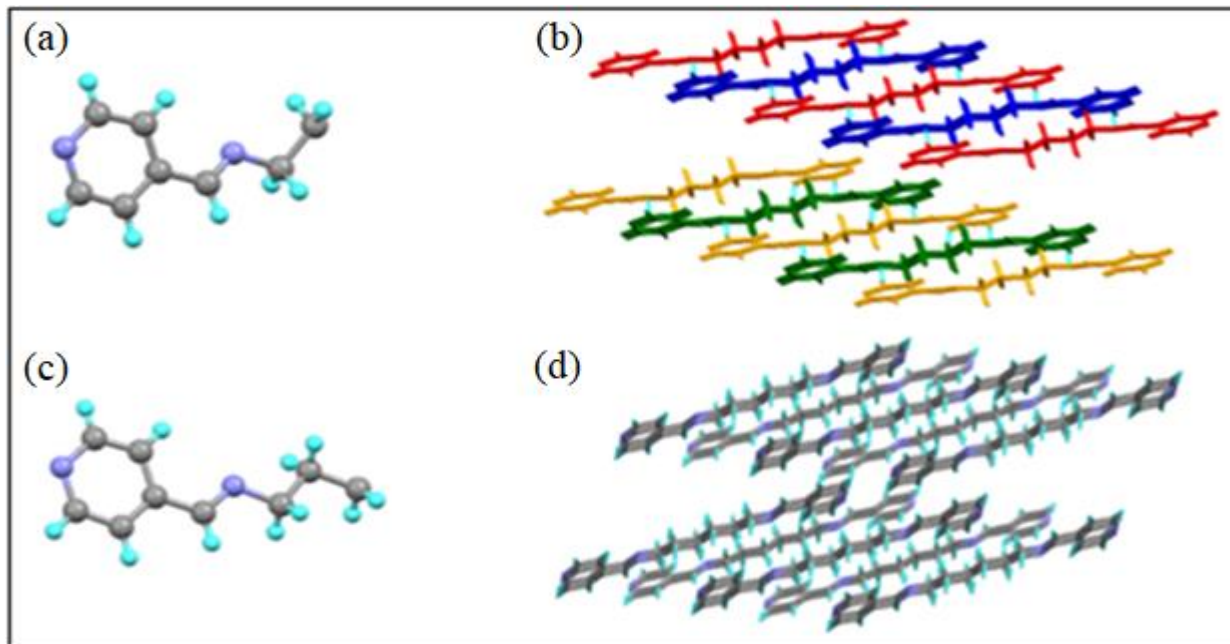


Figure 3.7: Illustration of the crystal structure of **L5c** and **L5d**: (a) asymmetric unit of **L5c**; (b) arrangement of **L5c** molecules in 3D; (c) asymmetric unit of **L5d**; (d) arrangement of **L5d** in 3D: Notice the hydrogen bond interaction between the pyridyl H and N=C-H moiety of the neighboring molecules

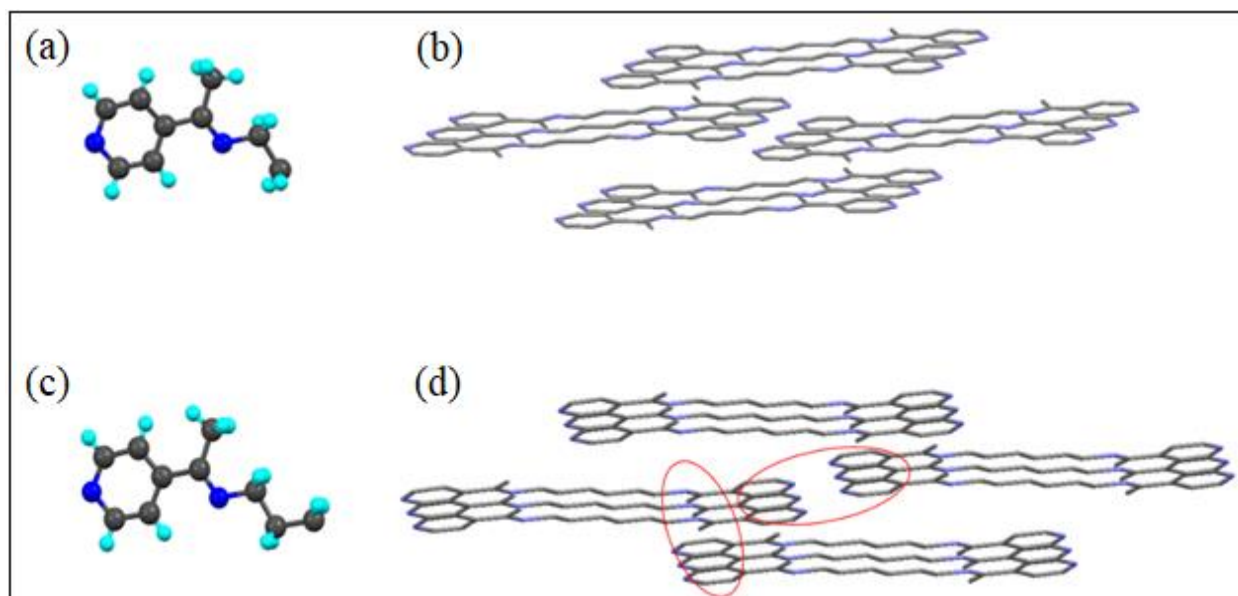


Figure 3.8: Illustration of the crystal structure of **L6c** and **L6d**: (a) asymmetric unit of **L6c**; (b) arrangement of **L6c** molecules in 3D; (c) asymmetric unit of **L6d**; (d) arrangement of **L6d** in 3D: Notice the arrangement of pyridyl groups and C=N moiety of the neighboring molecules.

The hexyl chain in the spacer adopts all *anti* conformation provides planar geometry to the molecule. The molecules are held together by CH \cdots N hydrogen bond interactions (2.740 Å, 3.663 Å, 171.84°) (Fig. 3.7c and 3.7d).

3.3.1.6 Crystal structural description of L6c and L6d: The compounds **L6c** and **L6d** crystallize in triclinic *P*-1 space group with half of the molecule present in the asymmetric unit. The butyl chain in **L6c** and hexyl chain in **L6d** adopts all *anti* conformation provides planarity to the molecule (Figure 3.8).

3.3.2 Powder XRD spectra

The powder XRD was taken for the compounds **L1c**, **L2a**, **L2b**, **L3c**, **L5c**, **L5d**, **L6c** and **L6d** (Figure 3.9). The calculated PXRD of the compounds were compared with that of the experimentally measured one in order to verify the phase purity of the compounds.

3.3.3 UV-visible absorption spectra of the Schiff base components: The compound **L2a** showed λ_{max} at 287 nm and a hump at 259 nm; while for compound **L1a**, peak maxima were observed at 300 nm with a hump at 262 nm. The compounds **L1b**, **L2b**, **L1c** and **L2c** showed some similarity in the absorption spectra. All the four compounds showed two peaks at 242–243 and 270–273 nm, which may be attributed to $\pi \rightarrow \pi^*$ and $n \rightarrow \pi^*$ transitions, respectively (Figure 3.10). The solid state UV-visible spectra of **L1c**, **L2a**, and **L2b** are shown in (Appendix figure A33). The chromophore, Py-C=N, is responsible for both the transitions in compounds **L1b**, **L2b**, **L1c** and **L2c**, while in **L1a** and **L2a**, the extended conjugation throughout the molecule shifts the peak to longer wavelength.

The UV-visible absorption spectra were measured in CHCl₃ at Conc.10⁻⁴M for the ligands **L3b**-**L6d**. The compounds **L3b**, **L3c** and **L3d** showed λ_{max} around at 244-247 nm and 272 nm that may be attributed to $\pi \rightarrow \pi^*$ and $n \rightarrow \pi^*$ transitions. The compounds **L4b**, **L4c** and **L4d** showed a peak at 242-243 nm and a hump at 265 nm. The compounds **L5b**, **L5c** and **L5d** showed two peaks at 244-245 nm and 275 nm. While the compounds **L6b**, **L6c** and **L6d** also showed UV absorption at 242-243 nm and 266-268 nm. Table 3.3 summarizes the absorption maxima of the compounds **L1-L6**. The solid state UV-visible spectra of all the compounds **L3b-L6d** were shown in (Appendix figure A34, A35).

3.3.4 Excitation spectra and photoluminescence spectra of L2a: The excitation and photoluminescence spectra were measured for **L2a** in CHCl₃. At 10⁻⁵ M concentration, **L2a** showed excitation maxima at 315 nm, at an emission wavelength of 365 nm (Figure 3.11).

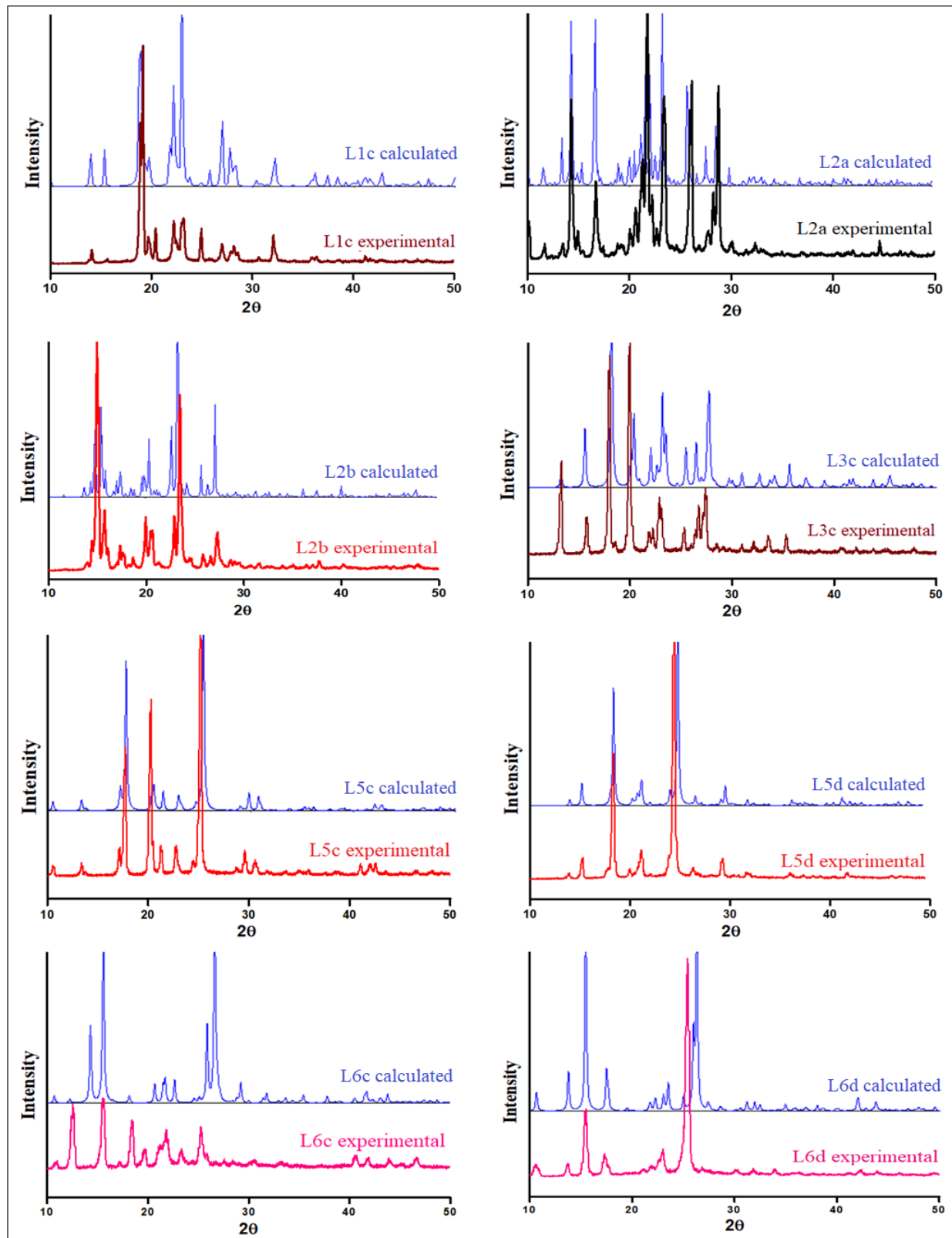


Figure 3.9: Experimentally measured and calculated powder XRD of (a) L1c, (b) L2a, (c) L2b, (d) L3c, (e) L5c, (f) L5d, (g) L6c and (h) L6d

The photoluminescence spectra at a concentration of 10^{-6} M showed a peak at 365 nm, when an excitation wavelength of 315 nm was used. Quenching of photoluminescence was observed as the concentration was increased (Figure 3.12). The solid state photoluminescence was negligible (peak at $\lambda = 535$ nm) with a very low quantum yield (Figure 3.13).

The excitation and PL spectra of **L1a** also show similar behavior (Figure A36). Tang *et al.* have reported Aggregation Induced Enhanced Emission (AIEE) for salicylaldehydeazine derivatives; which has two salicylaldehyde moieties connected by rotatable N–N single bond (Figure 3.14).^[25]

Table 3.3: UV-visible absorption maxima of the compounds **L1a-L6d**

Compound	UV-visible in CHCl ₃ (Conc. 10^{-4} M)	UV-visible in solid state
L1a	262, 300	200, 260, 297
L1b	243, 272	193, 237, 272
L1c	242, 272	235, 271
L2a	256, 287	253, 286
L2b	242, 270	232, 269
L2c	242, 270	195, 230, 268
L3b	247 & 272	236, 274
L3c	244 & 272	236, 274
L3d	244 & 272	236 & 274
L4b	243 & 265	235, 265, 300, 360
L4c	243 & 265	235, 270, 370
L4d	242 & 265	195, 233, 270, 440
L5b	244 & 275	195, 235, 280, 385
L5c	245 & 275	227, 272, 375
L5d	244 & 275	234, 280
L6b	242 & 266	225, 271, 390
L6c	242 & 268	194, 230, 270, 375
L6d	243 & 268	195, 230, 273, 325, 380

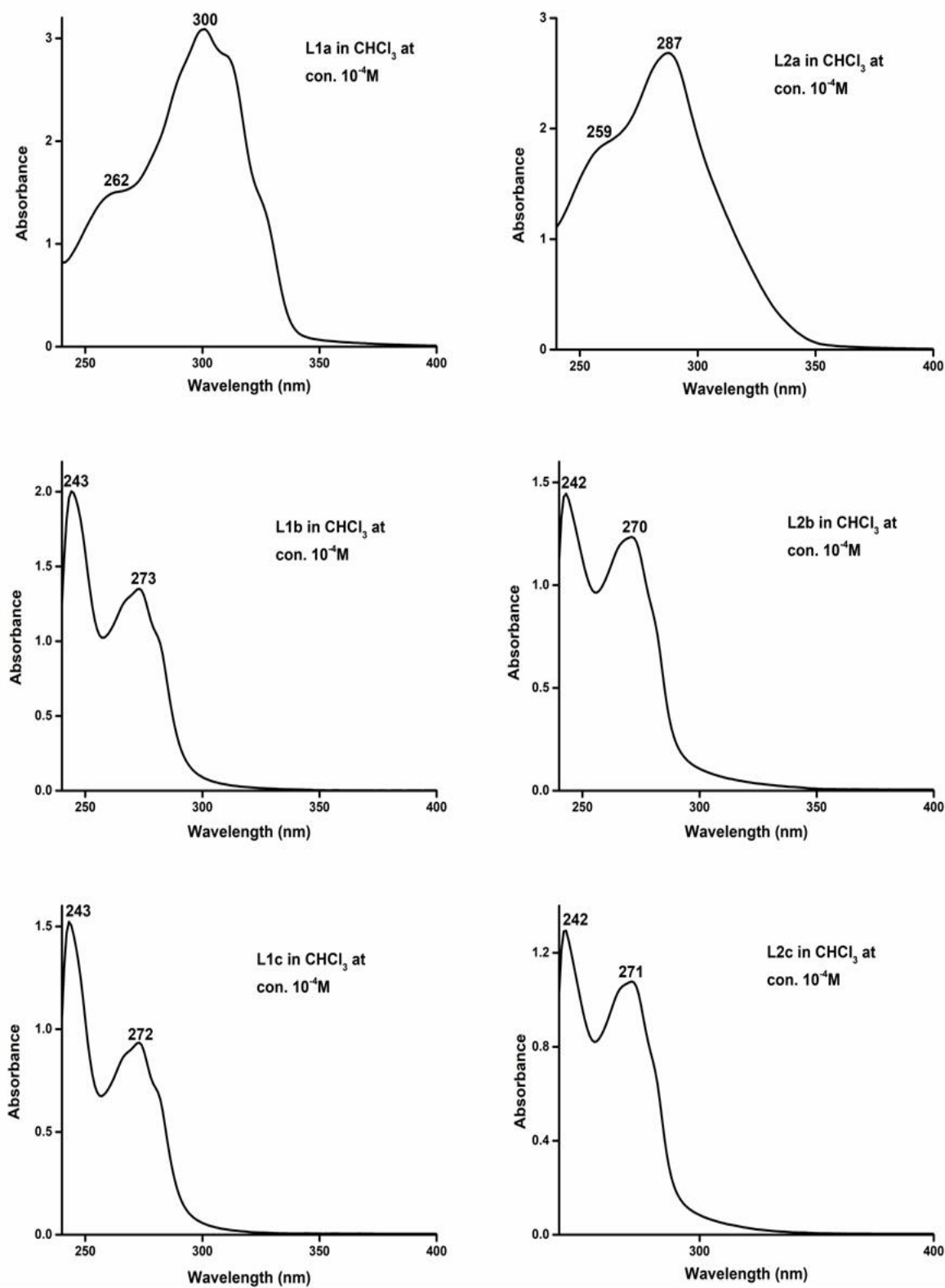


Figure 3.10: UV-visible absorption spectra of **L1a-L2c** in CHCl_3 at $\text{con. } 10^{-4}\text{M}$

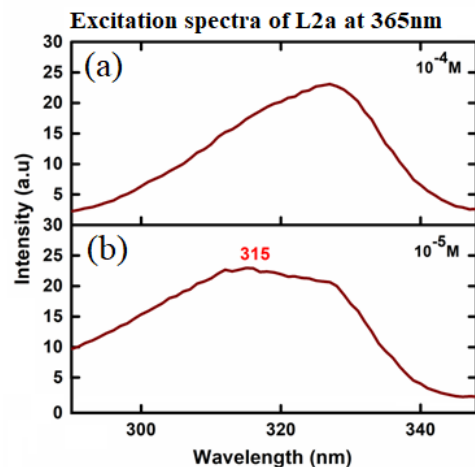


Figure 3.11: Excitation spectra of **L2a** in CHCl_3 in concentrations: (a) 10^{-4} M and (b) 10^{-5} M

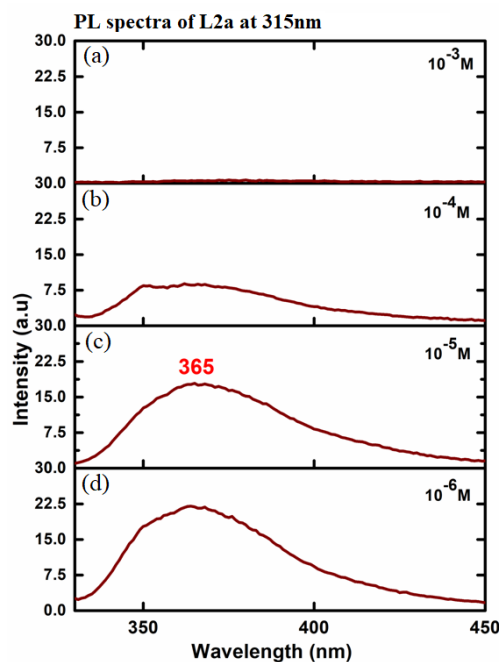


Figure 3.12: PL spectra of **L2a** in CHCl_3 in different concentrations: (a) 10^{-3} M; (b) 10^{-4} M; (c) 10^{-5} M; (d) 10^{-6} M

They have suggested that intramolecular hydrogen bonds of salicylaldimine moieties and stacking of molecules resulted in AIEE; which resulted due to the inhibition of free intramolecular rotation when changed from solution to aggregate state. Though the skeletal structure of **L2a** and **L1a** is similar to salicylaldehydeazines, but in **L2a** and **L1a** quenching of photoluminescence is observed on moving from “free state” to aggregated state.

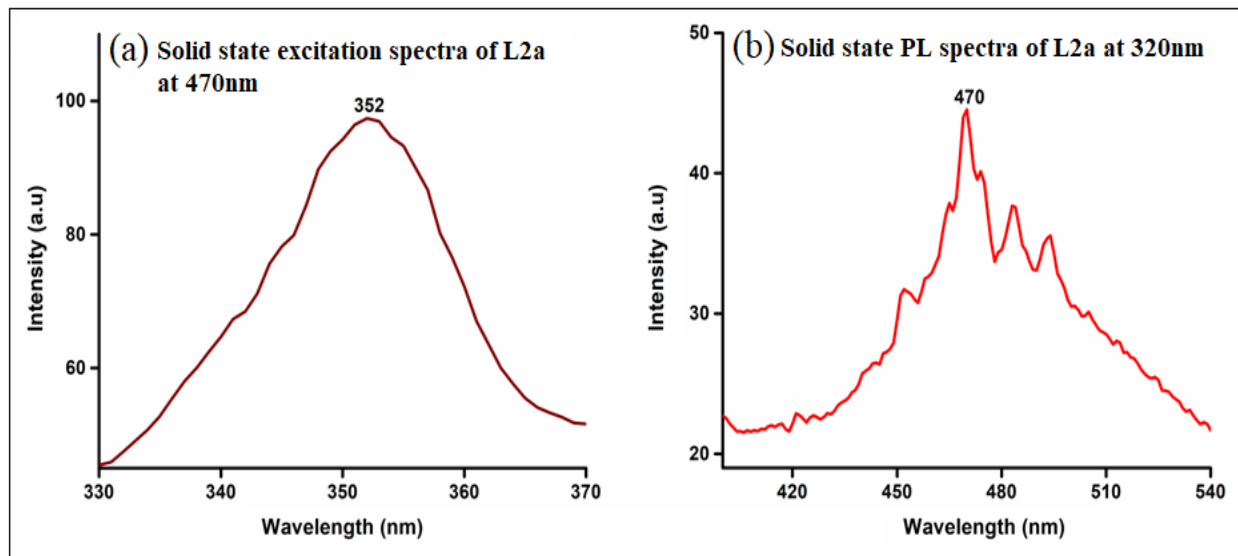


Figure 3.13: Excitation spectra (a) (emission was kept at 470 nm) and PL spectra (b) (at an excitation wavelength of 320 nm) of **L2a** in solid state.

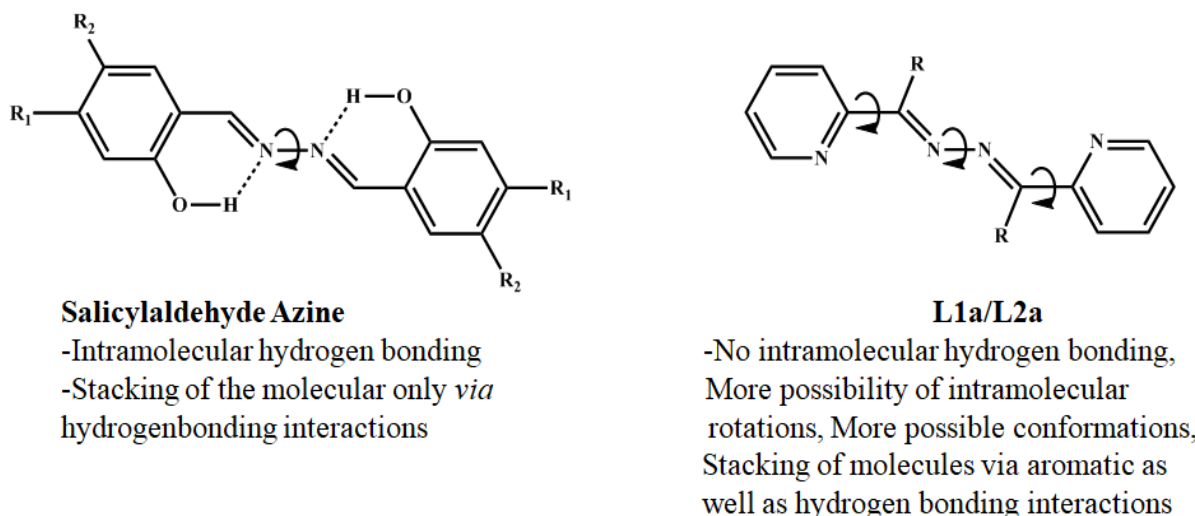


Figure 3.14: Comparison of **L1a/L2a** with salicylaldehyde azine

The crystal structure of **L2a** showed some important aspects about the packing of the molecules, which is associated with quenching of fluorescence of **L2a** in solid state. The arrangement of the molecules of **L2a** in a $\pi\cdots\pi$ stacked molecular pairs (dimers) facilitates the two molecules forming an excimer, which explains its non-fluorescent behavior in the solid state (Figure 3.4d).^[51]

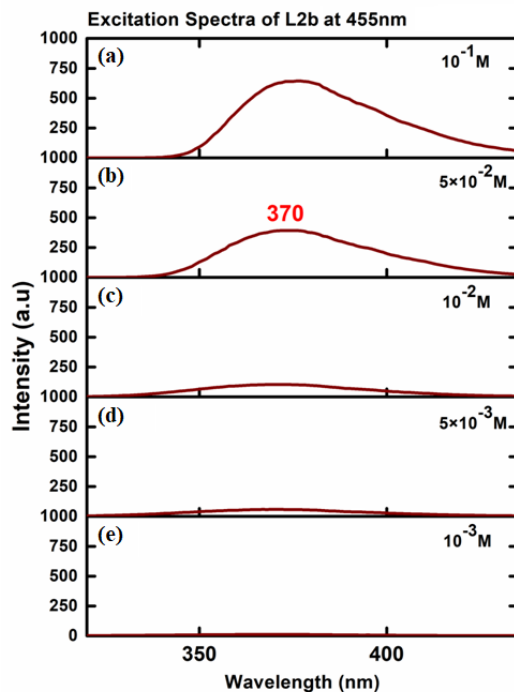


Figure 3.15: Excitation spectra of **L2b** in CHCl₃ in different concentrations: (a) 10⁻¹ M; (b) 5 × 10⁻² M; (c) 10⁻² M; (d) 5 × 10⁻³ M; (e) 10⁻³ M

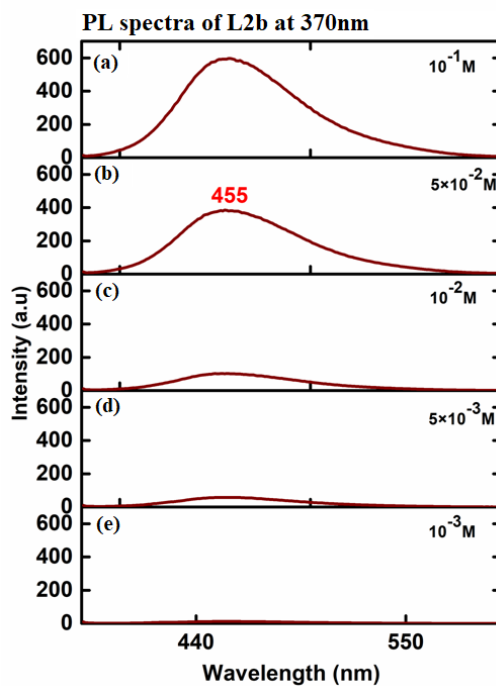


Figure 3.16: PL spectra of **L2a** in CHCl₃ in different concentrations: (a) 10⁻¹ M; (b) 5 × 10⁻² M; (c) 10⁻² M; (d) 5 × 10⁻³ M; (e) 10⁻³ M

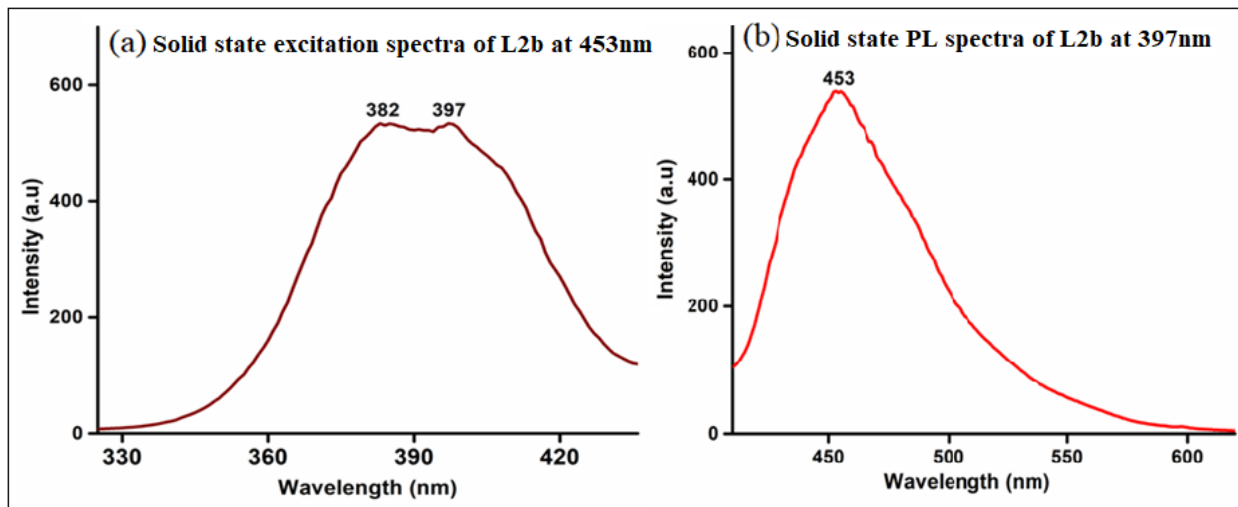


Figure 3.17: (a) Excitation spectra (emission was kept at 453 nm) and (b) PL spectra (at an excitation wavelength of 397 nm) of **L2b** in solid state

3.3.5 Photophysical properties of L2b, L3c, L5c, L5d, L6c and L6d:

3.3.5.1 Excitation spectra and photoluminescence spectra of L2b: The excitation spectra of **L2b** were taken in CHCl_3 by varying the concentration. The spectra showed maxima at a wavelength of 370–385 nm, when the emission wavelength was kept at 455 nm. Increasing the concentration of **L2b** resulted in increase in the intensity along with a slight red shift of the peak maxima. The excitation spectra of **L2b** at an emission wavelength of 370 nm are shown in (Figure 3.15). The photoluminescence spectra of **L2b** in CHCl_3 showed a weakly intense peak at 455 nm (when an excitation wavelength of 370 nm was used) at a concentration of 10^{-3} M. The change in concentration resulted in change in intensity of the peak; slight shift was observed in the peak position (Figure 3.16). The solid state photoluminescence spectra of **L2b** shows highly intense band at 453 nm (Figure 3.17). The enhancement of the luminescence intensity along with a red shift of peak positions for the solid **L2b** is related to crystallization induced enhanced emission.

3.3.5.2 Excitation spectra and photoluminescence spectra of L3c: The excitation spectra of **L3c** in CHCl_3 at different concentrations showed two peaks at 370 and 420 nm. With increase in concentration from 10^{-2} to 5×10^{-1} M the intensity is also increased with a slight red shift of λ_{max} (Figure 3.18). The PL spectra of **L3c** in CHCl_3 measured at an excitation wavelength of 420 nm. A weakly intense peak at 500 nm was observed at 10^{-2} M concentration.

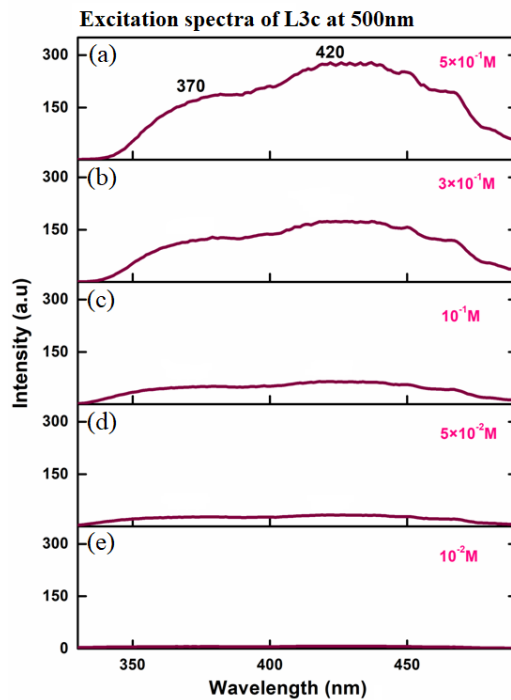


Figure 3.18: Excitation spectra of L3c in CHCl_3 in different concentrations: (a) $5 \times 10^{-1} \text{ M}$, (b) $3 \times 10^{-1} \text{ M}$, (c) 10^{-1} M (d) $5 \times 10^{-2} \text{ M}$ (e) 10^{-2} M

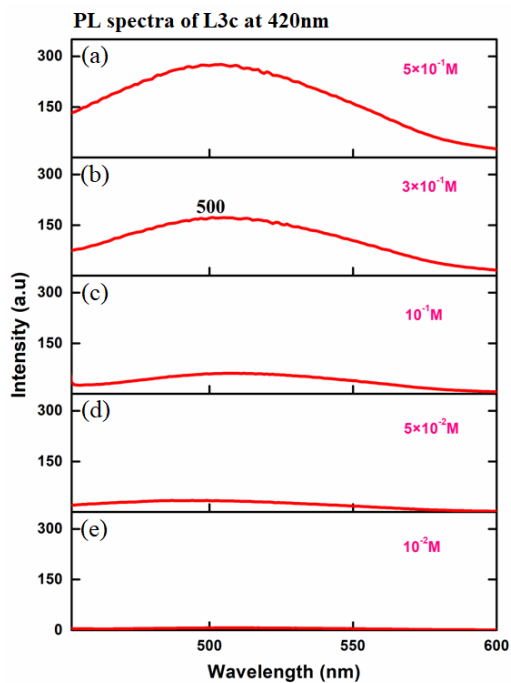


Figure 3.19: PL spectra of L3c in CHCl_3 in different concentrations: (a) $5 \times 10^{-1} \text{ M}$; (b) $3 \times 10^{-1} \text{ M}$; (c) 10^{-1} M ; (d) $5 \times 10^{-2} \text{ M}$; (e) 10^{-2} M

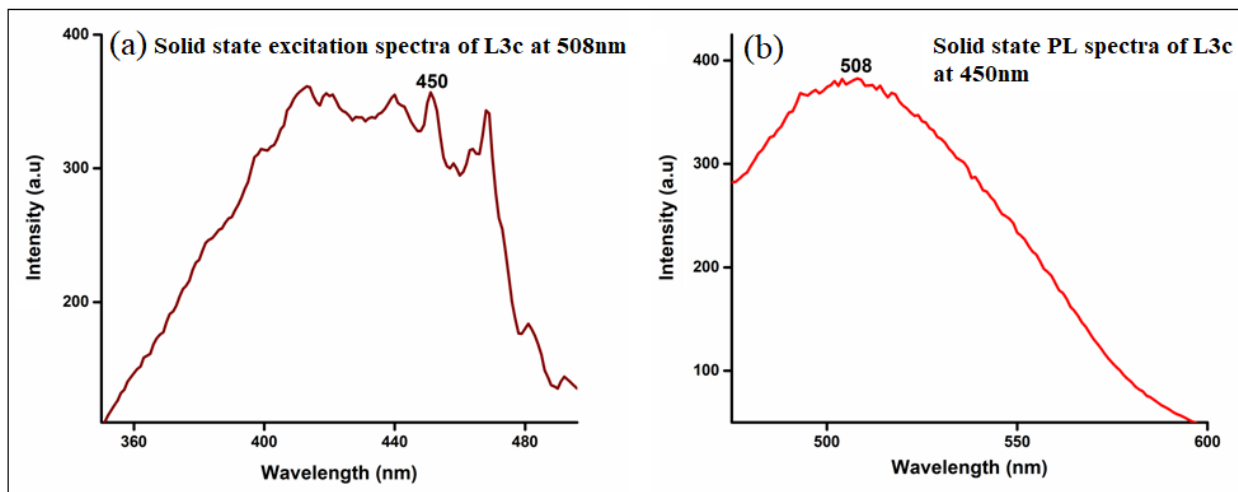


Figure 3.20: (a) Excitation spectra (emission was kept at 508 nm) and (b) PL spectra (at an excitation wavelength of 450 nm) of **L3c** in solid state

With increase in concentration the intensity of the peak was also increased (Figure 3.19). The structured emission bands of **L3c** molecules obtained at 460 nm while the solid state PL of **L3c** showed a highly intense peak at 508 nm (Figure 3.20).

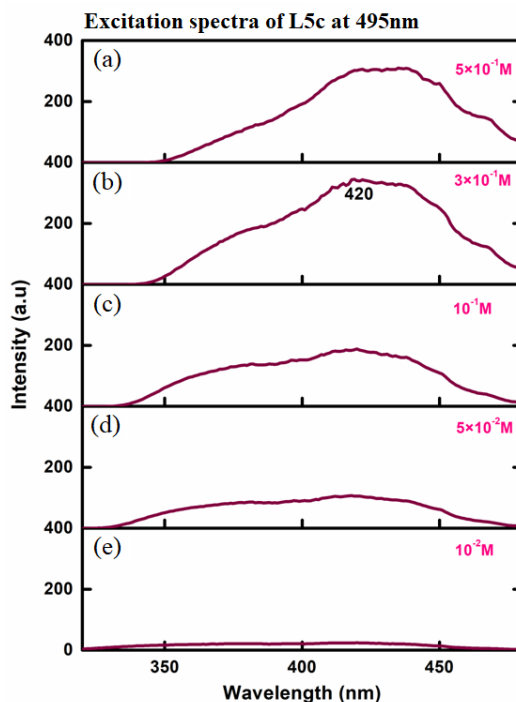


Figure 3.21: Excitation spectra of **L5c** in CHCl_3 at different concentrations:(a) $5 \times 10^{-1} \text{ M}$; (b) $3 \times 10^{-1} \text{ M}$; (c) 10^{-1} M ; (d) $5 \times 10^{-2} \text{ M}$; (e) 10^{-2} M

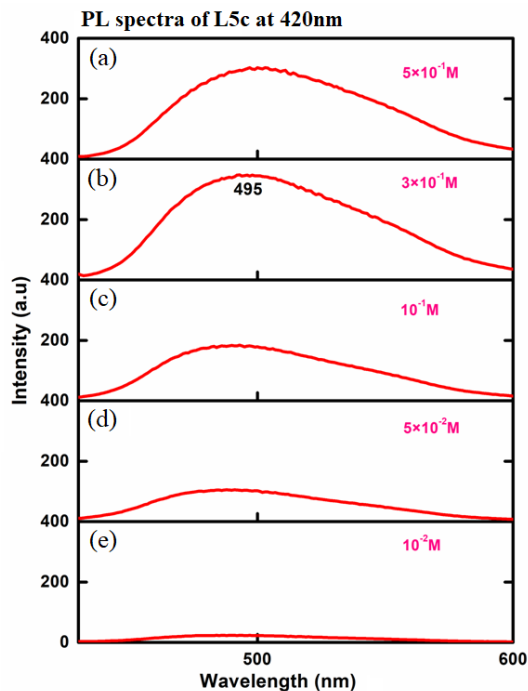


Figure 3.22: PL spectra of **L5c** in CHCl_3 at different concentrations: 5×10^{-1} M; (b) 3×10^{-1} M; (c) 10^{-1} M; (d) 5×10^{-2} M; (e) 10^{-2} M

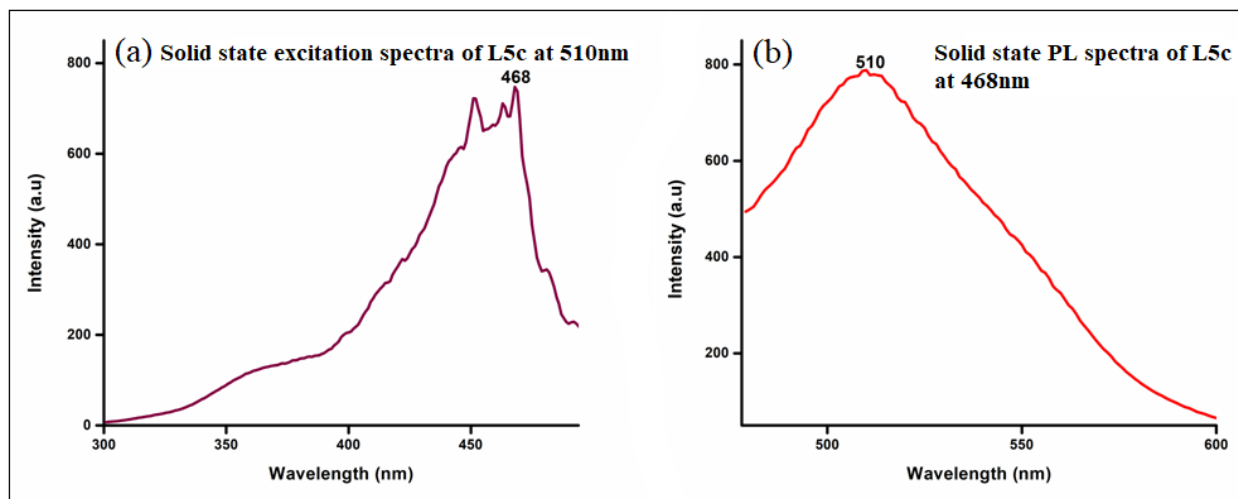


Figure 3.23: (a) Excitation spectra (emission was kept at 510 nm) and (b) PL spectra (at an excitation wavelength of 468 nm) of **L5c** in the solid state

3.3.5.3 Excitation spectra and photoluminescence spectra of L5c: The excitation spectra of **L5c** measured in CHCl_3 at different concentrations. At 10^{-2} M the spectra showed maxima at 350 and 420 nm (emission wavelength was at 490 nm). With increase in concentration the intensity

of the peak at 420 nm increased continuously and the peak at 350 nm becomes hump and disappeared at the concentration of 5×10^{-1} M (Figure 3.21). The PL spectra of **L5c** measured in CHCl_3 at different concentrations (excitation wavelength was kept at 420 nm). A weakly intense peak at 495 nm was observed at 10^{-2} M concentration. With increase in concentration to 5×10^{-1} M the intensity of the peak also increased accordingly (Figure 3.22). The structured emission of **L5c** molecules obtained at 415 nm when the excitation wavelength was kept at 350 nm (Appendix figure A37). The solid state PL spectra of **L5c** showed a highly intense peak at 510 nm (when the excitation wavelength was at 468 nm) (Figure 3.23).

3.3.5.4 Excitation spectra and photoluminescence spectra of L5d: The excitation spectra of **L5d** measured in CHCl_3 at different concentrations. At 10^{-2} M the spectra showed peak maxima at 355 nm and weak emission at 410 nm (at an emission wavelength of 480 nm). With increase in concentration the intensity of the peak at 410 nm increased continuously and the former peak becomes hump with red shift at the concentration of 5×10^{-1} M (Figure 3.24). The PL spectra of **L5d** measured in CHCl_3 at different concentrations (at an excitation wavelength of 410 nm). A weakly intense peak at 470 nm was observed at 10^{-2} M concentration.

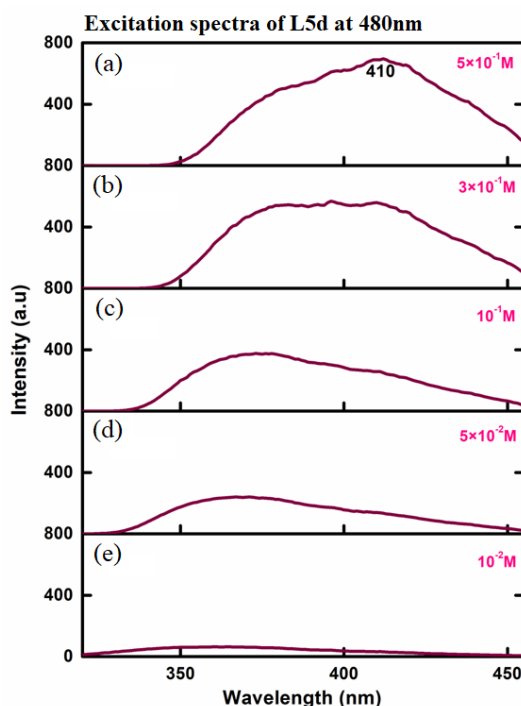


Figure 3.24: Excitation spectra of **L5d** in CHCl_3 at different concentrations:(a) 5×10^{-1} M; (b) 3×10^{-1} M; (c) 10^{-1} M; (d) 5×10^{-2} M; (e) 10^{-2} M

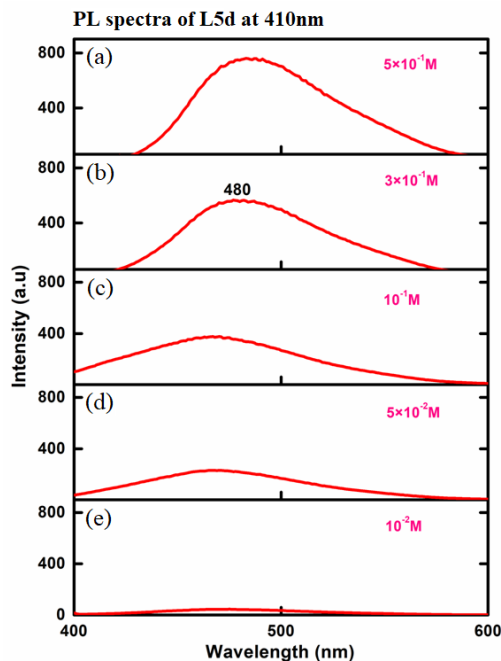


Figure 3.25: PL spectra of **L5d** in CHCl_3 at different concentrations: (a) 5×10^{-1} M; (b) 3×10^{-1} M; (c) 10^{-1} M; (d) 5×10^{-2} M; (e) 10^{-2} M

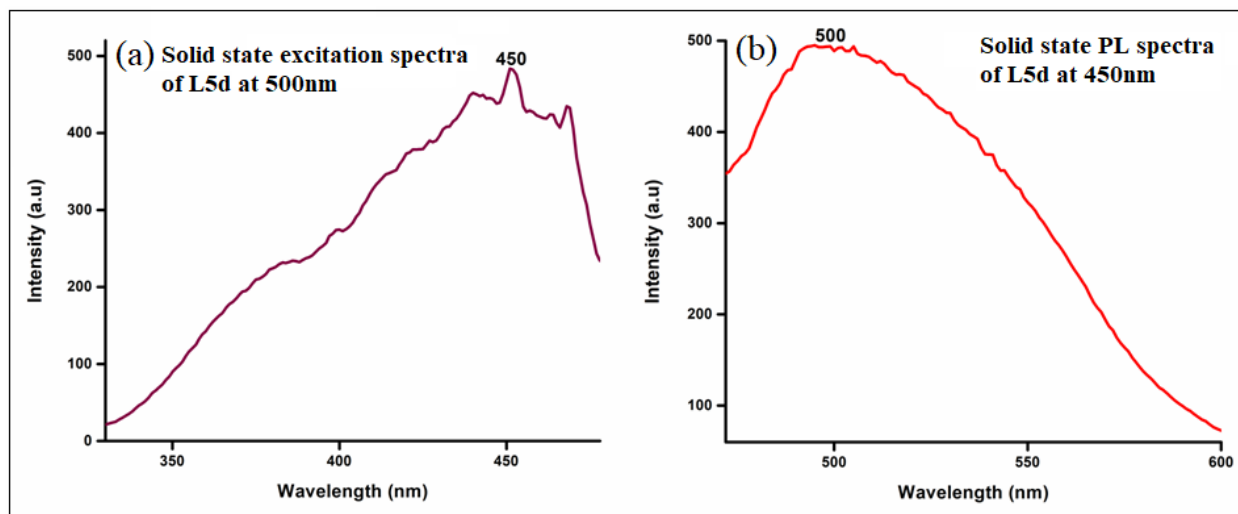


Figure 3.26: (a) Excitation spectra (emission was kept at 500 nm) and (b) PL spectra (at an excitation wavelength of 450 nm) of **L5d** in the solid state

With increase in concentration to 5×10^{-1} M the intensity of the peak increased with red shift to 480 nm (Figure 3.25). The structured emission of **L5d** molecules obtained at 415 nm when the excitation wavelength was kept at 355 nm (Appendix figure A38); the solid state PL spectra of

L5d showed a highly intense peak at 500 nm (at an excitation wavelength of 450 nm) (Figure 3.26).

3.3.5.5 Excitation spectra and photoluminescence spectra of L6c: The excitation spectra of **L6c** measured in CHCl_3 at different concentrations. At 10^{-2} M the spectra showed peak maxima at 420 nm (emission wavelength was kept at 500 nm). The intensity of the peak increased with increase in concentration and at 5×10^{-1} M the peak showed red shift to 440 nm (Figure 3.27). The PL spectra of **L6c** also measured in CHCl_3 at different concentrations (excitation wavelength was kept at 440 nm).

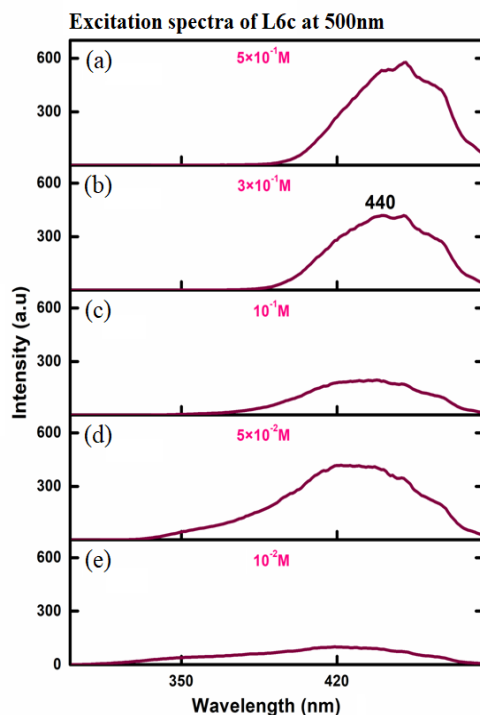


Figure 3.27: Excitation spectra of **L6c** in CHCl_3 at different concentrations: (a) 5×10^{-1} M; (b) 3×10^{-1} M; (c) 10^{-1} M; (d) 5×10^{-2} M; (e) 10^{-2} M

A weakly intense peak at 500 nm was observed which continuously increased with increase in concentration from 10^{-2} M to 5×10^{-1} M (Figure 3.28). The structured emission of **L6c** molecules obtained at 370 nm when the excitation wavelength was kept at 325 nm (Appendix figure A39) the solid state PL spectra of **L6c** showed a highly intense peak at 510 nm (when the excitation wavelength was kept at 468 nm) (Figure 3.29).

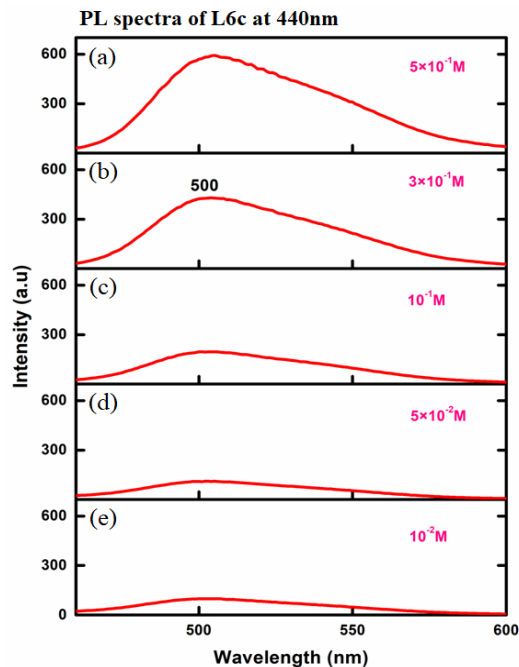


Figure 3.28: PL spectra of **L6c** in CHCl_3 at different concentrations: (a) 5×10^{-1} M; (b) 3×10^{-1} M; (c) 10^{-1} M; (d) 5×10^{-2} M; (e) 10^{-2} M

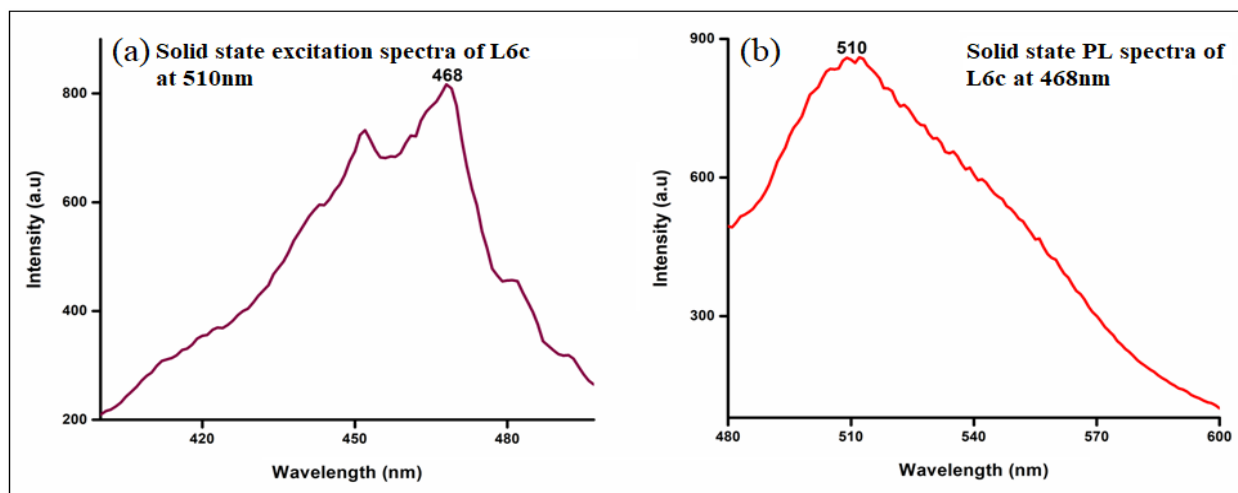


Figure 3.29: (a) Excitation spectra (emission was kept at 510 nm) and (b) PL spectra (at an excitation wavelength of 468 nm) of **L6c** in the solid state

3.3.5.6 Excitation spectra and photoluminescence spectra of L6d: The excitation spectra of **L6d** measured in CHCl_3 at different concentrations. At 10^{-2} M the spectra showed peak maxima at 375 nm (emission wavelength was kept at 515 nm).

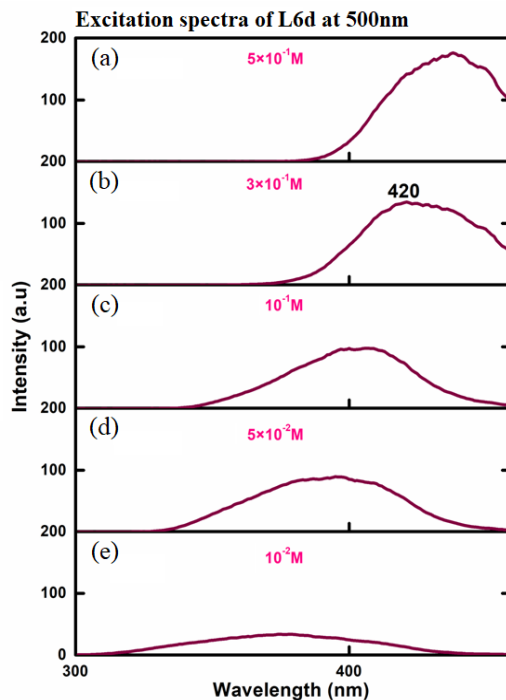


Figure 3.30: Excitation spectra of **L6d** in CHCl_3 at different concentrations: (a) $5 \times 10^{-1} \text{ M}$, (b) $3 \times 10^{-1} \text{ M}$, (c) 10^{-1} M (d) $5 \times 10^{-2} \text{ M}$ (e) 10^{-2} M

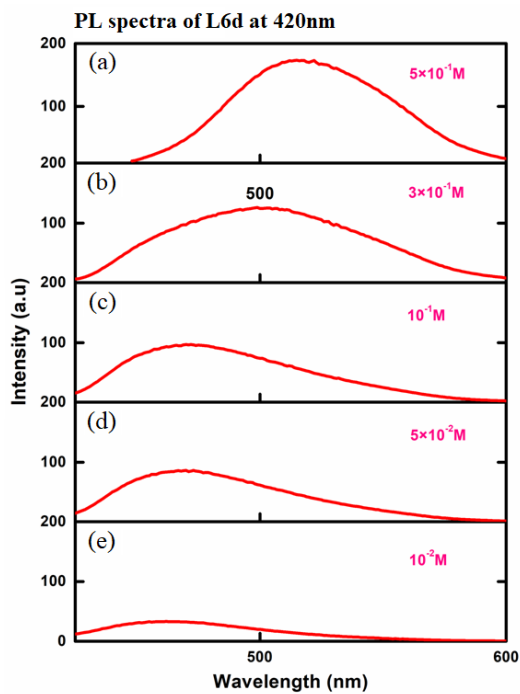


Figure 3.31: PL spectra of **L6d** in CHCl_3 at different concentrations: (a) $5 \times 10^{-1} \text{ M}$; (b) $3 \times 10^{-1} \text{ M}$; (c) 10^{-1} M ; (d) $5 \times 10^{-2} \text{ M}$; (e) 10^{-2} M

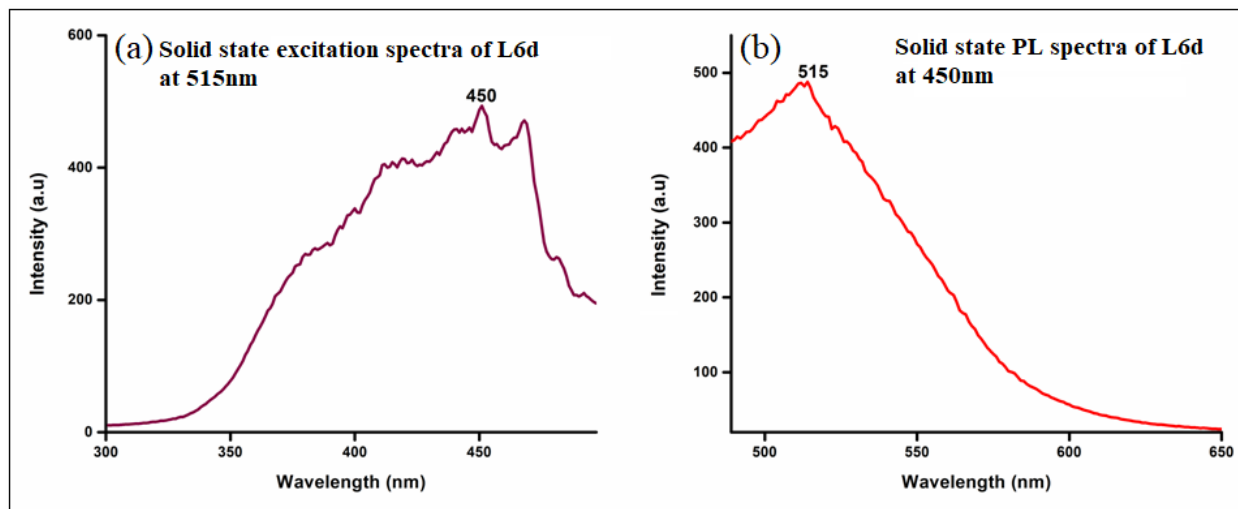
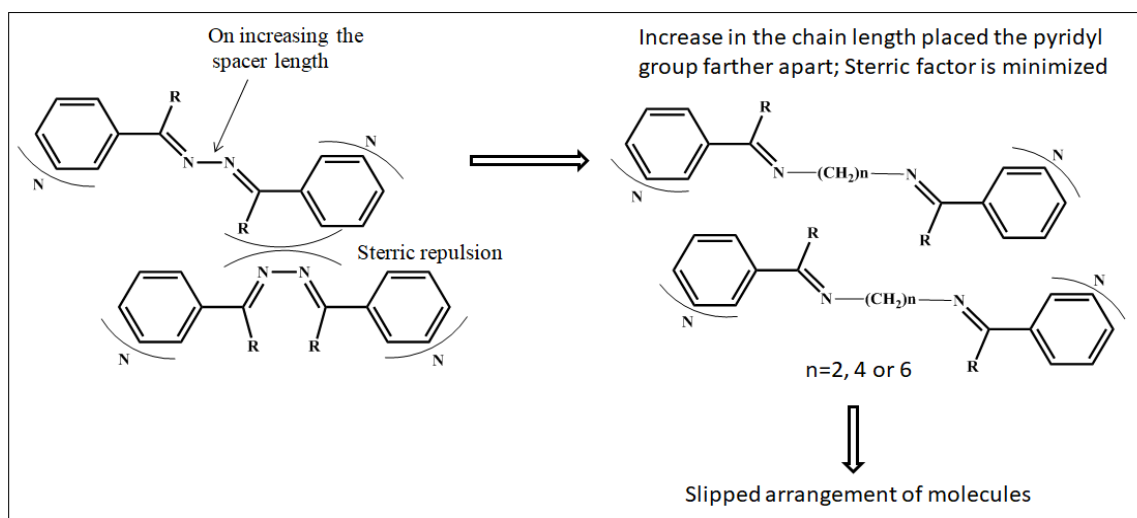


Figure 3.32: (a) Excitation spectra (emission was kept at 515 nm) and (b) PL spectra (at an excitation wavelength of 450 nm) of **L6d** in the solid state



Scheme 3.2: Formation of slipped type arrangement on increasing spacer length

The intensity of the peak increased with red shift in peak position with the increase in concentration and at 5×10^{-1} M the peak showed red shift to 437 nm (Figure 3.30). The PL spectra of **L6d** also measured in CHCl_3 at different concentrations (excitation wavelength was kept at 440 nm). A weakly intense peak at 462 nm was observed at 10^{-2} M concentration. With increase in concentration to 5×10^{-1} M the intensity of the peak increased with red shift to 515 nm (Figure 3.31). The structured emission of **L6d** molecules obtained at 370 nm when the excitation wavelength was kept at 325 nm (Appendix figure A40); the solid state PL spectra of **L6d** showed

a highly intense peak at 515 nm (when the excitation wavelength was kept at 450 nm) (Figure 3.32).

3.3.6 Correlating the photophysical properties of L2b, L3c, L5c, L5d, L6c and L6d with their structure: The crystal structure of **L2b**, **L5c**, **L5d**, **L6c** and **L6d** showed that although the spacers in those molecules has a flexible alkyl chain, the arrangement of the molecules in the solid state give them a “rigid” planar-like geometry. The enhanced emission in the solid state of these molecules can be interpreted in terms of simultaneous effects of intra- and intermolecular effects exerted by the aggregation of the molecules. The planar like geometry of the molecule in the solid state activates the radiation process, while the aggregation morphology resulting due to the supramolecular arrangement of the molecules also influences the emission process. The molecules in **L2b**, **L5c**, **L5d**, **L6c** and **L6d** are arranged in parallel manner but they are arranged in a specific slipped-type pattern, so that the excimer formation is avoided (Scheme 3.2). The presence of the ethyl spacer in **L2b**, butyl spacer in **L5c**, **L6c** and hexyl spacer in **L5d**, **L6d** made possible to have a slipped-type arrangement of the molecules.

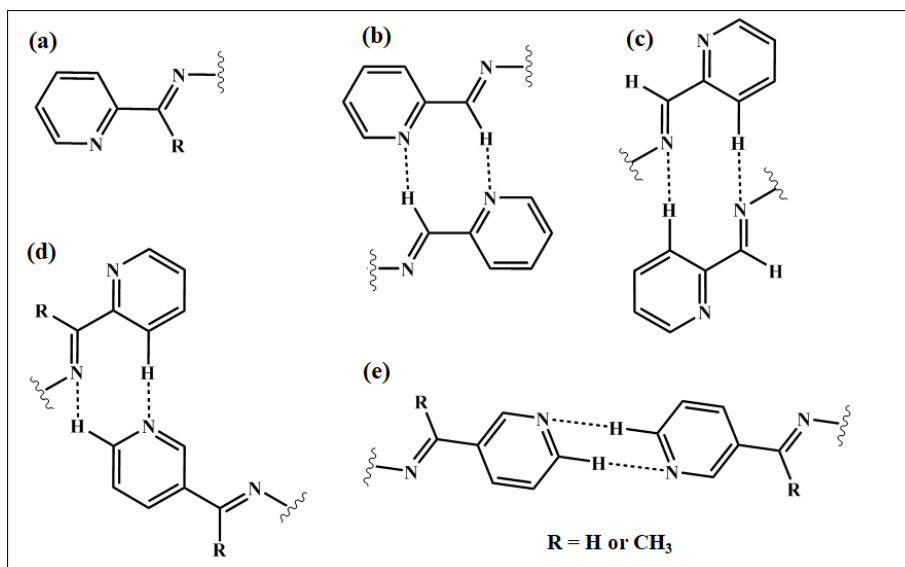


Figure 3.33: (a) pyridyl imine moiety; (b)-(e): possible non-covalently bonded moieties of pyridyl imines.

Moreover the molecules **L5c**, **L5d**, **L6c** and **L6d** are held together by C-H...N interactions thereby resulting in proper assembly of chromophore moieties which enhances the luminescence as increased from lower to higher concentrations. The crystal structure of **L3c** showed the formation of *gauche-anti-gauche* conformation of butyl spacer and hence a non planar molecular

geometry in the solid state. Though there is no planarity in the structure these molecules exhibiting considerable PL in the solid state. The molecules in **L3c** is non-covalently bound to form chromophores contains type-(e) dimers that enhanced the emission process in the solid state (Figure 3.33).

3.3.7 Excitation spectra and photoluminescence spectra of L1c: Interesting photoluminescence spectral properties were observed for **L1c**. The concentration dependent excitation spectra of **L1c** in CHCl_3 showed that at a concentration of 5×10^{-3} M, the spectra had maxima at 365 and 420 nm (emission wavelength was kept at 460 nm) (Figure 3.34). The PL spectra of **L1c** for a concentration of 5×10^{-3} M showed maxima at 460 nm, when an excitation wavelength of 420 nm was used. On increasing the concentration, the increase in the intensity of peak maxima was observed. However, at a concentration of 5×10^{-2} M, a hump appeared at 545 nm, intensity of which increases with increase in the concentration. Finally, at a concentration of 5×10^{-1} M, an intense peak was present at 545 nm while the peak at 460 nm disappeared (Figure 3.35). The solid-state photoluminescence spectra of **L1c** showed strong emission peak appeared in the region of 548 nm (Figure 3.36).

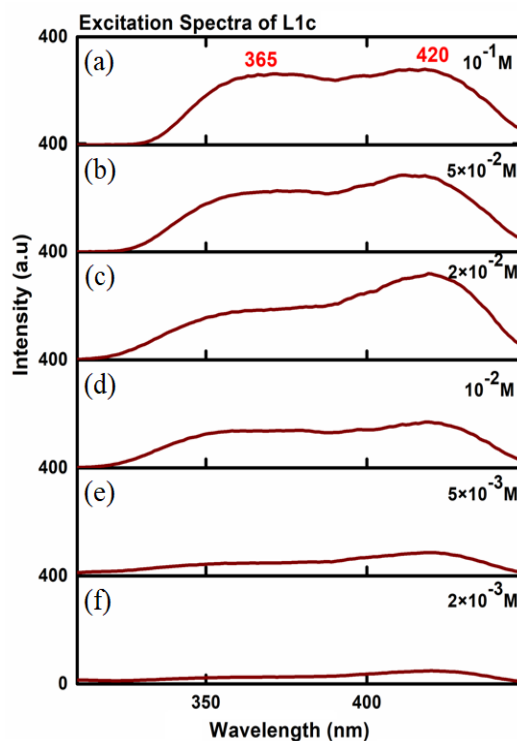


Figure 3.34: Excitation spectra of **L1c** in CHCl_3 at different concentrations: (a) 10^{-1} M (b) 5×10^{-2} M (c) 2×10^{-2} M (d) 10^{-2} M, (e) 5×10^{-3} M, (f) 2×10^{-3} M

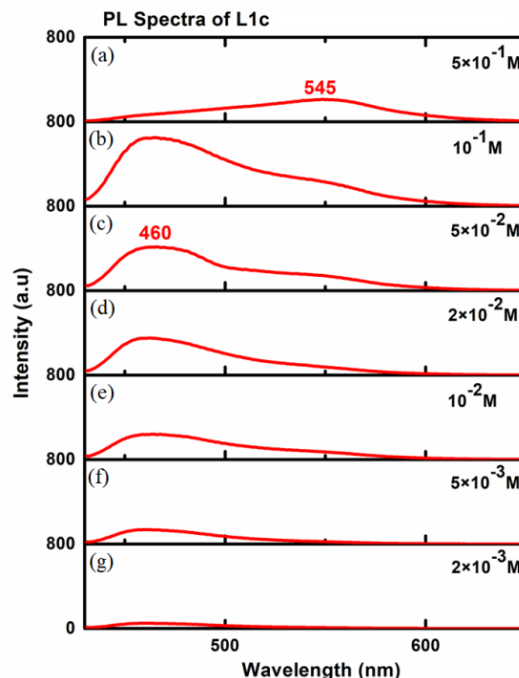


Figure 3.35: PL spectra of **L1c** in CHCl_3 at different concentrations: (a) 5×10^{-1} M; (b) 10^{-1} M; (c) 5×10^{-2} M; (d) 2×10^{-2} M; (e) 10^{-2} M; (f) 5×10^{-3} M; (g) 2×10^{-3} M

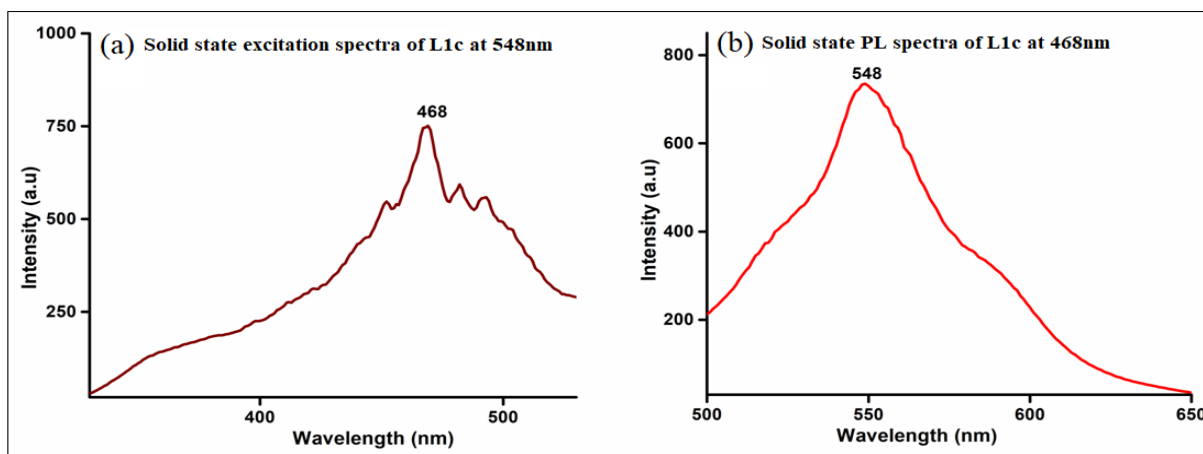


Figure 3.36: (a) Excitation spectra (emission was kept at 548 nm) and (b) PL spectra (at an excitation wavelength of 548 nm) of **L1c** in the solid state

The appearance of a new peak at a concentration of 5×10^{-1} M followed by a red shift of the same peak in case of solid **L1c** suggested the formation of non-covalently bonded species of the molecules. The large bathochromic shift of the emission peak suggested the formation of chromophore Type (b) dimers of **L1c** in the aggregated state (Figure 3.33). The excitation and

PL spectra were recorded for **L1b**, **L2c** and **L3b-L4d**. The λ_{\max} in PL of the compounds is given in the table 3.4.

Table 3.4: Photoluminescence spectral data in solution and solid state of the ligands

Compound	PL in CHCl ₃		PL Solid
L1a	363 nm (Excitation 330 nm; 10^{-5} M)	-----	469 nm (Excitation 300 nm)
L1b	455 nm (Excitation 420 nm; 5×10^{-2} M)	555 nm (Excitation 470 nm; 2×10^{-1} M)	555 nm (Excitation 470 nm)
L1c	460 nm (Excitation 420 nm; 10^{-1} M)	555 nm (Excitation 470 nm; 5×10^{-1} M)	548 nm (Excitation 470 nm)
L2a	365 nm (Excitation 327 nm; 10^{-4} M)	-----	469 nm (Excitation 320 nm)
L2b	370, 450 nm (Excitation 330 nm; 10^{-2} M)	455 nm (Excitation 370 nm; 10^{-1} M)	453 nm (Excitation 400 nm)
L2c	460 nm (Excitation 370 nm; 5×10^{-2} M)	500 nm (Excitation 450 nm; 2×10^{-1} M)	527 nm (Excitation 468 nm)
L3b	455 nm (Excitation 370 nm; 3×10^{-1} M)	515 nm (Excitation 420 nm; 5×10^{-1} M)	535 nm (Excitation 468 nm)
L3c	460 nm (Excitation 370 nm; 5×10^{-1} M)	500 nm (Excitation 420 nm; 5×10^{-1} M)	508 nm (Excitation 450 nm)
L3d	460 nm (Excitation 375 nm; 10^{-1} M)	480 nm (Excitation 410 nm; 5×10^{-1} M)	495 nm (Excitation 450 nm)
L4b	435 nm (Excitation 365 nm; 5×10^{-2} M)	520 nm (Excitation 465 nm; 5×10^{-1} M)	525 nm (Excitation 468 nm)
L4c	375 nm (Excitation 325 nm; 10^{-2} M)	490 nm (Excitation 450 nm; 5×10^{-1} M)	490 nm (Excitation 450 nm)
L4d	360 nm (Excitation 325 nm; 10^{-3} M)	490 nm (Excitation 420 nm; 5×10^{-1} M)	495 nm (Excitation 450 nm)

L5b	435 nm (Excitation 365 nm; 10^{-1} M)	490 nm (Excitation 420 nm; 5×10^{-1} M)	520 nm (Excitation 467 nm)
L5c	415 nm (Excitation 350 nm; 10^{-1} M)	500 nm (Excitation 420 nm; 5×10^{-1} M)	510 nm (Excitation 468 nm)
L5d	415 nm (Excitation 355 nm; 10^{-1} M)	485 nm (Excitation 410 nm; 5×10^{-1} M)	500 nm (Excitation 450 nm)
L6b	440 nm (Excitation 360 nm; 5×10^{-2} M)	500 nm (Excitation 440 nm; 5×10^{-1} M)	515 nm (Excitation 467 nm)
L6c	370 nm (Excitation 325 nm; 10^{-2} M)	505 nm (Excitation 450 nm; 5×10^{-1} M)	510 nm (Excitation 468 nm)
L6d	370 nm (Excitation 325 nm; 10^{-2} M)	515 nm (Excitation 435 nm; 5×10^{-1} M)	515 nm (Excitation 467 nm)

3.3.8 NMR assay for detecting the aggregation in L1c: The expected nature of the NMR spectra for non-aggregating compound includes sharp NMR resonance peaks at all concentrations and peak position is independent of the concentration. In case of aggregating compounds, higher concentrations result in self association of the molecules, while dilution will result in free state of the molecules. As a result, the effect of concentration changes will be observed in the NMR spectra. The NMR features that may become concentration dependent for aggregating compounds include chemical shifts, shape and intensity of the peaks.^[52] The ^1H NMR spectra of **L1c** was recorded as a function of compound concentration (Figure 3.37). The protons in the aromatic region show change in chemical shift when the concentration of **L1c** in CDCl_3 was increased from 10^{-2} M to 1 M. The crystal structure of **L1c** shows the packing of the molecules, where the imine proton (H_e in the Figure 3.37) is in close proximity with pyridyl nitrogen. The protons H_a , H_b and H_c interact with pyridyl ring of another molecule as shown in Figure 3.37d. The aromatic protons and the imine proton are becoming more shielded protons on increasing the concentration of **L1c**. The NOESY of **L1c** was recorded to further observe the aggregation of the molecules at high concentration (Figure 3.38).

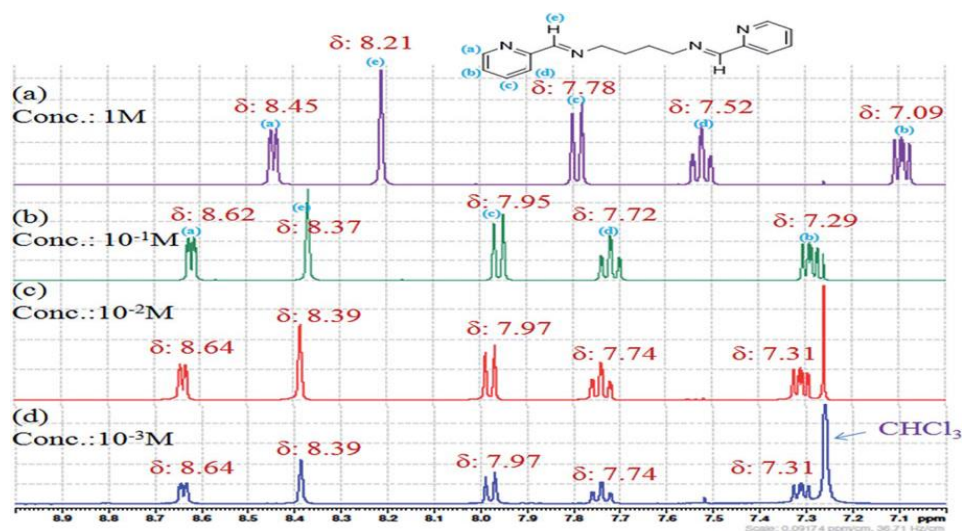


Figure 3.37: ^1H NMR spectra of **L1c** at different concentrations

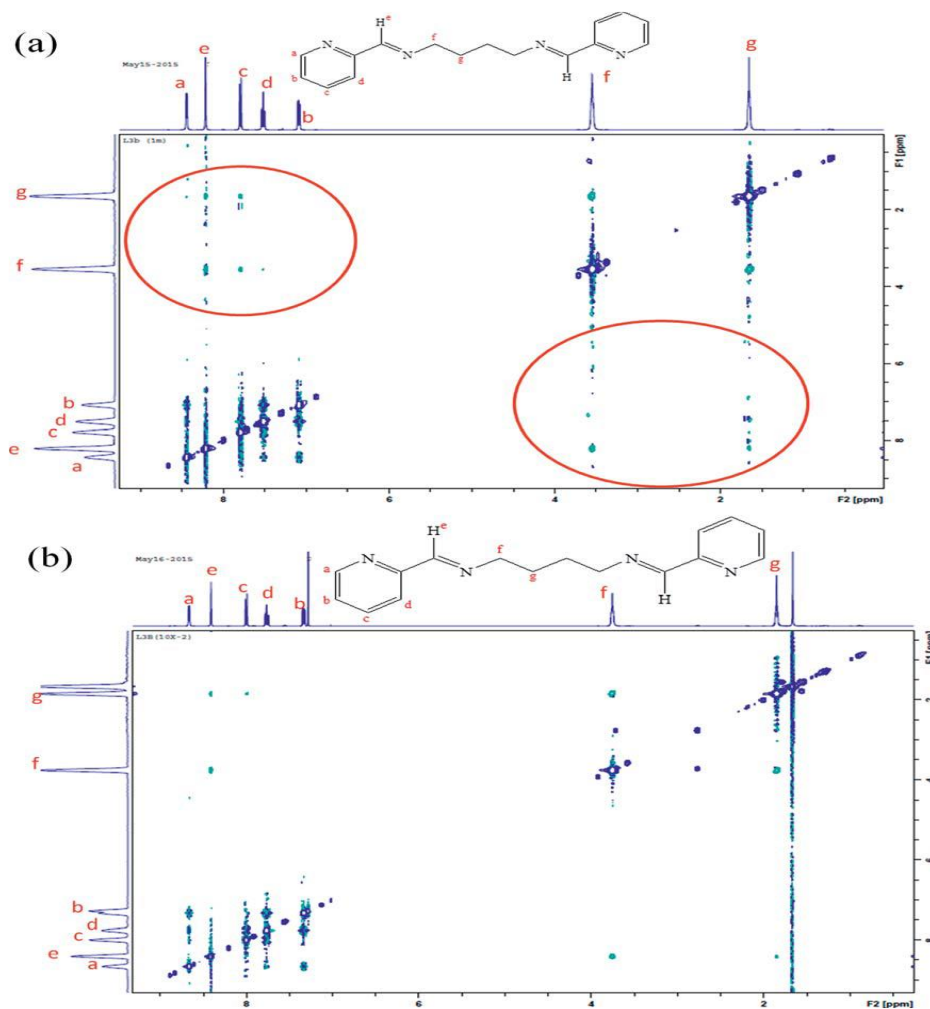


Figure 3.38: NOESY spectra of **L1c**

The spectra recorded at a concentration of 1 M of **L1c** in CDCl_3 shows interaction between the aromatic and the aliphatic protons (Figure 3.38), while very less interaction is observed at a concentration of 10^{-2} M. Further, quite intense interaction between the aromatic protons is observed at a higher concentration than that at a lower concentration.

3.4 Conclusions

The study on structure and photophysical property has reminiscent some important rationale pertaining the interplay of molecular geometry and non-covalent interactions in deciding the light emitting properties of compounds. A series of 18 Schiff base compounds (**L1a-L6d**) photophysical properties were investigated at different concentrations and in solid state. The compounds **L1a** and **L2a** exhibits PL spectra in dilute solution and quenching in PL spectra was observed on increasing concentration. Although the molecules **L1a** and **L2a** are rigid, doesn't show PL emission in the solid state, while the molecules with alkyl spacer endorse highly intense PL spectra in the solid state. This enhanced luminescence studies of the compounds are analyzed in correlation with the crystal packing in the aggregated solid state. Though the compounds **L2b**, **L5c**, **L5d**, **L6c** and **L6d** contains flexible alkyl chain in the spacer the crystal structure analysis elucidate the presence of planar geometry of the molecules and the escalated emission of the compounds is due to the non-covalent packing of molecules in a specific pattern propelled in extending the chromophores. The compounds **L1c** and **L3c** exhibit non-planar geometry. Irrespective of planarity in the crystal structure of **L1c** and **L3c**, molecules aggregate systematically by non-covalent interactions form dimerized chromophores impelled in the enhanced emission of the compounds.

3.5 References

- 1 C. T. Chen, *Chem. Mater.*, 2004, **16**, 4389–4400.
- 2 Y. Tao, C. Yang and J. Qin, *Chem. Soc. Rev.*, 2011, **40**, 2943–2970.
- 3 G. Mehes, K. Goushi, W. J. Potscavage Jr and C. Adachi, *Org. Electron.*, 2014, **15**, 2027–2037.
- 4 M. T. Ghoneim and M. M. Hussain, *Electronics*, 2015, **4**, 424–479.
- 5 B. Kim, X. Yue, B. Sui, X. Zhang, Y. Xiao, M. V Bondar, J. Sawada, M. Komatsu and K. D. Belfield, *European J. Org. Chem.*, 2015, **2015**, 5563–5571.

-
- 6 C. A. Huerta-Aguilar, P. Raj, P. Thangarasu and N. Singh, *RSC Adv.*, 2016, **6**, 37944–37952.
 - 7 Z. Liu, F. Hao, J. Liu, Y. Zhu, W. Du, Q. Zhang and J. Wu, *New J. Chem.*, 2018, **42**, 3947–3952.
 - 8 A. J. C. Kuehne and M. C. Gather, *Chem. Rev.*, 2016, **116**, 12823–12864.
 - 9 J. R. Lawrence, Y. Ying, P. Jiang and S. H. Foulger, *Adv. Mater.*, 2006, **18**, 300–303.
 - 10 A. Bandyopadhyay and A. J. Pal, *Appl. Phys. Lett.*, 2003, **82**, 1215–1217.
 - 11 Q. Zhang, J. He, H. Zhuang, H. Li, N. Li, Q. Xu, D. Chen and J. Lu, *Adv. Funct. Mater.*, 2016, **26**, 146–154.
 - 12 Q. Zhao and J. Z. Sun, *J. Mater. Chem. C*, 2016, **4**, 10588–10609.
 - 13 Y. Hong, J. W. Y. Lam and B. Z. Tang, *Chem. Soc. Rev.*, 2011, **40**, 5361–5388.
 - 14 Z. Zhao, C. Y. K. Chan, S. Chen, C. Deng, J. W. Y. Lam, C. K. W. Jim, Y. Hong, P. Lu, Z. Chang, X. Chen and others, *J. Mater. Chem.*, 2012, **22**, 4527–4534.
 - 15 H. Nie, K. Hu, Y. Cai, Q. Peng, Z. Zhao, R. Hu, J. Chen, S. J. Su, A. Qin and B. Z. Tang, *Mater. Chem. Front.*, 2017, **1**, 1125–1129.
 - 16 R. Hu, N. L. C. Leung and B. Z. Tang, *Chem. Soc. Rev.*, 2014, **43**, 4494–4562.
 - 17 J. Mei, N. L. C. Leung, R. T. K. Kwok, J. W. Y. Lam and B. Z. Tang, *Chem. Rev.*, 2015, **115**, 11718–11940.
 - 18 Z. Zhao, B. He and B. Z. Tang, *Chem. Sci.*, 2015, **6**, 5347–5365.
 - 19 B. Yang, X. Zhang, X. Zhang, Z. Huang, Y. Wei and L. Tao, *Mater. Today*, 2016, **19**, 284–291.
 - 20 X. Zhang, X. Zhang, S. Wang, M. Liu, Y. Zhang, L. Tao and Y. Wei, *ACS Appl. Mater. Interfaces*, 2013, **5**, 1943–1947.
 - 21 B. Xu, Z. Chi, Z. Yang, J. Chen, S. Deng, H. Li, X. Li, Y. Zhang, N. Xu and J. Xu, *J. Mater. Chem.*, 2010, **20**, 4135–4141.
 - 22 B. Wang, Y. Wang, J. Hua, Y. Jiang, J. Huang, S. Qian and H. Tian, *Chem. Eur. J.*, 2011, **17**, 2647–2655.
 - 23 J. Huang, N. Sun, J. Yang, R. Tang, Q. Li, D. Ma and Z. Li, *Adv. Funct. Mater.*, 2014, **24**, 7645–7654.
 - 24 G. Liu, S. Tian, C. Li, G. Xing and L. Zhou, *ACS Appl. Mater. Interfaces*, 2017, **9**, 28331–28338.
-

-
- 25 Y. Hong, J. W. Y. Lam and B. Z. Tang, *Chem. Commun.*, 2009, 4332–4353.
- 26 B. K. An, S. K. Kwon, S. D. Jung and S. Y. Park, *J. Am. Chem. Soc.*, 2002, **124**, 14410–14415.
- 27 D. Majhi, S. K. Das, P. K. Sahu, S. M. Pratik, A. Kumar and M. Sarkar, *Phys. Chem. Chem. Phys.*, 2014, **16**, 18349–18359.
- 28 F. Wurthner, T. E. Kaiser and C. R. Saha-Moller, *Angew. Chem. Int. Ed.*, 2011, **50**, 3376–3410.
- 29 P. Mazumdar, D. Das, G. P. Sahoo, G. Salgado-Moran and A. Misra, *Phys. Chem. Chem. Phys.*, 2015, **17**, 3343–3354.
- 30 E. Hadjoudis and I. M. Mavridis, *Chem. Soc. Rev.*, 2004, **33**, 579–588.
- 31 S. P. Anthony, S. Varughese and S. M. Draper, *J. Phys. Org. Chem.*, 2010, **23**, 1074–1079.
- 32 N. S. S. Kumar, S. Varghese, N. P. Rath and S. Das, *J. Phys. Chem. C*, 2008, **112**, 8429–8437.
- 33 R. Thomas, S. Varghese and G. U. Kulkarni, *J. Mater. Chem.*, 2009, **19**, 4401–4406.
- 34 S. Varghese and S. Das, *J. Phys. Chem. Lett.*, 2011, **2**, 863–873.
- 35 V. Karunakaran, D. D. Prabhu, S. Das and S. Varughese, *Phys. Chem. Chem. Phys.*, 2015, **17**, 18768–18779.
- 36 Y. Abe, Y. Takagi, M. Nakamura, T. Takeuchi, T. Tanase, M. Yokokawa, H. Mukai, T. Megumi, A. Hachisuga and K. Ohta, *Inorg. Chim. Acta*, 2012, **392**, 254–260.
- 37 J. Cheng, Y. Li, R. Sun, J. Liu, F. Gou, X. Zhou, H. Xiang and J. Liu, *J. Mater. Chem. C*, 2015, **3**, 11099–11110.
- 38 J. Tang, Y. B. Cai, J. Jing and J. L. Zhang, *Chem. Sci.*, 2015, **6**, 2389–2397.
- 39 G. Shen, F. Gou, J. Cheng, X. Zhang, X. Zhou and H. Xiang, *RSC Adv.*, 2017, **7**, 40640–40649.
- 40 Y. Tong, B. Liu, Y. Wu, B. Yang, G. Wen, Y. T. Yang, J. Chai and X. Hu, *Sensors Actuators B Chem.*, 2017, **252**, 794–802.
- 41 T. Kawasaki, T. Kamata, H. Ushijima, S. Murata, F. Mizukami, Y. Fujii and Y. Usui, *Mol. Cryst. Liq. Cryst.*, 1996, **286**, 257–262.
- 42 W. Tang, Y. Xiang and A. Tong, *J. Org. Chem.*, 2009, **74**, 2163–2166.
- 43 G. Dong, H. Cheng, D. Chun-Ying, Q. Chun-Qi and M. Qing-Jin, *New J. Chem.*, 2002,
-

- 26**, 796–802.
- 44 D. A. Edwards, G. M. Hoskins, M. F. Mahon, K. C. Malloy and G. R. G. Rudolph, *Polyhedron*, 1998, **17**, 2321–2326.
- 45 E. C. Kesslen, W. B. Euler and B. M. Foxman, *Chem. Mater.*, 1999, **11**, 336–340.
- 46 A. Mentecs, S. Sezek, M. E. Hanhan and O. Buyukgungor, *Turkish J. Chem.*, 2007, **31**, 667–676.
- 47 G. M. Sheldrick, *Acta Crystallogr. Sect. A*, 2008, **64**, 112–122.
- 48 O. V Dolomanov, L. J. Bourhis, R. J. Gildea, J. A. K. Howard and H. Puschmann, *J. Appl. Crystallogr.*, 2009, **42**, 339–341.
- 49 G. M. Sheldrick, *Acta Crystallogr. Sect. A*, 2014, **70**, C1437.
- 50 G. M. Sheldrick, *Acta Crystallogr. Sect. C*, 2015, **71**, 3–8.
- 51 G. V. Bunau, *Berichte der Bunsengesellschaft für Phys. Chem.*, 1970, **74**, 1294–1295.
- 52 S. R. LaPlante, R. Carson, J. Gillard, N. Aubry, R. Coulombe, S. Bordeleau, P. Bonneau, M. Little, J. O’Meara and P. L. Beaulieu, *J. Med. Chem.*, 2013, **56**, 5142–5150.

Chapter-4

1D Zn(II) Coordination Polymers of *Bis*-pyridyl-diimines: Anion Exchange and Methyl Orange Adsorption Studies

1D Zn(II) Coordination Polymers of *Bis*-pyridyl-diimines: Anion Exchange and Methyl Orange Adsorption Studies

4.1 Introduction

This chapter discusses the synthesis of CP with molecules containing rigid hydrazine spacer. The presence of N at different positions on pyridine ring provides variable conformational geometries leading to the formation diverse networks when coordinated to metal atoms. The network topologies of CPs ranging from 1D to 3D depends on various factors such as the geometry of the ligands, the coordination environment around metals centers, counter ions, solvents, guest molecules and the conditions of the reaction used.^[1-6] Among all the other factors, counter ions play an important role due to the size, shape, coordination ability and non-covalent interactions ability.^[7-10]

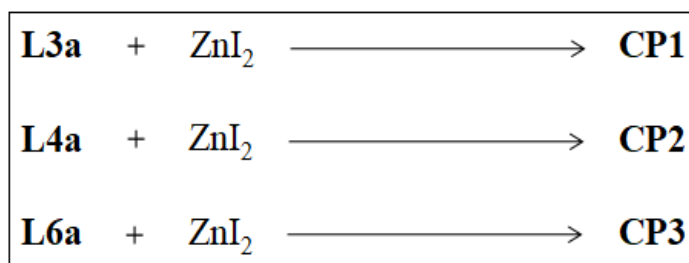
There are large numbers of reports on the use of anion acting as templates to synthesize the CPs. The counter anions of the CPs may either be coordinated to the metal center or act as void filling species in the network and may be involved in the extension of the coordination network.^[11-14] Custelcean *et al.*^[15] reported the separation of anions from the aqueous solutions by selective crystallization with a MOF containing urea functional ligands based on size and charge on the anions. They crystallized 1D Zn(II) MOFs of N,N-*bis*-(*m*-pyridyl)-urea (BPU) linked water containing Cl⁻, Br⁻, I⁻ anions where the halogen ions were coordinated to Zn(II) and formed hydrogen bond interactions with the urea groups. The NO₃⁻ and ClO₄⁻ anions were unaffected under the same conditions. Jian-ping Ma *et al.*^[16] reported a 2D cationic MOF of Cu(II) with fluorene based ligands and NO₃⁻ ions. They performed the anion exchange reactions with Cl⁻, Br⁻, I⁻, SCN⁻ and N₃⁻ under ambient conditions where the Cu(II) MOF acted as selective naked eye anionic receptor to recognize and completely separate the anions of similar geometry. Manna *et al.*^[17] synthesized a Zn (II) based dynamic cationic porous framework using a di-Schiff-base ligand incorporating NO₃⁻ anions. They studied the anion exchange with ClO₄⁻, N(CN)₂⁻, SCN⁻ and N₃⁻ ions and observed complete reversibility, partial reversibility, and irreversibility of the anion exchange depending upon the nature of the anions. They also observed the anion tunable response of the luminescence properties, where the ClO₄⁻ exchanged framework showed gradual increase in the emission intensity. The SCN⁻ and N₃⁻ exchanged frameworks showed decrease in the emission intensity because of the coordination affinity of SCN⁻ and N₃⁻ ions. Shi *et al.*^[18]

selectively captured the pollutant CrO_4^{2-} ions by the anion exchange of ClO_4^- ions from the mixture of NO_3^- , Cl^- , Br^- , I^- and CrO_4^{2-} anions using a $\text{Dy}^{3+}/\text{Zn}^{2+}$ heterometallic 3D MOF and also showed the release of CrO_4^{2-} ions by exchanging with CO_3^{2-} and SO_4^{2-} ions. Tzeng *et al.*^[19] reported the anion directed assembly of Zn(II) based CPs, where Cl^- and Br^- results in 1D CPs while I^- directed the formation of discrete macro cycle structures. They also explained photoluminescence properties of the CPs. Liu *et al.*^[20] reported a 1D CP of Ag(II) and the anion exchange was performed with Orange II (OII) dye where the formation of different phases was observed at different proportions of OII dye. They further explored the photocurrent responses and dielectric constants of the anion exchanged products.

Rapid industrialization and urbanization lead to the enhancement of serious environmental pollution problems now a days.^[21,22] Water is the source of our life being polluted by many ways especially by heavy metal anions, cations and organic dye molecules.^[23–25] Researchers developed various analytical methods to detect the pollutants but most of them have their limitations such as sensitivity, easy interference and cost effectiveness.^[26–28] The conventional water treatment techniques have limitations particularly in quantitative estimation of the water soluble organic pollutants. The variable network structures with tunable chemical features makes the CPs one of the prominent candidates from degradation of organic dyes.^[29–31] Li *et al.*^[32] reported a nanoporous Ag(I) CP with 3-(2-pyridyl)-4-(3-pyridyl)-5-(4-pyridyl)-1,2,4-triazole and ClO_4^- ions, which showed high performance on adsorption of carcinogenic dye Acid Red 26 (AR26) on anion exchange. They performed the dye removal studies on 13 dyes which differ in ionic charges, dimensions, and type of chromophoric moieties. They studied the effect of charge on the dyes and size of the dyes on the adsorption. The charge mismatch dyes which were Methylene Blue, Methyl Yellow, Tony Red, Neutral Red and over sized dyes which includes Crystal Violet, Eriochrome Black-T, Reactive Red 177, Food Green 3, and Rhodamine 6G showed negligible or limited adsorption. The dyes such as Mordant Red 5, Acid Red 4 and Acid Red 26 showed high adsorption. They also explored the single-crystal-to-single-crystal transformation by exchanging ClO_4^- ions with BF_4^- ions and studied the adsorption of CH_4 and N_2 by the CPs. Wen *et al.*^[33] synthesized two Cu(I) isomeric CPs and scrutinized their photo catalysis of Methylene Blue (MB). The degradation of MB was different in the two isomers. The isomer which contained closely packed ligands and have strong $\pi\cdots\pi$ interactions between the layers showed lower degradation than the other isomer. Wang *et al.*^[34] reported isostructural

Co(II) and Ni(II) CPs with **L6a** and 4,4'-oxy-bis-(benzoic acid) ligands and explored the photocatalytic activity of those CPs in the degradation of Methyl Orange (MO) and Malachite Green (MG). They investigated the change in photocatalytic activity with concentration and at various pH medium. Wang *et al.*^[35] also reported the selective catalytic activity of Fe(II) MOFs based on the position of N atom on the pyridine ring. They observed the selective MO degradation by the layer structured Fe(II) MOF equipped with **L6a** ligands while no activity occurred by the chain structured Fe(II) MOF with **L4a** ligands. However the low electron donating capacity of **L3a** and **L4a** compared to that in **L6a** prevents the ligands to boost the metal atoms to bound with O₂ which further interacts with the unsaturated double bonds of the dyes for the degradation process. Hussain *et al.*^[36] investigated the effect of different coordination environments of 1D Cu(II) CPs of pyridine-2,6-dicarbohydrazide based imine linked tritopic ligands on the photocatalytic degradation of RB and MO. The difference in coordination environment in those CPs were due to the coordinated water molecules and the coordinating modes of ligands.

The present chapter discusses the synthesis of three 1D Zn(II) coordination polymers **CP1**, **CP2** and **CP3** using **L3a**, **L4a**, and **L6a** ligands, respectively, where iodide acts as a counter anion (Scheme 4.1). The anion exchange reactions were performed in order to understand the role of counter anions in the structural modification of the CPs. The anions chosen for counter anion exchange studies were Cl⁻, SCN⁻, N₃⁻ and CO₃²⁻. Effect of difference in the geometry of the anions such as linear geometry of SCN⁻, N₃⁻ and trigonal planar of CO₃²⁻ and the coordination ability of the counter anions may lead to structural differences in the CPs during anion exchange. The photo adsorption of organic dyes Methyl Orange (MO) Methylene blue (MB), Malachite green (MG) and Rhodamine-B (RB), were also studied in this chapter for the CPs, **CP1**, **CP2** and **CP3**.



Scheme 4.1: Synthesis of **CP1**, **CP2** and **CP3**

4.2 Experimental Section

4.2.1 Synthesis of ligands: The compounds **L3a**, **L4a** and **L6a** were synthesized according to the usual method of preparation of Schiff bases, which involved the condensation reaction of primary diamines with an aldehyde/ketone precursor in alcoholic solution under reflux conditions.

4.2.1.1 Synthesis of 1,2-bis-(pyridin-3-ylmethylene)hydrazine (L3a): **L3a** was prepared by taking 0.93 ml (10 mmol) 3- pyridine carboxaldehyde and 0.25 ml (5 mmol) hydrazine hydrate. Yield: 76%, Melting point: 146 °C; IR (cm⁻¹ KBr pellet): 3086 (w), 3040 (w) , 2993 (w) 2932 (m), 1620 (s), 1582 (m), 1481 (m), 1412 (s), 1304 (s), 1219 (m), 1180 (w), 1088 (w), 1018 (s), 818 (s), 702 (s) (Fig. A41). ¹H NMR (400 MHz, CDCl₃) δ ppm: 8.89 (s, 2H), 8.57 (dd, *J* = 4.7, 1.4 Hz, 2H), 8.54 (s, 2H), 8.07 (d, *J* = 7.9 Hz, 2H), 7.26 (dd, *J* = 7.8, 4.8 Hz, 2H) (Appendix figure A42). ¹³C NMR (101 MHz, CDCl₃) δ ppm: 159.66, 151.97, 150.37, 134.72, 129.56, 123.68 (Appendix figure A43).

4.2.1.2 Synthesis of 1,2-bis-(1-(pyridin-3-yl)ethylidene)hydrazine (L4a): **L4a** was prepared by taking 1.12 ml (10 mmol) 3-acetyl pyridine and 0.25 ml (5 mmol) hydrazine hydrate. Yield: 85%, Melting point: 112 °C Elemental analysis (Experimental %): C, 71.38; H, 5.663; N, 23.91; (calculated%): C, 70.57; H, 5.92; N, 23.51; IR (cm⁻¹ KBr pellet): 3040 (w), 2962 (w), 1605 (s), 1481(w), 1412 (m), 1366 (m), 1288 (w), 1196 (m), 1119 (w), 1080 (w), 1018 (m), 972 (m), 818 (s) 702 (s) (Appendix figure A44). ¹H NMR (400 MHz, CDCl₃) δ ppm: 9.02–9.00 (m, 2H), 8.53 (dd, *J* = 4.8, 1.6 Hz, 2H), 8.09 (dt, *J* = 8.0, 2.0 Hz, 2H), 7.23 (m, 2H), 2.24 (s, 6H) (Appendix figure A45). ¹³C NMR (101 MHz, CDCl₃) δ ppm: 156.72, 150.56, 148.10, 133.73, 133.49, 123.16, 14.75 (Appendix figure A46). Powder XRD was recorded and compared with the calculated powder XRD of **L4a** (Appendix figure A47).

4.2.1.3 Synthesis of 1,2-bis-(1-(pyridin-4-yl)ethylidene)hydrazine (L6a): **L6a** was prepared by taking 1.12 ml (10 mmol) 4-acetyl pyridine and 0.25 ml (5 mmol) hydrazine hydrate. Yield: 46%, Melting point: 127 °C IR (cm⁻¹ KBr pellet): 3032 (m), 2978 (w), 2916 (w), 1612 (s), 1535 (m), 1497 (w), 1435 (w), 1404 (s), 1373 (s), 1296 (s), 1211 (w), 1057 (m), 987 (m), 825 (s), 771 (w), 671 (m), 571 (m) (Appendix figure A49). ¹H NMR (400 MHz, CDCl₃): δ 8.56–8.54 (m, 4H), 7.62–7.59 (m, 4H), 2.14 (s, 6H) (Appendix figure A50). ¹³C NMR (101 MHz, CDCl₃) δ ppm: 155.77, 150.16, 144.65, 120.53, 14.63 (Appendix figure A51).

4.2.2 Synthesis of $[\text{Zn}(\text{L3a})\text{I}_2]_n$, (CP1): L3a 0.1 mmol, (0.0210 g) was taken in 4 ml of ethanol-water (1:1) solution and 4 ml ethanolic solution of ZnI_2 (0.2 mmol, 0.0638 g) was slowly layered over it by taking 2 ml ethanol as buffer. Yellow block crystals were started forming within 24 hours. The crystals were separated and washed with ethanol-water (1:1) solution and dried under air. Yield: 83%. Elemental analysis (experimental %): C, 27.76; H, 1.912; N, 11.18; (calculated%): C, 27.22; H, 1.90; N, 10.58; IR (cm^{-1} KBr pellet): 3055 (w), 3024 (w), 1628 (s), 1512 (m), 1489 (m), 1419 (s), 1311 (m), 1195 (m), 1126 (w), 1095 (w), 1057 (m), 972 (m), 872 (m), 810 (m), 694 (s), 648 (m) (Figure 4.5a). Powder XRD was recorded and compared with the calculated powder XRD of CP1 (Figure 4.6a).

4.2.3 Synthesis of $[\text{Zn}(\text{L4a})\text{I}_2]_n$, (CP2): L4a 0.1 mmol, (0.0238 g) was taken in 4 ml of ethanol-water (1:1) solution and 4 ml ethanolic solution of ZnI_2 (0.2 mmol, 0.0638 g) was slowly layered over it by taking 2 ml ethanol as buffer. Yellowish-orange block crystals were started forming within 24 hours. The crystals were separated and washed with ethanol-water (1:1) solution and dried under air. Yield: 76%. Elemental analysis (experimental %): C, 30.16; H, 2.44; N, 9.82; (calculated %): C, 30.16; H, 2.53; N, 10.05; IR (cm^{-1} KBr pellet): 3055 (w), 2924 (w), 1612 (s), 1574 (w), 1519 (w), 1489 (m), 1419 (s), 1357 (s), 1296 (m), 1195 (m), 1118 (m), 1049 (m), 964 (m), 925 (w), 810 (s), 771 (w), 694 (s), 640 (s), 578 (w) (Fig. 4.7a). Powder XRD was recorded and compared with the calculated powder XRD of CP2 (Fig. 4.8a).

4.2.4 Synthesis of $[\text{Zn}(\text{L6a})_2\text{I}_2]_n$, (CP3): L6a 0.1 mmol, (0.0238 g) was taken in 4 ml of ethanol-water (1:1) solution and 4 ml ethanolic solution of ZnI_2 (0.1 mmol, 0.0319 g) was slowly layered over it by taking 2 ml ethanol as buffer. Reddish block crystals were started forming within 24 hours. The crystals were separated and washed with ethanol-water (1:1) solution and dried under air. Yield: 51%. Elemental analysis (experimental %): C, 30.07; H, 2.42; N, 9.82; (calculated%): C, 30.16; H, 2.53; N, 10.05; IR (cm^{-1} KBr pellet): 3066 (w), 2916 (w), 1612 (s), 1543 (w), 1504 (w), 1419 (s), 1365 (s), 1288 (m), 1265 (w), 1219 (m), 1064 (m), 1026 (s), 972 (w), 871 (w), 825 (s), 763 (m), 640 (m), 570 (s) (Figure 4.9a). Powder XRD was recorded and compared with the calculated powder XRD of CP3 (Figure 4.10a).

4.2.5 Anion Exchange Reactions: The anion exchange reactions were performed by suspending 1 mmol. of CP into an aqueous solution of 10 mmol. of sodium/ammonium salt of anion. The suspension was stirred for about 1 hour. It was then filtered and washed with few drops of water to separate excess of salt and dried. The resulted sample characterized by FT-IR and PXRD.

4.2.5.1 Anion Exchange Reaction of CP1 with Cl⁻: The anion exchange reaction was performed by taking 1 mmol (529.43 mg) of powdered **CP1** in an aqueous solution of NaCl (584.4 mg, 10 mmol). The resulted sample characterized by FT-IR and PXRD. FT-IR: 3070 (w), 1627 (m), 1604 (m), 1465 (w), 1427 (m), 1311 (w), 1195 (w), 1126 (w), 1103 (w), 1056 (m), 933 (w), 879 (m), 810 (m), 748 (w), 694 (s), 655 (m), 532 (w). The PXRD of the resulted CP was recorded (Figure 4.6b).

4.2.5.2 Anion Exchange Reaction of CP1 with SCN⁻: The anion exchange reaction was performed by taking 1 mmol (529.43 mg) of powdered **CP1** in an aqueous solution of KSCN (971.76 mg, 10 mmol). The resulted sample characterized by FT-IR and PXRD. FT-IR: 3047 (w), 2098 (w), 2059 (s), 1627 (m), 1604 (m), 1519 (w), 1473 (w), 1435 (m), 1311 (w), 1195 (m), 1126 (w), 1103 (w), 1056 (m), 1033 (w), 964 (m), 941 (w), 879 (m), 840 (w), 802 (m), 686 (s), 655 (m). The PXRD of the resulted CP was recorded (Figure 4.6c).

4.2.5.3 Anion Exchange Reaction of CP1 with N₃⁻: The anion exchange reaction was performed by taking 1 mmol (529.43 mg) of powdered **CP1** in an aqueous solution of NaN₃ (650.11 mg, 10 mmol). The resulted sample characterized by FT-IR and PXRD. FT-IR: 3093 (w), 2067 (s), 1627 (m), 1581 (w), 1481 (w), 1411 (m), 1342 (w), 1303 (w), 1219 (w), 1188 (w), 1095 (w), 1026 (w), 972 (w), 871 (w), 802 (m), 771 (w), 694 (s), 640 (m), 609 (w). The PXRD of the resulted CP was recorded (Figure 4.6d).

4.2.5.4 Anion Exchange Reaction of CP1 with CO₃²⁻: The anion exchange reaction was performed by taking 1 mmol (529.43 mg) of powdered **CP1** in an aqueous solution of Na₂CO₃ (1059.88 mg, 10 mmol). The resulted sample characterized by FT-IR and PXRD. FT-IR: 3032 (w), 1627 (m), 1581 (w), 1566 (w), 1504 (w), 1465 (w), 1419 (m), 1311 (m), 1219 (w), 1188 (w), 1126 (w), 1095 (w), 1018 (w), 972 (m), 941 (w), 864 (m), 833 (w), 802 (m), 702 (s), 617 (w). The PXRD of the resulted CP was recorded (Figure 4.6e).

4.2.5.5 Anion Exchange Reaction of CP2 with Cl⁻: The anion exchange reaction was performed by taking 1 mmol (557.48 mg) of powdered **CP2** in an aqueous solution of NaCl (584.4 mg, 10 mmol). The resulted sample characterized by FT-IR and PXRD. FT-IR: 3070 (w), 3032 (w), 1612 (m), 1519 (w), 1473 (w), 1427 (m), 1365 (m), 1327 (w), 1296 (w), 1195 (w), 1134 (w), 1095 (m), 1049 (s), 979 (w), 817 (s), 779 (s), 694 (s), 655 (m), 570 (w). The PXRD of the resulted CP was recorded (Figure 4.8b).

4.2.5.6 Anion Exchange Reaction of CP2 with SCN⁻: The anion exchange reaction was performed by taking 1 mmol (557.48 mg) of powdered **CP2** in an aqueous solution of NH₄SCN (971.76 mg, 10 mmol). The resulted sample characterized by FT-IR and PXRD. FT-IR: 2059 (s), 1612 (m), 1558 (w), 1543 (w), 1519 (w), 1481 (w), 1419 (m), 1365 (m), 1303 (m), 1195 (m), 1118 (m), 1095 (m), 1041 (s), 995 (w), 956 (w), 817 (s), 779 (m), 702 (s), 640 (m), 570 (w). The PXRD of the resulted CP was recorded (Figure 4.8c).

4.2.5.7 Anion Exchange Reaction of CP2 with N₃⁻: The anion exchange reaction was performed by taking 1 mmol (557.48 mg) of powdered **CP2** in an aqueous solution of NaN₃ (650.11 mg, 10 mmol). The resulted sample characterized by FT-IR and PXRD. FT-IR: 3078 (w), 3032 (w), 2059 (s), 1612 (m), 1573 (w), 1558 (w), 1519 (w), 1473 (w), 1427 (m), 1365 (w), 1342 (m), 1296 (w), 1195 (w), 1134 (w), 1095 (w), 1056 (m), 972 (w), 948 (w), 817 (m), 786 (m), 694 (s), 648 (m), 609 (w), 570 (w). The PXRD of the resulted CP was recorded (Figure 4.8d).

4.2.5.8 Anion Exchange Reaction of CP2 with CO₃²⁻: The anion exchange reaction was performed by taking 1 mmol (557.48 mg) of powdered **CP2** in an aqueous solution of Na₂CO₃ (1059.88 mg, 10 mmol). The resulted sample characterized by FT-IR and PXRD. FT-IR: 3032 (w), 2954 (w), 1651 (m), 1604 (m), 1543 (m), 1512 (m), 1489 (m), 1411 (s), 1365 (s), 1296 (w), 1203 (w), 1118 (w), 1080 (w), 1018 (m), 972 (w), 918 (w), 864 (w), 817 (m), 771 (w), 702 (s), 655 (w), 617 (w), 578 (w), 516 (w). The PXRD of the resulted CP was recorded (Figure 4.8e).

4.2.5.9 Anion Exchange Reaction of CP3 with Cl⁻: The anion exchange reaction was performed by taking 1 mmol (557.48 mg) of powdered **CP3** in an aqueous solution of NaCl (584.4 mg, 10 mmol). The resulted sample characterized by FT-IR and PXRD. FT-IR: 3062 (w), 1612 (s), 1543 (w), 1504 (w), 1419 (s), 1365 (m), 1288 (w), 1219 (w), 1064 (m), 1026 (m), 972 (w), 833 (s), 763 (m), 640 (m), 578 (s). The PXRD of the resulted CP was recorded (Figure 4.10b).

4.2.5.10 Anion Exchange Reaction of CP3 with SCN⁻: The anion exchange reaction was performed by taking 1 mmol (557.48 mg) of powdered **CP3** in an aqueous solution of NH₄SCN (971.76 mg, 10 mmol). The resulted sample characterized by FT-IR and PXRD. FT-IR: 3093 (w), 2075 (s), 1612 (s), 1543 (w), 1419 (m), 1365 (w), 1288 (w), 1219 (w), 1056 (m), 1026 (m), 964 (w), 833 (s), 763 (m), 640 (m), 578 (s). The PXRD of the resulted CP was recorded (Figure 4.10c).

4.2.5.11 Anion Exchange Reaction of CP3 with N₃⁻: The anion exchange reaction was performed by taking 1 mmol (557.48 mg) of powdered **CP3** in an aqueous solution of NaN₃ (650.11 mg, 10 mmol). The resulted sample characterized by FT-IR and PXRD. FT-IR: 3062 (w), 2059 (s), 1612 (s), 1543 (w), 1504 (w), 1419 (m), 1365 (m), 1288 (w), 1219 (w), 1056 (m), 1026 (m), 972 (w), 871 (w), 825 (s), 763 (m), 640 (m), 578 (m). The PXRD of the resulted CP was recorded (Figure 4.10d).

4.2.5.12 Anion Exchange Reaction of CP3 with CO₃²⁻: The anion exchange reaction was performed by taking 1 mmol (557.48 mg) of powdered **CP3** in an aqueous solution of Na₂CO₃ (1059.88 mg, 10 mmol). The resulted sample characterized by FT-IR and PXRD. FT-IR: 3332 (m), 3032 (w), 2924 (w), 1589 (m), 1504 (s), 1373 (s), 1296 (w), 1219 (w), 1049 (w), 987 (w), 956 (w), 879 (w), 825 (s), 771 (w), 709 (w), 678 (m), 570 (m). The PXRD of the resulted CP was recorded (Figure 4.10e).

Table 4.1: Crystallographic data and refinement parameters of **L4a**, **CP1**, **CP2** and **CP3**

Compound	L4a	CP1	CP2	CP3
Empirical formula	C ₁₄ H ₁₄ N ₄	C ₆ H ₅ I ₂ N ₂ Zn	C ₇ H ₇ I ₂ N ₄ Zn	C ₁₄ H ₁₄ I ₂ N ₄ Zn
Formula Wt.	238.29	529.41	557.48	557.46
Crystal system	Monoclinic	Orthorhombic	Orthorhombic	Triclinic
Space group	<i>P</i> 2 ₁ / <i>c</i>	<i>Pnma</i>	<i>Pnma</i>	<i>P</i> - 1
<i>a</i> /Å	9.797(2)	8.5318(12)	8.1421(15)	6.9535(2)
<i>b</i> /Å	3.9121(7)	15.509(2)	15.896(3)	8.8583(3)
<i>c</i> /Å	15.805(3)	11.3830(14)	13.336(3)	14.9249(4)
α /°	90.00	90.00	90.00	93.599(2)
β /°	106.24(2)	90	90.00	97.787(2)
γ /°	90.00	90.00	90.00	104.017(2)
<i>V</i> /Å ³	581.6(2)	1506.2(4)	1726.0(6)	879.34(5)
<i>Z</i>	2	4	4	2
<i>D</i> _{calcd} /g cm ⁻³	1.361	2.335	2.145	2.105
<i>T</i> /K	93(2)	93(2)	296(2)	93(2)
Theta (°) range	10.406 to 58	9.912 to 49.978	1.99 to 25.13	9.986 to 49.996

for data used				
Reflections collected	3508	5407	13811	9790
R_{int}	0.0167	0.0147	0.0314	0.0122
No. of parameters refined	83	92	101	192
Final R (With $I > 2\sigma(I)$)	$R_1 = 0.0367,$ $wR_2 = 0.1043$	$R_1 = 0.0173,$ $wR_2 = 0.0418$	$R_1 = 0.0213,$ $wR_2 = 0.0547$	$R_1 = 0.0153,$ $wR_2 = 0.0421$
GOF on F^2	1.050	1.233	1.045	1.302

4.2.6 Single Crystal X-ray Diffraction: The single crystal XRD of **CP2** was done at IISER Mohali, where the single crystal data were collected on a Xcalibur, Sapphire 3 X-ray diffractometer that uses graphite monochromated Mo $K\alpha$ radiation ($\lambda = 0.71073 \text{ \AA}$) by the ω -scan method. The structures were solved by direct methods and refined by least square methods on F^2 using SHELX-97.^[37] Non-hydrogen atoms were refined anisotropically and hydrogen atoms were fixed at calculated positions and refined using a riding model.

The single crystal XRD of **L4a**, **CP1** and **CP3** were done in BITS Pilani, Hyderabad Campus, where the single crystal data were collected on a XtaLAB Pro: Kappa dual offset/far diffractometer. The crystal was kept at 93(2) K during data collection. Using Olex2,^[38] the structure was solved with the ShelXT structure solution program^[39] using Intrinsic Phasing and refined with the ShelXL refinement package using Least Squares minimization.^[40]

The crystal data and structure refinements of **L4a**, **CP1**, **CP2** and **CP3** are summarized in table 4.1. The ORTEP of **L4a** is shown in appendix figure A48 and the ORTEP of **CP1**, **CP2** and **CP4** are shown in appendix figures A54-A56.

4.3 Results and Discussion

4.3.1 Structural Description of L4a and the Coordination Polymers CP1, CP2 and CP3:

The crystal structural analysis of **L4a**, **CP1**, **CP2** and **CP3** was done in order to study the effect of change in N position in the ligand on the geometry of the CPs. The analysis on the effect of anions non-covalent interactions on the overall geometry of the CPs is discussed in the subsequent sections.

4.3.1.1 Structural features of L4a: The crystal structure of **L4a** reveals that it has crystallized in monoclinic $P2_1/c$ space group with half of the molecule present in the asymmetric unit. The N (pyridyl) to N(pyridyl) distance of the molecule is 10.727 Å. These molecules propagate together by weak CH \cdots N (2.692 Å, 3.564 Å, 156.42°; 2.964 Å, 3.879 Å, 168.27°) and $\pi\cdots\pi$ interactions with a centroid to centroid distance of 3.912 Å (Figure 4.1).

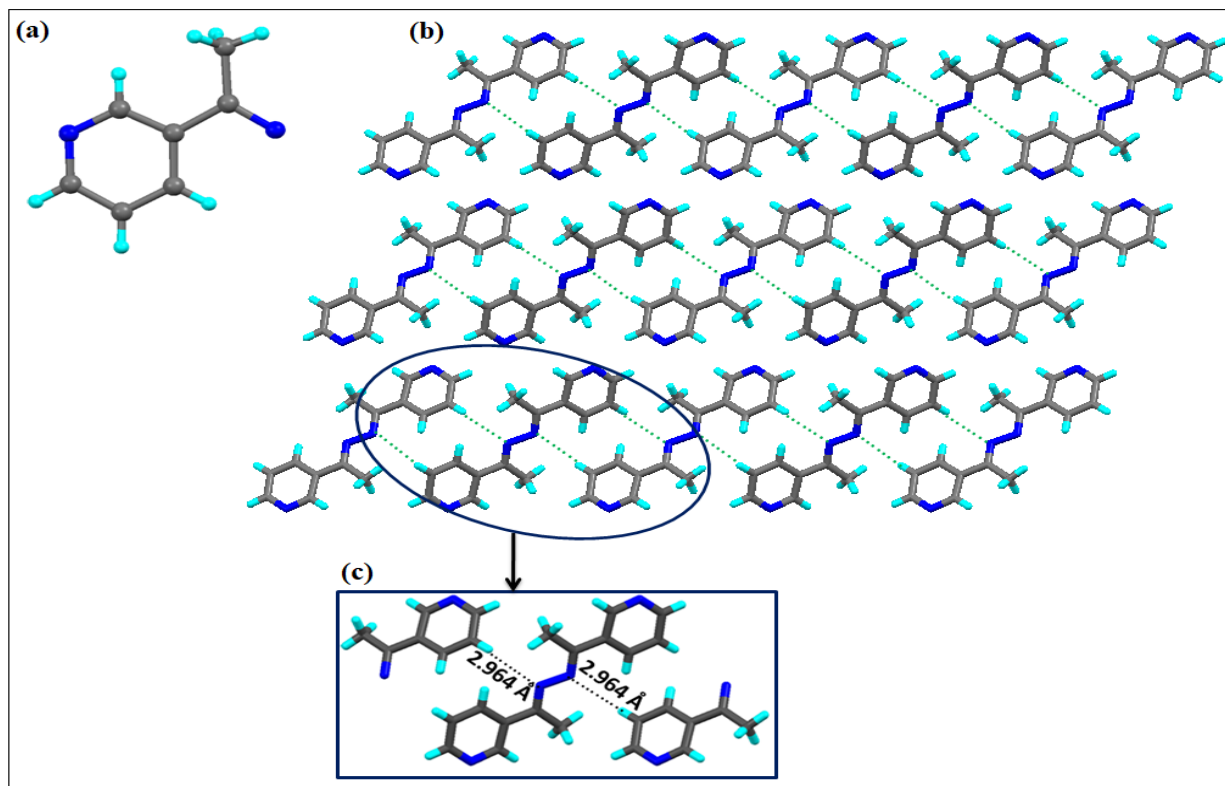


Figure 4.1: Illustration of crystal structure of **L4a**: (a) Asymmetric unit (b) arrangement of molecules along 'b' axis (c) CH \cdots N interactions between CH of pyridyl rings and N of imine group.

4.3.1.2 Structural features of CP1

The single crystal XRD analysis reveals that the compound **CP1** crystallizes into orthorhombic crystal system with $Pnma$ space group. The asymmetric unit contains half of the **L3a**, one unit of Zn(II) and two moieties of I $^-$. The central metal Zn(II) attains distorted tetrahedral geometry where two N atoms of two different **L3a** units (Zn-N: 2.071 Å) and two I atoms (Zn-I: 2.550 Å, 2.556 Å) satisfied the coordination environment. The tetrahedral coordination environment of Zn(II) center and positioning of the N in the **L3a** resulted in the formation of 1D zigzag structure. These 1D chains further interacted with adjacent chains aromatic $\pi\cdots\pi$ interactions

with a centroid to centroid distance of 3.442 Å. The 1D chains further stack in 3D as shown in figure 4.2

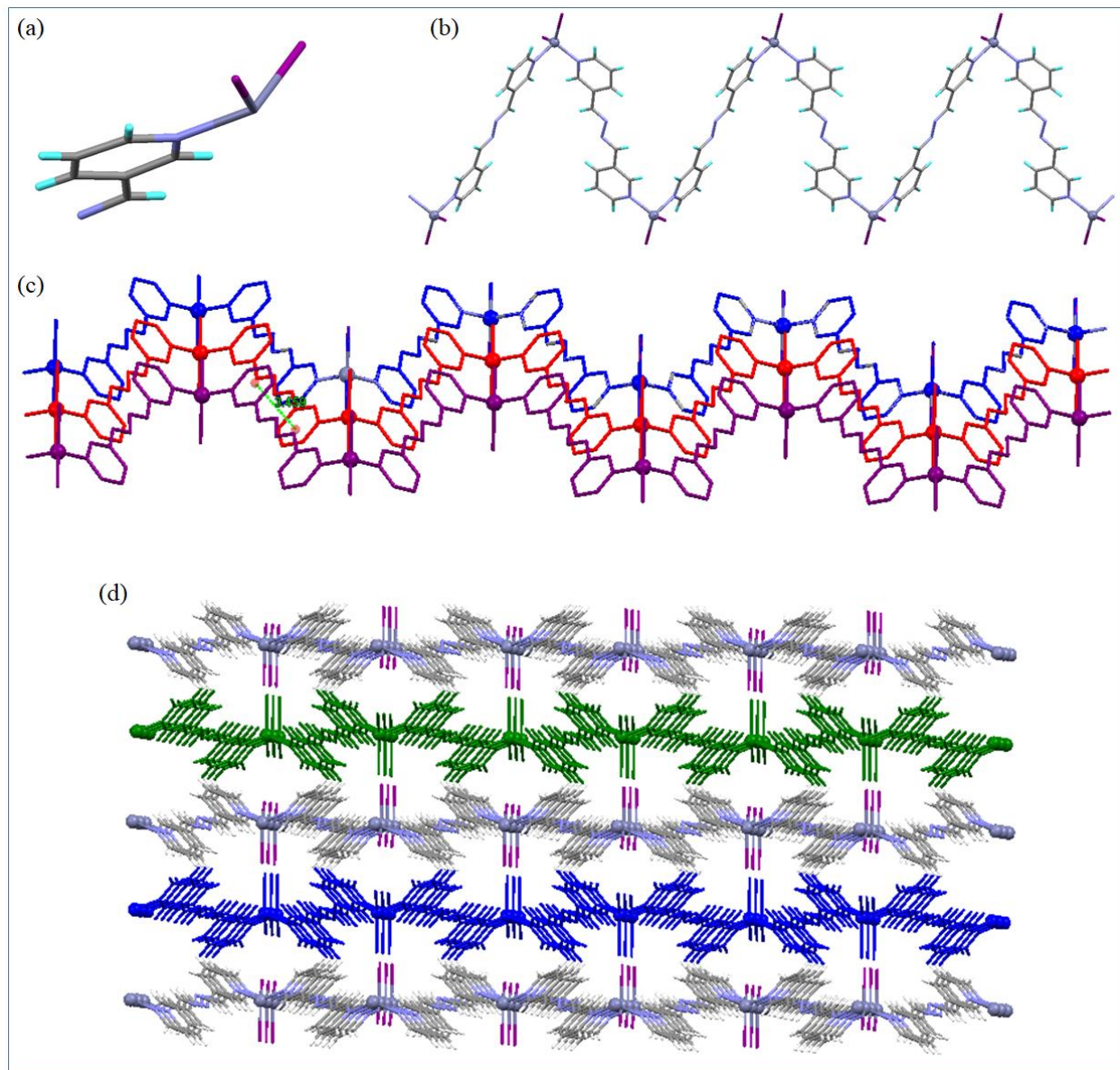


Figure 4.2: Illustration of crystal structure of **CP1**: (a) Asymmetric unit of **CP1** (b) 1D zigzag chain; Notice the tetrahedral coordination geometry around Zn metal (c) $\pi\cdots\pi$ interactions between pyridyl rings resulted in stacking of the chains to form layers (hydrogen atoms are omitted for clarity); (d) packing of the chains in the 3D

4.3.1.3 Structural features of CP2: The compound **CP2** crystallizes into orthorhombic crystal system with *Pnma* space group. The asymmetric unit contains half of the **L4a**, one Zn(II) and

two I⁻ moieties (Figure 4.3a). The central metal Zn(II) attains distorted tetrahedral geometry where two N atoms of two different **L4a** units (Zn-N: 2.081 Å) and two I atoms (Zn-I: 2.544 Å, 2.562 Å) satisfied the coordination environment. The **L4a** molecules linked with ZnI₂ and propagated to form a 1D zigzag structure. These 1D chains further interacted with adjacent chains *via* aromatic $\pi\cdots\pi$ interactions with a centroid to centroid distance of 3.863 Å.

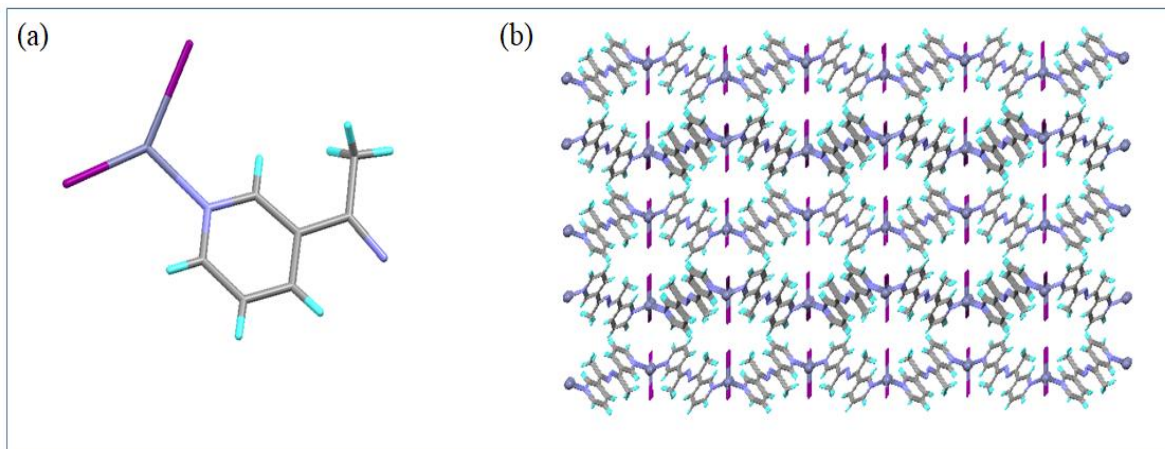


Figure 4.3: Illustration of crystal structure of **CP2**: (a) Asymmetric unit of **CP2**; (b) Stacking of the chains in 3D

The structure of **CP2** is similar to that of **CP1**, but the presence of methyl group in the ligand resulted in increase in the distance between the adjacent chains. This is evident from the aromatic centroid to centroid distances in **CP1** and **CP2**. Further the overall stacking of the chains in 3D also shows that the steric effect of methyl group resulted in increase in separation between the iodide groups of the chains in adjacent layers (Figure 4.3b).

4.3.1.4 Structural features of CP3: The compound **CP3** crystallizes in triclinic crystal system with *P*-1 space group. The asymmetric unit contains two half **L6a** units, one Zn(II) and two I⁻ units. The central metal Zn(II) attains distorted tetrahedral geometry where two N atoms of two different **L6a** units (Zn-N: 2.065 Å, 2.070 Å) and two I⁻ (Zn-I: 2.535 Å, 2.553 Å) satisfied the coordination environment. The **L6a** molecules linked with ZnI₂ and propagated to form a 1D zigzag structure. These 1D chains form aromatic C-H \cdots I (3.140 Å) non-covalent interactions with the adjacent 1D chains to extend the network into 3D structure (Figure 4.4). These C-H \cdots I interactions further increased the distance between the pyridyl rings by the formation of slided arrangement and prevents the formation of $\pi\cdots\pi$ interactions between the 1D layers as observed in case of **CP1** and **CP2**.

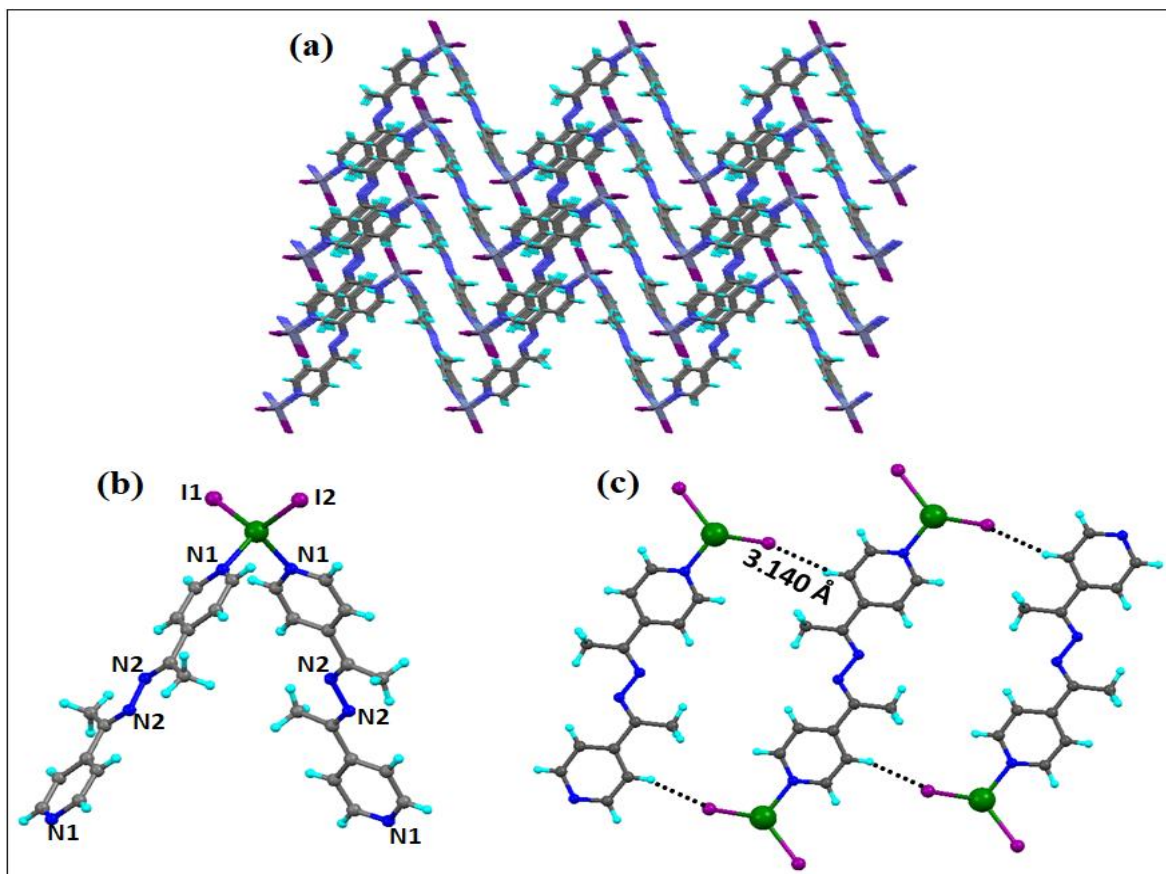
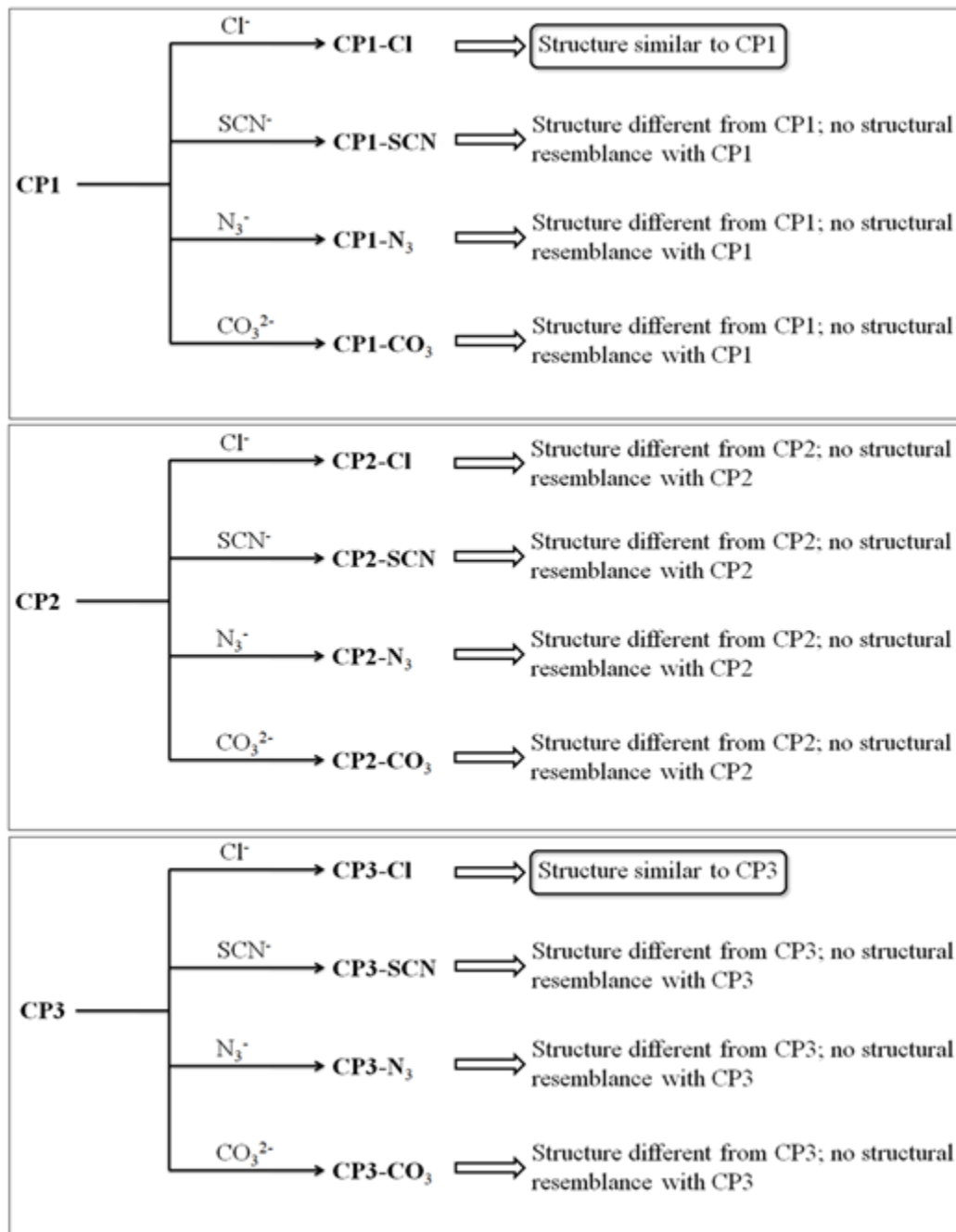


Figure 4.4: Illustration of crystal structure of **CP3**: (a) 1D zigzag arrangement of **CP3** along ‘b’ axis; (b) distorted tetrahedral coordination geometry around Zn(II) atoms; (c) non-covalent interactions between aromatic CH and iodine.

4.3.2 Anion Exchange Reactions: The anion exchange reactions were performed by stirring the suspended powdered CPs (**CP1**, **CP2** or **CP3**) in aqueous solution of sodium/potassium/ammonium salts of the Cl^- , SCN^- , N_3^- or CO_3^{2-} for about 1-2 hours. After anion exchange, the resultant precipitate was filtered, washed with deionized water and dried. The resultant solid was characterized by IR spectra, EDX and powder XRD analysis. Scheme 4.2 summarizes the observations of anion exchange reactions.

4.3.2.1 Anion exchange reactions of CP1 with Cl^- , SCN^- , N_3^- and CO_3^{2-} : The anion exchange reaction of **CP1** with Cl^- , SCN^- , N_3^- and CO_3^{2-} anions resulted in complete exchange of I^- ions with Cl^- , SCN^- , N_3^- and CO_3^{2-} anions. The anion exchanged products of **CP1** with SCN^- , N_3^- and CO_3^{2-} showed specific IR absorption bands respectively, at 2059 cm^{-1} (for CN); 2067 cm^{-1} (for N_3); 1581 & 1566 cm^{-1} (for CO_3^{2-}) (Figure 4.5).



Scheme 4.2: Anion exchange reactions of **CP1**, **CP2** and **CP3**

The powder XRD spectra of **CP1** and the anion exchanged compound **CP1-Cl** showed similarity in the powder XRD pattern which may confirm the similarity in the network geometry. The powder XRD spectra of **CP1-SCN⁻**, **CP1-N₃⁻**, **CP1-CO₃²⁻** showed completely different powder XRD pattern, which confirms the structural transformation during anion exchange (Figure 4.6).

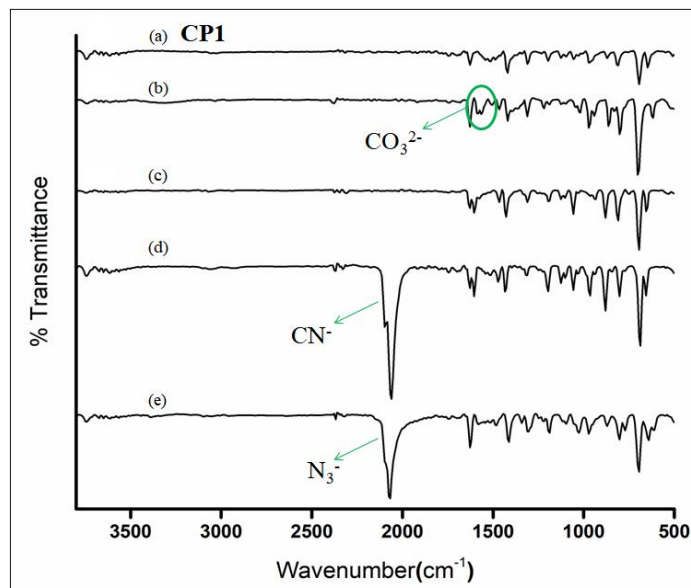


Figure 4.5: IR spectra of (a) **CP1**; (b) **CP1-CO₃²⁻**; (c) **CP1-Cl⁻**; (d) **CP1-SCN⁻**; (e) **CP1-N₃⁻**

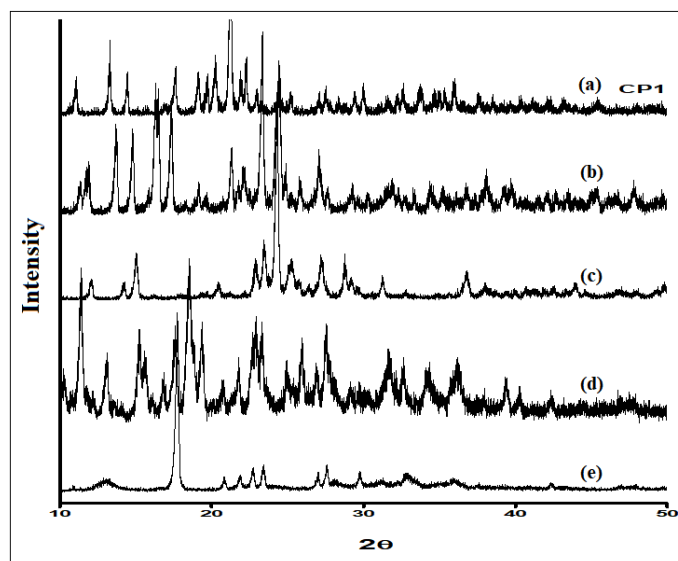


Figure 4.6: Powder XRD Spectra of (a) **CP1**; (b) **CP1-Cl⁻**; (c) **CP1-SCN⁻**; (d) **CP1-N₃⁻**; (e) **CP1-CO₃²⁻**.

4.3.2.2 Anion exchange reactions of CP2 with Cl⁻, SCN⁻, N₃⁻ and CO₃²⁻: The anion exchange reaction of **CP2** with Cl⁻, SCN⁻, N₃⁻ and CO₃²⁻ anions resulted in the exchange of I⁻ ions with Cl⁻, SCN⁻, N₃⁻ and CO₃²⁻ anions. The anion exchanged products of **CP2** with SCN⁻, N₃⁻ and CO₃²⁻ showed specific IR absorption bands respectively, at 2068 cm⁻¹ (for CN); 2083 cm⁻¹ (for N₃); 1512 cm⁻¹ (for CO₃²⁻) (Figure 4.7). The powder XRD spectra of **CP2** and the anion exchanged

compounds CP2-Cl^- , CP2-SCN^- , CP2-N_3^- , CP2-CO_3^{2-} showed completely different powder XRD pattern, which confirms the structural transformation during anion exchange (Figure 4.8).

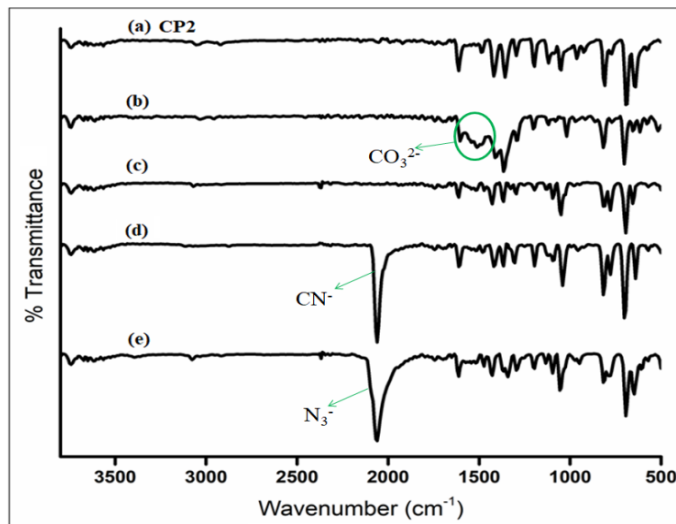


Figure 4.7: IR spectra of (a) CP2 ; (b) CP2-CO_3^{2-} ; (c) CP2-Cl^- ; (d) CP2-SCN^- ; (e) CP2-N_3^-

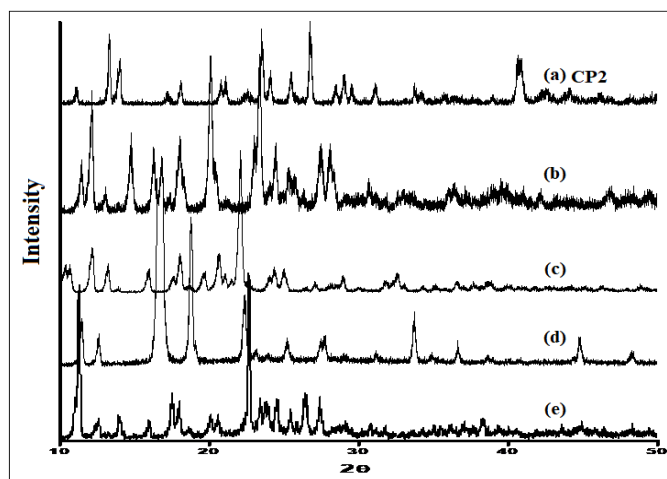


Figure 4.8: Powder XRD Spectra of (a) CP2 ; (b) CP2-Cl^- ; (c) CP2-SCN^- ; (d) CP2-N_3^- (e) CP2-CO_3^{2-} .

4.3.2.3 Anion exchange reactions of CP3 with Cl^- , SCN^- , N_3^- and CO_3^{2-} : The anion exchange reaction of CP3 with Cl^- , SCN^- , N_3^- and CO_3^{2-} anions resulted in the exchange of labile I^- ions with Cl^- , SCN^- , N_3^- and CO_3^{2-} anions. The anion exchanged products of CP3 with SCN^- , N_3^- and CO_3^{2-} showed specific IR absorption bands respectively, at 2068 cm^{-1} (for CN); 2075 cm^{-1} (for N_3); 1504 & 1373 cm^{-1} (for CO_3^{2-}) (Figure 4.9).

The powder XRD spectra of **CP3** and the anion exchanged compound **CP3-Cl** showed similarity in the powder XRD pattern which confirms the similarity in the network geometry. However the powder XRD spectra of **CP3-SCN⁻**, **CP3-N₃⁻**, **CP3-CO₃²⁻** showed completely different powder XRD pattern, which confirmed the structural transformation during anion exchange (Figure 4.10).

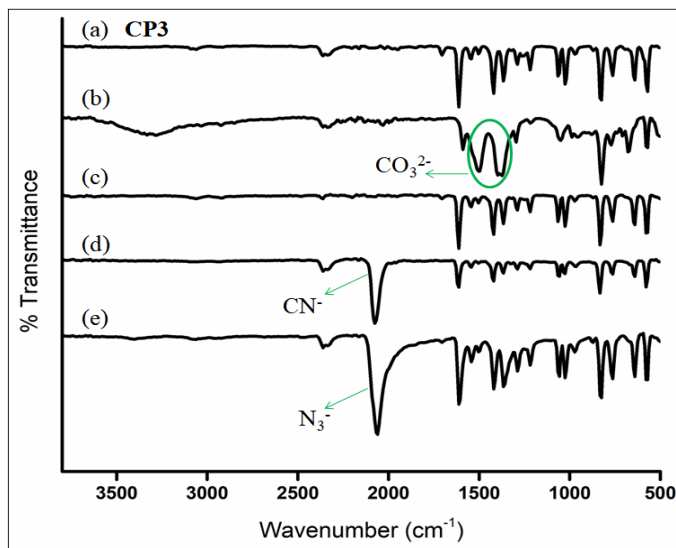


Figure 4.9: IR spectra of (a) **CP3**; (b) **CP3-CO₃²⁻**; (c) **CP3-Cl**; (d) **CP3-SCN⁻**; (e) **CP3-N₃⁻**

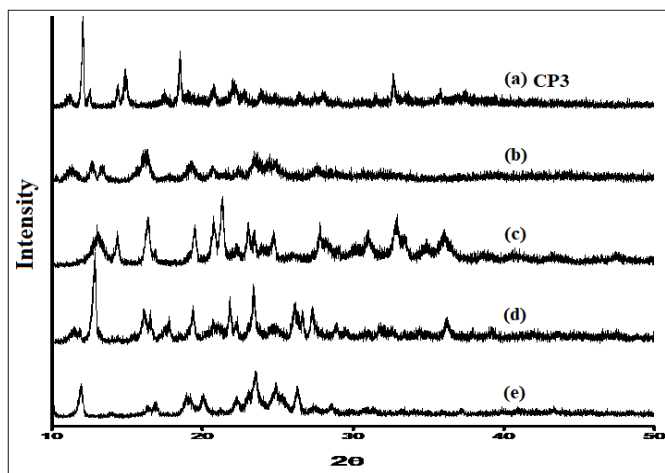


Figure 4.10: Powder XRD Spectra of (a) **CP3**; (b) **CP3-Cl**; (c) **CP3-SCN⁻**; (d) **CP3-N₃⁻** (e) **CP3-CO₃²⁻**.

4.3.3 Consequences of anion exchange on the geometry of CPs: The structural transformations in **CP1**, **CP2** and **CP3** on exchange of counter anions can be explained in terms

of the size, shape and coordinating ability of the counter anions involved. The counter anion studied for the anion exchange reaction involve: (i) Cl^- , (ii) SCN^- and N_3^- of linear geometry and (iii) trigonal planar shape of CO_3^{2-} . The crystal structure of **CP1** exhibits 1D zigzag network, where the **L3a** molecules adopt 180° torsion angle between C-N-N-C atoms. Lee *et al.*^[41] reported the direct reaction of **L3a** with ZnCl_2 ; which resulted in 1D helical chain network where the **L3a** molecules showed 175.66° torsion angle (C-N-N-C). When the reaction of **L3a** was performed in presence of NaSCN another isomer, a square wavy 1D chain network contain **L3a** ligands with 165.58° torsion angle in the geometry.^[41] In the current study **CP1** is a zigzag network and after anion exchange with Cl^- i.e **CP1-Cl** may result in the formation of the square wavy network, which is inferred by comparing the calculated powder XRD pattern of square wavy network and the powder pattern of **CP1-Cl**. Anion exchange of **CP1** with Cl^- results the square wavy network may be due to the closeness of overall geometry of the structure of **CP1** and the square wavy network CP (Figure 4.11).

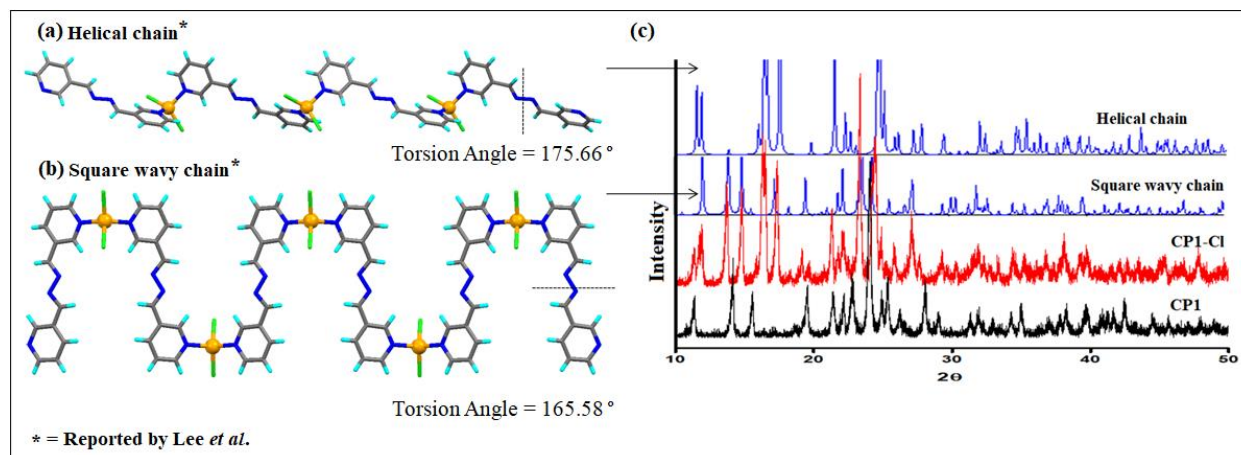


Figure 4.11: CPs of **L3a** with ZnCl_2 (a) Helical chain network and (b) Square wavy network^[41] and (c) their comparative powder XRD with **CP1-Cl**

The geometry of **CP2** also exhibits 1D zigzag network where the **L4a** molecules adopt 180° torsion angle between C-N-N-C atoms. Khanpour *et al.*^[42] reported two Zn CPs of **L4a** with SCN^- and N_3^- anions displayed 1D looped chain structures. The powder XRD of the anion exchanged CPs, **CP2-SCN** and **CP2-N₃**, were compared it was observed that **CP2-SCN** showed similar pattern as that of the calculated powder XRD pattern of the structure reported by Khanapour *et al.* This confirmed the structural transformation from zigzag chain to looped chain structure. But the powder XRD of **CP2-N₃** showed some similarity in peaks position with **CP2**

and some similarity with the CP reported by Khanpour *et al.* Hence structural change from zigzag network to another network expected in **CP2-N₃**. In these anion exchange reactions of **CP2-SCN** and **CP2-N₃**, the difference in the geometry of the anion I⁻ with that of SCN⁻ and N₃⁻ (linear) resulted into the change in the geometry of the CPs **CP2-SCN** and **CP2-N₃** (Figure 4.12).

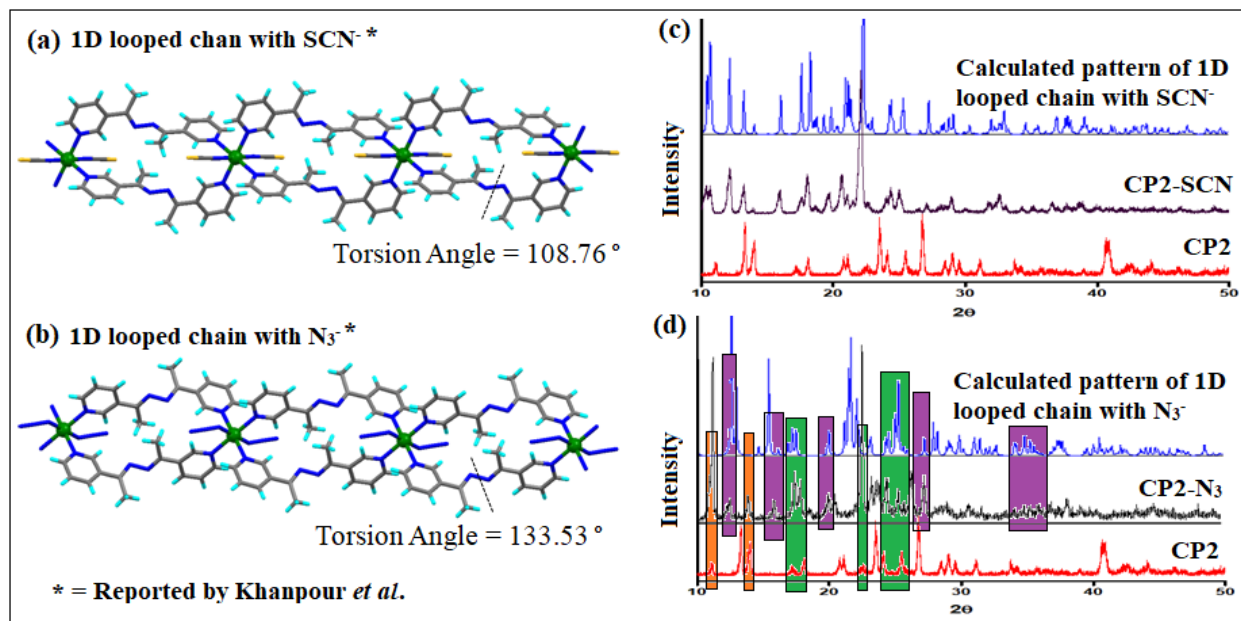


Figure 4.12: CPs of **L4a** with (a) Zn-SCN and (b) Zn-N₃^[42] (c) Powder XRD comparison of reported structure, **CP2-SCN** and CP2 (d) Powder XRD comparison of reported structure, **CP2-N₃** and CP2

The geometry of **CP3** also showed a zigzag network of **L6a** molecules with 180° torsion angle between C-N-N-C atoms. Niu *et al.*^[43] reported a 1D zigzag chain CP of **L6a** with ZnCl₂. The anion exchange of **CP3** with Cl⁻ i.e. **CP1-Cl** may also formed the zigzag network as it was observed in the report by Niu *et al.* and it was confirmed by comparing the calculated Powder pattern of the reported structure with **CP1-Cl** (Figure 4.12).

Though the CPs, **CP1**, **CP2** and **CP3**, attains 1D structure, it was observed that the anion geometry is playing an important role in modifying the geometry of CPs during counter anion exchange. The observation includes the following points. (1) The counter anion exchange of **CP1** and **CP3** by Cl⁻ ions which is similar to that of I⁻ ions, resulted in minimum structural modifications. (2) The anion exchange with the linear anions SCN⁻ and N₃⁻ anions which have

completely different geometry than I resulted in reassembling of the CPs to change into 1D looped chain geometry. (3) The exchange with trigonal planar CO_3^{2-} anions resulted in complete structural modification as no similarity appeared in the powder XRD pattern. The change in the geometry along with the counter anions is also expected to result in modified properties of CPs.

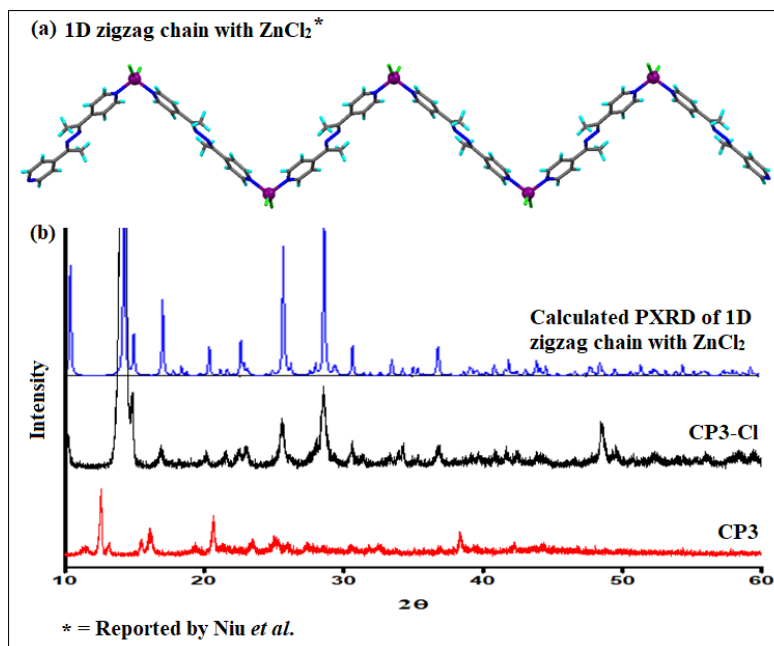


Figure 4.13: (a) 1D looped chain structures of **L6a** with ZnCl_2 ^[43] and the (b) Powder XRD comparison of reported structure, **CP3-Cl** and **CP3**

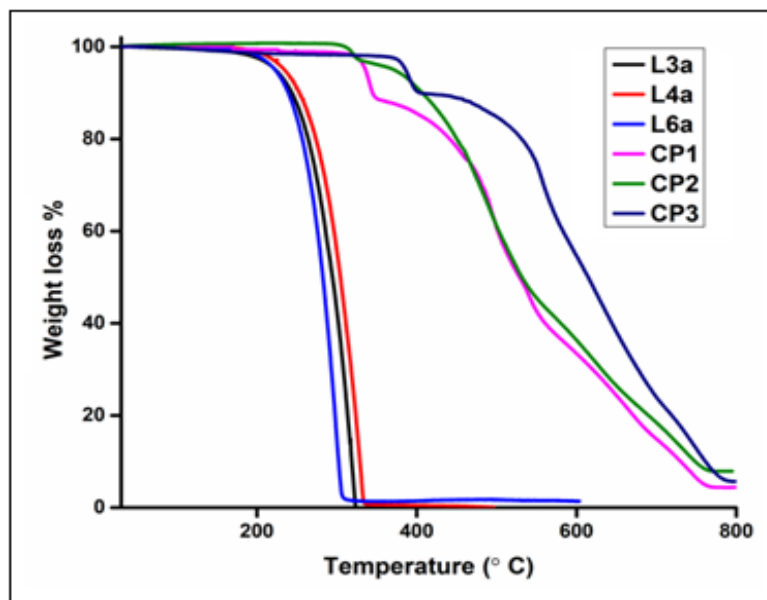


Figure 4.14: TGA of synthesized ligands and ZnI_2 CPs

4.3.4 Thermo Gravimetric Analysis of CPs: The TGA analysis results reveals that the ligands **L3a**, **L4a** and **L6a** are thermally stable upto 170° C and almost complete decomposition of ligands took place at 335 °C. The CPs due to the polymerization of ligands with ZnI₂ the CPs, **CP1**, **CP2** and **CP3** are thermally stable upto 300 °C, 290 °C and 350 °C, respectively. The thermal stability of anion exchanged CPs are also investigated. The TGA of anion exchanged CPs showed the stability in the order as **CP1-Cl** > **CP1-SCN** > **CP1-N₃** > **CP1-CO₃** (Appendix figure A57).

4.3.5 Dye Adsorption study of CPs: The adsorption properties **CP1**, **CP2** and **CP3**, derived from *bis*-pyridyl-*bis*-imine Schiff base ligands **L3a**, **L4a** and **L6a**, were studied which included the adsorption of organic dyes i.e Methylene Blue (MB), Malachite Green (MG), Rhodamine-B (RB) and Methyl Orange (MO).

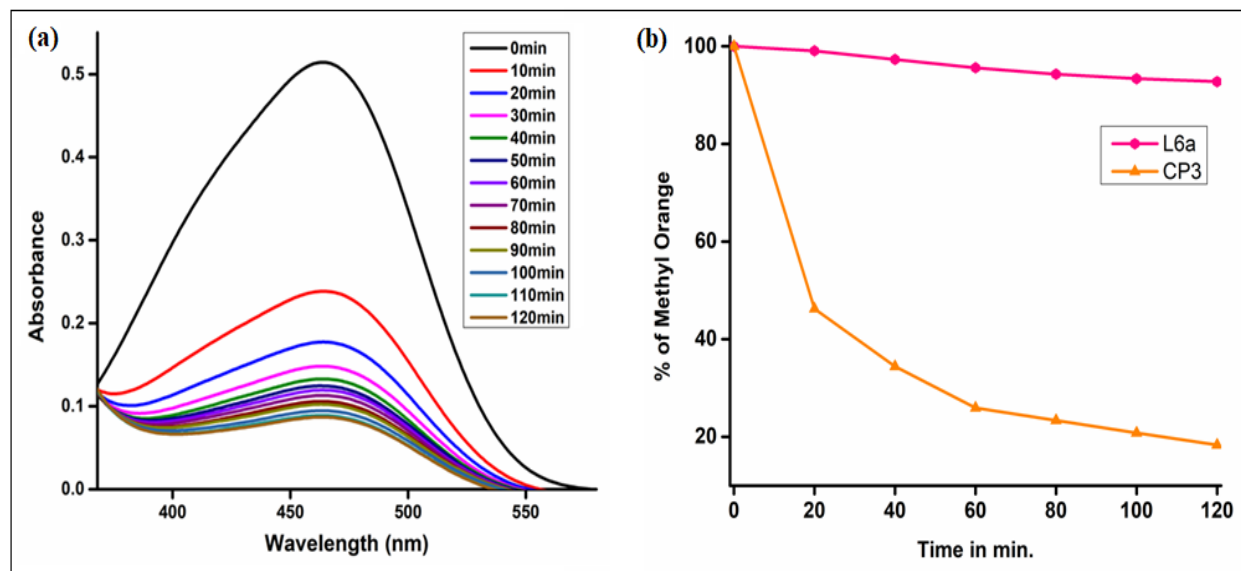


Figure 4.15: Adsorption of (a) Methyl Orange (MO) and (b) Percentage (%) adsorption of MO in presence of **L6a** and **CP3**

Among the three CPs, **CP3** displayed significant adsorption of MO. The adsorption property of CPs are mainly depends on the co-ordination environment of the central metal ion, the π -electrons donating tendency of organic ligands, and the extent of the metal-dye interactions formed in CPs.

To study the adsorption of MO, 20 mg powder of **CP3** was dispersed in 20 ml of 2×10^{-5} M aqueous solution of MO and stirred the suspension for about 2 hours. After regular time intervals

of 10 min. the reaction mixture suspension was centrifuged and UV-visible absorption spectra was recorded. Figure 4.15a showed the decreased in the absorption intensity peak corresponding to MO with time. It was observed that 82% of adsorption was achieved within 60 min. The powder XRD of **CP3** was compared with that of MO-adsorbed **CP3**. It showed different patterns due to the change in the network geometry after MO adsorption (Figure 4.16). The **CP3** showed negligible adsorption with MB, MG and RB dyes (Appendix figure A58).

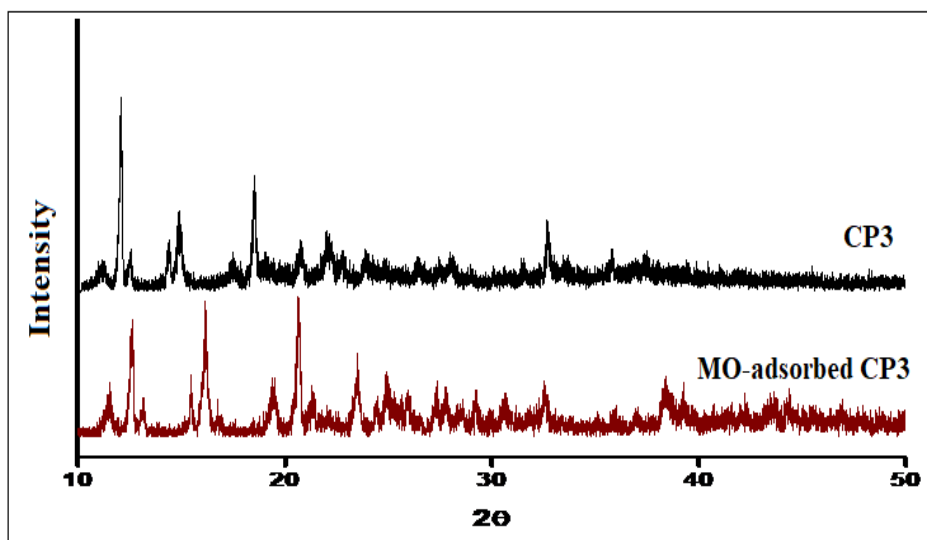


Figure 4.16: Correlated powder XRD of **CP3** and MO-adsorbed **CP3**

4.4 Conclusions

CP1, **CP2** and **CP3** formed 1D zigzag chain structures with **L3a**, **L4a** and **L6a** respectively. As the CPs are prepared with I^- counter ions, the CPs were subjected to counter anion exchange reactions with Cl^- , SCN^- , N_3^- and CO_3^{2-} anions. By comparing the X-ray diffraction of previous reports and the anion exchanged products it was observed that when the anion exchange was performed with Cl^- , network geometry similar to the parent CP resulted but the anion exchange with SCN^- and N_3^- resulted into different network geometries while the anion exchange with CO_3^{2-} also showed structural modification. These results suggested that during the anion exchange by changing the geometry of the exchangeable anion, the network geometry of the resulting CP also been changed. Along with that the adsorption studies of the CPs **CP1**, **CP2** and **CP3** were also investigated. The selective adsorption of MO by **CP3** was observed whereas the **CP1** and **CP2** are inactive toward dye adsorption.

4.5 References

- 1 C. Healy and W. Schmitt, *Coord. Chem. Rev.*, 2018, **371**, 67–85.
- 2 Y. X. Sun and W. Y. Sun, *CrystEngComm.*, 2015, **17**, 4045–4063.
- 3 T. S. B. Baul, S. Kundu, S. Mitra, H. Hopfl, E. R. T. Tiekink and A. Linden, *Dalton. Trans.*, 2013, **42**, 1905–1920.
- 4 S. J. Jennifer and A. K. Jana, *Cryst. Growth Des.*, 2017, **17**, 5318–5329.
- 5 G. Hou, L. Bi, B. Li and L. Wu, *Inorg. Chem.*, 2010, **49**, 6474–6483.
- 6 L. L. Han, T. P. Hu, K. Mei, Z. M. Guo, C. Yin, Y. X. Wang, J. Zheng, X. P. Wang and D. Sun, *Dalton. Trans.*, 2015, **44**, 6052–6061.
- 7 J. Liu, S. B. Xia, Y. Duan, T. Liu, F. Cheng and C. K. Sun, *Polymers*, 2018, **10**, 165.
- 8 C. Yi, L. Zhang, R. Hu, S. S. C. Chuang, J. Zheng and X. Gong, *J. Mater. Chem. A*, 2016, **4**, 12730–12738.
- 9 Y. Kataoka, Y. Miyazaki, K. Sato, T. Saito, Y. Nakanishi, Y. Kiatagwa, T. Kawakami, M. Okumura, K. Yamaguchi and W. Mori, *Supramol. Chem.*, 2011, **23**, 287–296.
- 10 G. Mahmoudi, A. Bauza, A. Frontera, P. Garczarek, V. Stilinovic, A. M. Kirillov, A. Kennedy and C. Ruiz-Perez, *CrystEngComm*, 2016, **18**, 5375–5385.
- 11 H. Schmidbaur, T. Probst, O. Steigelmann and G. Muller, *Heteroat. Chem.*, 1990, **1**, 161–165.
- 12 B. L. Fei, W. Y. Sun, K. B. Yu and W. X. Tang, *Dalton. Trans.*, 2000, 805–811.
- 13 V. T. Yilmaz, E. Soyer and O. Buyukgungor, *Polyhedron*, 2010, **29**, 920–924.
- 14 W. H. Jiang, H. Z. Zhang, G. F. Hou, D. S. Ma, B. Liu and Y. H. Yu, *RSC Adv.*, 2017, **7**, 45641–45651.
- 15 R. Custelcean, T. J. Haverlock and B. A. Moyer, *Inorg. Chem.*, 2006, **45**, 6446–6452.
- 16 J. P. Ma, Y. Yu and Y. B. Dong, *Chem. Commun.*, 2012, **48**, 2946–2948.
- 17 B. Manna, A. K. Chaudhari, B. Joarder, A. Karmakar and S. K. Ghosh, *Angew. Chem. Int. Ed.*, 2013, **125**, 1032–1036.
- 18 P. Shi, B. Zhao, G. Xiong, Y. Hou and P. Cheng, *Chem. Commun.*, 2012, **48**, 8231–8233.
- 19 B. C. Tzeng, B. S. Chen, S. Y. Lee, W. H. Liu, G. H. Lee and S. M. Peng, *New J. Chem.*, 2005, **29**, 1254–1257.
- 20 D. Liu, F. F. Lang, X. Zhou, Z. G. Ren, D. J. Young and J. P. Lang, *Inorg. Chem.*, 2017, **56**, 12542–12550.

-
- 21 Q. Wang and Z. Yang, *Environ. Pollut.*, 2016, **218**, 358–365.
 - 22 Y. Teng, J. Yang, R. Zuo and J. Wang, *J. Earth Sci.*, 2011, **22**, 658–668.
 - 23 H. Nakamura, *Anal. Methods*, 2010, **2**, 430–444.
 - 24 U. Shanker, M. Rani and V. Jassal, *Environ. Chem. Lett.*, 2017, **15**, 623–642.
 - 25 S. Vasudevan and M. A. Oturan, *Environ. Chem. Lett.*, 2014, **12**, 97–108.
 - 26 D. Curiel, M. Mas-Montoya and G. Sanchez, *Coord. Chem. Rev.*, 2015, **284**, 19–66.
 - 27 Y. Wu, G. P. Yang, Y. Zhao, W. P. Wu, B. Liu and Y. Y. Wang, *Dalton. Trans.*, 2015, **44**, 3271–3277.
 - 28 Z. Zhu, M. Wang, C. Xu, Z. Zong, D. Zhang, S. Bi and Y. Fan, *J. Solid State Chem.*, 2017, **256**, 176–183.
 - 29 Y. Zhu, Y. M. Wang, S. Y. Zhao, P. Liu, C. Wei, Y. L. Wu, C. K. Xia and J. M. Xie, *Inorg. Chem.*, 2014, **53**, 7692–7699.
 - 30 B. Wu, W. H. Zhang, Z. G. Ren and J. P. Lang, *Chem. Commun.*, 2015, **51**, 14893–14896.
 - 31 Y. Y. Jia, G. J. Ren, A. L. Li, L. Z. Zhang, R. Feng, Y. H. Zhang and X. H. Bu, *Cryst. Growth Des.*, 2016, **16**, 5593–5597.
 - 32 C. P. Li, H. Zhou, S. Wang, H. H. Yuan, S. Z. Zhang and M. Du, *Chem. Commun.*, 2017, **53**, 4767–4770.
 - 33 T. Wen, D. X. Zhang and J. Zhang, *Inorg. Chem.*, 2012, **52**, 12–14.
 - 34 X. Wang, H. Xu, Y. Han, Y. Li, C. Sheng, Z. Xu, J. Xu and M. Wang, *Inorg. Chim. Acta*, 2017, **461**, 15–20.
 - 35 H. Xu, Y. Gou, J. Ye, Z. Xu and Z. Wang, *J. Solid State Chem.*, 2016, **237**, 323–329.
 - 36 N. Hussain and V. K. Bhardwaj, *Dalton. Trans.*, 2016, **45**, 7697–7707.
 - 37 G. M. Sheldrick, *Acta Crystallogr. Sect. A*, 2008, **64**, 112–122.
 - 38 O. V Dolomanov, L. J. Bourhis, R. J. Gildea, J. A. K. Howard and H. Puschmann, *J. Appl. Crystallogr.*, 2009, **42**, 339–341.
 - 39 G. M. Sheldrick, *Acta Crystallogr. Sect. A*, 2015, **71**, 3–8.
 - 40 G. M. Sheldrick, *Acta Crystallogr. Sect. C*, 2015, **71**, 3–8.
 - 41 G. H. Lee and H. T. Wang, *Molecules*, 2006, **11**, 589–596.
 - 42 M. Khanpour and A. Morsali, *Eur. J. Inorg. Chem.*, 2010, **2010**, 1567–1571.
 - 43 W. J. Niu, J. L. Wang, Y. Bai and D. B. Dang, *Spectrochim. Acta Part A*, 2012, **91**, 61–66.
-

Chapter-5

Influence of Reaction Conditions on Construction of 2D and 3D Cd(II) Coordination Polymers

Influence of Reaction Conditions on Construction of 2D and 3D Cd(II) Coordination Polymers

5.1 Introduction

Coordination polymers (CPs), with the desirable applications^[1-8] can be achieved by pre-designing the structures using suitable organic ligands and metal salts. There are other crucial factors such as ligand to metal ratio,^[9,10] solvent molecules,^[11,12] guest molecules,^[13] and reaction conditions^[14] which are important in tuning the self-assembled structures to give a precious architecture with fruitful applications. Different CPs with same metal salts and ligands can be achieved by the influence of metal coordination preferences,^[15,16] temperature association,^[17] and removal or exchange of solvent or guest molecules.^[18]

However external parameters such as reaction conditions, like different pH range, temperature and steric effects of solvents or guests influence the dimensionality and structure of CPs along with the effects of metal and ligands. Gu *et al.*^[19] reported CPs of lanthanides such as Pr, Nd, Eu and Gd with 5-(2'-carboxyphenyl) nicotinic acid where pH and an auxiliary ligand, 2,2'-bipyridine ligand influence the structure of CPs. The influence of pH on structure is mainly based on the protonating extent of ligand where at pH 4 ligand was partially deprotonated and at pH 6, it is completely deprotonated and at pH 4-5, both the forms of the ligand exist which results into the formation of different structures. Kang *et al.*^[20] constructed three Mn metal organic frameworks with a dicarboxyphenyl-terpyridine ligand by regulating the binary solvent mixture ratios. They reported a 1D chain structure with DMA/H₂O solvent mixture in 1:1 ratio, a 2D structure obtained when the DMA/H₂O mixture changes to 5:1 ratio and a 3D structure obtained when only DMA used as solvent. They further observed the significant effect of their catalytic performance in the CO₂ cyclo addition to epoxides. Roy *et al.*^[21] reported Co coordination polymers with 4,4'-methylene-*bis*-pyrazole and 5-substituted derivatives of isophthalic acid and explored the mutually inclusive effect of temperature and substitution on coordination geometry of metal resulting into the changes in crystal packing. They observed the effect of temperature variation on the changes in the self assembly which resulted in different geometry of Co CPs with tunable pore size. The CPs formed pink colored crystals with octahedral geometry when the reaction performed at 80 °C and purple colored tetrahedral and square pyramidal geometry CPs

obtained when the reaction processed at 120° C. They further observed the photo catalytic studies with the CPs.

CPs based on pyridyl based ligands, **L3a**, **L4a**, **L5a** and **L6a**, which have imine spacers, are explored widely by various groups (Figure 5.1).^[22-35] Dong *et al.*^[22] in 2000, first reported the structure of **L3a** and the CPs of **L3a** with Cd(NO₃)₂·4H₂O and Co(NO₃)₂·6H₂O metal salts. The CPs were synthesized by layering metal salts in methanol (Cd) or ethanol (Co) over the ligand in methylene chloride in a metal to ligand molar ratio of 1:2. The crystal structure of CPs exhibits two-dimensional non-interpenetrating polycyclohexane motifs in chair conformations. They performed the same reaction by varying the solvent system. The ligand was taken in non-polar solvent (benzene) and Cd(NO₃)₂·4H₂O in methanol and Co(NO₃)₂·6H₂O in ethanol respectively with metal to ligand molar ratio of 1:2. In case of **L3a** with Cd(NO₃)₂·4H₂O, a brick wall structural motif formed while with Co(NO₃)₂·6H₂O a 3D network resulted. The CPs with **L4a** in benzene with same metal salts, resulted in the formation of 1D chains. Their results showed that the construction of the CPs primarily depends on the choice of solvent system and largely independent on metal to ligand molar ratio.

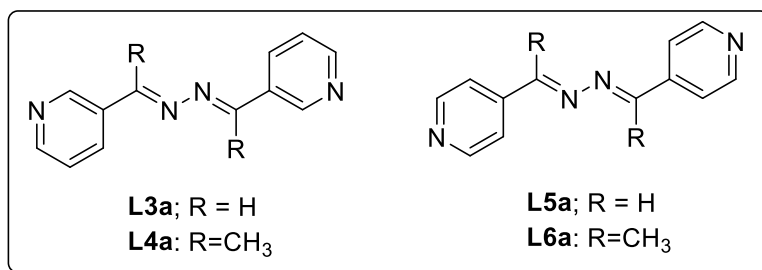


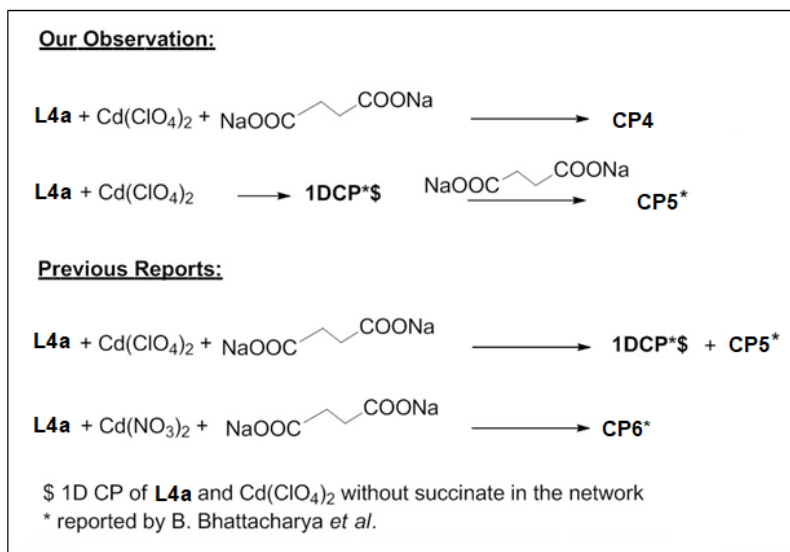
Figure 5.1: Pyridyl based Schiff bases **L3a**, **L4a**, **L5a** and **L6a**

Since then, many CPs were prepared with different metal salts of Co(II), Ni(II), Cu(II), Zn(II), Ag(I), Hg(II), Pb(II) and **L3a**, **L5a** and **L6a**.^[23-29] Maity *et al.*^[30] and Singh *et al.*^[31] investigated the photophysical properties of ‘Cd(II)’ and ‘Zn(II)’ CPs of **L3a**, **L4a** and **L5a**. Dong *et al.*^[32] reported CPs of **L4a** with Cd(NO₃)₂ and showed the effect of solvents on the structures. Hashemi *et al.*^[33] also reported CPs of **L4a** with Zn(II) and NO₃⁻, ClO₄⁻, N₃⁻ and SCN⁻ anions. They also synthesized CPs using metal salts of Hg(II) and Pb(II).

Though the CPs of **L4a** are widely explored, the interplay of reaction conditions on the dimensionality of the CPs still warrants further study. The present chapter discusses the coordination polymers of Cd(II) with **L4a** in presence of disodium succinate. **L4a** is an

exobidentate ligand and the 3-pyridyl group in it gives flexibility due to the 3-position of N which provides many possible geometries of the CPs. The N-N spacer group in **L4a** is rigid, which may reflect in forming robust CPs. In order to provide a flexible structure, the succinate is introduced into the network. Thus, **L4a** and succinate are selected so that they can lead to the formation of robust and flexible network. It is observed in the present work that the ligand **L4a** with $\text{Cd}(\text{ClO}_4)_2$ in presence of disodium succinate resulted in a 2D structure, **CP4**, $\{[\text{Cd}_2(\text{L4a})(\text{C}_4\text{H}_4\text{O}_4)_2] \cdot 5\text{H}_2\text{O}\}_n$. In contrast, in 2013, Bhattacharya *et al.*^[34] synthesized a 3D CP, **CP6**, $\{[\text{Cd}(\text{L4a})(\text{C}_4\text{H}_4\text{O}_4)] \cdot (\text{H}_2\text{O})_4\}_n$ with $\text{Cd}(\text{NO}_3)_2$ using this ligand in combination with disodium succinate and in 2015 synthesized another 3D CP, **CP5**, $\{[\text{Cd}(\text{L4a})(\text{C}_4\text{H}_4\text{O}_4)(\text{H}_2\text{O})] \cdot 3(\text{H}_2\text{O})\}_n$ with $\text{Cd}(\text{ClO}_4)_2$ and **L4a** in combination with disodium succinate^[35] (Scheme 5.1). Thus it is essential to analyze and correlate the structural features of the Cd(II) CPs of **L4a** and succinate with a focus on the following points:

1. Analysis of the structural features of **CP4**, **CP5** and **CP6** by comparing their asymmetric unit, coordination environment of Cd(II) centers, geometry of **L4a** and geometry & binding modes of succinate.
2. Comparison of the reaction conditions leading to the formation of **CP4**, **CP5** and **CP6**.



Scheme 5.1: Reaction sequence of the synthesis of **CP4**, **CP5**^[35] and **CP6**^[34]

5.2 Experimental Section

5.2.1 Synthesis of CP4 $\{[\text{Cd}_2(\text{L4a})(\text{C}_4\text{H}_4\text{O}_4)_2] \cdot 5\text{H}_2\text{O}\}_n$, (**CP4**): An aqueous solution (4 ml) of disodium succinate (0.2 mmol, 0.0324 g) was mixed with an ethanolic solution (4 ml) of 2,5-*bis*-

(3-pyridyl)-3,4-diaza,-2,4-hexadiene (**L4a**) (0.1 mmol, 0.0238 g) and stirred for 15 min. to mix it well. $\text{Cd}(\text{ClO}_4)_2 \cdot 6\text{H}_2\text{O}$ (0.2 mmol, 0.0838 g) was dissolved in (4 ml) ethanol and the solution was slowly layered to the above mixed ligand solution using 3 ml buffer (ethanol). The yellow flattered crystals were obtained after two weeks. The crystals were separated and washed with ethanol-water (1:1) mixture and dried under air. Anal. Calc: C 33.48, H 4.60, N 7.10; Found: C 33.32, H 4.68 N 7.09; IR (cm^{-1} KBr pellet): 3402 (b), 3070 (w), 2970 (w), 1574 (vs), 1474 (w), 1420 (vs), 1366 (w), 1296 (s), 1234 (w), 1196 (s), 1134 (w), 1088 (w), 1034 (s), 887 (w), 810 (s), 771 (w) (Appendix figure A59). Powder XRD was recorded and compared with the calculated powder XRD of **CP4** (Appendix figure A60).

5.2.2 Single-Crystal X-ray Diffraction: The single crystal XRD was done at IISER Mohali where the single crystal data were collected on a Bruker Kappa APEX II diffractometer equipped with a CCD detector and sealed-tube monochromated $\text{MoK}\alpha$ radiation using the program APEX2. By using the program SAINT for the integration of the data, reflection profiles were fitted, and values of F^2 and $\sigma(F^2)$ for each reflection were obtained. Data were also corrected for Lorentz and polarization effects. The subroutine XPREP was used for the processing of data that included determination of space group, application of an absorption correction (SADABS), merging of data, and generation of files necessary for solution and refinement. The structure was solved by direct methods and refined by least square methods on F^2 using SHELX-97.^[36] Non-hydrogen atoms were refined anisotropically and hydrogen atoms were fixed at calculated positions and refined^[37] using a riding model. The crystal data and structure refinements of **CP4** are summarized in Table 5.1.

Table 5.1: Crystallographic data and refinement parameters of **CP4**

Identification Code	CP4
Empirical formula	$\text{C}_{22}\text{H}_{32}\text{Cd}_2\text{N}_4\text{O}_{13}$
Formula Wt.	785.31
Crystal system	Monoclinic
Space group	$P2_1/n$
$a/\text{\AA}$	13.4548(15)
$b/\text{\AA}$	8.5938(9)
$c/\text{\AA}$	25.244 (3)
$\alpha/^\circ$	90.00

$\beta/^\circ$	93.711(4)
$\gamma/^\circ$	90.00
$V/\text{\AA}^3$	2912.8(5)
Z	4
$D_{\text{calcd}}/\text{g cm}^{-3}$	1.791
T/K	296(2)
Theta ($^\circ$) range for data used	1.62 to 25.02
R_{int}	0.0168
Reflections collected	15491
No. of parameters refined	380
Final R (With $I > 2\sigma(I)$)	$R_1 = 0.0207,$ $wR_2 = 0.0462$
GOF on F^2	1.053

5.3 Results and Discussion

5.3.1 Crystal Structure Description of CP4: Crystal structure description of **CP4** shows that it crystallizes in the monoclinic space group $P2_1/n$. Based on the single crystal structure of **CP4**, there are two types of Cd(II) centers: (i) heptacoordinated (Cd1) and (ii) hexa-coordinated (Cd2). In the asymmetric unit, one Cd1, one Cd2, two succinates, two half units of ligand, and two water molecules are present (Figure 5.3a).

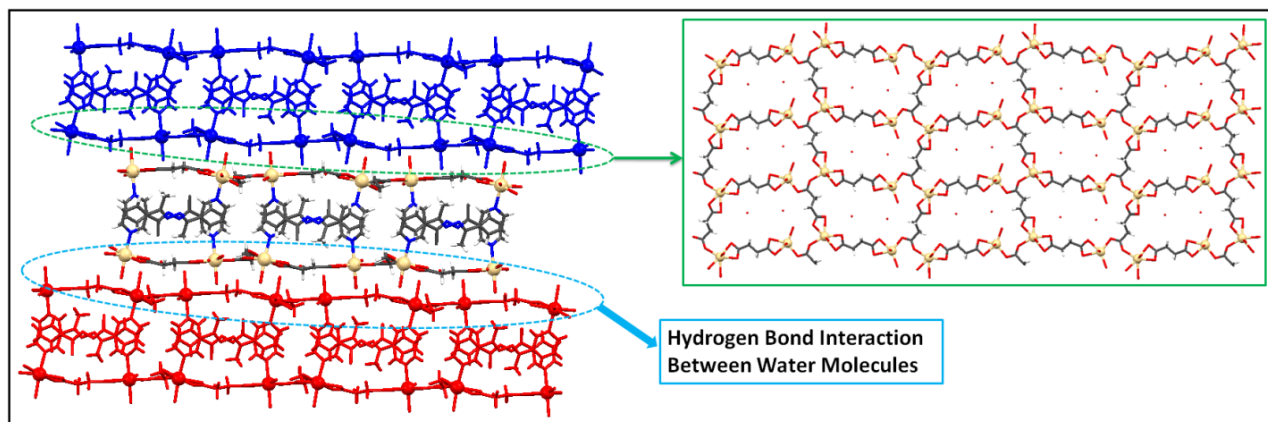


Figure 5.2: Illustration of crystal structure of **CP4**: 2D-bilayer structure of **CP4** three such layers are shown in different colors; Notice the Cd(II)-succinate layer of (4,4)-topology

Cd1 centre attains distorted pentagonal bipyramidal geometry, where the hepta coordination requirement is attained *via* two chelating succinates (Cd-O: 2.462 Å, 2.362 Å, 2.310 Å, 2.637 Å), succinate as monodentate coordinating unit (Cd-O: 2.300 Å), one H₂O molecule (Cd-O: 2.319 Å) and one ligand *via* the pyridyl nitrogen (Cd-N: 2.374 Å). Cd2 shows the distorted octahedral geometry, where the coordination environment is satisfied by one succinate *via* chelating mode (Cd-O: 2.303 Å, 2.464 Å), another succinate as monodentate coordinating unit (Cd-O: 2.227 Å), two H₂O molecules (Cd-O: 2.245 Å, 2.315 Å) and one ligand *via* the pyridyl nitrogen (Cd-N: 2.377 Å).

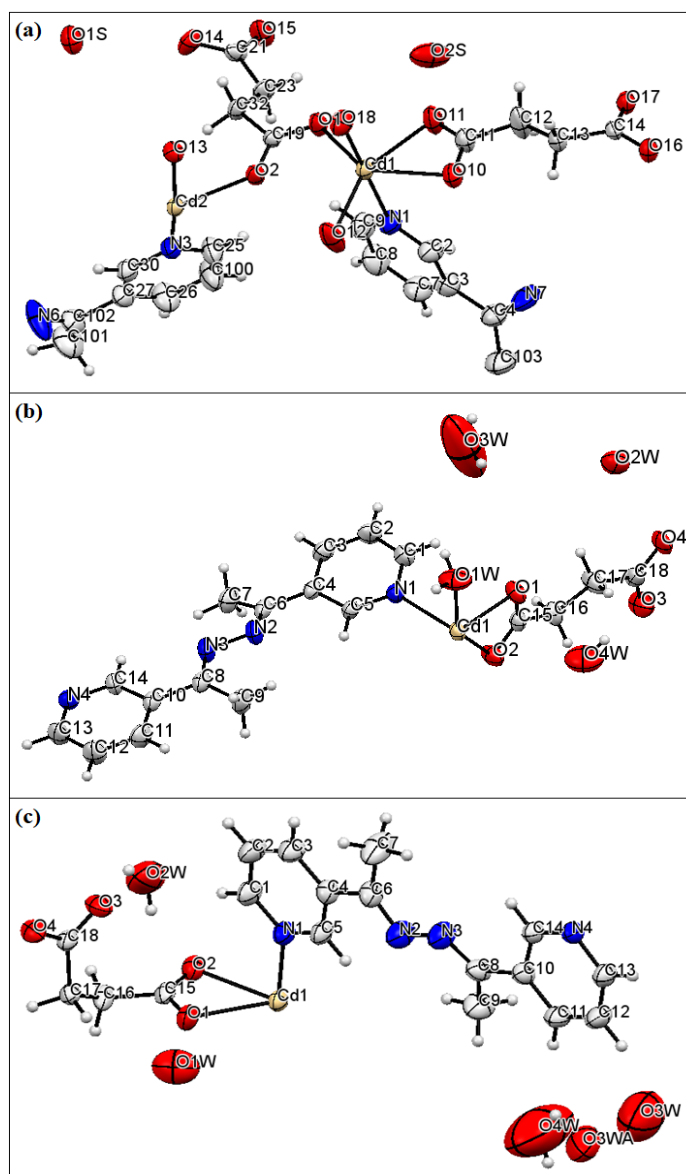


Figure 5.3: Asymmetric unit of (a) **CP4**; (b) **CP5**^[35] (Structure generated from CCDC 1426874) and (c) **CP6**^[34] (Structure generated from CCDC 930300; H atoms are not labeled)

The extended network resulted from Cd(II) centers, **L4a** and succinates can be described as a 2D-bilayer network, where the layers of Cd(II) and succinates are linked *via* **L4a**. The Cd(II)-succinate layers can be described as a 2D network of (4,4) topology, where the two types of Cd(II) centers form the nodes while the $-(\text{CH}_2)_2-$ of succinate act as the spacer. The loops of the Cd-succinates are occupied by water molecules (Figure 5.2). Two such layers of Cd(II)-succinates are joined by **L4a**, where the *trans* coordinating mode of the ligand was observed. The adjacent bilayers are held together by hydrogen bonding interactions between the coordinated water molecules and the non-coordinated water molecules present between the bilayers.

5.3.2 Analysis of structural features in CP4, CP5 and CP6: Comparison of the structural features in **CP4**, **CP5** and **CP6** were done to analyze the geometrical differences in the CPs due to different reaction conditions. The comparison was made specifically on (i) Coordination environment around Cd(II), (ii) Geometry of **L4a** in **CP4**, **CP5** and **CP6**, (iii) Geometry of succinate in **CP4**, **CP5** and **CP6** and (iv) Network differences in **CP4**, **CP5** and **CP6**.

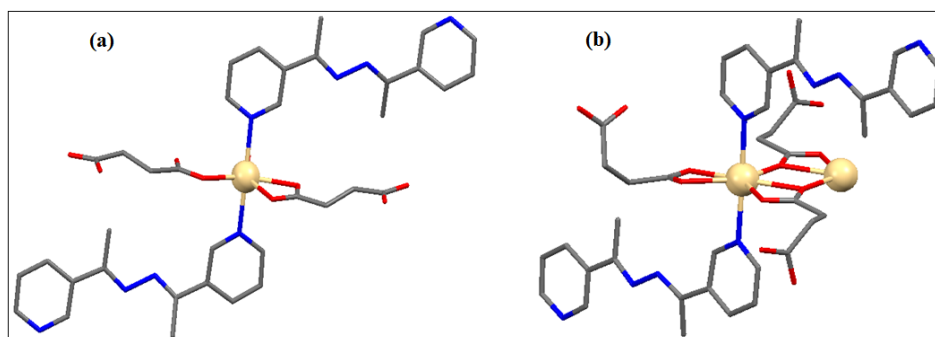


Figure 5.4: Coordination environment around Cd(II) in (a) **CP5**^[35] (Structure generated from CCDC 1426874) and (b) **CP6**^[34] (Structure generated from CCDC 930300) (Note: H-atoms were removed for clarity)

5.3.2.1 Coordination environment around Cd(II): **CP4** crystallizes in monoclinic $P2_1/n$ space group, while **CP5** and **CP6** crystallize in Orthorhombic $P2_1na$ and Monoclinic $P2_1/c$ space groups, respectively. The asymmetric unit of **CP4** contains two **L4a** half units, two succinate units, two types of Cd(II) and five water molecules (Figure 5.3a). The asymmetric unit of **CP5** contains **L4a**, succinate, Cd(II) and four water molecules whereas asymmetric unit of **CP6** contains **L4a**, succinate, Cd(II) and five water molecules (Figure 5.3b and 5.3c)^[34,35].

In **CP4**, two types of Cd(II) are present, one of them has distorted pentagonal bipyramidal and the other distorted octahedral (Figure 5.5). In **CP5**, Cd(II) forms an octahedral geometry with two **L4a** ligands, one monodentate, one chelating succinate molecules and one water molecule (Figure 5.4a). In **CP6**, Cd(II) forms a pentagonal bipyramidal geometry with two **L4a** ligands, one chelating bidentate and two bridging- succinate molecules (Figure 5.4b).

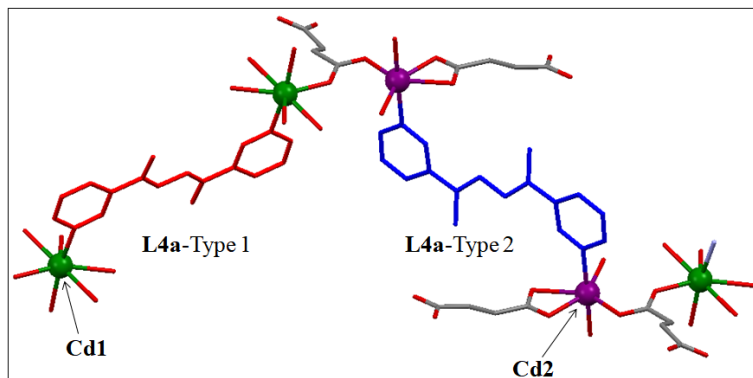


Figure 5.5: Coordination environment around Cd(II) in **CP4** (Note: H-atoms were removed for clarity)

5.3.2.2 Geometry of L4a in CP4, CP5 and CP6: The geometry of the ligand **L4a** in **CP4**, **CP5** and **CP6** differ with respect to the torsion angles and interplanar angles between imine and pyridyl planes. The torsion angle C-N-N-C bond in **L4a** in case of **CP4** is 180° , while in **CP5** and **CP6** it is 163.24° and 164.45° respectively. The torsion angles of other bonds are shown in (Figure 5.6). It can be seen from the figure that the ligand **L4a** in **CP5** and **CP6** are similar (only slight variations in the angles).

In **CP4**, two types of **L4a** are observed, where in one type (**L4a-type1**) the pyridyl and imine groups of the **L4a** are almost planar, while in another type (**L4a-type2**), they are oriented in angle of around -22° . Further it can be observed that the **L4a-type1** is connecting the Cd1 centers (hepta-coordinated), while **L4a-type2** is connecting the Cd2 centers (Octahedral) (Figure 5.6).

5.3.2.3 Geometry of Succinate in CP4, CP5 and CP6: Succinate is a dicarboxylate, which can lead to varied possibilities of binding to metal ions. The coordination complex resulted from the combination of Cd(II) and succinate, without any other coordinating moiety, is a highly corrugated 2D network (Figure 5.7a), where the hepta-coordinated Cd(II) centers are linked via succinates. The $-(CH_2)_2-$ of succinate adopts gauche conformation and out of the two carboxylate

groups in a succinate, one of them is chelating while the other one chelating and bridging other Cd(II) center (Figure 5.7).

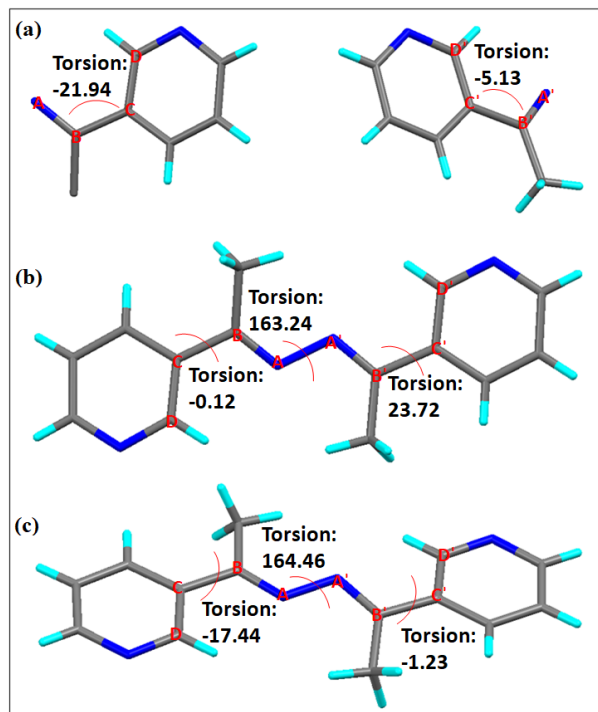


Figure 5.6: Geometries of **L4a** in (a) **CP4**, (b) **CP5**^[35] (Structure generated from CCDC 1426874) and (c) **CP6**^[34] (Structure generated from CCDC 930300)

In **CP4**, two types of succinates (Type 1 and Type 2) are present. In type 1 succinate, both the carboxylates adopt chelating binding mode, while in type 2 succinate, one of the carboxylates is chelating while in the other one, the two O atoms act as monodentate donor coordinating to two different Cd(II) centers. Type 1 succinate coordinates two different Cd(II) centers (Cd1- heptacoordinated and Cd2-octahedral) and type 2 succinate coordinates three Cd(II) centers (two Cd1- heptacoordinated and one Cd2-octahedral). The $-(\text{CH}_2)_2-$ of succinate adopts anti conformation in both types of succinates (Figure 5.8a). In **CP5**, only one type of succinate is present in which one carboxylate group adopts chelating mode while in the other carboxylate group, one O is involved in coordinating to Cd(II) center. The $-(\text{CH}_2)_2-$ of succinate in **CP5** adopts anti conformation (Figure 5.8b). In **CP6**, the succinate adopts a binding mode similar to the one observed in the coordination complex of Cd-succinate, i.e. out of the two carboxylate groups, one is chelating to the Cd(II) center while the other one is chelating and bridging another Cd(II) center and the $-(\text{CH}_2)_2-$ of succinate adopts gauche conformation. In **CP6**, polynuclear Cd(II)

moieties are resulted due to the oxo bridging of the succinates. Further, it can be observed that a 2D-layer is resulted in **CP4**, a 1D chain in **CP5**, while a corrugated 2D-layer results in **CP6**.

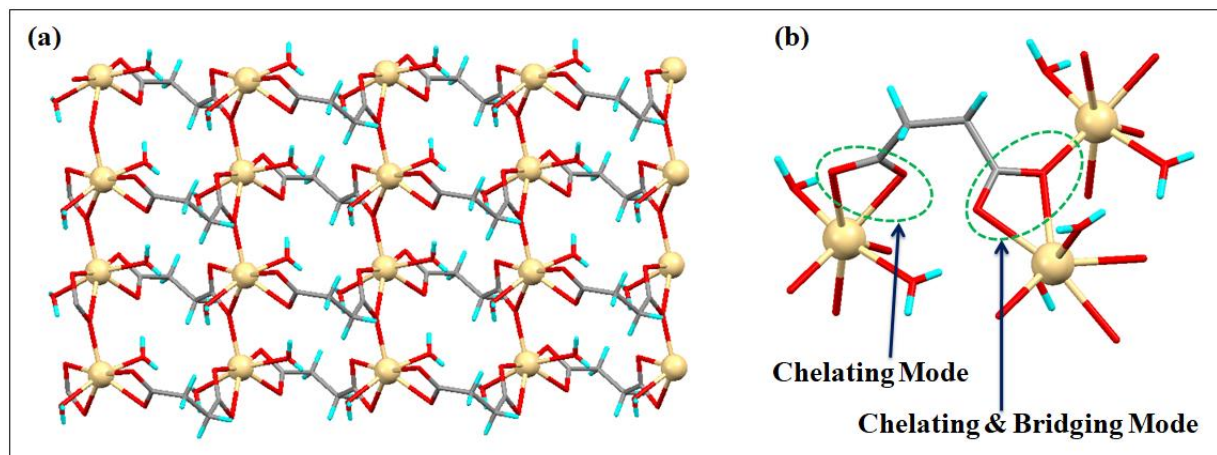


Figure 5.7: Illustration of Crystal Structure of Cd(II) Succinate : (a) 2D corrugated sheet; (b) Binding modes of succinate; Notice the gauche conformation of $-(\text{CH}_2)_2-$ of succinate (Structure generated from CCDC 153411)

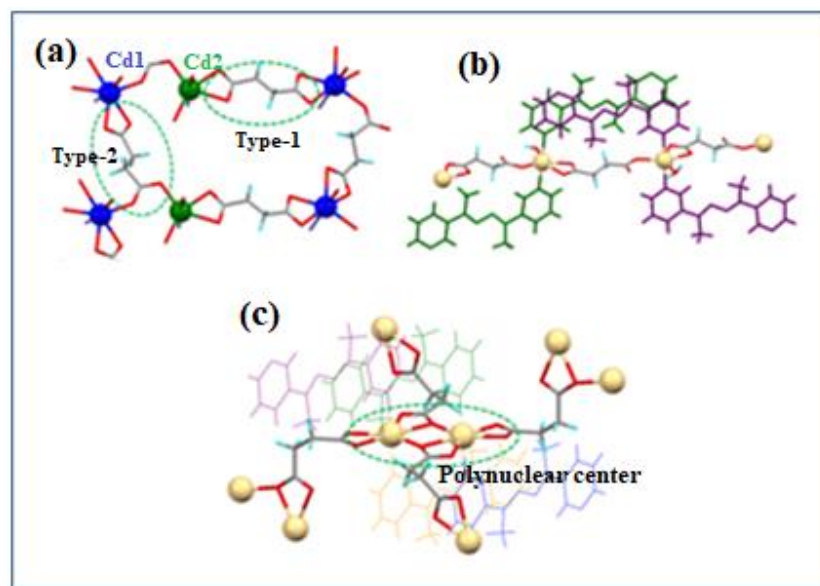


Figure 5.8: Binding modes of succinates in (a) **CP4**; (b) **CP5**^[35] (Structure generated from CCDC 1426874) and (c) **CP6**^[34] (Structure generated from CCDC 930300)

5.3.2.4 Network differences in CP4, CP5 and CP6: The final structure of **CP4** is a 2D bilayer, while **CP5** and **CP6** result in different type of 3D networks. In **CP4**, 2D-bilayer is formed by the

linking of two 2D-sheets of Cd-succinate by **L4a** (Figure 5.1), while in **CP5**, Cd-succinate 1D chains are connected by **L4a** to result in a 3D network (Figure 5.9). The 3D network in **CP5** is an outcome of the wavy 1D Cd(II)-succinate chain and 3-pyridylcoordinating moiety of **L4a** (Figure 5.9).

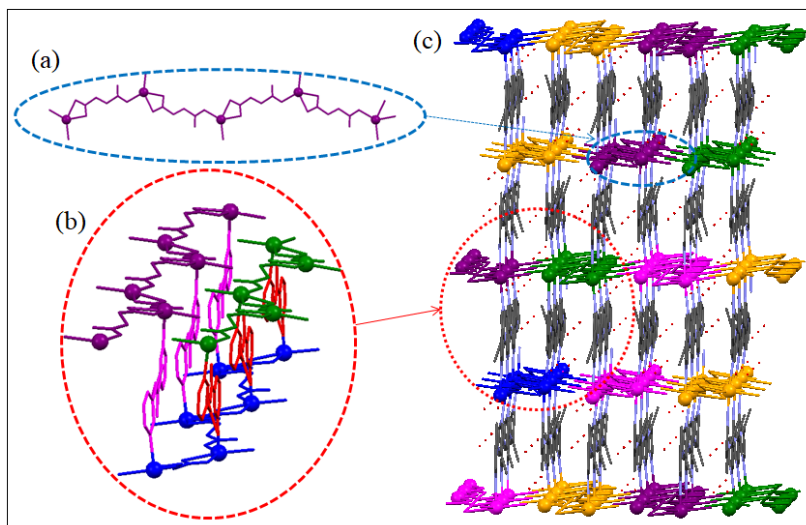


Figure 5.9: Illustration of crystal structure of **CP5**^[35]: (a) 1D chain of Cd(II) and succinate; (b) linking of chains by **L4a**; (c) 3D framework formed in **CP5** (Structures generated from CCDC 1426874)

In **CP6**, the corrugated 2D sheets of Cd(II)-succinate are linked by **L4a** to result in an overall 3D network. The adjacent 2D sheets of Cd(II)-succinate in **CP6** are arranged in a parallel manner and resulting in the formation of channels, which are occupied by water molecules (Figure 5.10).

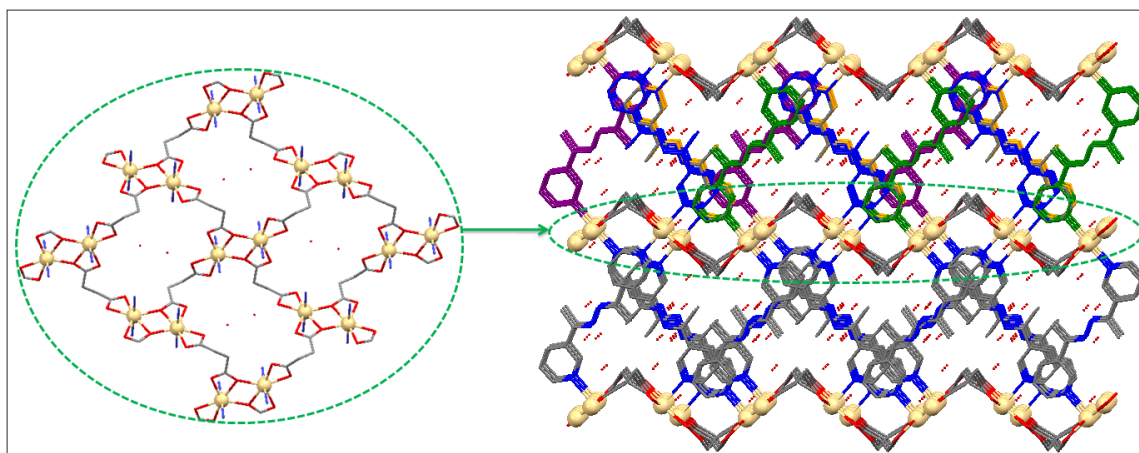
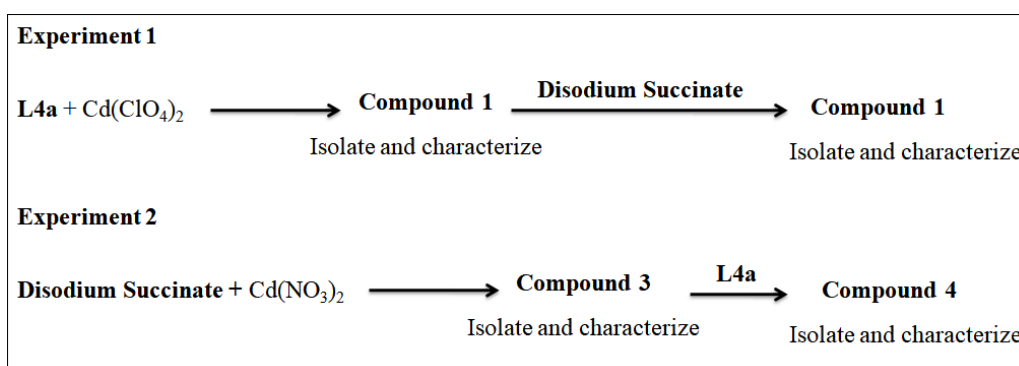


Figure 5.10: Illustration of crystal structure of **CP6**^[34]: (a) 2D corrugated sheet of Cd(II) and succinate; (b) linking of sheets by **L4a** (Structure generated from CCDC 930300)

5.3.2.5 Effect of reaction conditions on the geometry of CPs: Explanation of structural differences may be obtained by analyzing the anion exchange reaction and other controlled experiments (Scheme 5.2). In experiment 1, ligand **L4a** was reacted with $\text{Cd}(\text{ClO}_4)_2$ and the resulting compound 1 was analyzed by single crystal XRD and powder XRD. It was observed that compound 1 is a 1D looped chain of $\text{Cd}(\text{II})$ and **L4a** with ClO_4^- being coordinated to $\text{Cd}(\text{II})$ center. This is the same **1DCP** which was reported earlier by Bhattacharya *et al.*^[35] The compound 1 on reaction with disodium succinate (anion exchange reaction) resulted in compound 2. The powder XRD of compound 2 was analyzed and compared with the calculated powder XRD of **CP4**, **CP5** and **CP6**.



Scheme 5.2: Effect of reaction conditions on the resulting geometry of CPs

The powder XRD of compound 2 matched well with the calculated powder XRD of **CP5** (Appendix figure A61). It can be inferred that formation of **CP5** is *via* the 1D CP of $\text{Cd}(\text{II})$ and **L4a**. On observing the structural features of **1DCP** and **CP5**, it may be concluded that the succinate moiety has replaced the ClO_4^- and partial **L4a** from **1DCP** (Figure 5.11). Hence some of the structural features of **1DCP** is carried forward during the formation of **CP5**.

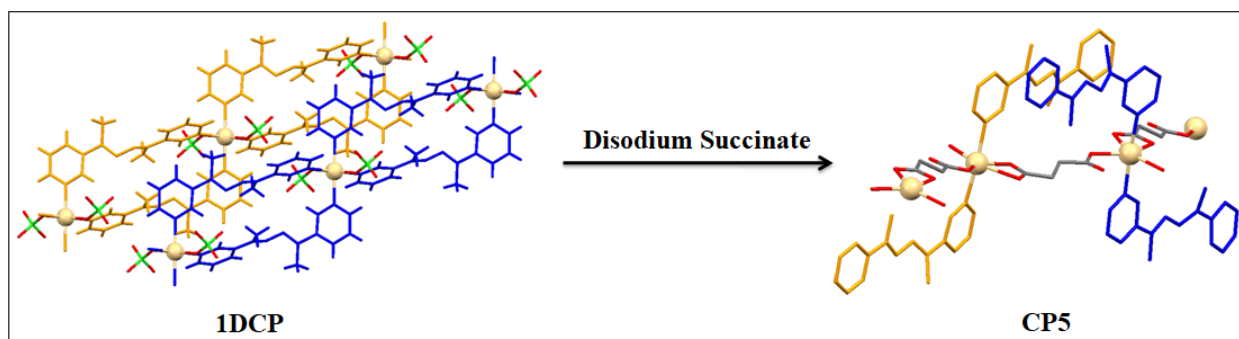


Figure 5.11: Structural transformation of **1DCP** (Structure generated from CCDC 1426873) to **CP5** (Structures generated from CCDC 1426874) on reaction with disodium succinate

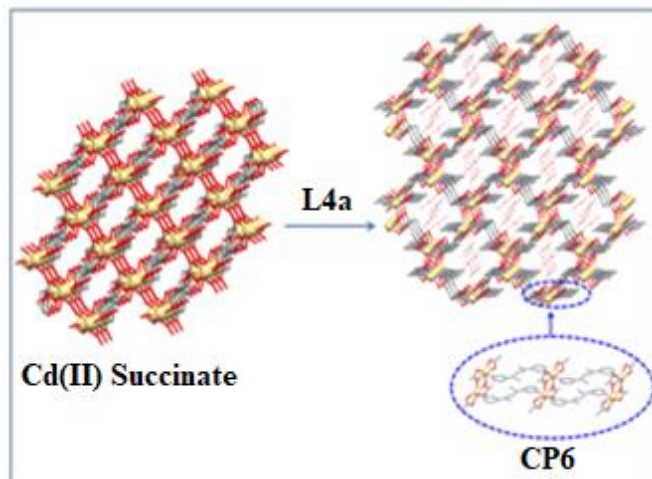


Figure 5.12: Structural transformation of Cd(II)-Succinate (Structure generated from CCDC 153411) to **CP6** (Structure generated from CCDC 930300) on reaction with **L4a**

In experiment 2, the reaction of $\text{Cd}(\text{NO}_3)_2$ with disodium succinate resulted in formation of compound 3. Finally compound 4 was isolated from the reaction of Cd(II)-succinate with **L4a**. Analysis of powder XRD of compound 4 inferred it to be **CP6**. The close observation of the structure of **CP6** hinted that it might be formed *via* Cd(II)-succinate complex. Hence some of the structural features of Cd(II)-succinate is retained during the formation of **CP6** (Figure 5.12).

5.3.3 Thermogravimetric Analysis: The Thermal Gravimetric Analysis of **CP4** showed a weight loss of 13.4% at 40 °C till 140 °C, which corresponds to the loss of water molecules (Calculated: 11.4% for the loss of five water molecules) (Figure 5.13). The dehydrated **CP4** was stable up to 250 °C. Further increase in temperature resulted in collapse of **CP4** framework and the decomposition continues till 327 °C (Figure 5.13). The TGA of **CP5**^[35] and **CP6**^[34] showed the dehydration process from 40 °C to 105 °C and the framework decomposition occurred at 240–250 °C (Table 5.2).

Table 5.2: TGA of CP4, CP5 and CP6		
Coordination Polymer	Temperature range corresponding to loss of water molecules	Temperature range corresponding to framework decomposition
CP4	40 °C- 140 °C	250 °C- 327 °C
CP5	40 °C- 104 °C	250 °C- 290 °C
CP6	40 °C- 105 °C	240 °C- 290 °C

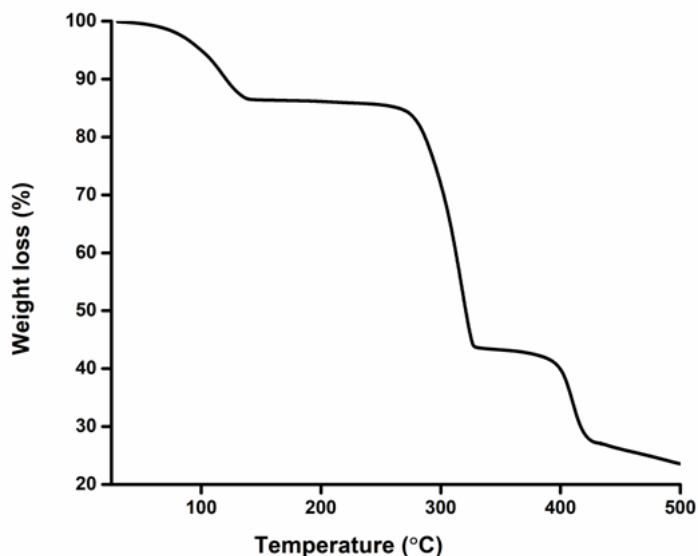


Figure 5.13: Thermal Gravimetric Analysis (TGA) of **CP4** to determine its thermal stability

5.3.4 Photophysical Properties of CPs: Cd(II) based coordination polymers **CP4**, **CP5** and **CP6** are expected to show ligand based luminescence.^[38–40] It was observed that for some of the molecules the supramolecular arrangements of the molecules due to non-covalent interactions lead to some interesting emission properties of the compounds. The CPs of these types of ligands should also result in varied photophysical properties due to their different arrangements and geometries in the solid state.

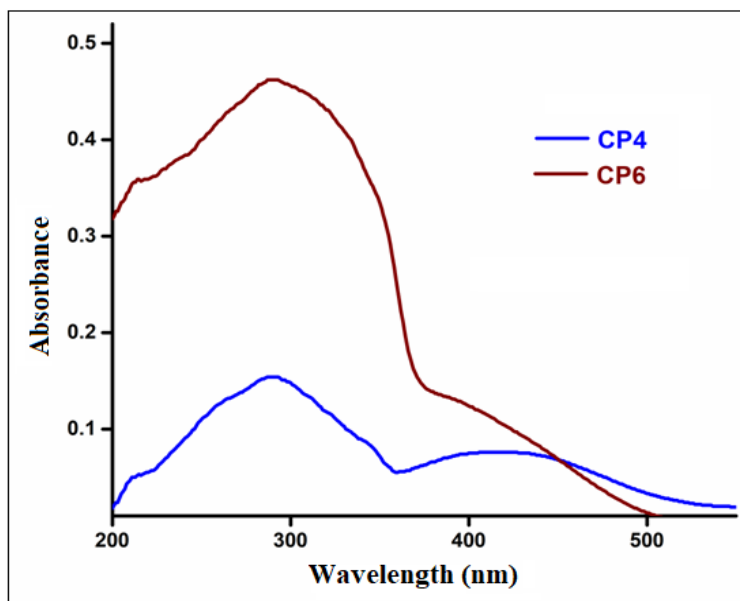


Figure 5.14: Solid UV-visible spectra of **CP4** and **CP6**

Further the interaction of the CPs with solvents of different polarities may also lead to variations in the photophysical properties.^[41–43] The UV-visible spectra of **CP4** in solid state showed two absorbance peaks at 290 nm and 415 nm while **CP6** showed peaks at 290 nm and 400 nm (Figure 5.14).

Table 5.3: Emission maxima in the PL spectra of CP4, CP5 and CP6	
Compound	Emission maxima wavelength (Excitation wavelength was 240 nm in L4a, CP4 and CP6) (nm)
L4a	483
CP4	484
CP5	394
CP6	484

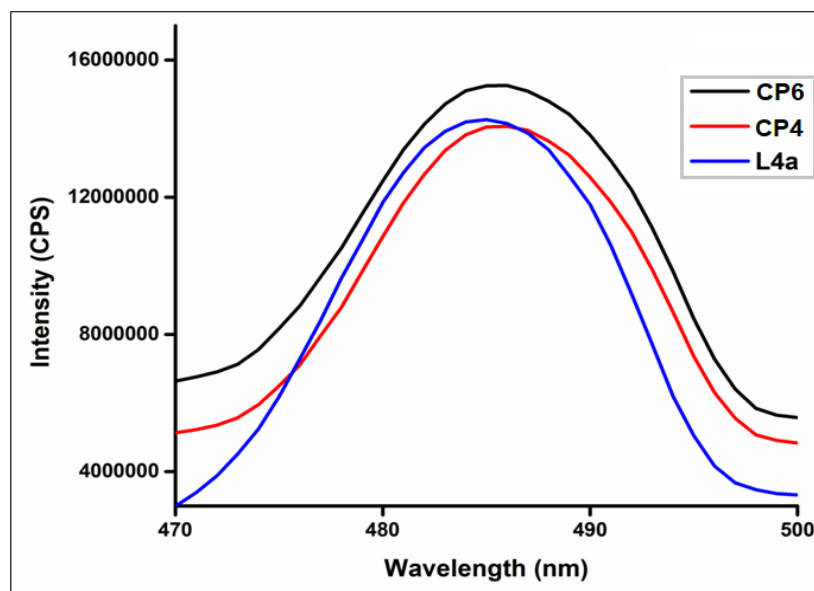


Figure 5.15: Solid state PL spectra of L4a, CP4 and CP6

The photoluminescence spectra of **L4a**, **CP4** and **CP6** were studied in solid state at room temperature, while the PL of **CP5** was reported by Bhattacharya *et al.* (Table 5.3). The solid state PL of both **CP4** and **CP6** exhibited emission at 470 nm when excitation wavelength was 240 nm. (Figure 5.15)

The emission wavelengths observed for **L4a**, **CP4**, **CP5**^[35] and **CP6** in the solid state indicate that the fluorescence emission of the coordination polymers **CP4**, **CP5** and **CP6** may be ascribed to the ligand based luminescence.

The PL of **CP4** was recorded in solvents (DMF, DMSO, Methanol, Acetonitrile, Dioxane, DCM and CHCl_3) at 10^{-4} M concentration, due to the low solubility of **CP4**. The PL of **CP4** in different solvents resembled the solid state PL in terms of emission maxima (~ 480 nm), but there was variation in the peak intensity.

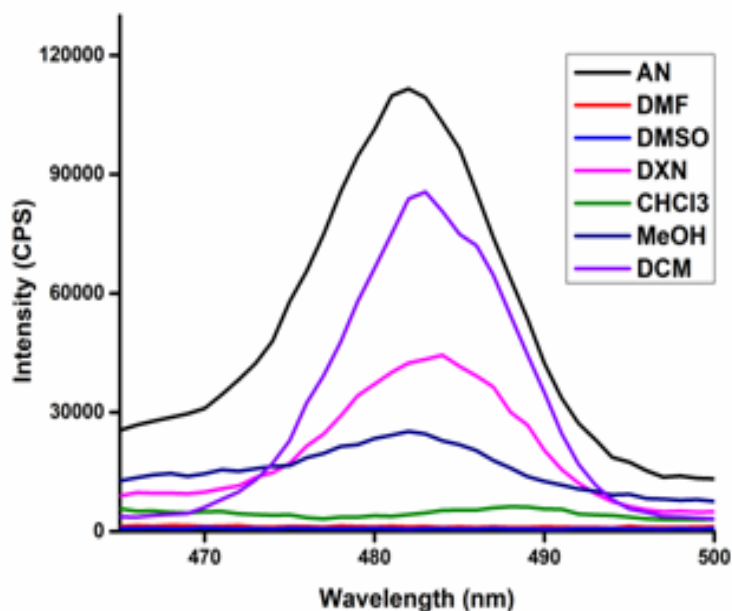


Figure 5.16: PL Spectra of **CP4** in different solvents (Acetonitrile (AN), DMF, DMSO, Dioxane (DXN), CHCl_3 , MeOH and DCM)

The low concentration of **CP4** in the solvents resulted in very less intense peaks compared to solids. It was further observed that the PL of **CP4** measured in DMF and DMSO didn't show any emission maxima ~ 480 nm, while maximum intense peak was observed in acetonitrile. (Figure 5.16)

The PL of 1:1 mixture of solvent mixtures was also measured and in case of acetonitrile- CHCl_3 mixture, it was observed that the emission maxima at 483 nm started to quench as the ratio of CHCl_3 in the solvent mixture was increased (Appendix figure A62). The PL of the liquid suspension of **CP4** in different organic solvents was also examined by taking 2 mg of **CP4** in 1 mL solvents. A homogeneous suspension was prepared by sonication. Although a peak was low compared to the solid state PL, the structured emission peaks were observed ~ 469 nm (Figure 5.17)

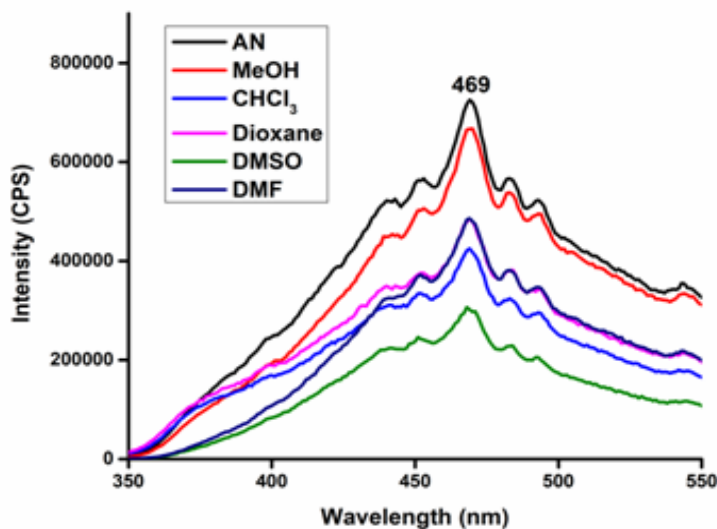


Figure 5.17: PL Spectra of **CP4** in slurry of different solvents (Acetonitrile (AN), DMF, DMSO, Dioxane, CHCl_3 , MeOH) (Excitation wavelength = 240 nm)

The effect of solvents on the peak intensity was also observed, which were similar to the solution PL of **CP4**. Overall the PL of **CP4** in dilute solutions and in homogeneous suspension in various solvents showed that the influence of interactions between the **CP4** network and solvent molecules play an important role in controlling the fluorescence emissions.

5.4 Conclusions

The reaction of Cd(II) with an exobidentate Schiff Base ligand, **L4a**, 2,5-bis-(3-pyridyl)-3,4-diaza-2,4-hexadiene, and disodium succinate has shown to form CPs of different geometries (**CP4**, **CP5** and **CP6**). **CP4** is a 2D bilayer structure while **CP5** and **CP6** are 3D structures of different topology. The effect of the reaction condition on the structural differences of CPs were explored by analyzing their crystal structures, observing the structural features of **1DCP** of **L4a** with $\text{Cd}(\text{ClO}_4)_2$ and 2D corrugated CP of Cd(II)-Succinate. Further, the controlled experiments including anion exchange reaction has suggested that the formation of **CP5** and **CP6** might have occurred in a stepwise manner there by resulting in different networks. The formation of **CP5** might have involved the initial step as the reaction of **L4a** with $\text{Cd}(\text{ClO}_4)_2$, which is followed by reaction with disodium succinate. Whereas in **CP6**, the initial step may be reaction of Cd(II) and succinate, which is followed by reaction with **L4a**.

5.5 References

- 1 G. Ferey, C. Serre, T. Devic, G. Maurin, H. Jobic, P. L. Llewellyn, G. De Weireld, A. Vimont, M. Daturi and J. S. Chang, *Chem. Soc. Rev.*, 2011, **40**, 550–562.
- 2 M. P. Suh, H. J. Park, T. K. Prasad and D. W. Lim, *Chem. Rev.*, 2011, **112**, 782–835.
- 3 Y. S. Bae, A. M. Spokoyny, O. K. Farha, R. Q. Snurr, J. T. Hupp and C. A. Mirkin, *Chem. Commun.*, 2010, **46**, 3478–3480.
- 4 P. J. Langley, J. Hulliger, R. Thaimattam and G. R. Desiraju, *New J. Chem.*, 1998, **22**, 1307–1309.
- 5 I. Castro, W. P. Barros, M. L. Calatayud, F. Lloret, N. Marino, G. De Munno, H. O. Stumpf, R. Ruiz-Garcia and M. Julve, *Coord. Chem. Rev.*, 2016, **315**, 135–152.
- 6 Y. Yoshida, K. Inoue and M. Kurmoo, *Inorg. Chem.*, 2009, **48**, 10726–10736.
- 7 Z. Duan, Y. Zhang, B. Zhang and D. Zhu, *J. Am. Chem. Soc.*, 2009, **131**, 6934–6935.
- 8 M. Cortijo, S. Herrero, R. Jimenez-Aparicio, J. Perles, J. L. Priego and J. Torroba, *Cryst. Growth Des.*, 2013, **14**, 716–722.
- 9 A. Beheshti, W. Clegg, V. Nobakht and R. W. Harrington, *Cryst. Growth Des.*, 2013, **13**, 1023–1032.
- 10 R. Wang, L. Liu, L. Lv, X. Wang, R. Chen and B. Wu, *Cryst. Growth Des.*, 2017, **17**, 3616–3624.
- 11 R. Bolligarla, B. K. Tripuramallu, V. Sreenivasulu and S. K. Das, *Indian J. Chem.*, 2011, **50**, 1410.
- 12 M. Arici, O. Z. Yesilel, M. Tas and H. Demiral, *Inorg. Chem.*, 2015, **54**, 11283–11291.
- 13 S. Roy, H. M. Titi, B. K. Tripuramallu, N. Bhunia, R. Verma and I. Goldberg, *Cryst. Growth Des.*, 2016, **16**, 2814–2825.
- 14 J. P. Zhang, Y. Y. Lin, X. C. Huang and X. M. Chen, *Dalton. Trans.*, 2005, 3681–3685.
- 15 A. Aijaz, E. C. Sanudo and P. K. Bharadwaj, *Cryst. Growth Des.*, 2011, **11**, 1122–1134.
- 16 A. Das, B. Bhattacharya, D. K. Maity, A. Halder and D. Ghoshal, *Polyhedron*, 2016, **117**, 585–591.
- 17 J. Z. Huo, X. M. Su, X. X. Wu, Y. Y. Liu and B. Ding, *CrystEngComm*, 2016, **18**, 6640–6652.
- 18 S. Kitagawa and K. Uemura, *Chem. Soc. Rev.*, 2005, **34**, 109–119.
- 19 J. Gu, Z. Gao and Y. Tang, *Cryst. Growth Des.*, 2012, **12**, 3312–3323.

-
- 20 X. M. Kang, W. M. Wang, L. H. Yao, H. X. Ren and B. Zhao, *Dalton. Trans.*, 2018, **47**, 6986–6994.
- 21 M. Roy, S. Sengupta, S. Bala, S. Bhattacharya and R. Mondal, *Cryst. Growth Des.*, 2016, **16**, 3170–3179.
- 22 Y. B. Dong, M. D. Smith, R. C. Layland and H. C. Zur Loye, *Chem. Mater.*, 2000, **12**, 1156–1161.
- 23 J. Zhou, L. Du, Y. F. Qiao, Y. Hu, B. Li, L. Li, X. Y. Wang, J. Yang, M. J. Xie and Q. H. Zhao, *Cryst. Growth Des.*, 2014, **14**, 1175–1183.
- 24 G. Mahmoudi, A. Morsali and M. Zeller, *Inorg. Chim. Acta*, 2009, **362**, 217–225.
- 25 D. Dang, Y. Zheng, Y. Bai, X. Guo, P. Ma and J. Niu, *Cryst. Growth Des.*, 2012, **12**, 3856–3867.
- 26 V. Vajpayee, S. Lee, S. H. Kim, S. C. Kang, T. R. Cook, H. Kim, D. W. Kim, S. Verma, M. S. Lah, I. S. Kim and others, *Dalton. Trans.*, 2013, **42**, 466–475.
- 27 S. Parshamoni, S. Sanda, H. S. Jena, K. Tomar and S. Konar, *Cryst. Growth Des.*, 2014, **14**, 2022–2033.
- 28 S. Dey, S. A. Iqbal and S. P. Rath, *New J. Chem.*, 2014, **38**, 1458–1470.
- 29 S. Parshamoni, J. Telangae and S. Konar, *Dalton. Trans.*, 2015, **44**, 20926–20935.
- 30 D. K. Maity, B. Bhattacharya, R. Mondal and D. Ghoshal, *CrystEngComm*, 2014, **16**, 8896–8909.
- 31 D. Singh and C. M. Nagaraja, *Cryst. Growth Des.*, 2015, **15**, 3356–3365.
- 32 Y. B. Dong, M. D. Smith and H. C. Zur Loye, *Inorg. Chem.*, 2000, **39**, 4927–4935.
- 33 L. Hashemi and A. Morsali, *J. Inorg. Organomet. Polym. Mater.*, 2010, **20**, 856–861.
- 34 B. Bhattacharya, R. Dey, P. Pachfule, R. Banerjee and D. Ghoshal, *Cryst. Growth Des.*, 2012, **13**, 731–739.
- 35 D. K. Maity, B. Bhattacharya, A. Halder and D. Ghoshal, *Dalton. Trans.*, 2015, **44**, 20999–21007.
- 36 G. M. Sheldrick, *Acta Crystallogr. Sect. A*, 2008, **64**, 112–122.
- 37 APEXZ, SADABS, SAINT, Bruker AXS inc. Madison, WI, USA, 2008.
- 38 M. D. Allendorf, C. A. Bauer, R. K. Bhakta and R. J. T. Houk, *Chem. Soc. Rev.*, 2009, **38**, 1330–1352.
- 39 F. Baig, R. Kant, V. K. Gupta and M. Sarkar, *RSC Adv.*, 2015, **5**, 51220–51232.
-

- 40 M. Das, F. Baig and M. Sarkar, *RSC Adv.*, 2016, **6**, 57780–57792.
- 41 B. Chen, Y. Yang, F. Zapata, G. Lin, G. Qian and E. B. Lobkovsky, *Adv. Mater.*, 2007, **19**, 1693–1696.
- 42 Y. Li, H. Song, Q. Chen, K. Liu, F. Y. Zhao, W. J. Ruan and Z. Chang, *J. Mater. Chem. A*, 2014, **2**, 9469–9473.
- 43 Y. Rachuri, B. Parmar, K. K. Bisht and E. Suresh, *Dalton. Trans.*, 2017, **46**, 3623–3630.

Chapter-6

Porous 3D Cd(II) Coordination Polymer of *Bis*-pyridyl-diimine and Benzene-1,3- disulfonate ligands: Iodine and Methyl Orange Adsorption Studies

Porous 3D Cd(II) Coordination Polymer of *Bis*-pyridyl-diiminie and Benzene-1,3-disulfonate Ligands: Iodine and Methyl Orange Adsorption Studies

6.1 Introduction

The science of porous materials is not only familiar for their mesmerizing architectures ranging from 1D, 2D and 3D but also for their ability of efficient interactions to show the adsorption aptitude and host-guest capability to accommodate the guest molecules to explore their potential applications. Host-guest chemistry is leading to the development of multifunctional synthetic host materials in the recent years.^[1-3] In the formation of host-guest supramolecules, the host molecules selectively capture the guest molecules through non-covalent interactions such as hydrogen bonding, ionic, van der waals and hydrophobic interactions. Multi functional CPs at higher dimensions equipped with empty channels prompted guest inclusion properties via adsorption. The presence of electron rich aromatic frame works could possibly adsorb guest molecules in the pores through non-covalent interactions. I₂ is known to be an important probe to study the host-guest interactions.

Adsorption of I₂ by various CPs was explored widely by several groups.^[4-6] Xin *et al.*^[7] reported a metal-organic framework (MOF) of Copper (I) halide in which I₂ and I⁻ together were incorporated into the channels. They studied the liberation and adsorption of I₂ in the MOF and also investigated the luminescence property of the MOF resulted by the anion exchange of I⁻ with SCN⁻. Horike *et al.*^[8] reported Fe-based porous coordination polymers (PCPs) to investigate the reduction of I₂ to I₅⁻ by the reversible redox property powered by the conversion of Fe²⁺ to Fe³⁺ and obtained electrical conductivity in the PCP. Hashemi *et al.*^[9] reported a nanoporous Pb(II) CP with **L6a**, nitrate and thiocyanate ions (**TMU-15**). They observed the I₂ adsorption by immersing the crystals of **TMU-15** into cyclohexane solution of I₂ for about 48 hours and for the controlled liberation process I₂ adsorbed **TMU-15** was immersed in ethanol. They also summarized the effect of pore size on delivery of I₂ in the Pb(II) CPs by comparing with previously reported **TMU-1** and **TMU-2**. They identified that the pore size in **TMU-15** is smaller than **TMU-1** but bigger than in **TMU-2** so the liberation of iodine from **TMU-15** is faster than from **TMU-1** but slower than from **TMU-2**.^[9] Safarifard *et al.*^[10] reported two Zn(II)

micro porous CPs of **L6a** with 1,4-benzene-dicarboxylate (**TMU-16**) and **L6a** with amino-1,4-benzene-dicarboxylate (**TMU-16-NH₂**). They performed the I₂ adsorption and desorption studies using hexane solution of I₂ for adsorption and ethanol for desorption. They also pertain the effect of free amine groups in **TMU-16-NH₂** which showed highly efficient I₂ adsorption than **TMU-16** with in 30 min. Recently Arici *et al.*^[11] reported the effect of presence of solvent molecules in the pores on the adsorption of I₂ and CO₂. They desolvated the CP but with one DMF molecule in pores for one of the CP they synthesized, and observed the I₂ and CO₂ adsorption. The CP with one DMF molecule showed adsorption of I₂ and CO₂ but the desolvated CP doesn't show the adsorption of I₂ and CO₂ due to the closed pores or flexibility of frame work with pores of smaller size which were not sufficient for adsorption.

Adsorption studies of CPs are playing a crucial role mainly in the purification of waste water from different sources of contaminations especially environmental, industrial, pharmaceutical, and radioactive waste released from nuclear plants^[12-14]. The organic dyes can be removed/degraded by adsorption, photo catalysis, and ion exchange etc. Among these, the removing dyes by adsorption method attributed most preferable path due to effectiveness, low cost, and ecofriendly technique^[15-17]. Mahata *et al.*^[18] first reported the degradation of dyes by MOFs in 2006. They reported Co, Ni and Zn MOFs with 4,4'-oxy-bis-(benzoate), and 4,4'-bipyridine ligands where all the MOFs are active towards the degradation of dye pollutants orange-G, Rhodamine-B, Remazol Brilliant Blue-R and Methylene blue. There after several groups reported the dye degradation studies using various CPs^[19-21]. Li *et al.*^[22] reported the competitive removal of dyes Methyl Orange (MO) and Rhodamine-B by photo degradation and adsorption, where degradation by chemical oxidation showed much higher removal efficiency than physical adsorption. Wang *et al.*^[23] and Zhang *et al.*^[24] reported Cd CPs and utilized the Fenton technologies where generation of sulfate radicals from persulfates resulted in the degradation of MO. Hao *et al.*^[25] reported the Zn and Cd CPs and investigated the variation of MO degradation with pH from 1-9 where highest degradation of MO was obtained at pH 3. Biradha *et al.*^[26] reported Cu(II) and Cd(II) complexes with N-pyridin-3-yl-2-[4-(pyridin-3-ylcarbamoylmethyl)phenyl]acetamide ligands in presence of different anions where the Cd(II) complex with ligand and ClO₄⁻ anions exhibits remarkable adsorption of fluorescein dianion (FSD) and methyl orange (MO). They also explored the separation of anionic dye MO from the mixture of MO and methylene blue.

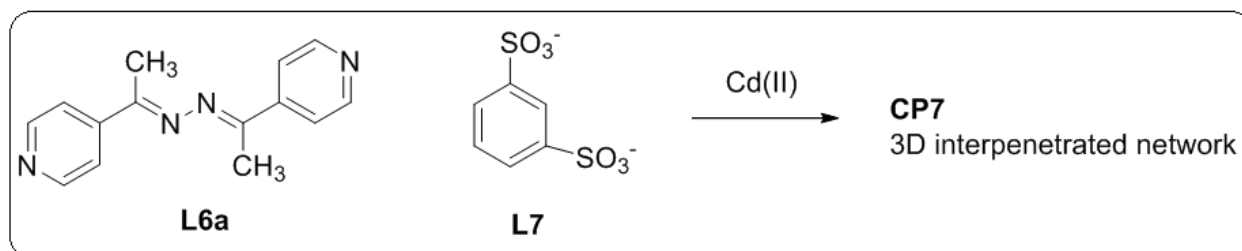
Ciurtin *et al.*^[27] in 2001 reported the mono hydrated structure of **L6a** along with its Co based CP. Since then the CPs of **L6a** were explored widely by diverse groups^[28–30]. Wang *et al.*^[31] reported the catalytic degradation of MO and MG dyes using the Ni and Co CPs of **L6a**. Ghoshal and group^[32] in 2013 synthesized the Cd(II) MOFs using **L6a** and succinate ligands that showed the selective adsorption of gases by tuning the building blocks. Later on they further reported MOFs of Mn, Fe, Co, Cu, Zn and Cd metals containing **L6a** ligands along with dicarboxylates such as glutarate, 1,3benzenedicarboxylate (1,3bdc), 1,4benzenedicarboxylate (1,3bdc), and 5-amino-1,3-benzenedicarboxylate where different sizes of dicarboxylates were used to tune the linkers and size of pores for various gas adsorption studies.^[33–35] Hao *et al.*^[36] reported Co, Ni and Cd MOFs with **L6a** and aromatic dicarboxylates. They have reported the construction of stable MOFs by means of different pillars and size of solvent molecules to control the channel size and permanent porosity.

There are several reports of CPs contained sulfonate functional ligands exhibits various application in the sensing, separation, luminescence and in catalysis etc.^[37–39] Kitagawa and group^[40] reported CPs contained free sulfonate functional groups on the pore surfaces and explored the highly proton conductivity of the CPs. Zhu *et al.*^[41] reported alkaline earth metal complexes with arene-disulfonates to determine the enrichment of coordination modes of SO_3^- functions with the introduction of hydroxyl group at ortho position to SO_3^- groups and explored the luminescence of complexes and sensing Tb(III) ions with complexes. Prats *et al.*^[42] synthesized the MOFs of alkaline earth metals, Ca, Mg, Sr and Ba with disulphonates and explored them for catalytic alkenes hydrogenation and ketones hydrosilylation activities. Horike *et al.*^[43] synthesized a porous CP with the immobilized Na ions using a bifunctional carboxylate-sulphonate based ligand and investigated the adsorption of CO_2 , acetone and benzene. Yawer *et al.*^[44] in 2014 reported the CP with benzene-1,3-disulphonate, which is the only report of CPs of benzene-1,3-disulphonate to date.

In the present work, 2,5-bis-(4-pyridyl)-3,4-diaza-2,4-hexadiene (**L6a**) and benzene-1,3-disulphonate (**L7**) is used to synthesize a CP of Cd(II), **CP7** (Scheme 6.1). The ligands selected in this work include an *exobidentate* ligand, **L6a**, which is rigid and has C=N in the spacer. Along with **L6a**, the presence of **L7**, was taken to explore the possible coordinating modes of sulphonate with metal ions. The presence of N and O atoms in the CP contributes in various intermolecular interactions to accomplish diverse applications of **C71**.

The analysis and study on **CP7** is focused on the following points:

- (i) It is well known that the dicarboxylates along with **L6a** has offered stability to the CPs, as dicarboxylates leads to the formation of metal clusters at the nodes. So the role of **L7**, which is a disulphonate, in assembling **CP7** is analyzed.
- (ii) Adsorption-desorption studies and dye degradation studies are done on **CP7** in order to analyze the effectiveness of azine pores in I₂ adsorption/dye degradation.



Scheme 6.1 Synthesis of **CP7** from **L6a** and **L7**

6.2 Experimental Section

6.2.1 General: Melting points were determined in open capillary tubes on a MPA120-Automated Melting Point apparatus. The IR spectra were recorded in FTIR ABB Bomen MB-3000. UV-visible absorption spectra were recorded in Shimadzu Spectrophotometer with model UV-2450. Elemental analysis (C, H, N, S) were performed using Elementar Vario ELIII model at SAIF-STIC Cochin. Powder X-ray diffraction (XRD) data were recorded with a Rigaku Miniflex II, $\lambda = 1.54$, Cu K α . ¹H NMR and ¹³C NMR spectra were measured on Bruker 400 MHz NMR spectrometer.

6.2.2 Single-Crystal X-ray Diffraction: The single crystal data were collected on a XtaLAB Pro: Kappa dual offset/far diffractometer. The crystal was kept at 93(2) K during data collection. Using Olex2,^[45] the structure was solved with the ShelXT^[46] structure solution program using Intrinsic Phasing and refined with the ShelXL^[47] refinement package using Least Squares minimization. The crystal structure data of **L6a** and **CP7** are summarized in table 6.1. The ORTEP of **L6a** is shown in (appendix figure A53).

Table 6.1 Crystallographic data and refinement parameters of **L6a** and **CP7**

Compound	L6a	CP7
Empirical formula	C ₁₄ H ₁₄ N ₄	C ₃₄ H ₃₂ Cd N ₈ O ₆ S ₂
Formula Wt.	238.29	825.19

Crystal system	Monoclinic	Triclinic
Space group	$P2_1/c$	$P-1$
$a/\text{\AA}$	15.144(2)	9.8572(5)
$b/\text{\AA}$	7.7696(10)	14.2441(7)
$c/\text{\AA}$	11.1165(14)	15.6512(9)
$\alpha/^\circ$	90.00	96.235(4)
$\beta/^\circ$	106.259(14)	94.357(4)
$\gamma/^\circ$	90.00	100.569(4)
$V/\text{\AA}^3$	1255.7(3)	2137.1(2)
Z	4	2
$D_{\text{calcd}}/\text{g cm}^{-3}$	1.260	1.282
T/K	93(2)	93(2)
Theta ($^\circ$) range for data used	9.742 to 49.994	10.076 to 49.998
R_{int}	0.0151	0.0968
Reflections collected	7721	26858
No. of parameters refined	165	464
Final R [With $I > 2\sigma(I)$]	$R_1 = 0.0315,$ $wR_2 = 0.0807$	$R_1 = 0.0935,$ $wR_2 = 0.2366$
GOF on F^2	1.030	1.090

6.2.3 Synthesis of 2,5-bis-(4-pyridyl)-3,4-diaza-2,4-hexadiene (L6a): L6a was synthesized according to the literature procedure.^[29] Yield: 49%, Melting point: 127 °C, IR (cm^{-1} KBr pellet): 3032 (m), 2978 (w), 2916 (w), 1612 (s), 1535 (m), 1497 (w), 1435 (w), 1404 (s), 1373 (s), 1296 (s), 1211 (w), 1057 (m), 987 (m), 825 (s), 771 (w), 671 (m), 571 (m) (Appendix figure A49). ^1H NMR (400 MHz, Chloroform-*d*): δ 8.56–8.54 (m, 4H), 7.62–7.59 (m, 4H), 2.14 (s, 6H) (Appendix figure A50). ^{13}C NMR (101 MHz, CDCl_3) δ ppm: 155.77, 150.16, 144.65, 120.53, 14.63 (Appendix figure A51). Elemental analysis Found (%): C, 69.90; H, 6.424; N, 23.92; Calculated: C, 70.57; H, 5.92; N, 23.51. Powder XRD was recorded and compared with the calculated powder XRD of L6a (Appendix figure A52).

6.2.4 Synthesis of $[\text{Cd}(\text{L6a})_2(\text{L7})]_n$, (CP7): 4 mL aqueous solution of **L7** (0.2 mmol, 0.0564 g) was mixed with 4 ml ethanolic solution of **L6a** (0.4 mmol, 0.0952 g) and stirred for 20 min. $\text{Cd}(\text{ClO}_4)_2 \cdot 6\text{H}_2\text{O}$ (0.2 mmol, 0.0838 g) was dissolved in 4 ml of ethanol and the solution was slowly layered above the solution of **L6a** and **L7**. Orange block crystals were obtained after one week. Yield 40%, IR (cm^{-1} KBr pellet): 3402 (m), 3070 (w), 1605 (s), 1543 (w), 1504 (w), 1420 (m), 1373 (w), 1296 (w), 1242 (s), 1173 (s), 1095 (m), 1065 (w), 1026 (s), 833 (m), 825 (w), 764 (w), 694 (m), 609 (s), 579 (m), 548 (m) (Appendix figure A63). Elemental analysis Found (%): C, 48.54; H, 4.01; N, 13.5; S, 6.46; Calculated: C, 49.49; H, 3.91; N, 13.58; S, 7.77. Powder XRD was recorded and compared with the calculated powder XRD of **CP7** (Appendix figure A64).

6.2.5 Iodine adsorption and desorption: The iodine adsorption study was performed using iodine solution ($0.005 \text{ mol. L}^{-1}$) in hexane. The freshly prepared crystals of **CP7** were dipped into 3 ml of the iodine solution and after time interval of 30 min., UV-visible spectra were recorded. The iodine desorption study was performed by taking the iodine adsorbed **CP7** crystals and dipping into 3 ml of pure ethanol solution, followed by recording the UV-visible spectra.

6.2.6 Dye adsorption studies: 10 mg of **CP7** was added to an aqueous solution of dye and the solution was stirred at room temperature. After some time intervals the UV-visible spectra were recorded.

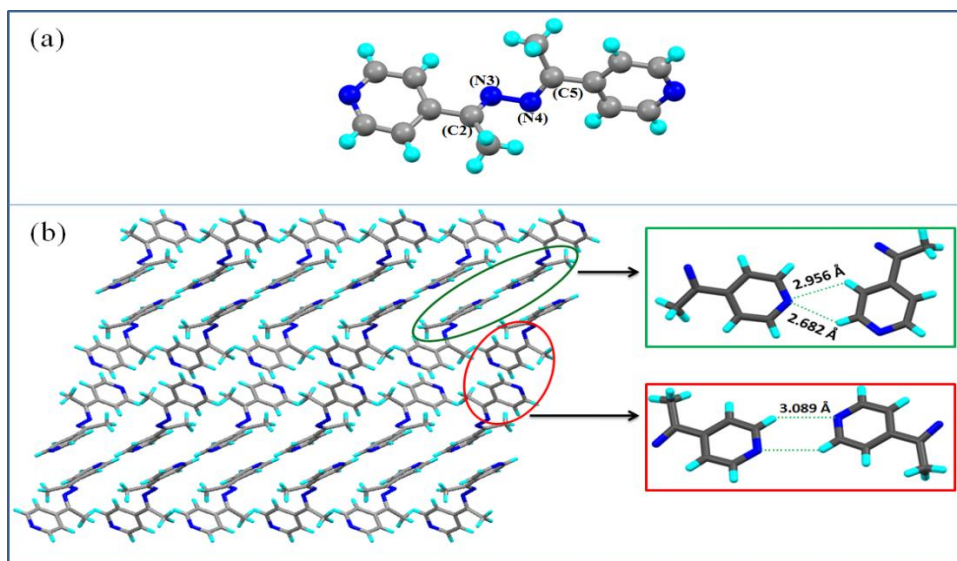


Figure 6.1: Illustration of crystal structure of **L6a**: (a) Asymmetric unit (b) arrangement of molecules along 'b' axis and $\text{CH}\cdots\text{N}$ interactions between the pyridyl rings of adjacent molecules

6.3 Results and Discussion

6.3.1 Crystal structural description of L6a: The compound **L6a** crystallizes in monoclinic $P2_1/c$ space group with one molecule present in the asymmetric unit. The pyridyl-N to pyridyl-N distance of the molecule is 11.878 Å. The C2-N3-N4-C5 torsion angle in **L6a** is 115.66° (Figure 6.1a). The two pyridyl rings of a molecule of **L6a** are tilted with an interplanar angle of 67.66°. The extended network of **L6a** shows that the molecules are held together by weak CH...N (2.682 Å, 3.388 Å, 133.22°; 2.956 Å, 3.508 Å, 119.45°; 3.089 Å, 3.871 Å, 142.78°) and CH... π interactions (Figure 6.1b).

The crystal structure of hydrated **L6a** is reported by Ciurtin *et al.*^[27] The crystal structure analysis of hydrated **L6a** showed that the asymmetric unit has half **L6a** and a water molecule (Figure 6.2a). The crystal structure of hydrated **L6a** showed that the water molecules formed strong OH...N interactions (2.108 Å, 2.861 Å, 157.02°) with that of **L6a** molecules and geometry of the molecules in hydrated **L6a** is symmetrical (Figure 6.2b). In case of **L6a** (unhydrated), due to the formation of weak CH...N interactions, the molecules are twisted and attained reduced symmetrical structure compared to hydrated **L6a** (Figure 6.1a and Figure 6.2a).

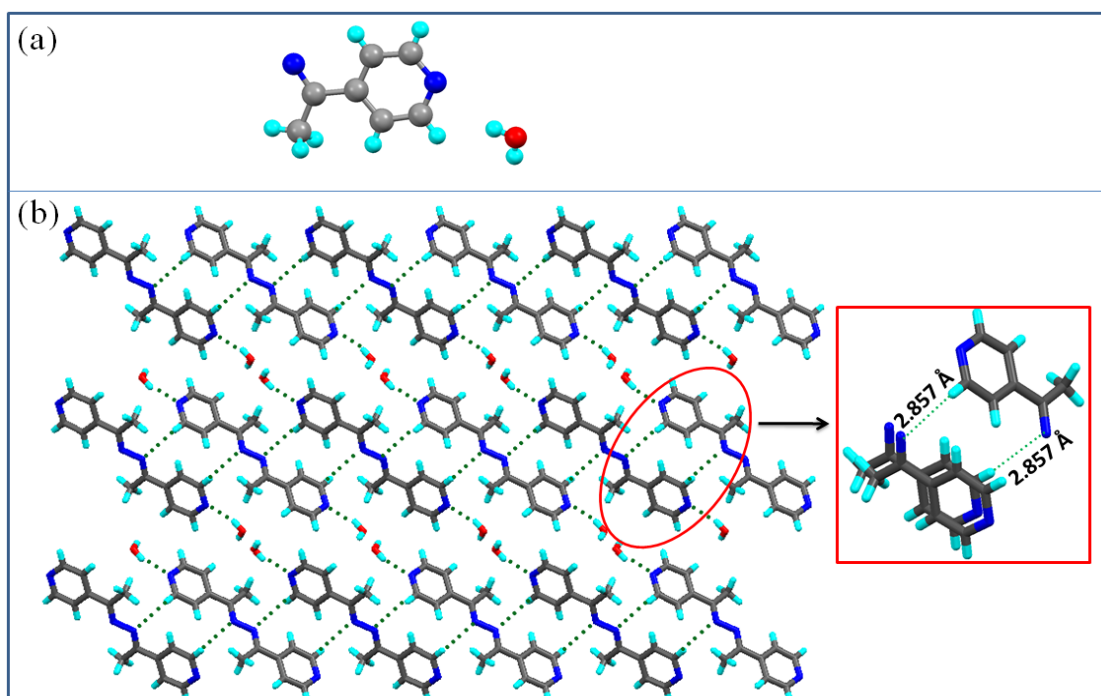


Figure 6.2: Illustration of crystal structure of hydrated **L6a**^[27]: (a) Asymmetric unit (b) arrangement of molecules along 'b' axis and CH...N interactions between adjacent **L6a** molecules (Structures generated from CCDC166626)

6.3.2 Crystal structural description of CP7: The compound **CP7** crystallizes in triclinic crystal system with $P-1$ space group. The single crystal XRD analysis reveals that in **CP7**, the asymmetric unit consists of one Cd, two **L6a** and one **L7** units (Fig. 6.3a).

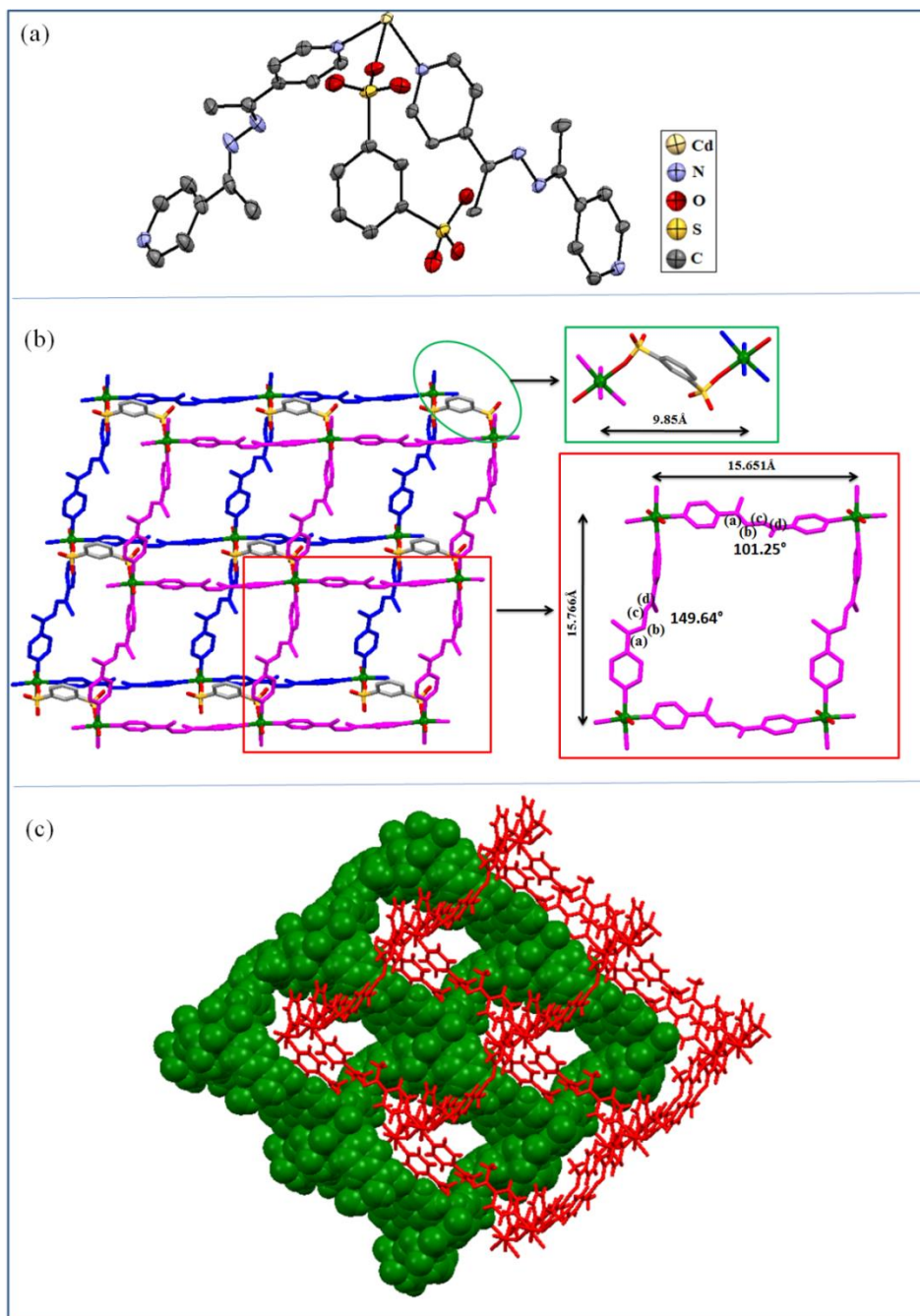


Figure 6.3: Illustration of crystal structure of **CP7**: (a) ORTEP plot exhibiting the asymmetric unit of **CP7** (b) 3D network of **CP7** (part of one network is shown; magenta and blue colors are shown of the layers of Cd-**L6a** and **L7** is joining these two layers) (c) Two interpenetrated 3D networks (Networks are shown in different colors).

The Cd center attains distorted octahedral geometry where the coordination environment around Cd satisfied by four 'N's of four different **L6a** units (Cd-N: 2.303Å, 2.306Å, 2.322Å, 2.326Å) and two 'O's of two **L7** units (Cd-O: 2.286Å, 2.294Å). Two different types of **L6a** molecules participated in **CP7** formation. The two types of **L6a** molecules in **CP7** have different geometries which include different C2-N3-N4-C5 torsion angle leading to difference in their end-to-end coordination length (Figure 6.3b). **L6a** molecules with Cd (II) metals formed 2D layers which are linked by **L7** molecules and resulted in extending the network into 3D (Figure 6.3b). Two such 3D networks interpenetrate and resulting in small pores within **CP7** (Figure 6.3c).

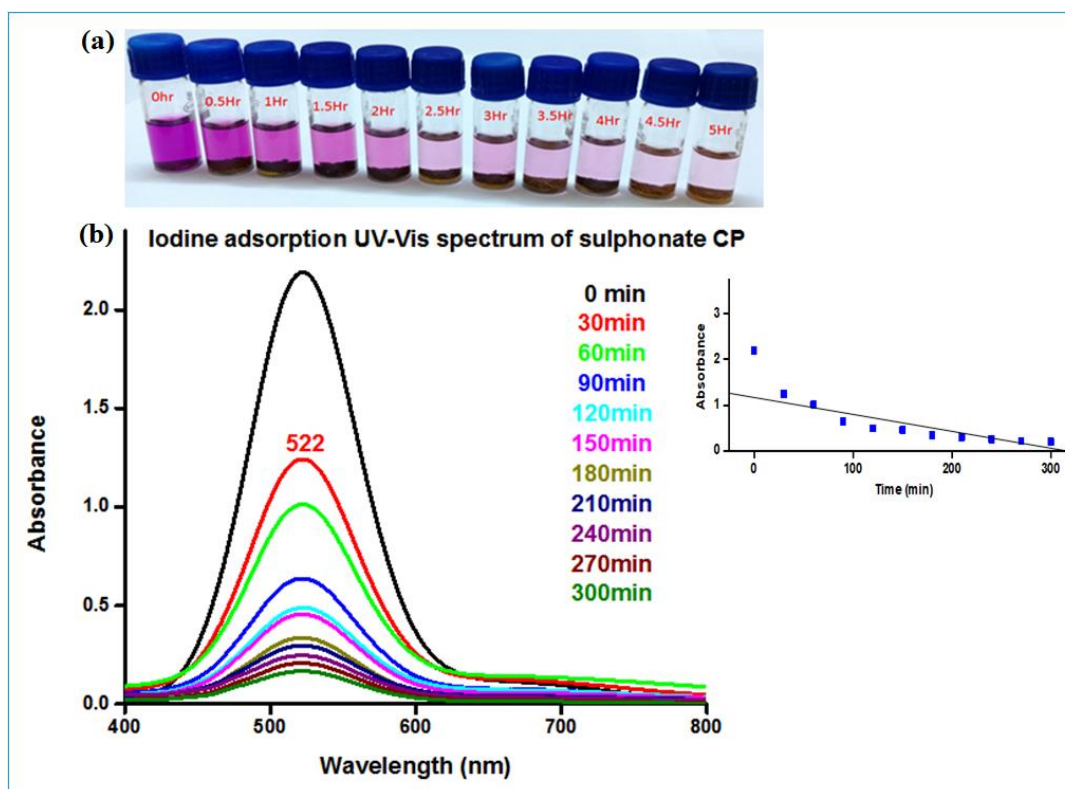


Figure 6.4: (a) Photograph showing the gradual change in color of solution when 100 mg of **CP7** dipped in hexane solution of iodine ($0.005 \text{ mol. L}^{-1}$), (b) The UV-visible spectra of the iodine solution at different time intervals

6.3.3 Adsorption and Desorption of Iodine in CP7: To study the iodine adsorption in **CP7**, a freshly prepared sample of **CP7** (100 mg) was dipped into 3 ml of hexane solution of Iodine ($0.005 \text{ mol. L}^{-1}$) and the UV-visible spectra of the solution was monitored at regular time interval of 30 min. for about five hours (Figure 6.4). A peak at 522 nm (corresponding to I_2) was

observed at the start of the experiment (0 min.) and it was observed that the intensity of the peak decreased continuously with time. The decrease in the intensity is proportional to the concentration of the iodine adsorbed on **CP7**. The color of the crystals **CP7** turned to dark brown and the dark pink color of the hexane solution of iodine faded (Figure 6.4). The solid state UV-visible spectrum of **CP7** also shows the appearance of shoulder peak ~ 500 nm.

The desorption of iodine from **CP7** was performed by dipping the adsorbed crystals of **CP7** in ethanol at room temperature and the liberation process was recorded using UV-visible spectroscopy. The UV-visible spectrum of the ethanol solution showed appearance of peaks at absorption maxima ~ 220 nm and 270 nm. The intensity of the peaks increased gradually with time (Figure 6.5). The intensity of the absorption band at 220 nm is due to the presence of I_2 and the absorption band at 270 nm is due to I_3^- ions.

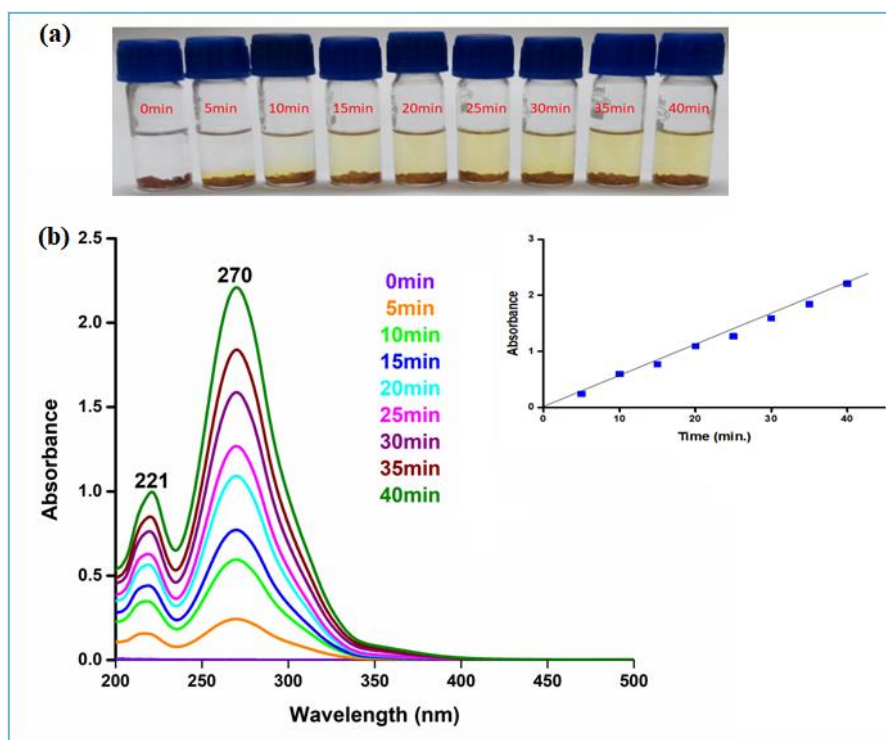


Figure 6.5: (a) Photograph showing the gradual change in color of solution when iodine adsorbed **CP7** crystals were dipped in ethanol, (b) UV-visible spectra of the ethanol solution at different time intervals.

The Thermal Gravimetric Analysis (TGA) was performed in **CP7**, **CP7** after I_2 adsorption (**CP7_Adsorbed**) and **CP7** after desorption of iodine (**CP7_Desorbed**). The TGA of **CP7**

showed that the network was stable up about 250 °C as it an interpenetrated 3D network and above 250 °C, the weight loss was continuous with the decomposition of ligands. In **CP7_Adsorbed**, about 14% of weight loss within 100 °C-230 °C may be accounted for the removal of iodine from the network and beyond that subsequent decomposition of ligands takes place.

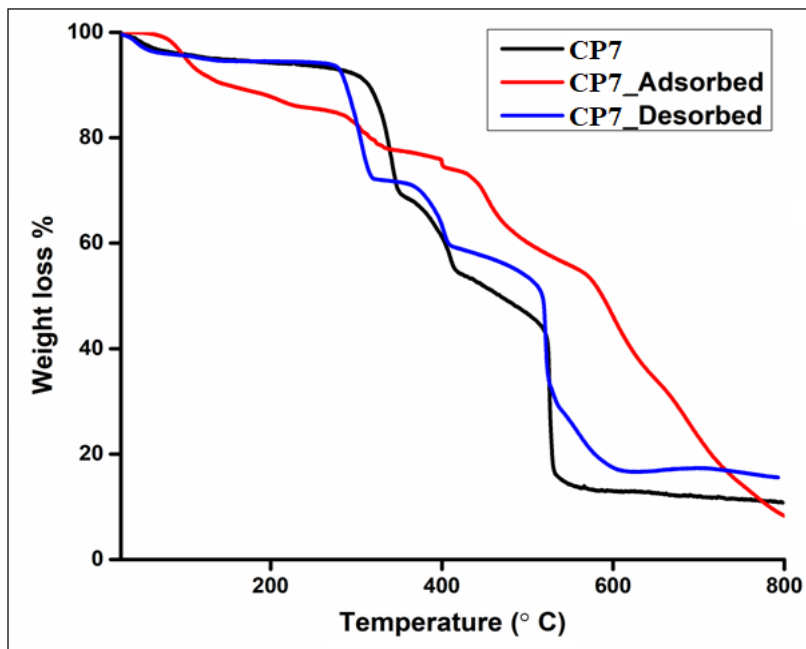


Figure 6.6: Thermo-gravimetric analysis of CP7, CP7_Adsorbed and CP7_Desorbed

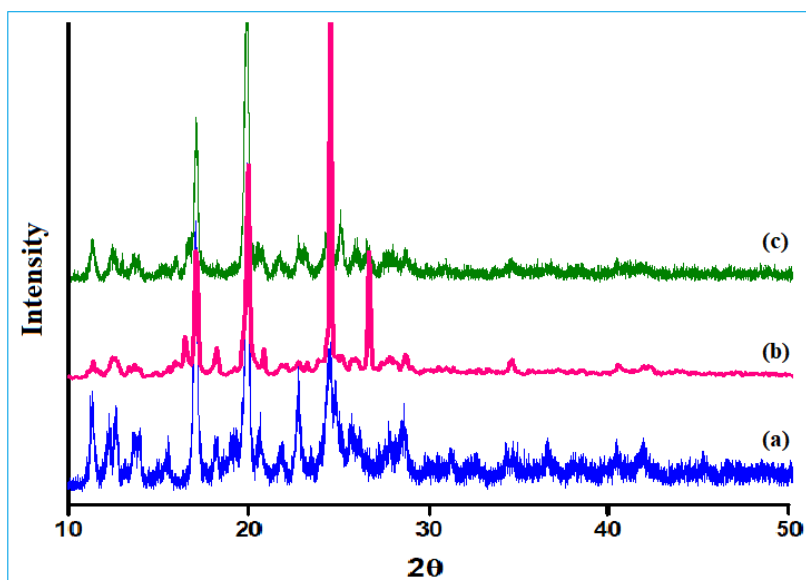


Figure 6.7: Powder XRD of (a) CP7, (b) CP7_Adsorbed and (c) CP7_Desorbed

The TGA of **CP7_Desorbed** is similar to that of **CP7** (Figure 6.6). The powder XRD of **CP7**, **CP7_Adsorbed** and **CP7_Desorbed** were recorded (Figure 6.7). The powder XRD pattern of **CP7** matches with that of the calculated powder XRD, which verifies the phase purity of **CP7**. Adsorption of iodine in **CP7** has resulted in changes in the intensity of some peaks but overall pattern is same as that of **CP7**. The desorption of iodine from **CP7** has also not affected the powder XRD pattern. These results indicate that the adsorption and desorption of iodine from **CP7** has not resulted in structural changes or any other disintegration of network of **CP7**.

6.3.4 Adsorption and separation of Dyes by CP7: The dye adsorption studies of **CP7** for Methyl Orange (MO), Methylene Blue (MB), Malachite Green (MG) and Rhodamine-B (RB) were performed. **CP7** exhibited high selectivity towards the adsorption of MO.

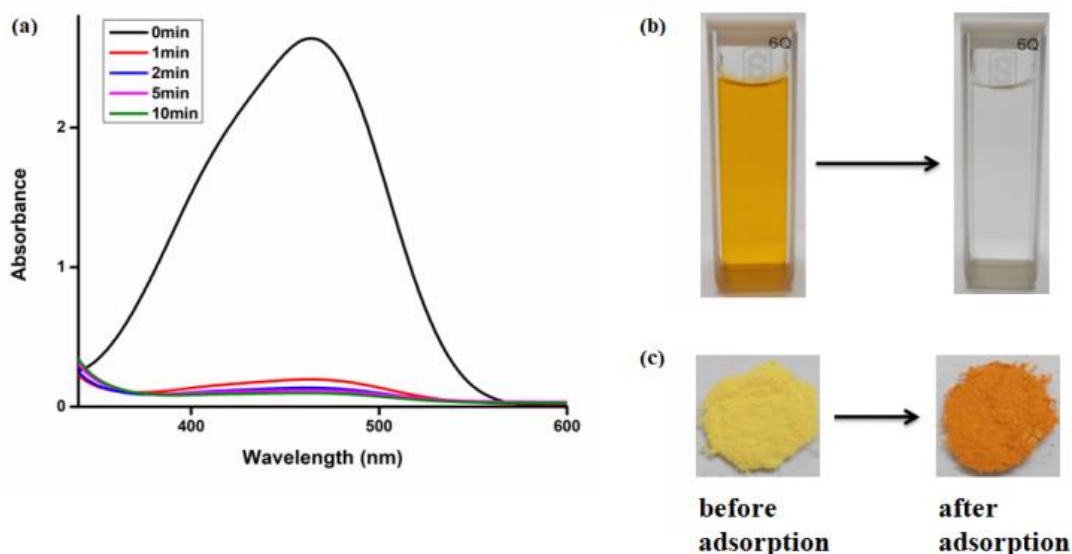


Figure 6.8: (a) UV-visible spectra of an aqueous solution of 5×10^{-4} M of MO in presence of **CP7** at regular time interval (b) Color change in aqueous solution due to dye adsorption by **CP7** (c) **CP7** before and after dye adsorption

In the dye adsorption experiment, 10 mg of **CP7** was stirred in aqueous solution of a dye (MO (5×10^{-4} M), MB (10^{-4} M), MG (10^{-5} M) and RB (2×10^{-5} M)) for about 30 min. and UV-visible spectra of the solution was recorded at regular intervals (Figure 6.8-6.9). In case of MO, the orange color of the solution faded within a very short period of time (Figure 6.8b). The UV-visible spectra showed that the concentration of MO was rapidly decreased by 96% (Figure 6.8a). The color of **CP7** also changed from yellow to orange during adsorption indicating the

presence of MO in **CP7** (Figure 6.8c). Apart from MO, the other dyes, MB, MG and RB, didn't get adsorbed in **CP7**. The UV-visible spectra of their solution showed negligible decrease in adsorption maxima over a period of time (Figure 6.9).

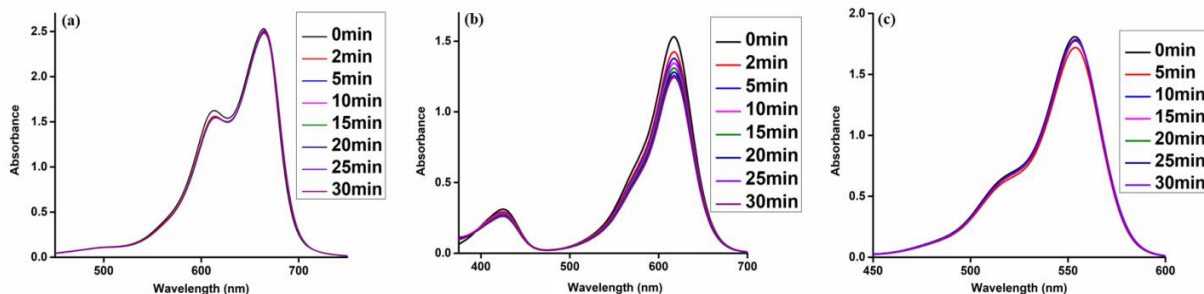


Figure 6.9: UV-visible spectra of dye degradation by **CP7** from aqueous solutions of (a) 5×10^{-4} M MB, (b) 10^{-5} M MG, and (c) 2×10^{-5} M RB

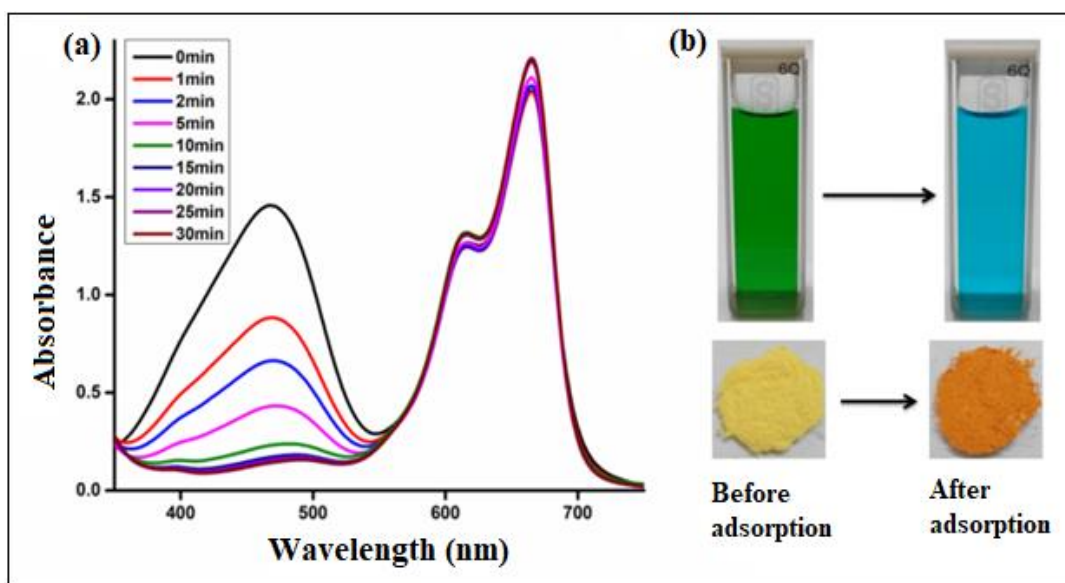


Figure 6.10: UV-visible spectra of aqueous solution contain a mixture of 5×10^{-4} M of MO and 10^{-4} M of MB. (b) Change in color of solution and in solid **CP7** before and after adsorption.

The mixture separation of MO and MB was also performed in which the green colored aqueous mixture of MO and MB was stirred for about 30 min. MO was efficiently scavenged by **CP7** while the blue colored MB retained in the solution (Figure 6.10). The selectivity of **CP7** in adsorbing MO over the other dye may be ascribed to the chemical nature and size of the dyes. In **CP7**, the interpenetrated networks will not allow the adsorption of very large organic molecules.

The presence of azo and SO₃ functionality in MO along with a linear, flexible geometry is leading to its effective adsorption by **CP7**. The other dye molecules have rigid structures thereby couldn't get adsorbed on **CP7** (Figure 6.10).

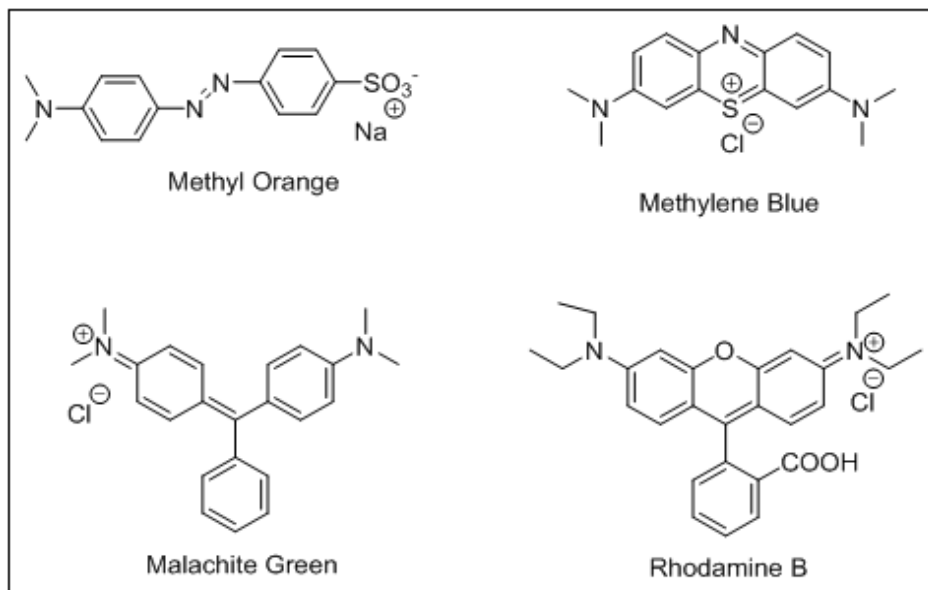


Figure 6.11: Structural formula of the dyes used for adsorption studies of **CP7**

6.4 Conclusion

The reaction of Cd(II) with an exo bidentate Schiff Base ligand, 2,5-*bis*-(4-pyridyl)-3,4-diaza-2,4-hexadiene (**L6a**) and benzene-1,3-disulphonate (**L7**) resulted in a 3D interpenetrated coordination polymer **CP7**. The single crystal structures of **L6a** and previously reported hydrated **L6a** were studied to understand the effect of presence of H₂O molecules on the geometry of the ligand. The 3D interpenetrated structure of **CP7** resulted in small pores which were capable of incorporating small guest molecules. The adsorption and desorption of iodine in **CP7** showed that the porous nature and the presence of hetero atoms in the polymer resulted in successful adsorption of iodine. Further the chemical nature and size of the pores in **CP7** were the important features in providing selectivity in the organic dye adsorption.

6.5 References

- 1 T. K. Maji, K. Uemura, H. C. Chang, R. Matsuda and S. Kitagawa, *Angew. Chem. Int. Ed.*, 2004, **116**, 3331–3334.
- 2 K. Biradha and M. Fujita, *Angew. Chem. Int. Ed.*, 2004, 2002, **114**, 3542–3545.

- 3 M. H. Zeng, Q. X. Wang, Y. X. Tan, S. Hu, H. X. Zhao, L. S. Long and M. Kurmoo, *J. Am. Chem. Soc.*, 2010, **132**, 2561–2563.
- 4 P. Cui, L. Ren, Z. Chen, H. Hu, B. Zhao, W. Shi and P. Cheng, *Inorg. Chem.*, 2012, **51**, 2303–2310.
- 5 G. Mukherjee and K. Biradha, *Cryst. Growth Des.*, 2014, **14**, 3696–3699.
- 6 Y. Rachuri, K. K. Bisht, B. Parmar and E. Suresh, *J. Solid State Chem.*, 2015, **223**, 23–31.
- 7 B. Xin, G. Zeng, L. Gao, Y. Li, S. Xing, J. Hua, G. Li, Z. Shi and S. Feng, *Dalton. Trans.*, 2013, **42**, 7562–7568.
- 8 S. Horike, M. Sugimoto, K. Kongpatpanich, Y. Hijikata, M. Inukai, D. Umeyama, S. Kitao, M. Seto and S. Kitagawa, *J. Mater. Chem. A*, 2013, **1**, 3675–3679.
- 9 L. Hashemi and A. Morsali, *CrystEngComm*, 2014, **16**, 4955–4958.
- 10 V. Safarifard and A. Morsali, *CrystEngComm*, 2014, **16**, 8660–8663.
- 11 M. Arici, O. Z. Yesilel, M. Tas and H. Demiral, *Inorg. Chem.*, 2015, **54**, 11283–11291.
- 12 C. A. Martinez-Huitle, M. A. Rodrigo, I. Sires and O. Scialdone, *Chem. Rev.*, 2015, **115**, 13362–13407.
- 13 C. Gadipelly, A. Perez-Gonzalez, G. D. Yadav, I. Ortiz, R. Ibanez, V. K. Rathod and K. V. Marathe, *Ind. Eng. Chem. Res.*, 2014, **53**, 11571–11592.
- 14 N. Saha, M. S. Rahman, M. B. Ahmed, J. L. Zhou, H. H. Ngo and W. Guo, *J. Environ. Manage.*, 2017, **185**, 70–78.
- 15 A. X. Yan, S. Yao, Y. G. Li, Z. M. Zhang, Y. Lu, W. L. Chen and E. B. Wang, *Chem. Eur. J.*, 2014, **20**, 6927–6933.
- 16 P. Y. Du, H. Li, X. Fu, W. Gu and X. Liu, *Dalton. Trans.*, 2015, **44**, 13752–13759.
- 17 Y. Y. Jia, G. J. Ren, A. L. Li, L. Z. Zhang, R. Feng, Y. H. Zhang and X. H. Bu, *Cryst. Growth Des.*, 2016, **16**, 5593–5597.
- 18 P. Mahata, G. Madras and S. Natarajan, *J. Phys. Chem. B*, 2006, **110**, 13759–13768.
- 19 L. L. Wen, F. Wang, J. Feng, K. L. Lv, C. G. Wang and D. F. Li, *Cryst. Growth Des.*, 2009, **9**, 3581–3589.
- 20 T. Wen, D. X. Zhang, J. Liu, R. Lin and J. Zhang, *Chem. Commun.*, 2013, **49**, 5660–5662.
- 21 X. Wang, F. Sui, H. Lin, J. Zhang and G. Liu, *Cryst. Growth Des.*, 2014, **14**, 3438–3452.
- 22 H. Li, Q. Li, Y. He, Z. Xu and Q. Tang, *New J. Chem.*, 2017, **41**, 15204–15209.
- 23 X. Wang, M. Zhang, B. Yu, K. Van Hecke and G. Cui, *Spectrochim. Acta Part A*, 2015,

- 139, 442–448.
- 24 X. Zhang, Y. G. Liu, Z. C. Hao and G. H. Cui, *J. Inorg. Organomet. Polym. Mater.*, 2017, **27**, 37–45.
- 25 J. Hao, B. Yu, K. Van Hecke and G. Cui, *CrystEngComm*, 2015, **17**, 2279–2293.
- 26 K. Maity and K. Biradha, *Cryst. Growth Des.*, 2016, **16**, 3002–3013.
- 27 D. M. Ciurtin, Y. B. Dong, M. D. Smith, T. Barclay and H. C. Zur Loye, *Inorg. Chem.*, 2001, **40**, 2825–2834.
- 28 A. Mukherjee, R. Chakrabarty and G. K. Patra, *Inorg. Chem. Commun.*, 2009, **12**, 1227–1230.
- 29 A. R. Kennedy, K. G. Brown, D. Graham, J. B. Kirkhouse, M. Kittner, C. Major, C. J. McHugh, P. Murdoch and W. E. Smith, *New J. Chem.*, 2005, **29**, 826–832.
- 30 T. M. Ross, S. M. Neville, D. S. Innes, D. R. Turner, B. Moubaraki and K. S. Murray, *Dalton. Trans.*, 2010, **39**, 149–159.
- 31 X. Wang, H. Xu, Y. Han, Y. Li, C. Sheng, Z. Xu, J. Xu and M. Wang, *Inorg. Chim. Acta*, 2017, **461**, 15–20.
- 32 B. Bhattacharya, R. Dey, P. Pachfule, R. Banerjee and D. Ghoshal, *Cryst. Growth Des.*, 2012, **13**, 731–739.
- 33 B. Bhattacharya, R. Haldar, R. Dey, T. K. Maji and D. Ghoshal, *Dalton. Trans.*, 2014, **43**, 2272–2282.
- 34 B. Bhattacharya, R. Haldar, D. K. Maity, T. K. Maji and D. Ghoshal, *CrystEngComm*, 2015, **17**, 3478–3486.
- 35 B. Bhattacharya, D. K. Maity, R. Mondal, E. Colacio and D. Ghoshal, *Cryst. Growth Des.*, 2015, **15**, 4427–4437.
- 36 X. R. Hao, G. Yang, K. Z. Shao, Z. M. Su, G. Yuan and X. L. Wang, *J. Solid State Chem.*, 2013, **198**, 143–148.
- 37 Z. J. Li, J. Yao, Q. Tao, L. Jiang and T. B. Lu, *Inorg. Chem.*, 2013, **52**, 11694–11696.
- 38 N. Singh, U. P. Singh and R. J. Butcher, *CrystEngComm*, 2017, **19**, 7009–7020.
- 39 G. Zhang, G. Wei, Z. Liu, S. R. J. Oliver and H. Fei, *Chem. Mater.*, 2016, **28**, 6276–6281.
- 40 P. Ramaswamy, R. Matsuda, W. Kosaka, G. Akiyama, H. J. Jeon and S. Kitagawa, *Chem. Commun.*, 2014, **50**, 1144–1146.
- 41 Z. B. Zhu, W. Wan, Z. P. Deng, Z. Y. Ge, L. H. Huo, H. Zhao and S. Gao,

- CrystEngComm*, 2012, **14**, 6675–6688.
- 42 A. E. Platero-Prats, M. Iglesias, N. Snejko, A. Monge and E. Gutierrez-Puebla, *Cryst. Growth Des.*, 2011, **11**, 1750–1758.
- 43 S. Horike, R. Matsuda, D. Tanaka, M. Mizuno, K. Endo and S. Kitagawa, *J. Am. Chem. Soc.*, 2006, **128**, 4222–4223.
- 44 M. Yawer, S. Sharma, M. Kariem and H. N. Sheikh, *J. Inorg. Organomet. Polym. Mater.*, 2014, **24**, 1077–1085.
- 45 O. V Dolomanov, L. J. Bourhis, R. J. Gildea, J. A. K. Howard and H. Puschmann, *J. Appl. Crystallogr.*, 2009, **42**, 339–341.
- 46 G. M. Sheldrick, *Acta Crystallogr. Sect. A*, 2015, **71**, 3–8.
- 47 G. M. Sheldrick, *Acta Crystallogr. Sect. C*, 2015, **71**, 3–8.

Chapter-7

Rationalization of Results and Conclusions

Rationalization of Results and Conclusions

7.1 Influence of non-covalent interactions to enhance emission of ligands **L2b-L6d**

The work presented in chapter-3 analyzed the photoluminescence properties of a series of 18 *bis*-pyridyl-diimine Schiff base compounds equipped with alkyl group in the spacer and explained the enhanced emission in the solid state of the compounds. The alkyl spacer of the compounds included ethyl, butyl and hexyl chains whose flexibility due to the attainment of varied (*anti* or *gauche*), conformations and resulted in the formation of linear or non-linear geometry of the molecules. The compounds **L1a** and **L2a** contain continuous conjugation throughout the molecule but were not exhibiting luminescence property due to the excimer formation in the solid state. The compounds **L2b**, **L5c**, **L5d**, **L6c** and **L6d** exhibits all *anti* conformations in the alkyl spacer which provided planarity to the molecules. The arrangement of these molecules shows the formation of J-aggregates and enhances of luminescence in the solid state. The compounds **L1c** and **L3c** contain butyl chain in the spacer, which adopted *gauche-anti-gauche* conformation and resulted in non-linear geometry. Though the structure of **L1c** and **L3c** are non-linear, these molecules also exhibit considerable luminescence in the solid state. The modified photoluminescence property of these compounds in the solid state is described by analyzing their crystal structures. The packing of the molecules of **L1c** and **L3c** in the solid state resulted in the formation of non-covalent bonded chromophoric dimers and hence led to enhanced emissions. In this chapter the photoluminescence of the compounds were compared using their crystal structure analysis.

7.2 Construction of Zn(II) coordination polymers with single ligand system: Effect of change in coordination site on the structure, their anion exchange and adsorption studies

Chapter 4 discusses the structures of 1D Zn(II)coordination polymers **CP1**, **CP2** and **CP3** constructed by change in the position of the nitrogen in the pyridyl group of ligands **L3a**, **L4a** and **L6a**, which resulted in shifting in the coordinating atom of the ligand. The effect of *exo*-bidentate rigid geometry of the ligands, **L3a**, **L4a** and **L6a**, and tetrahedral coordination preference of Zn(II) resulted in 1D zigzag networks in the CPs (**CP1**, **CP2** and **CP3**) with ZnI₂.

The structural features, geometry of ligands and non-covalent interactions were explained by the crystal packing of CPs. Effect of counter anion exchange on structures of CPs were studied by performing anion exchange reactions of CPs **CP1**, **CP2** and **CP3** with Cl^- , SCN^- , N_3^- and CO_3^{2-} anions. Changes in structural features of the CPs (**CP1**, **CP2** and **CP3**) were observed on anion exchange of I^- counter ions with SCN^- , N_3^- and CO_3^{2-} while the anion exchange with Cl^- resulted in similar geometry. The CPs resulted after the anion exchange of CPs (**CP1**, **CP2** and **CP3**) with SCN^- , N_3^- and CO_3^{2-} were analyzed with powder XRD. The anion exchange described the modifications in the structural features based on geometry and coordinating ability of anions used in the exchange process. In chapter 4, along with anion exchange studies, the adsorption of organic dye methyl orange with **CP3** was also explained.

7.3 Effect of reaction conditions on the structural features of coordination polymers

Chapter 5 describes the CPs (**CP4**, **CP5** and **CP6**) synthesized using Cd(II) and 2,5-bis-(3-pyridyl)-3,4-diaza-2,4-hexadiene (**L4a**) in presence of sodium succinate. The geometry of the CPs was dependent on the reaction conditions involved during the synthesis. **CP4** is a 2D structure where **CP5** and **CP6** are 3D structures with different topologies. The structural differences were elucidated by comparing their crystal structure. Analysis of the **IDCP** of ligand **L4a** with $\text{Cd}(\text{ClO}_4)_2$ and series of controlled experiments resulted in identifying the path of assembling the CPs **CP5** and **CP6**. The observation of these experiments suggested that the stepwise reaction of **L4a** and $\text{Cd}(\text{ClO}_4)_2$, followed by the reaction with succinate generates **CP5**, while on changing the reaction sequence, wherein first step involves the reaction of succinate and $\text{Cd}(\text{ClO}_4)_2$, followed by the reaction with **L4a** resulted **CP6**. The observation of chapter 5 also suggested the **CP4**, to be a kinetically controlled compound.

7.4 3D interpenetrated coordination network of Cd(II) with bis-pyridyl-diimine and disulfonate ligands and its adsorption studies

The work in chapter 6 discussed about the structural aspects of interpenetrated 3D coordination polymer (**CP7**) of Cd(II) with **L6a** and benzene-1,3-disulfonate ligands. The adsorption and desorption studies of iodine with respect to time is analyzed using **CP7**. The adsorption study reveals the presence and importance of channels in the CP to accommodate the guest molecules and the presence of functional walls of the channels provides a direction about the mechanism of

the adsorption process. Along with **CP7**, the crystal structure of **L6a** and its structural features were compared with the previously reported hydrated **L6a**. Further the organic dye, methyl orange (MO) adsorption from water was also examined by the adsorption process of **CP7**. The presence of significant functional linkers and the intermolecular non-covalent interactions drive the selective MO adsorption by **CP7**. The properties and applications of **CP7** provide an understanding of structure property relationship.

7.5 Future Scope of present work

- ❖ Coordination Polymers of *bis*-pyridyl-diimine ligands with alkyl spacers can be explored. The present thesis work discusses the photophysical properties and CPs of *bis*-pyridyl-alkyl-diimine ligands. The flexibility of the ligands can be utilized in generating new networks and to explore interesting applications.
- ❖ Novel coordination polymers and metal organic frameworks (MOF) of *bis*-pyridyl-diimine along with dicarboxylates and disulfonates can be synthesized. The use of dicarboxylates and disulfonates may result in metal clusters along with higher dimensionality networks. The CPs of protonated sulfonates can be further exploited in proton conduction application.
- ❖ The present thesis work discusses the photophysical properties and CPs of *bis*-pyridyl-alkyl-diimine ligands. Tridentate and tetradentate ligands of pyridyl based Schiff base can be explored for enhanced photophysical properties. These ligands can also be utilized in synthesizing higher dimensional CPs.
- ❖ In the present thesis, CPs of Zn(II) and Cd(II) resulted in crystalline materials and hence their structural features were studied. CPs with transition metals such as Co(II), Ni(II), Cu(II), Ag(II), Hg(II) etc. and lanthanides and actinides can also be prepared by performing various techniques to obtain good quality crystals. As lanthanides exhibit multi coordination ability and interesting luminescence properties it can explore interesting higher dimensional architectures with functional channels and photoluminescence applications.
- ❖ After synthesizing various CPs applications in gas storage, separation, sensing, catalysis, luminescence, host-guest chemistry, semiconductors, photovoltaic cells etc. can be explored.

Appendices

Appendix Figures

Figure A1: IR Spectra of ligand **L1c**

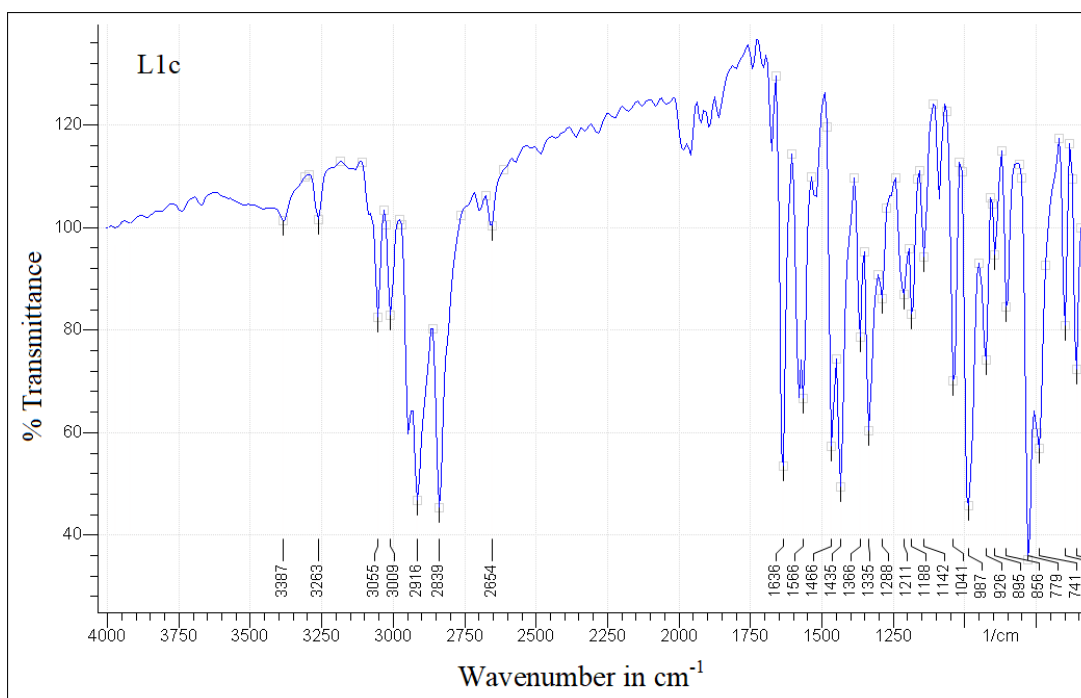


Figure A2: ^1H NMR Spectra of ligand **L1c**

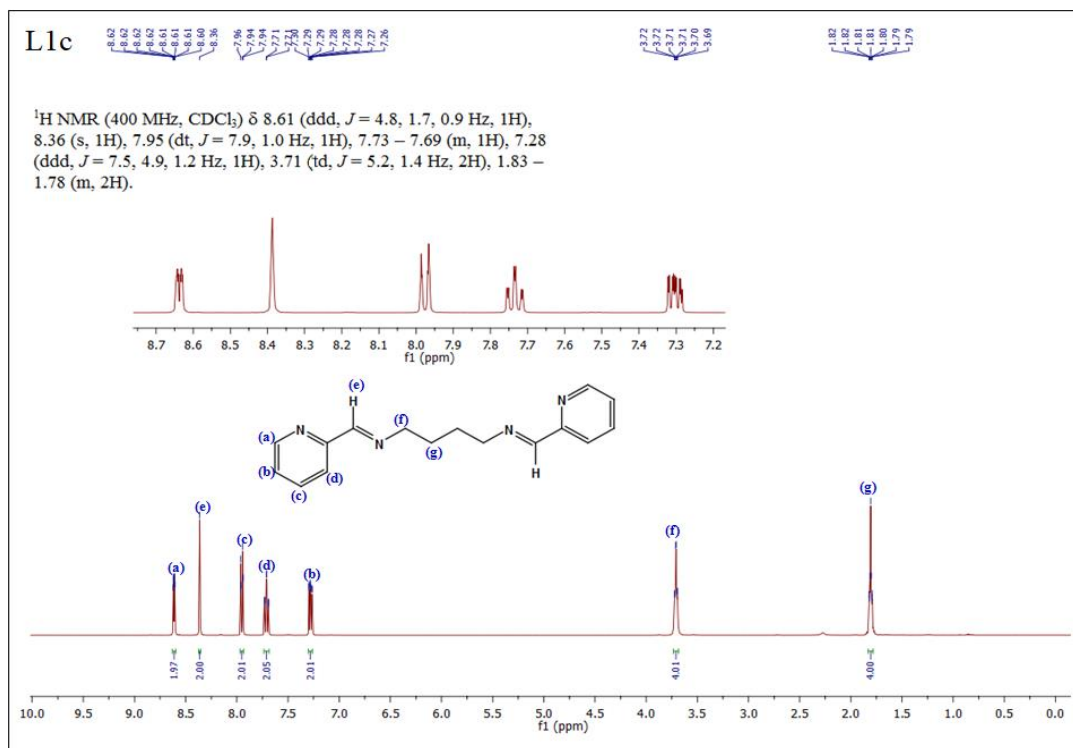


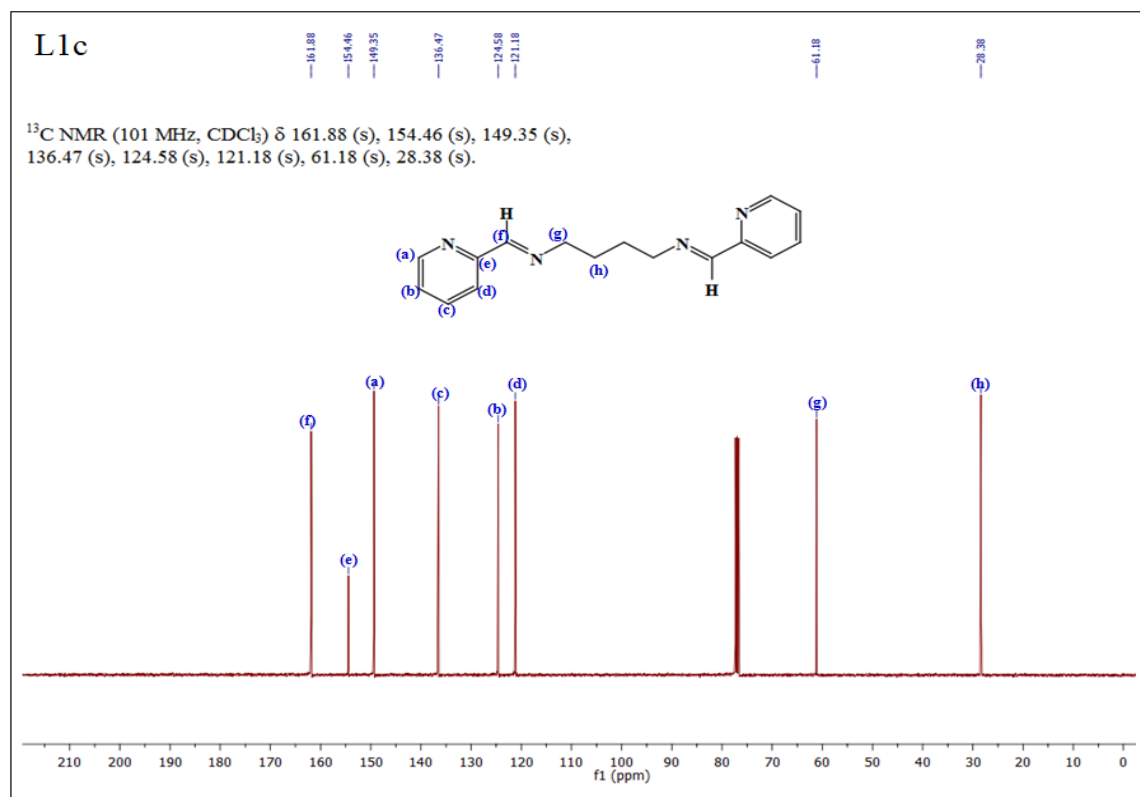
Figure A3: ^{13}C NMR Spectra of ligand L1c

Figure A4: IR Spectra of ligand L2a

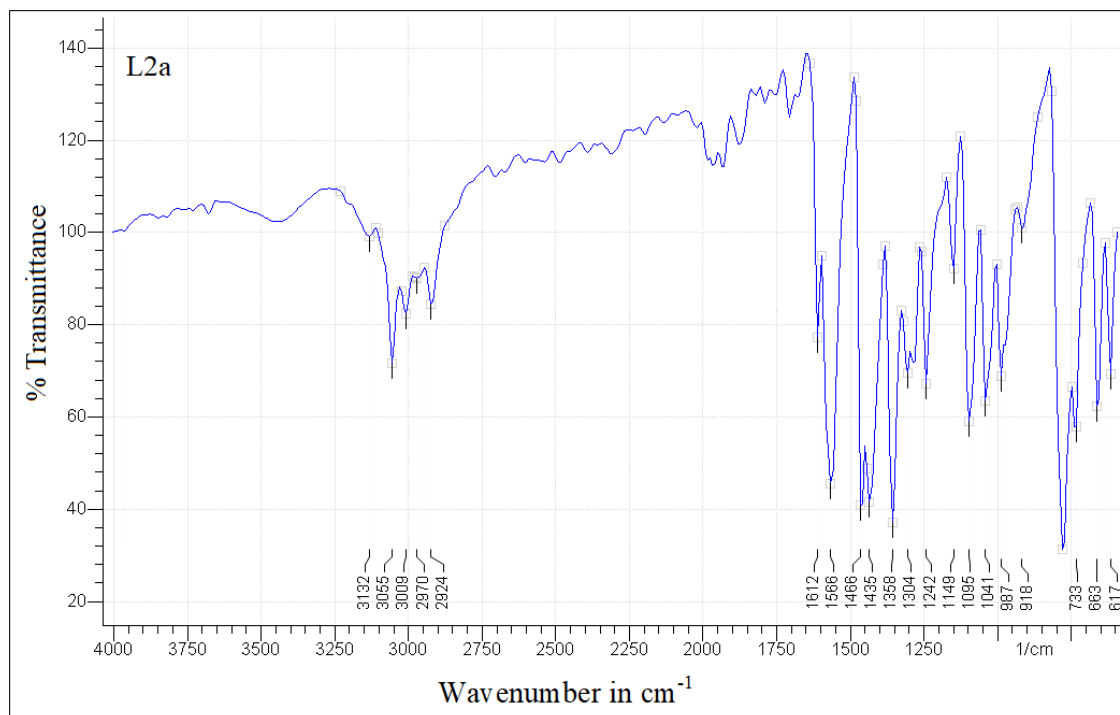


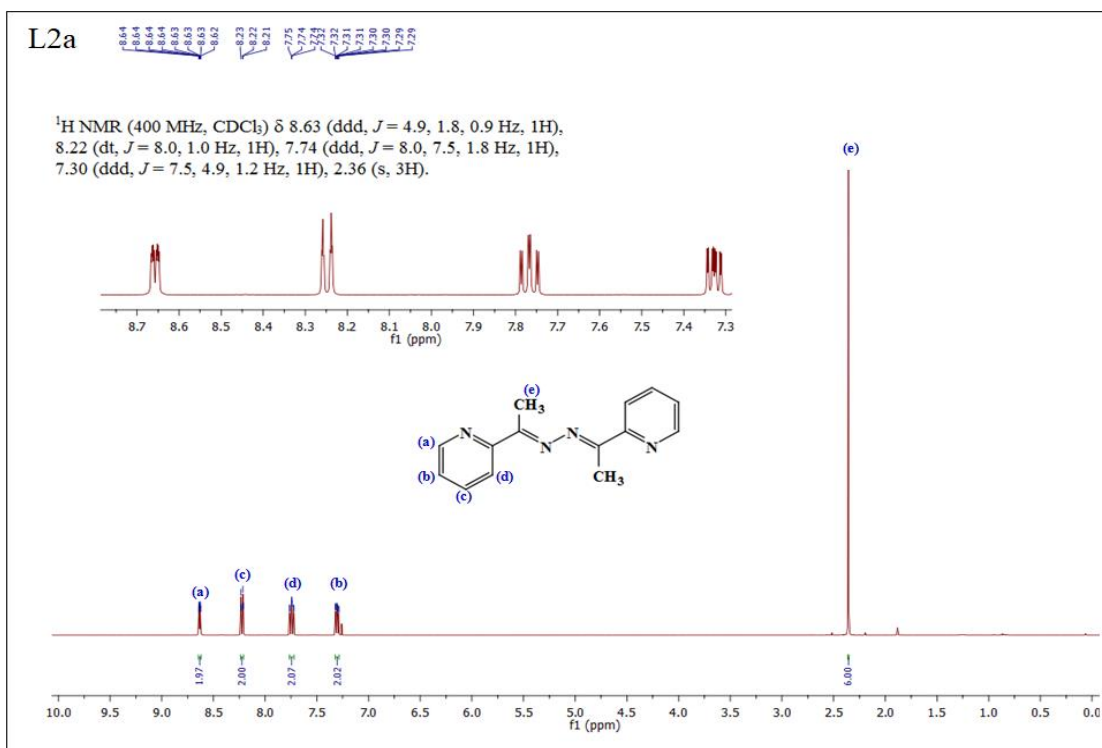
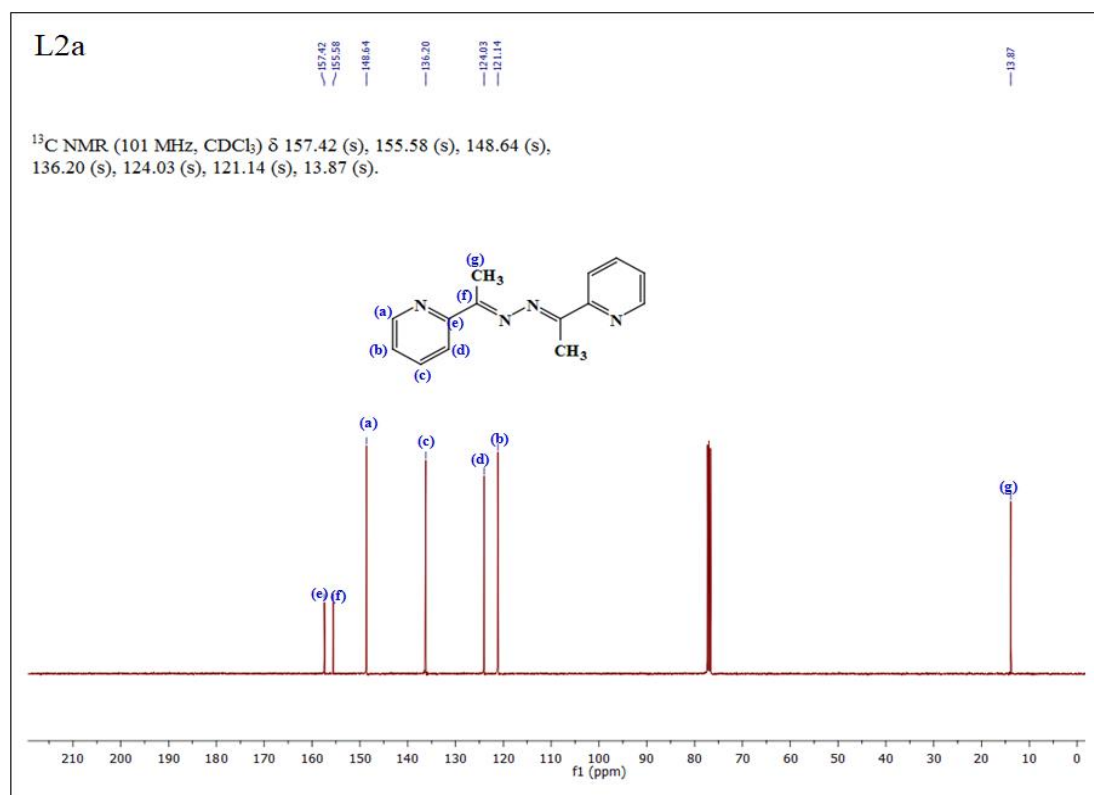
Figure A5: ^1H NMR Spectra of ligand **L2a**Figure A6: ^{13}C NMR Spectra of ligand **L2a**

Figure A7: IR Spectra of ligand **L2b**

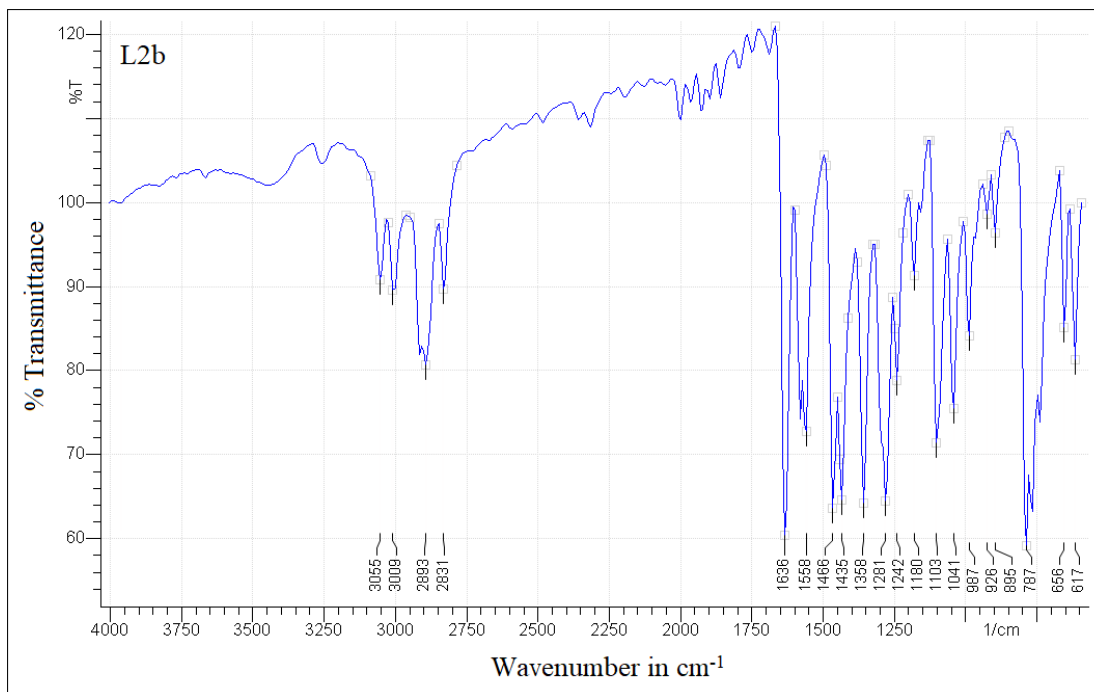


Figure A8: ^1H NMR Spectra of ligand **L2b**

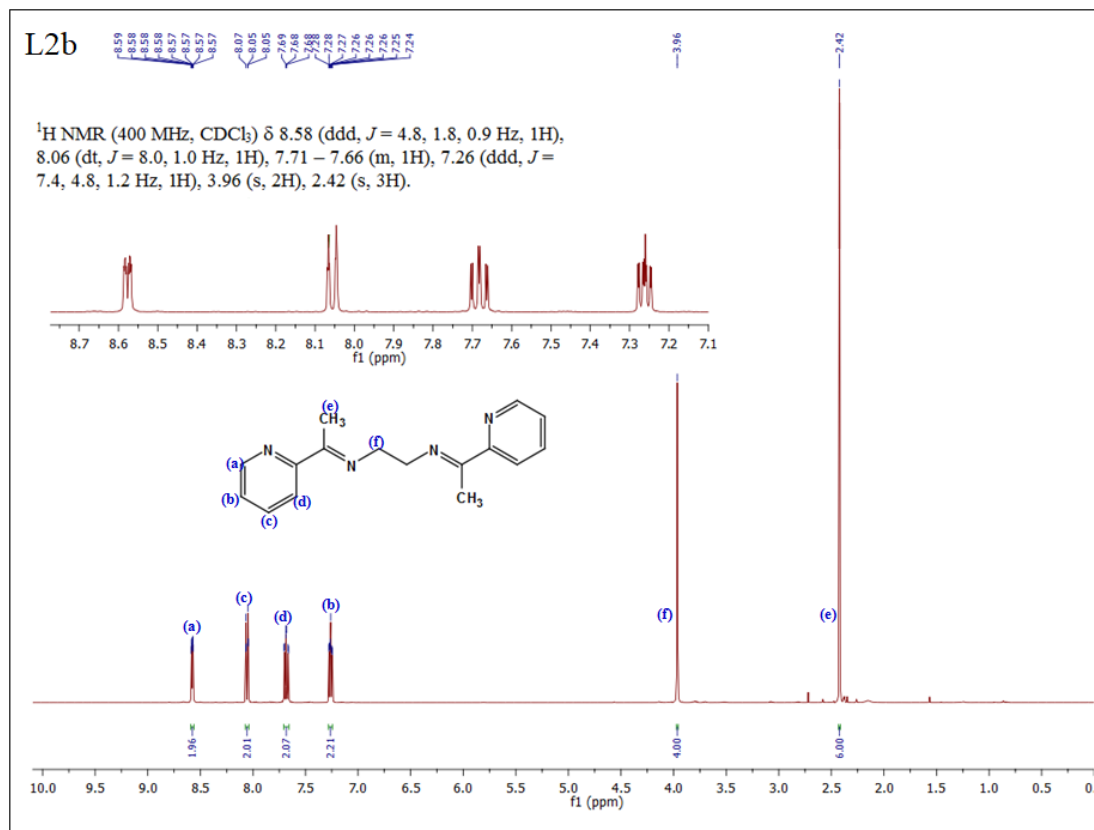


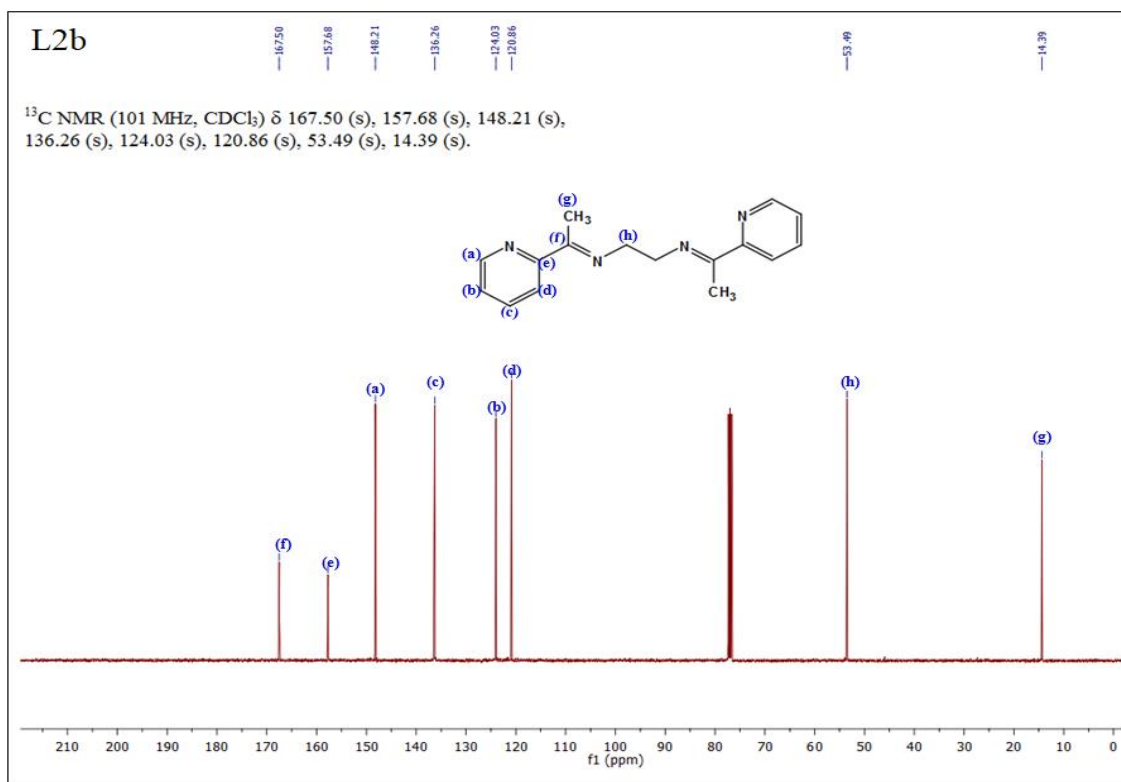
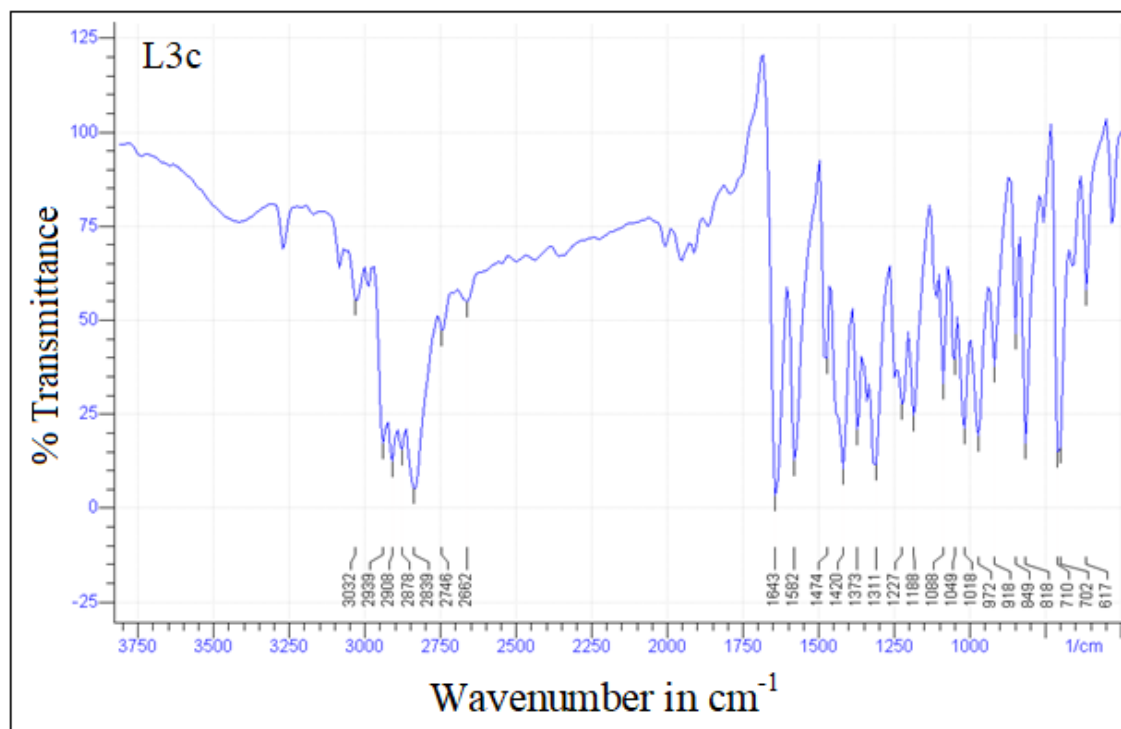
Figure A9: ^{13}C NMR Spectra of ligand **L2b**Figure A10: IR Spectra of ligand **L3c**

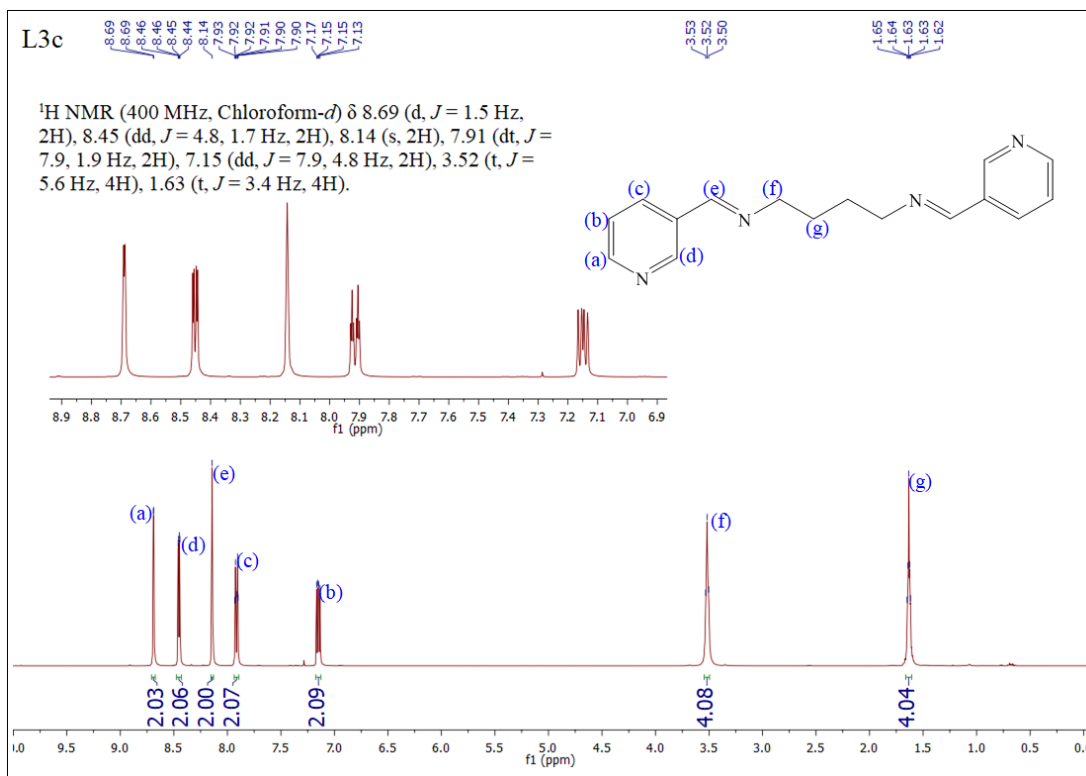
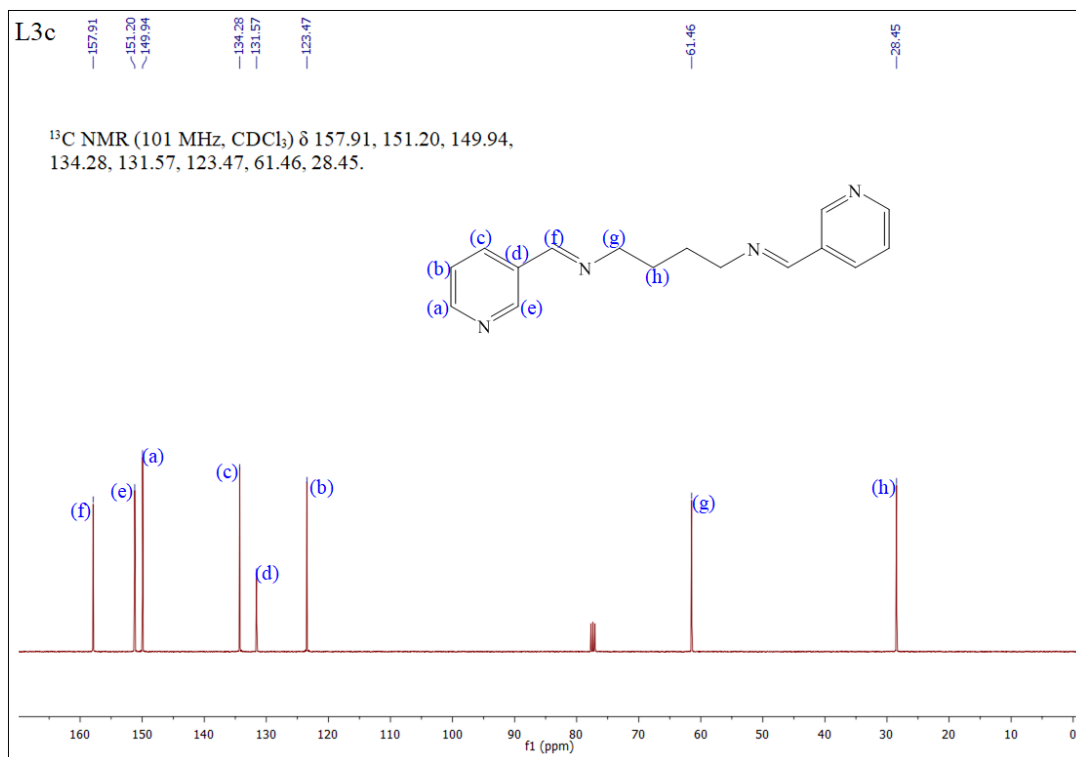
Figure A11: ^1H NMR Spectra of ligand **L3c**Figure A12: ^{13}C NMR Spectra of ligand **L3c**

Figure A13: IR Spectra of ligand **L5c**

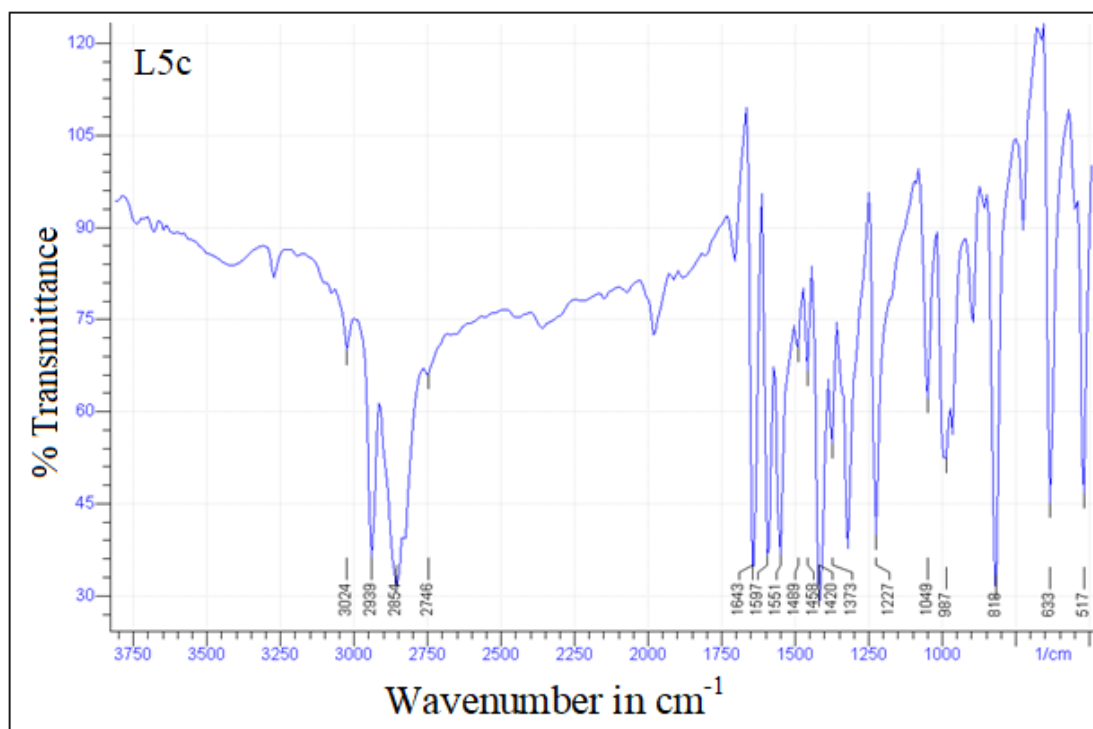


Figure A14: ^1H NMR Spectra of ligand **L5c**

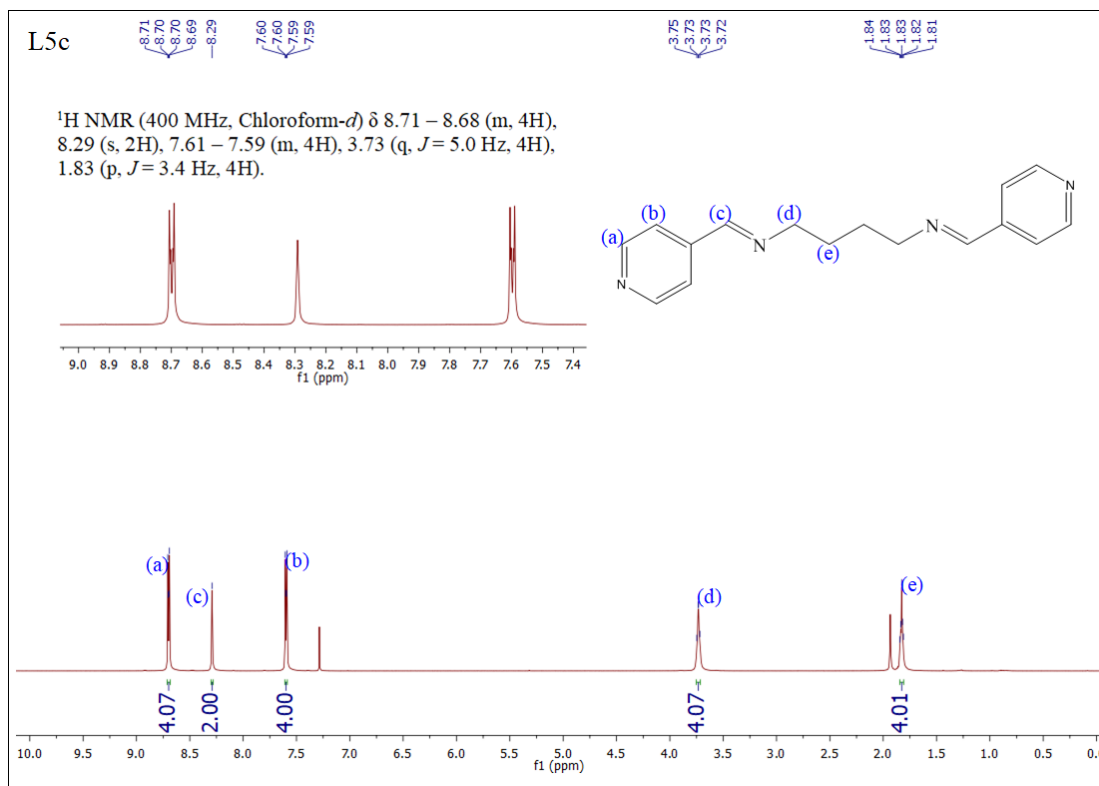


Figure A15: ^{13}C NMR Spectra of ligand **L5c**

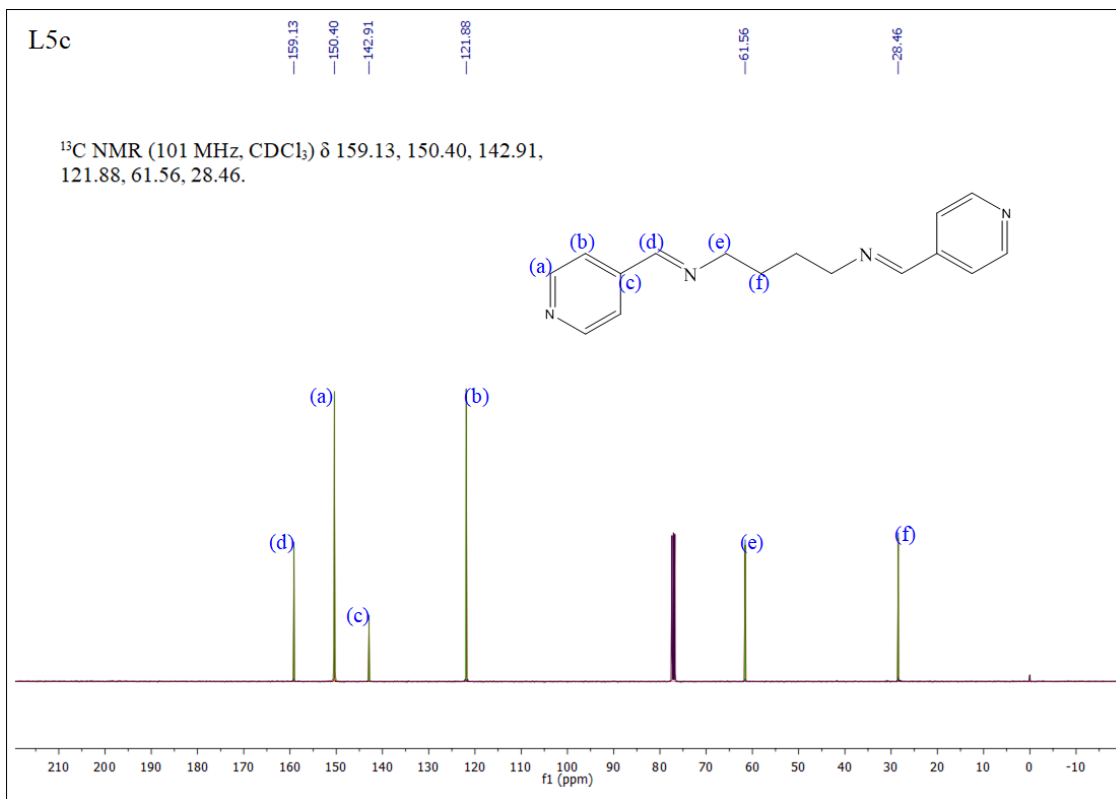


Figure A16: IR Spectra of ligand **L5d**

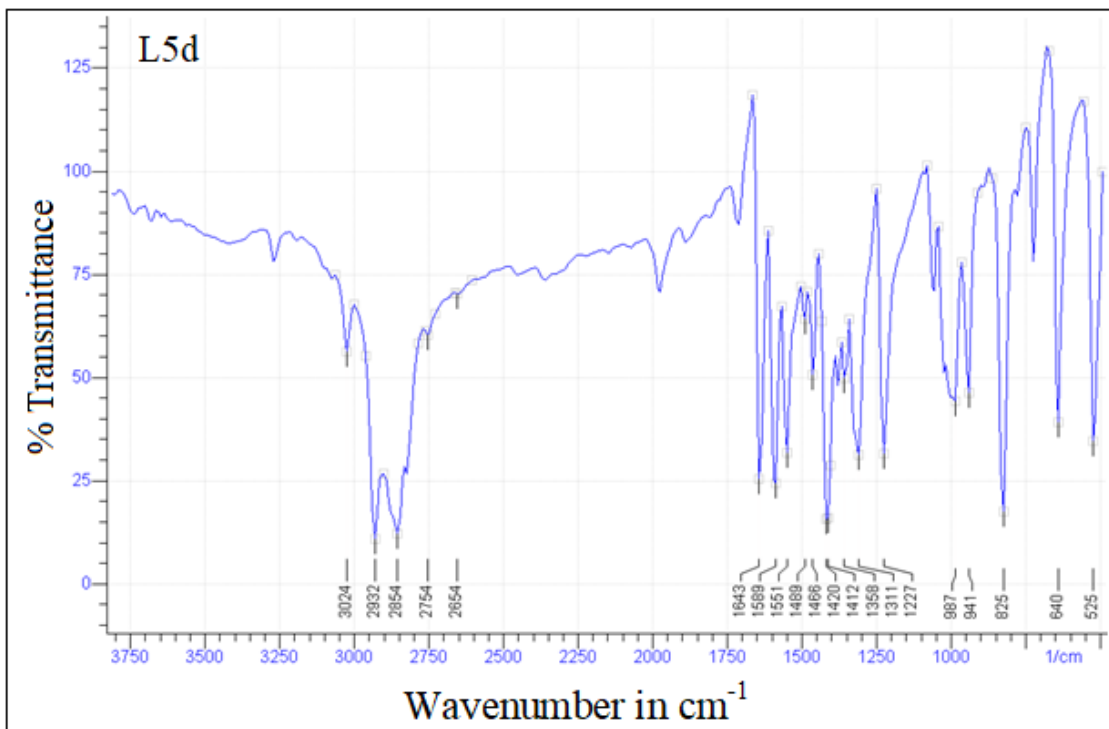


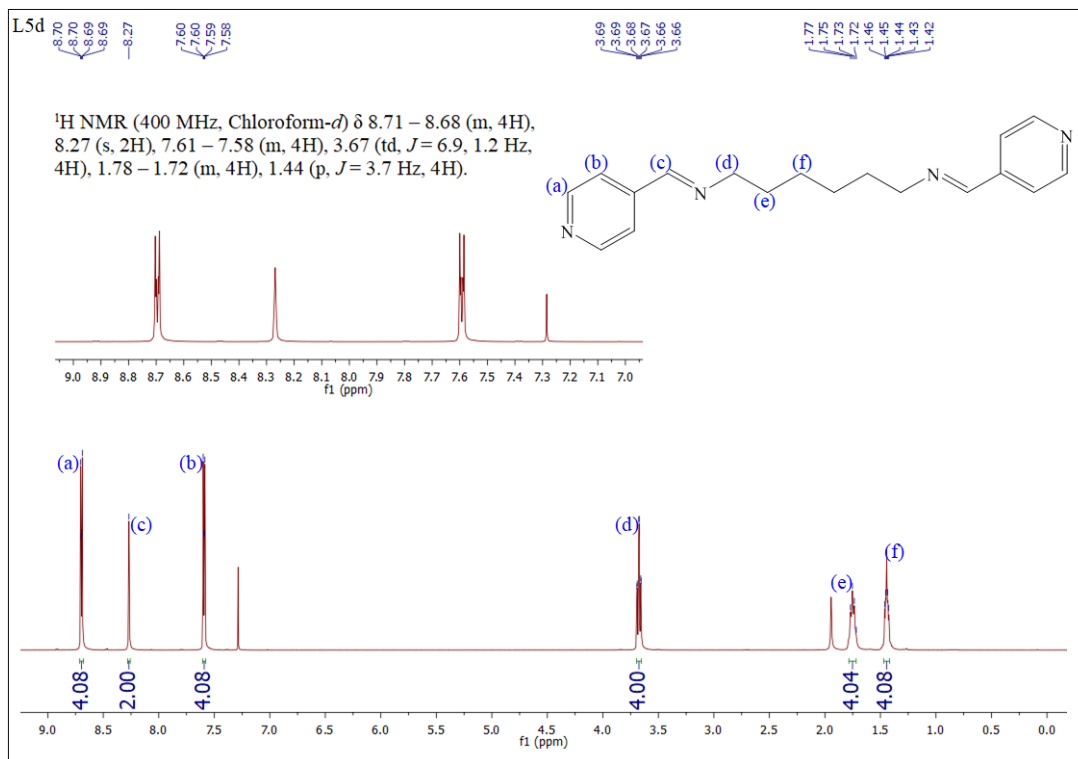
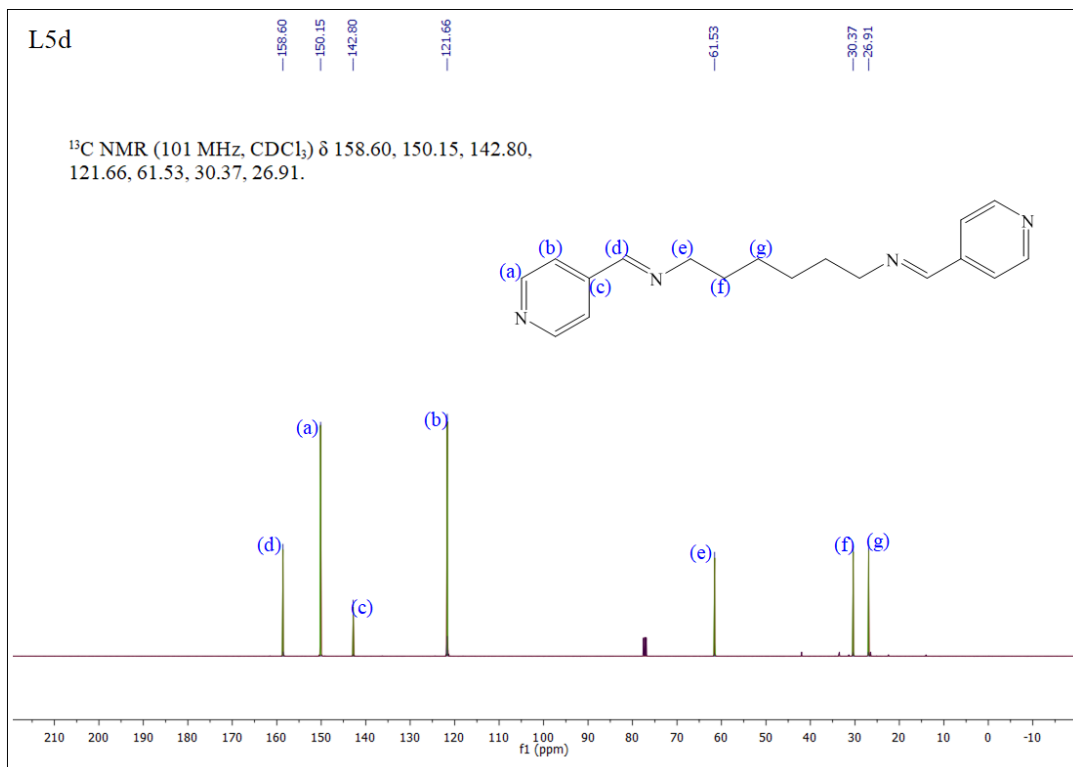
Figure A17: ^1H NMR Spectra of ligand **L5d**Figure A18: ^{13}C NMR Spectra of ligand **L5d**

Figure A19: IR Spectra of ligand **L6c**

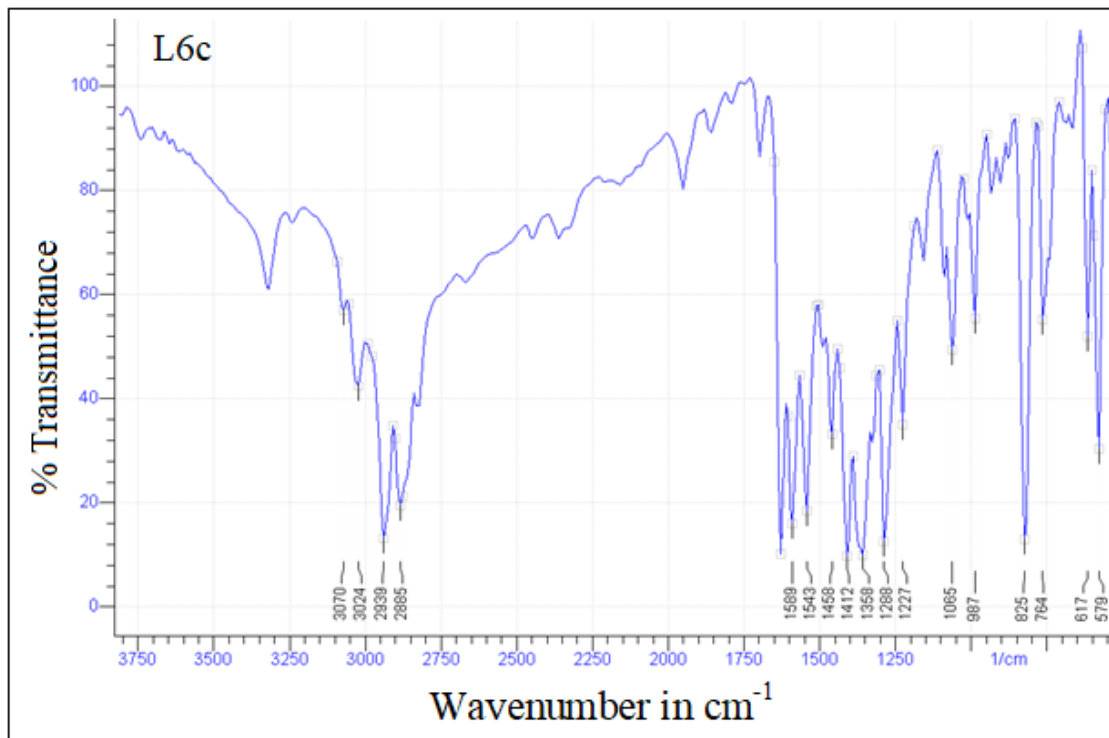


Figure A20: ^1H NMR Spectra of ligand **L6c**

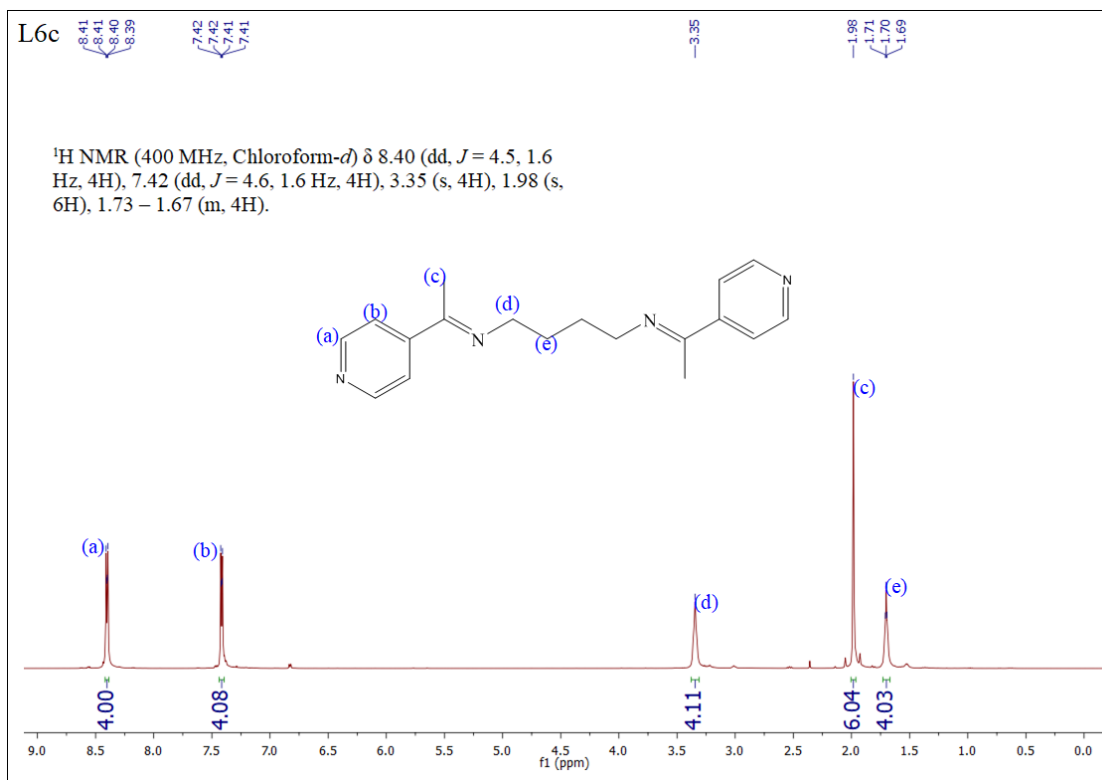


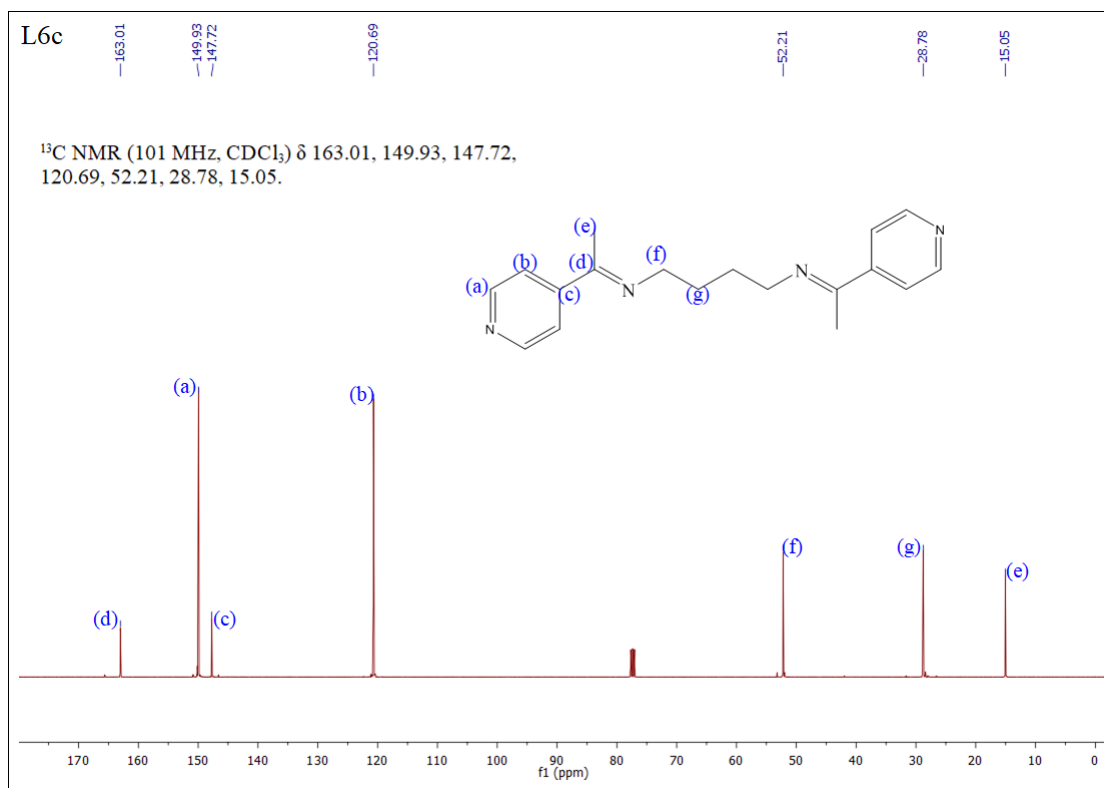
Figure A21: ^{13}C NMR Spectra of ligand L6c

Figure A22: IR Spectra of ligand L6d

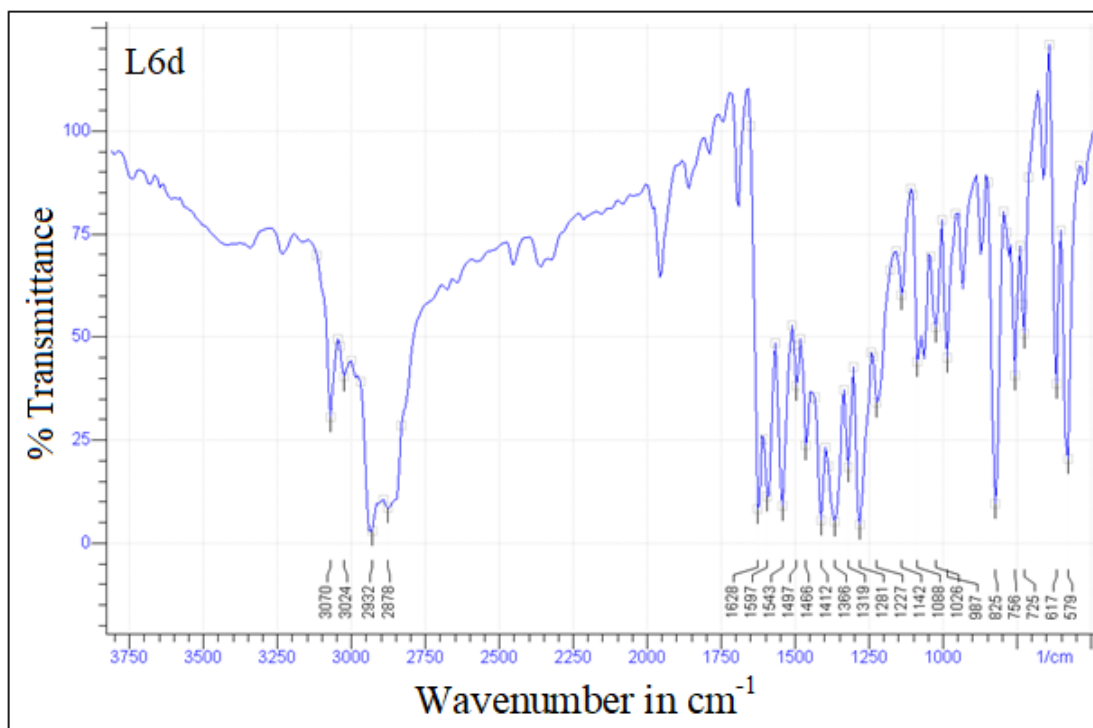


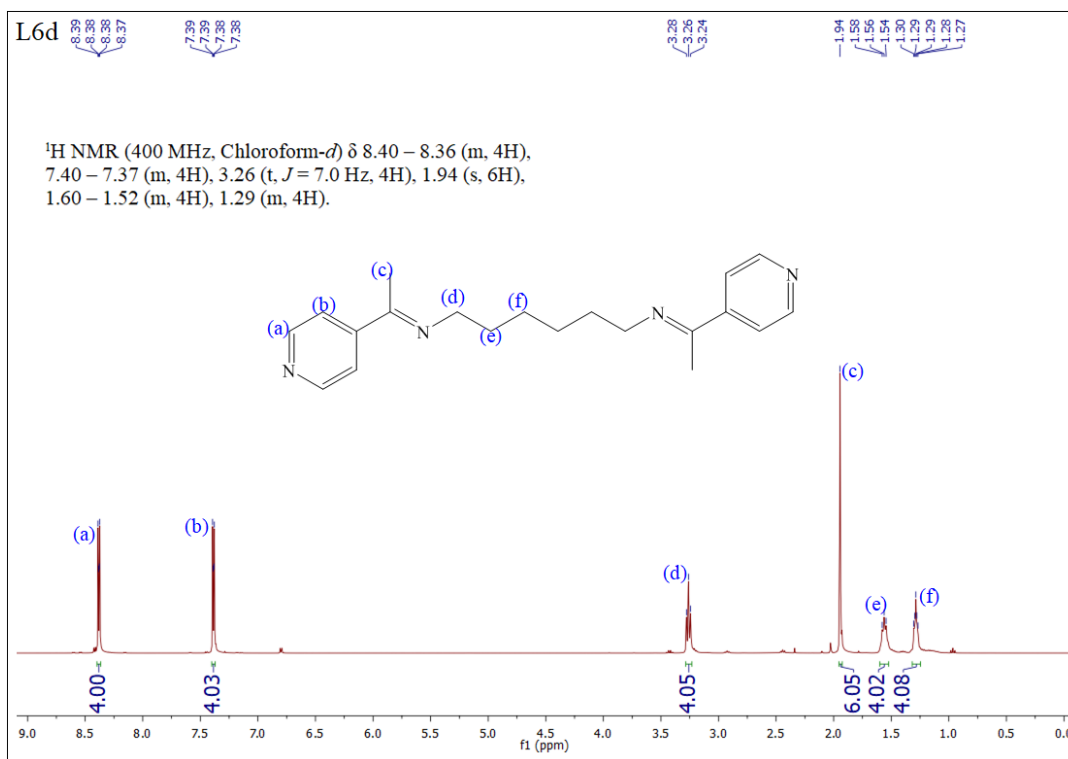
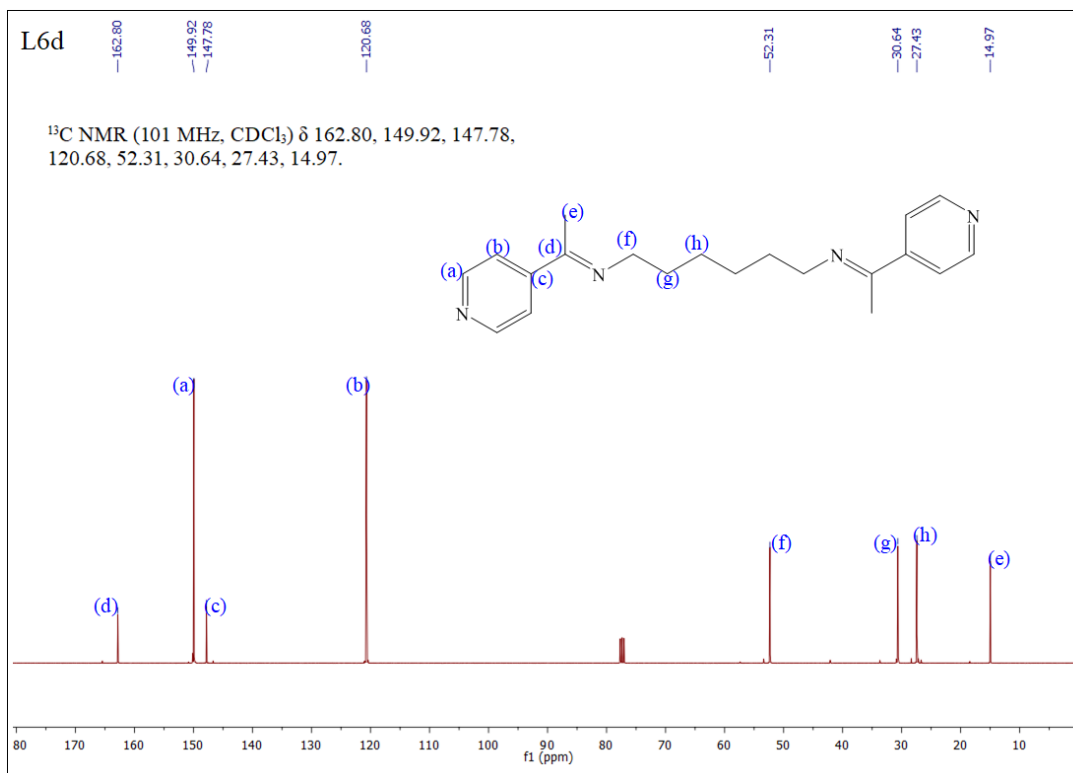
Figure A23: ^1H NMR Spectra of ligand **L6d**Figure A24: ^{13}C NMR Spectra of ligand **L6d**

Figure A25: ORTEP of L1c

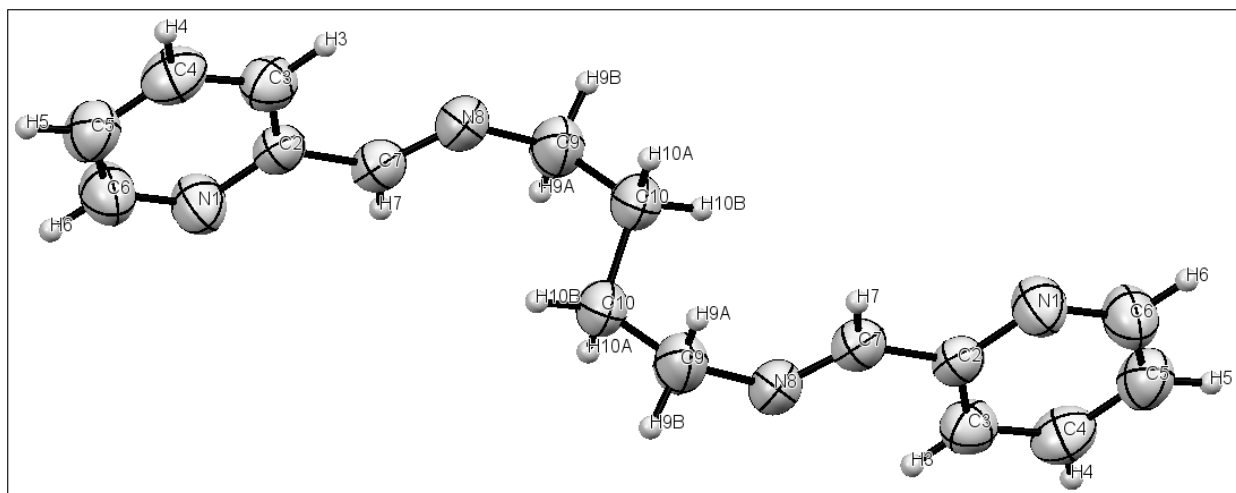


Figure A26: ORTEP of L2a

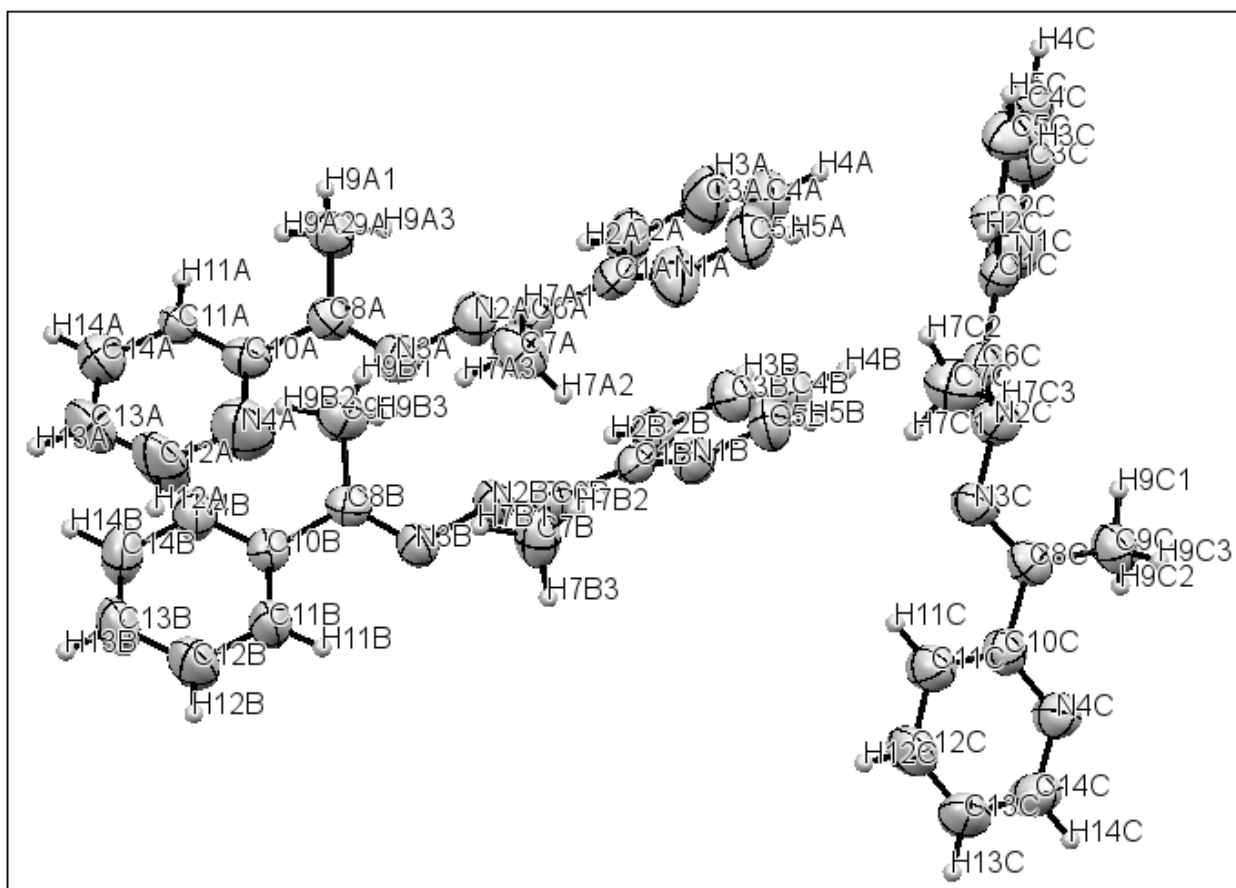


Figure A27: ORTEP of L2b

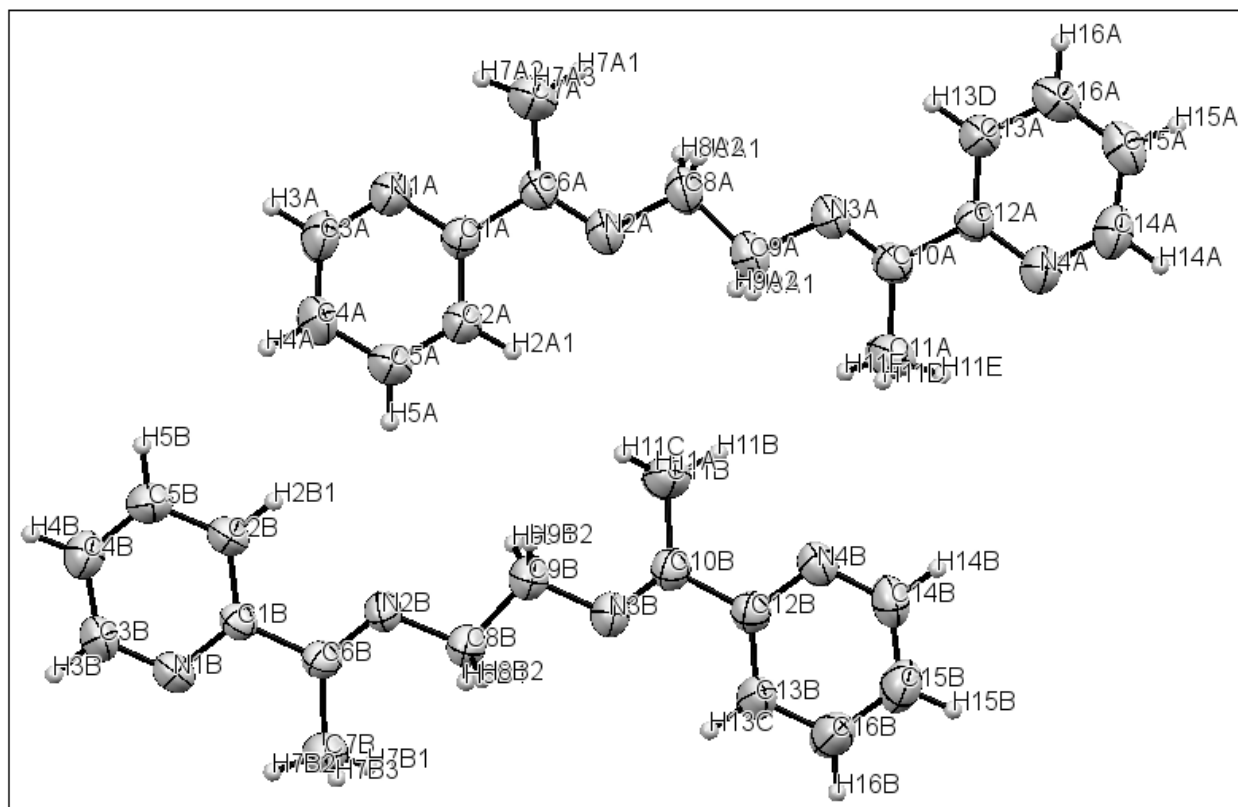


Figure A28: ORTEP of L3c

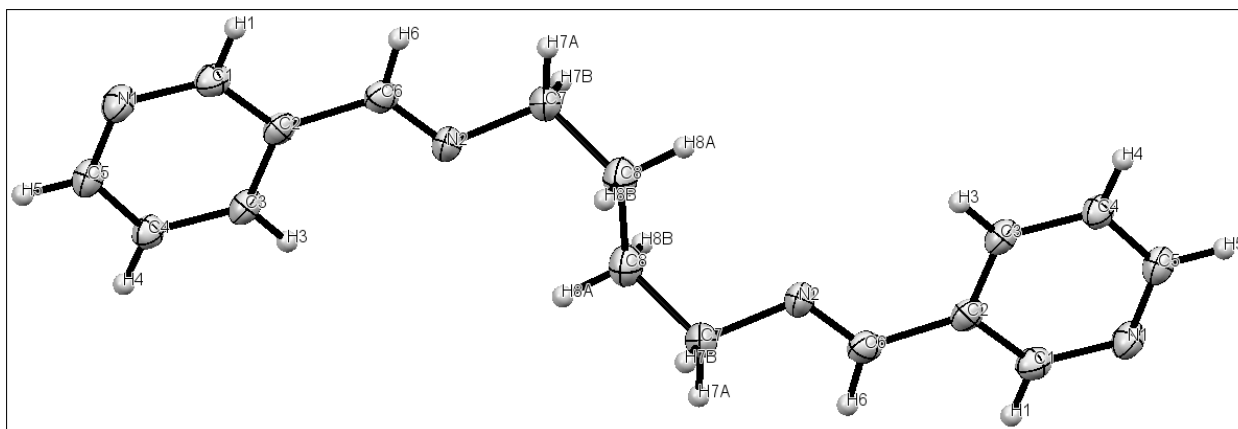


Figure A29: ORTEP of **L5c**

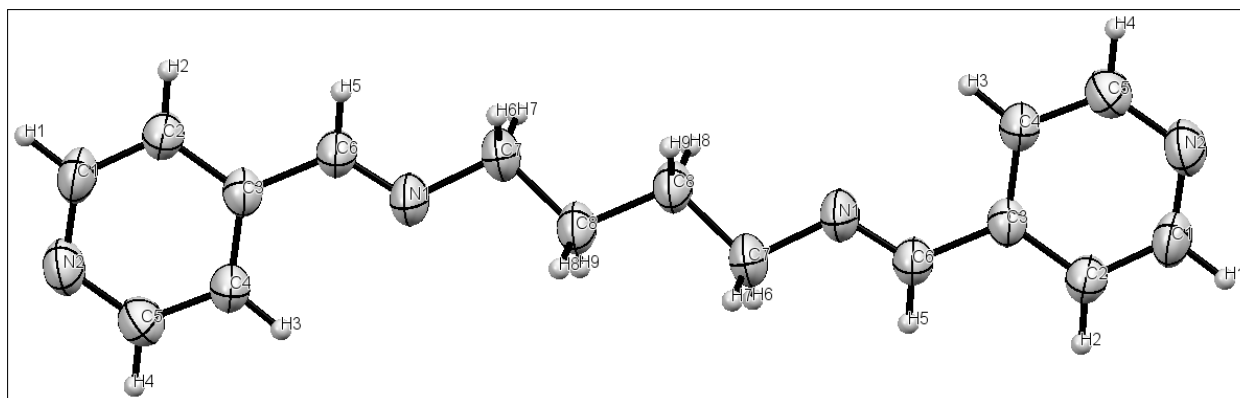


Figure A30: ORTEP of **L5d**

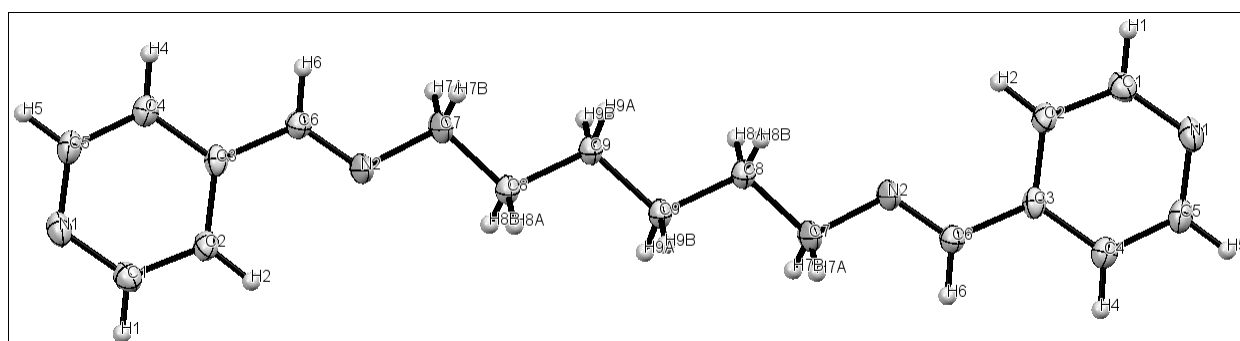


Figure A31: ORTEP of **L6c**

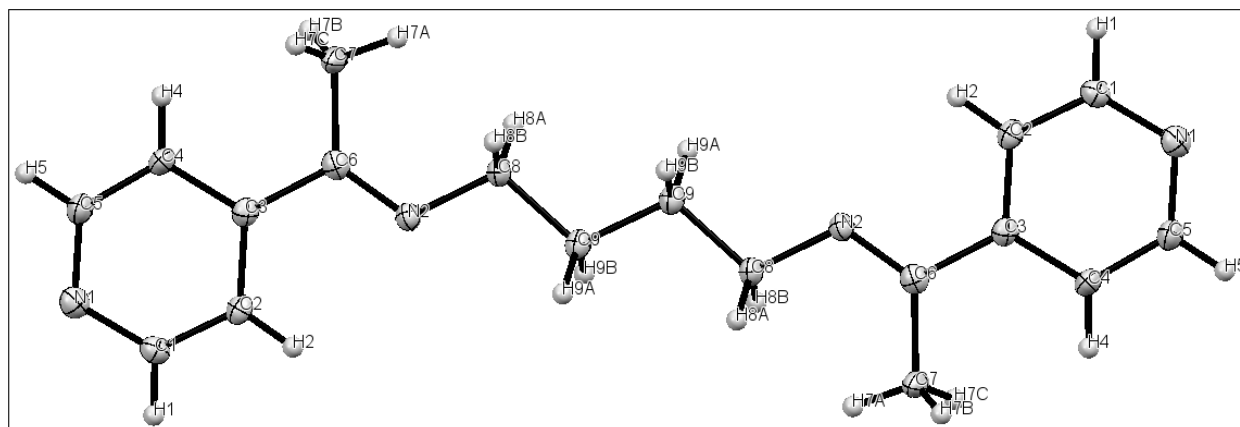


Figure A32: ORTEP of **L6d**

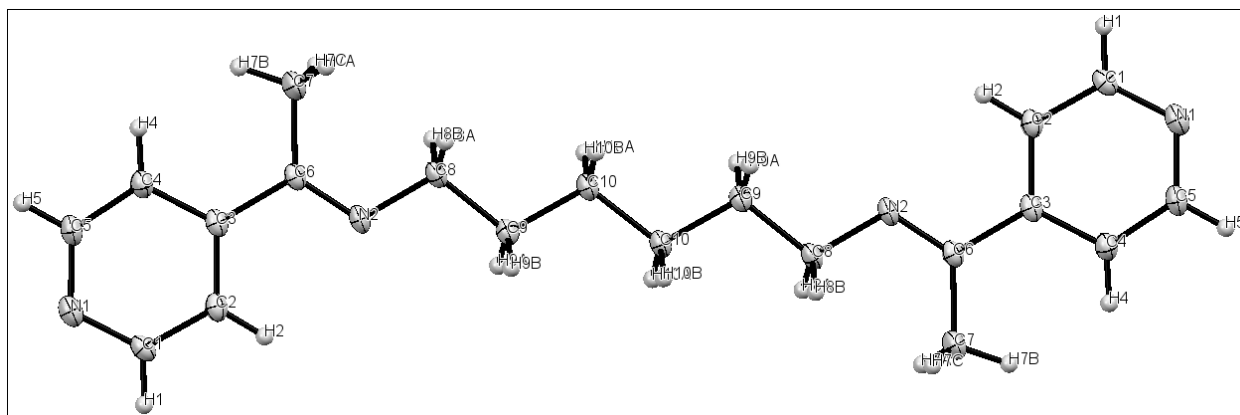


Figure A33: Solid UV-visible spectra of **L1c**, **L2a** and **L2b**

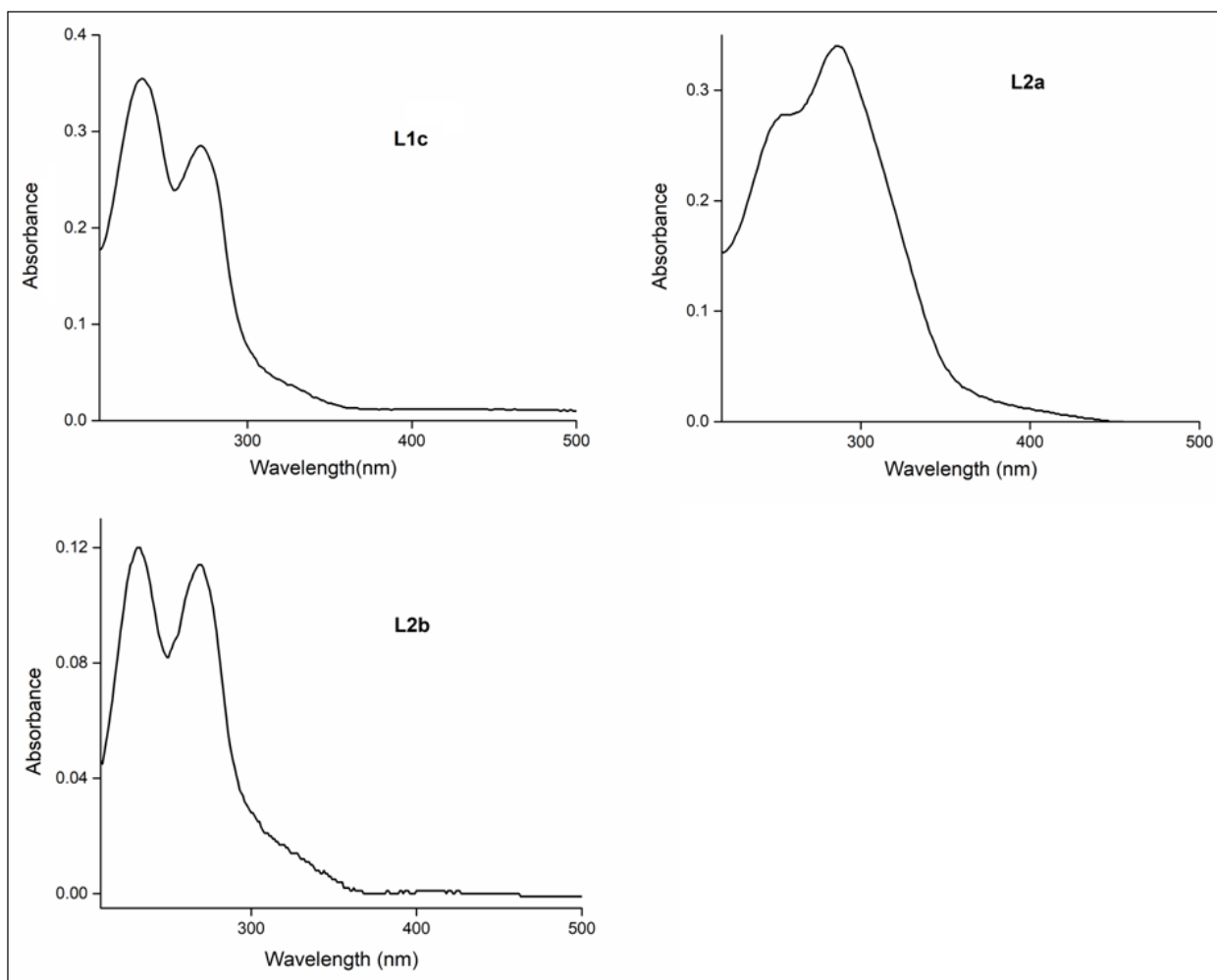


Figure A34: Solid UV-visible spectra of L3b, L3c, L3d, L4b, L4c and L4d.

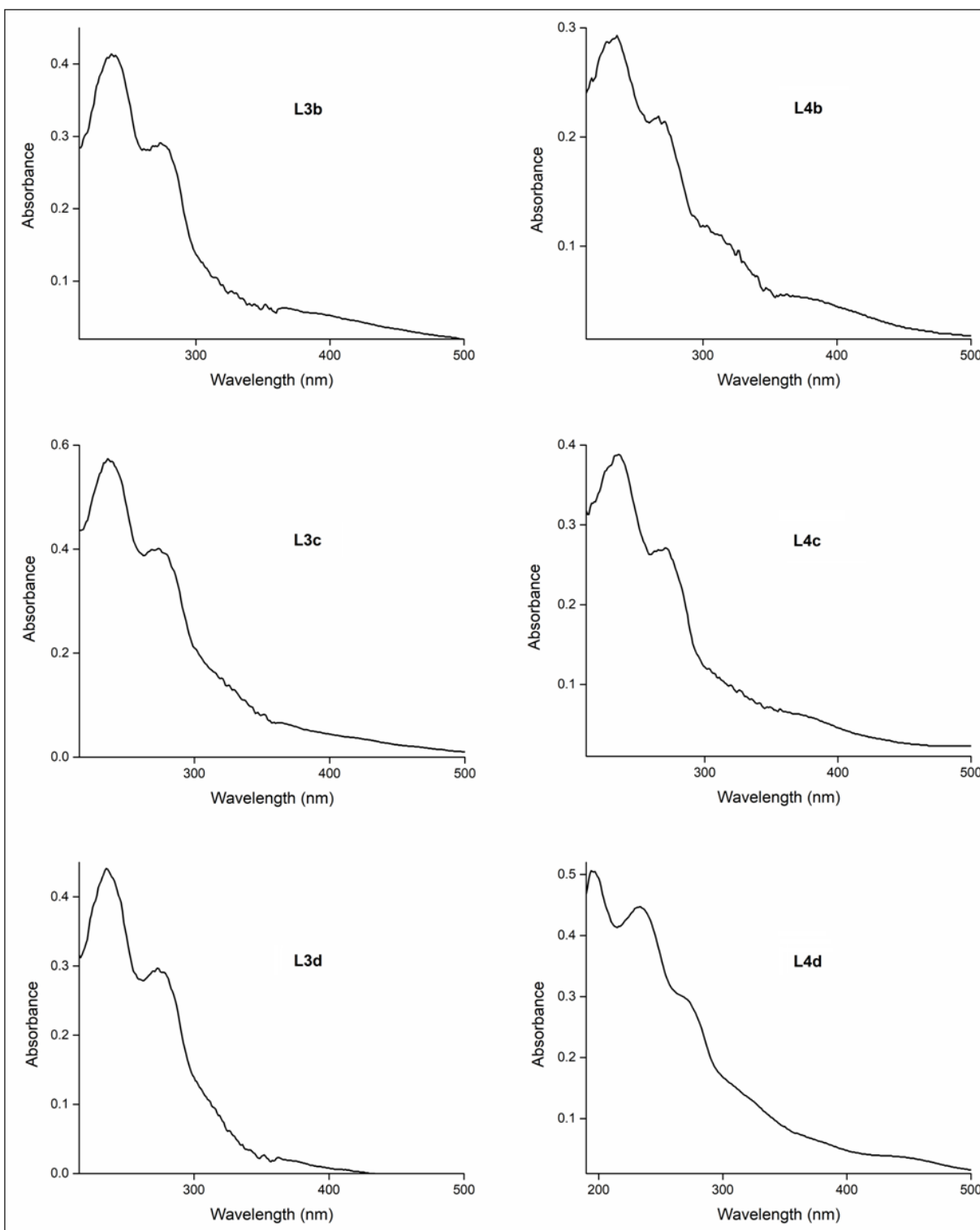


Figure A35: Solid UV-visible spectra of **L5b**, **L5c**, **L5d**, **L6b**, **L6c** and **L6d**.

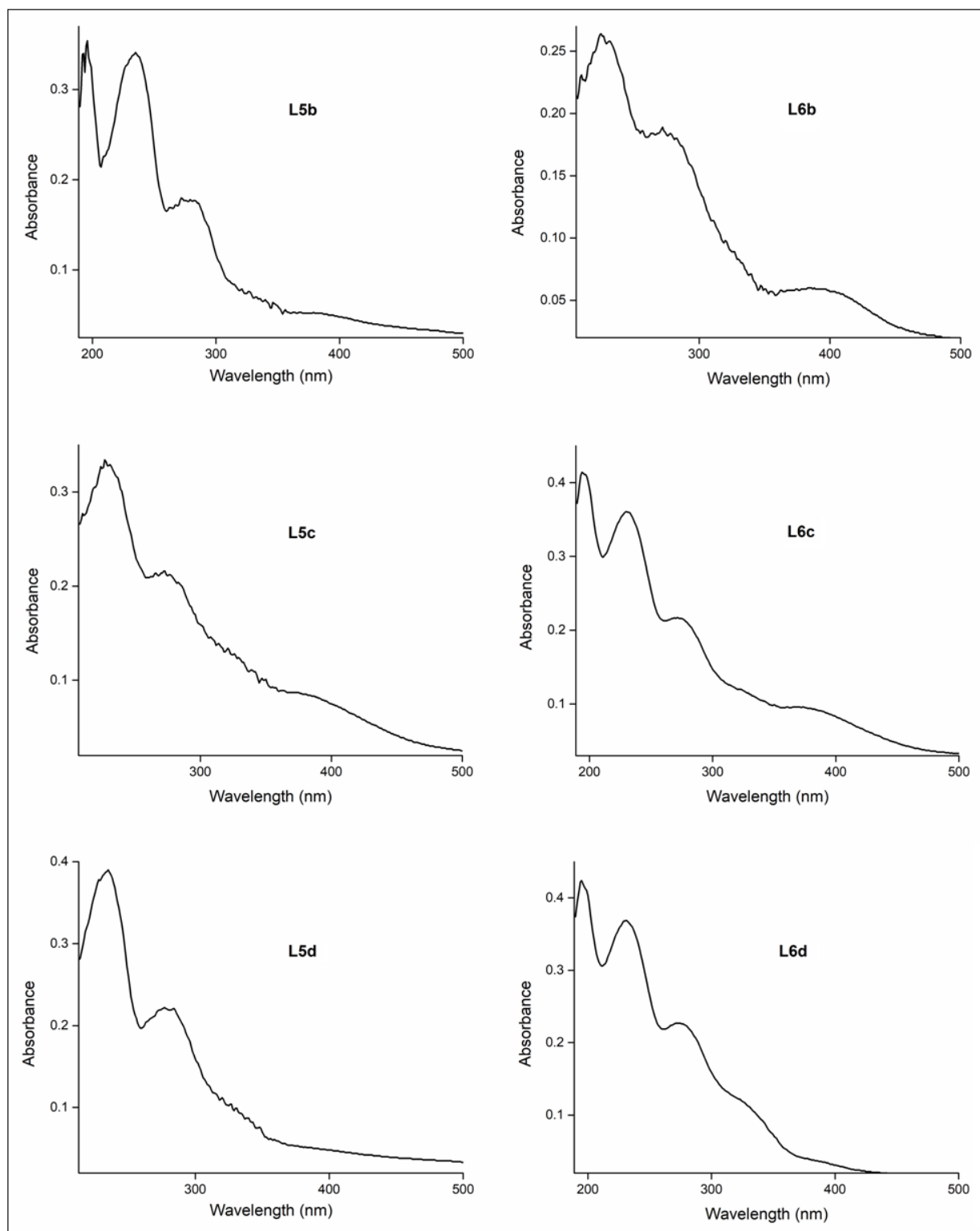


Figure A36: Excitation and PL spectra of **L1a** in solid state.

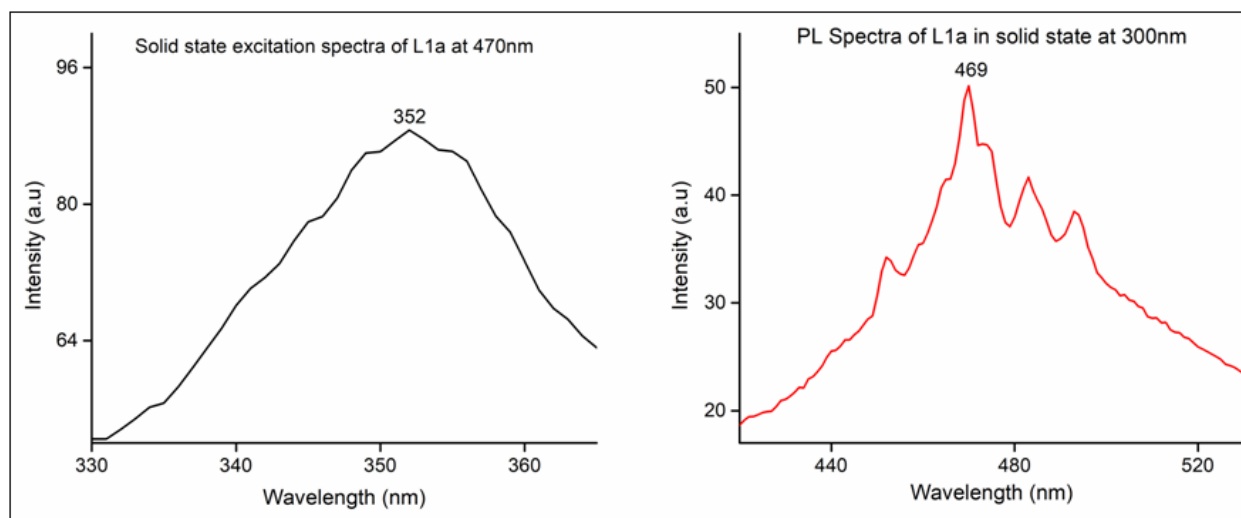


Figure A37: PL spectra (Structured emission) of **L5c**

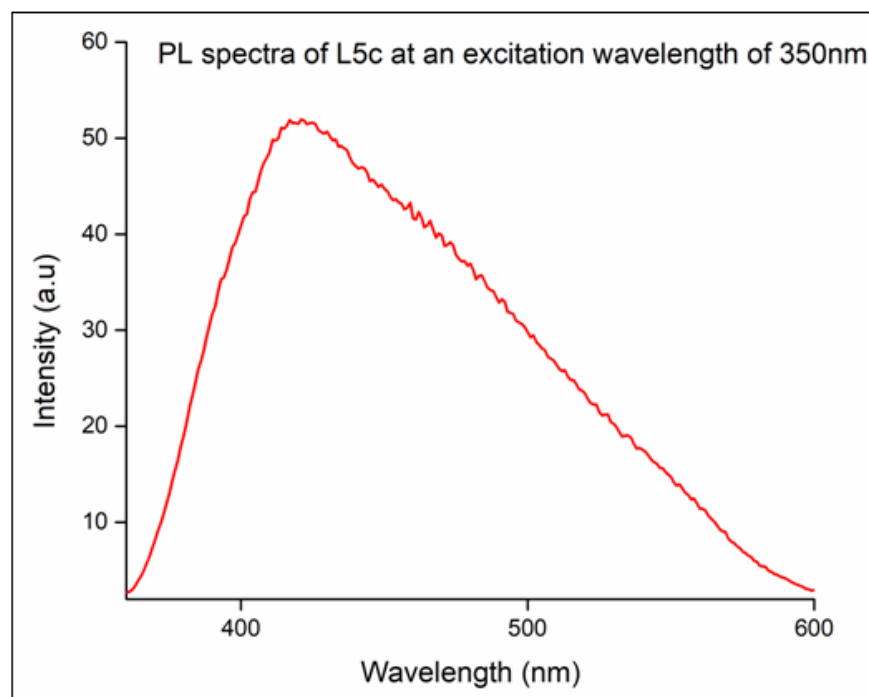


Figure A38: PL spectra (Structured emission) of **L5d**

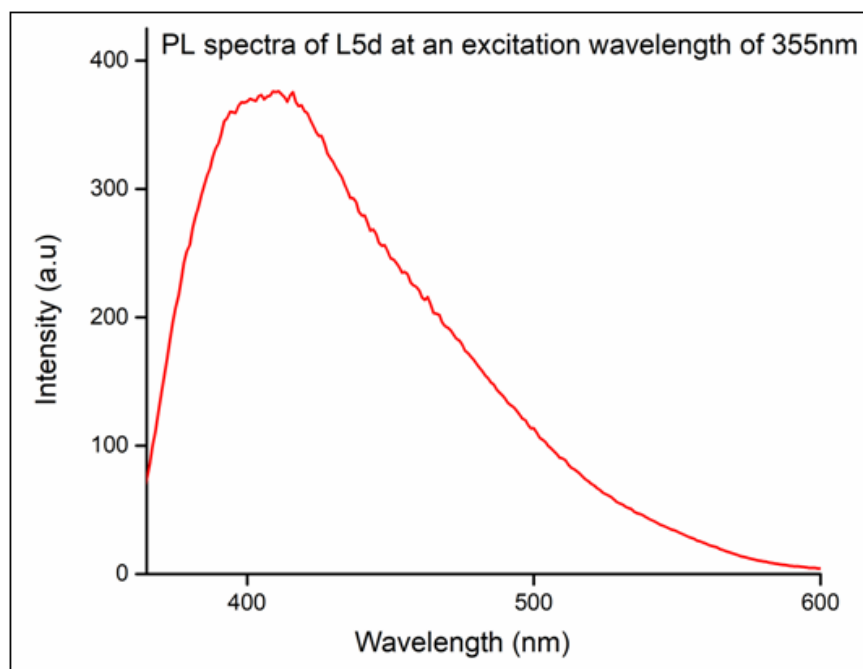


Figure A39: PL spectra (Structured emission) of **L6c**

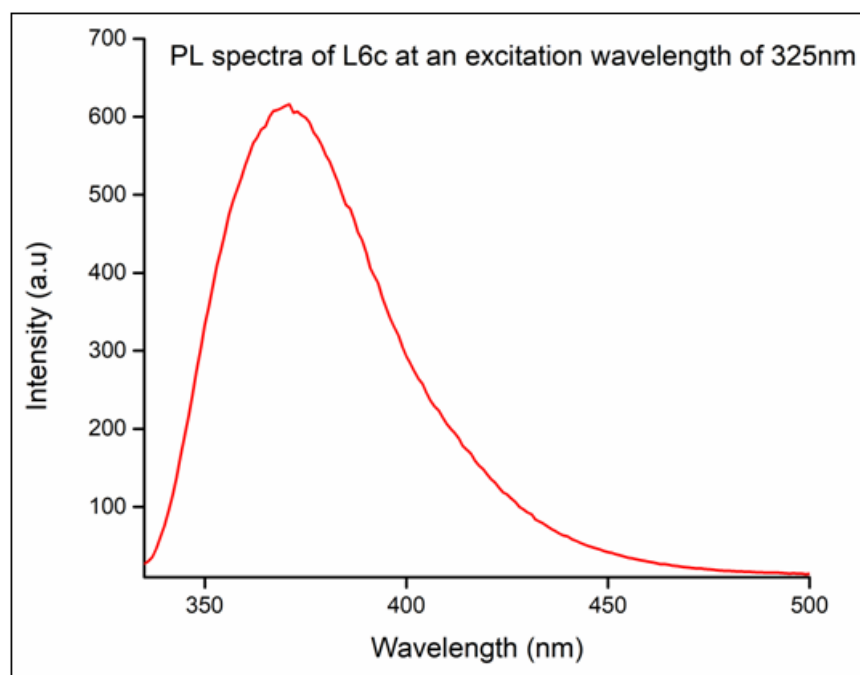


Figure A40: PL spectra (Structured emission) of **L6d**

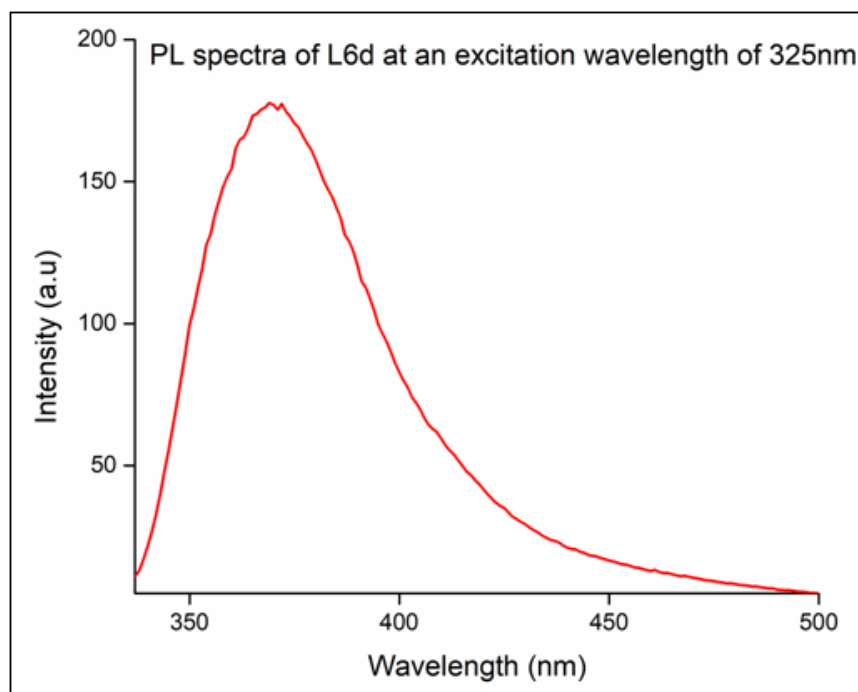


Figure A41: IR spectra of **L3a**

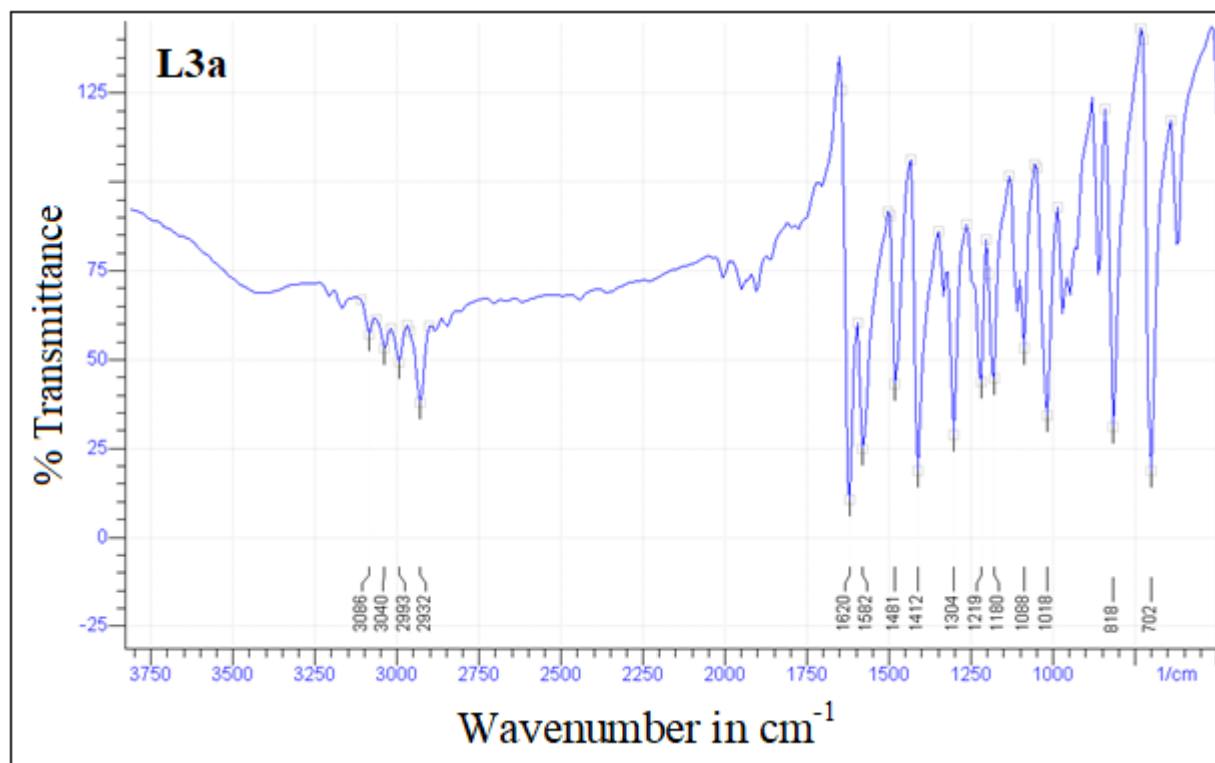


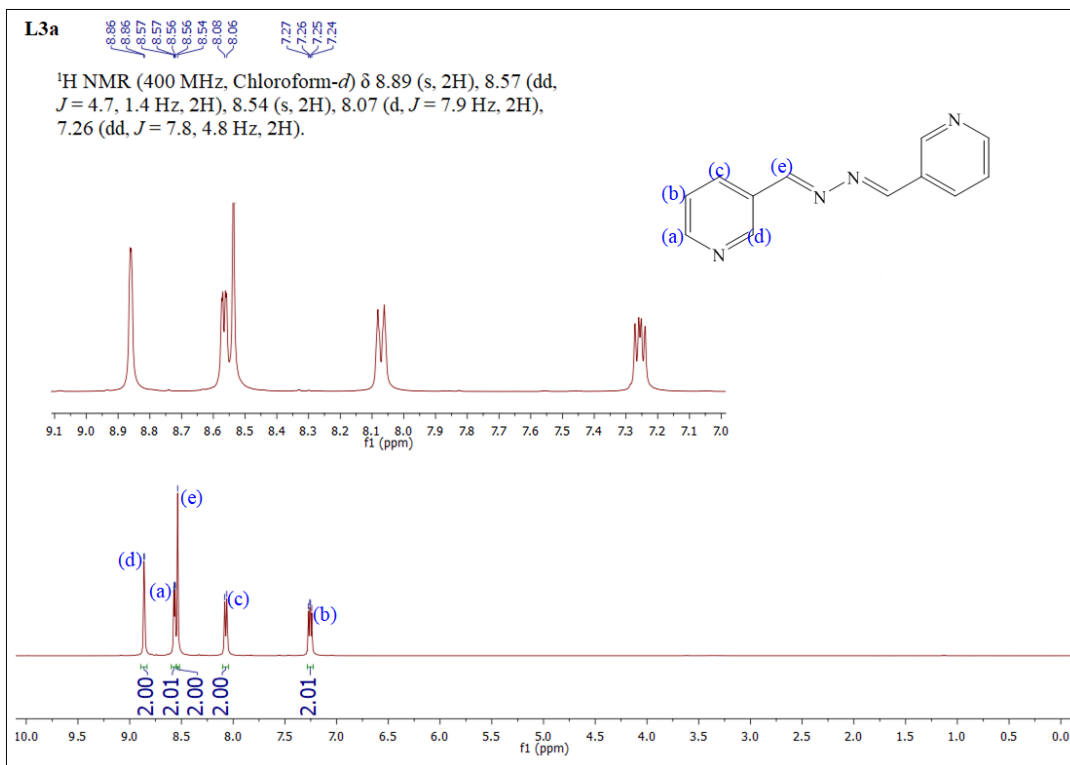
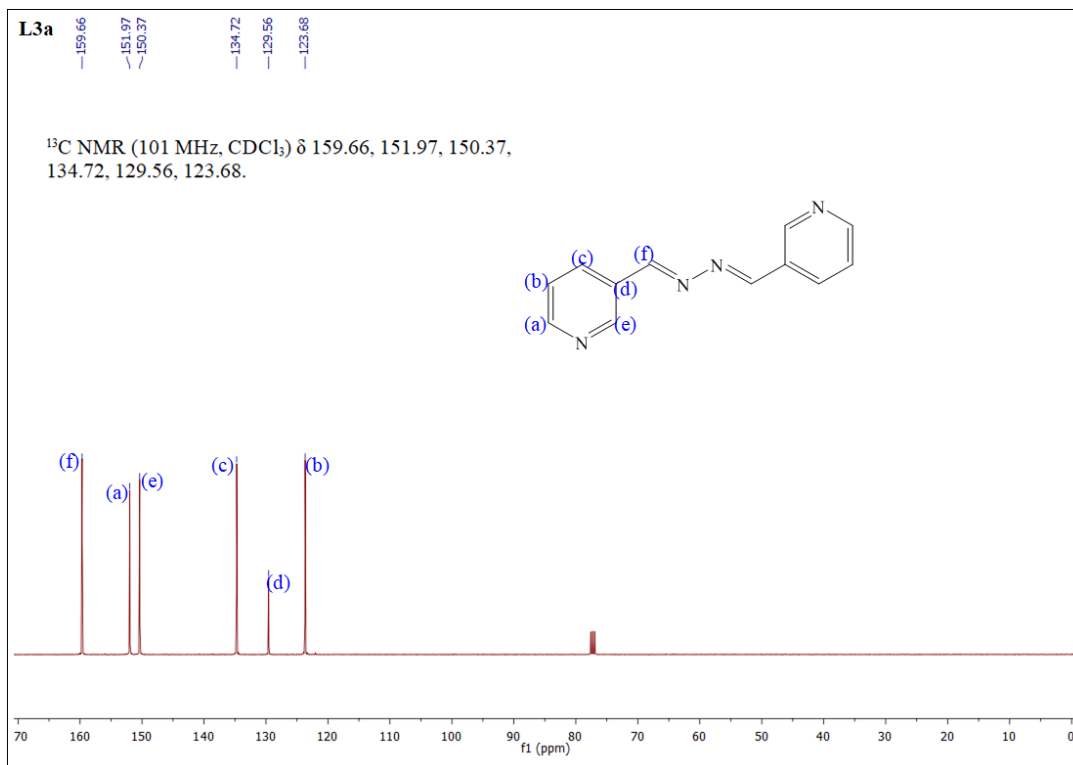
Figure A 42: ^1H NMR spectra of **L3a**Figure A43: ^{13}C NMR spectra of **L3a**

Figure A44: IR spectra of **L4a**

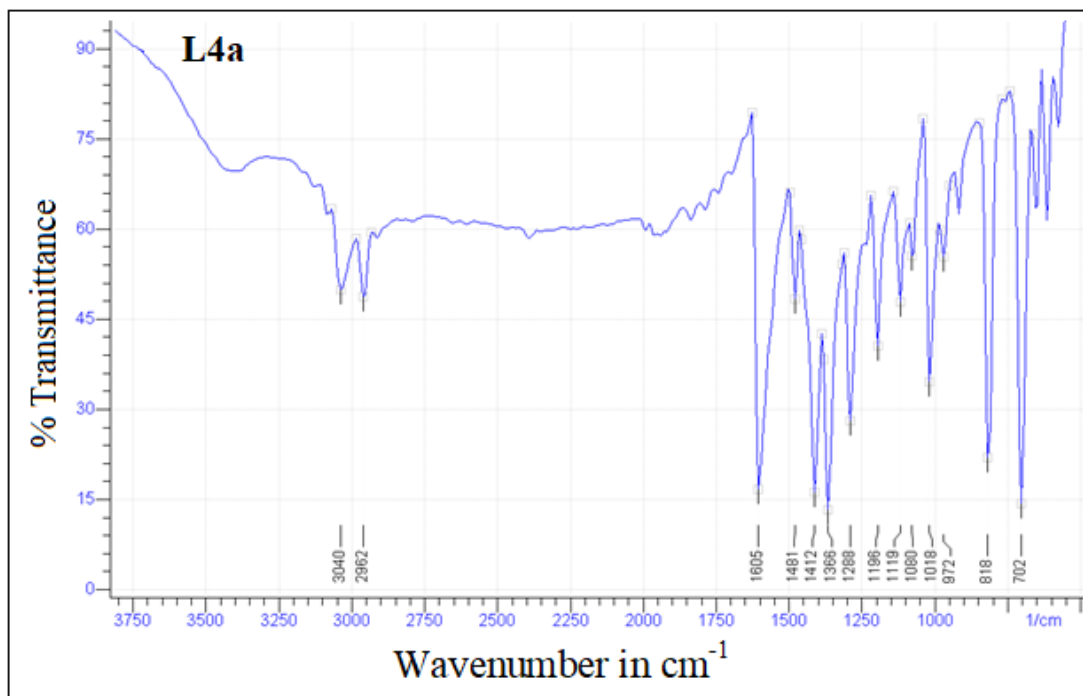


Figure A45: ^1H NMR spectra of **L4a**

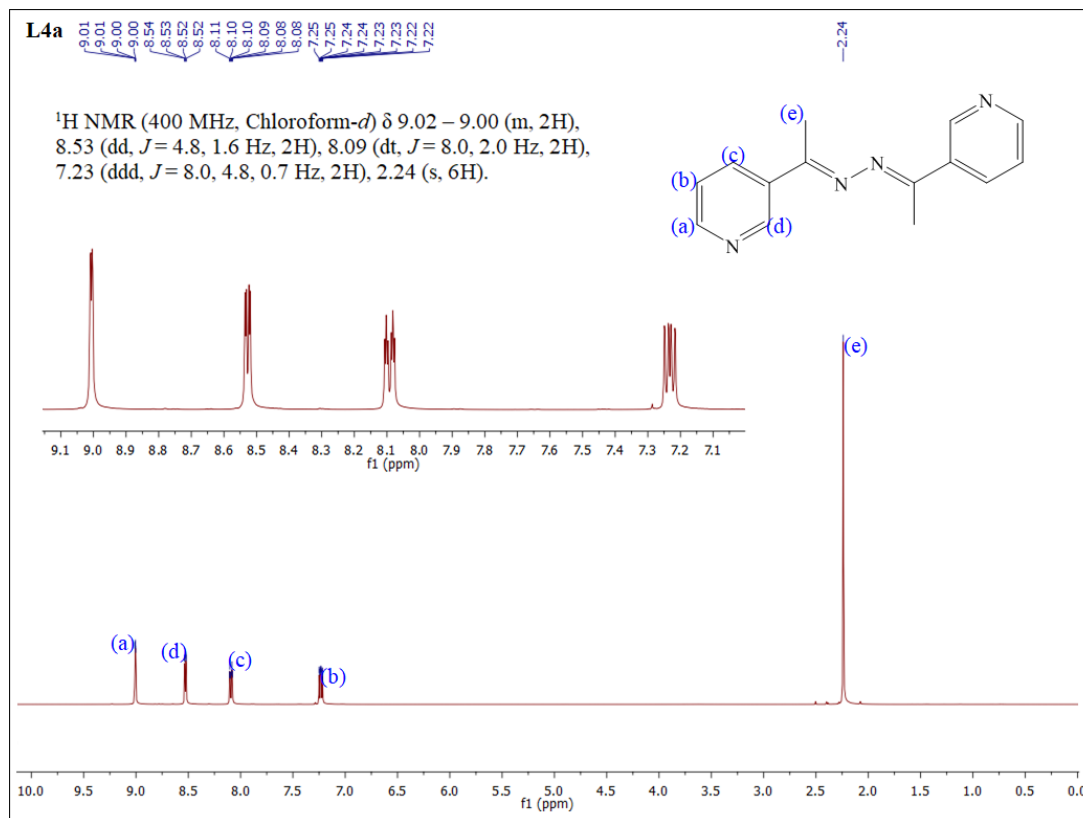


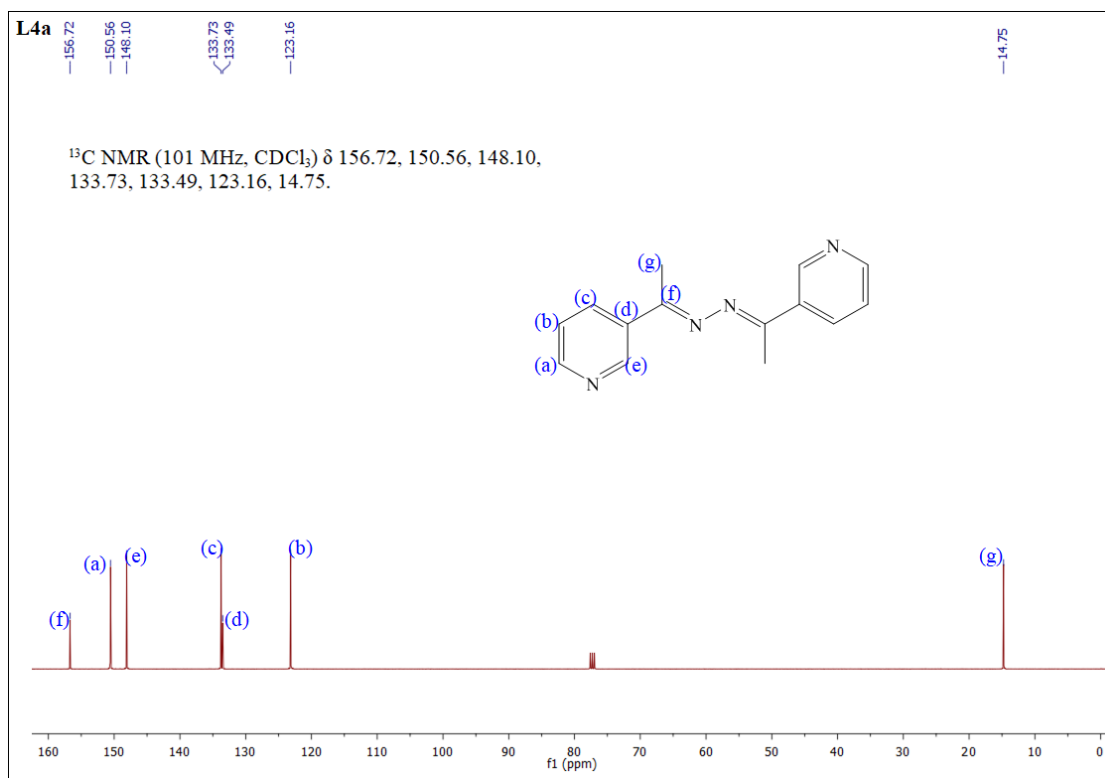
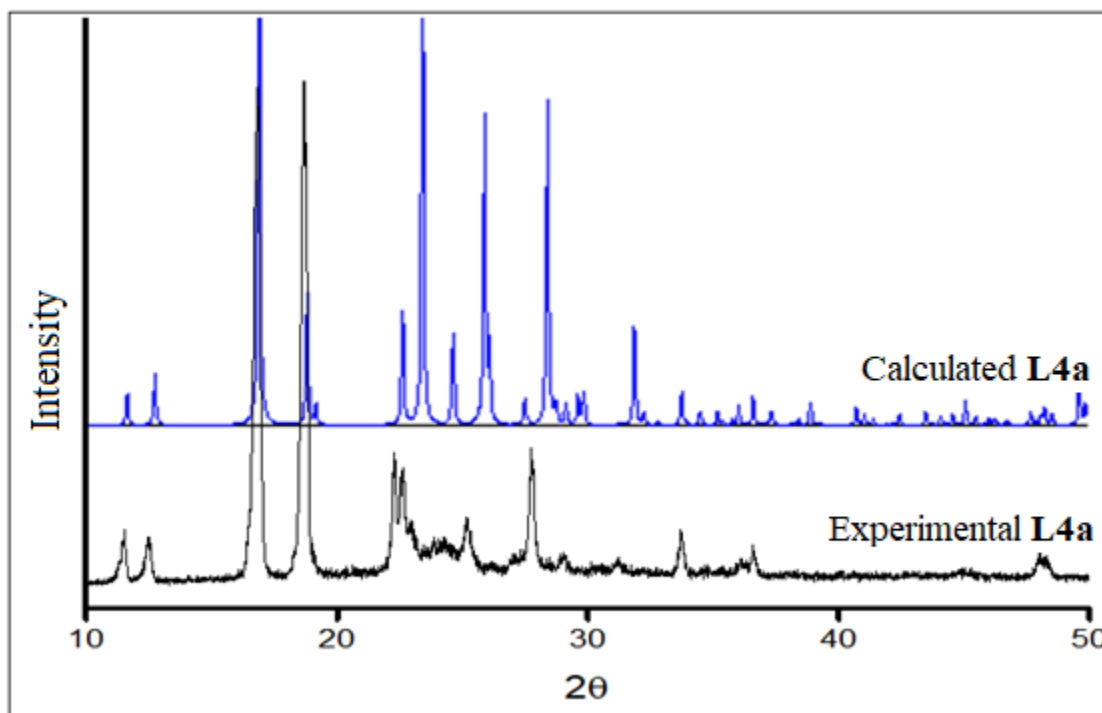
Figure A46: ^{13}C NMR spectra of **L4a**Figure A47: Experimental and calculated Powder XRD of **L4a**

Figure A48: ORTEP of L4a

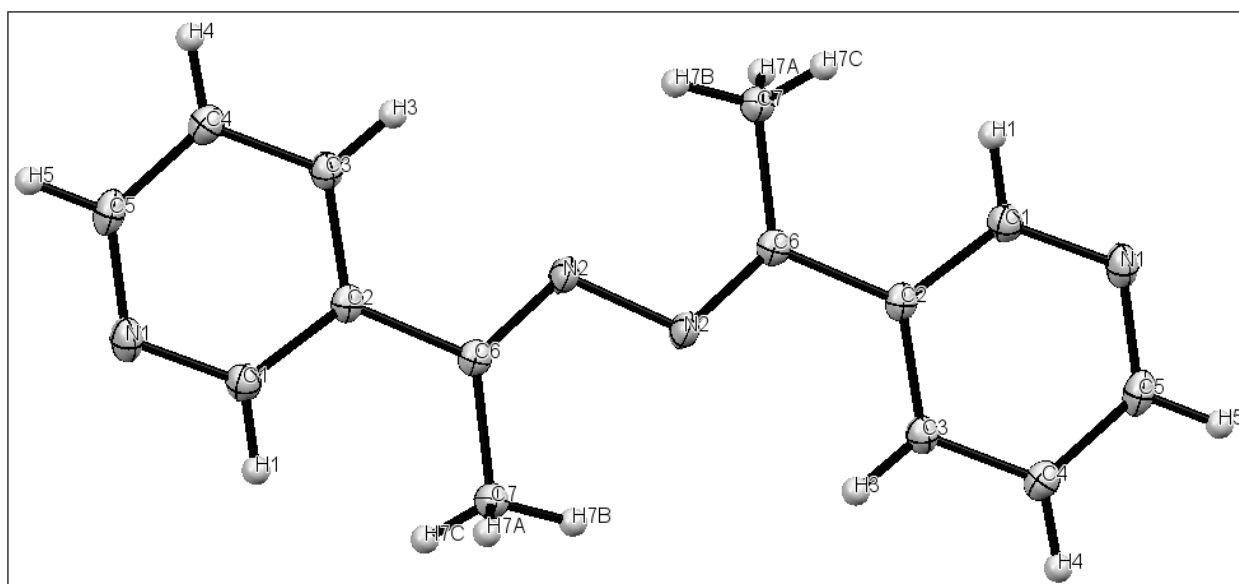


Figure A49: IR spectra of L6a

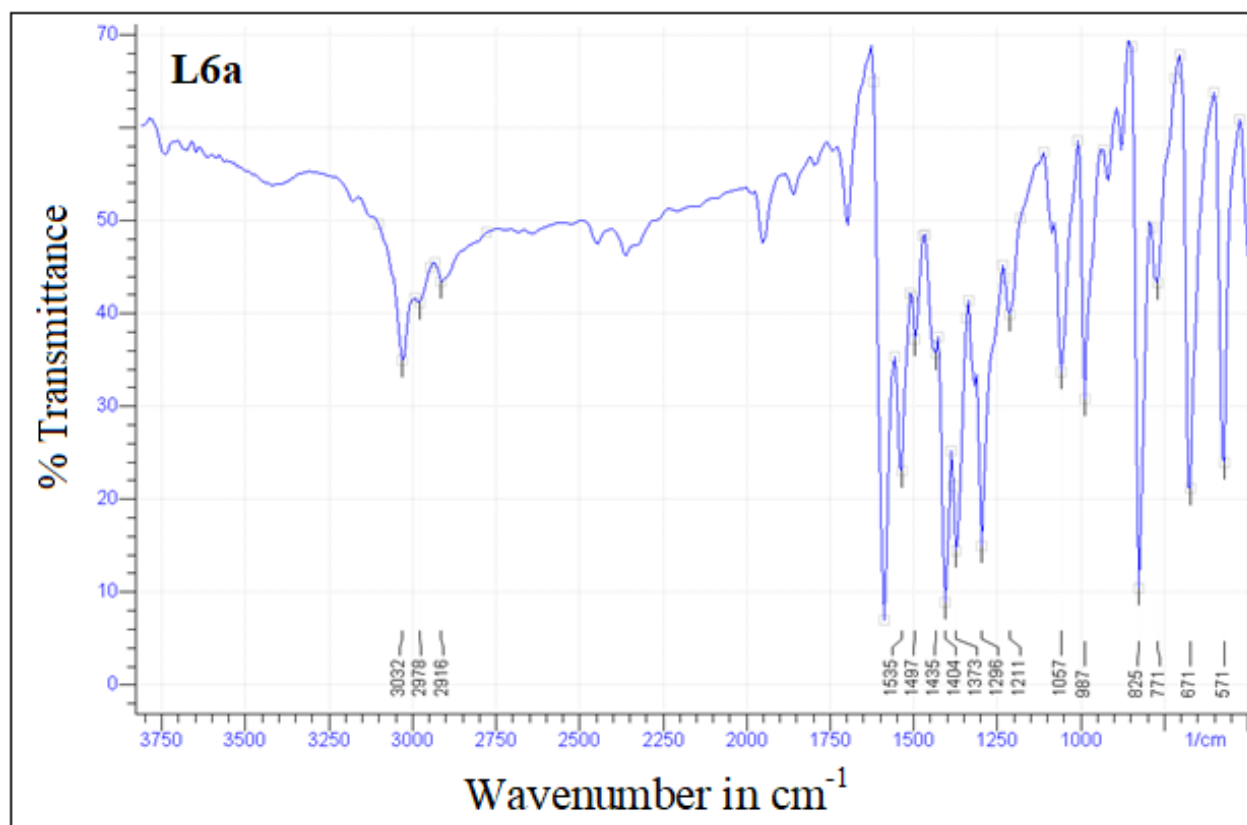


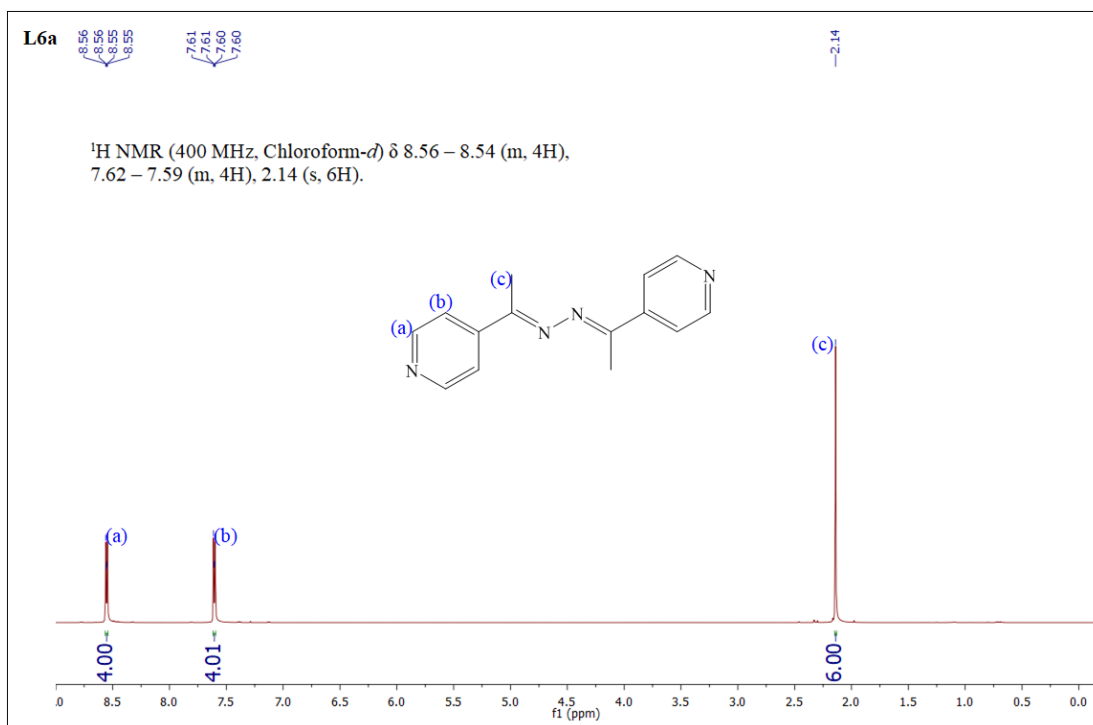
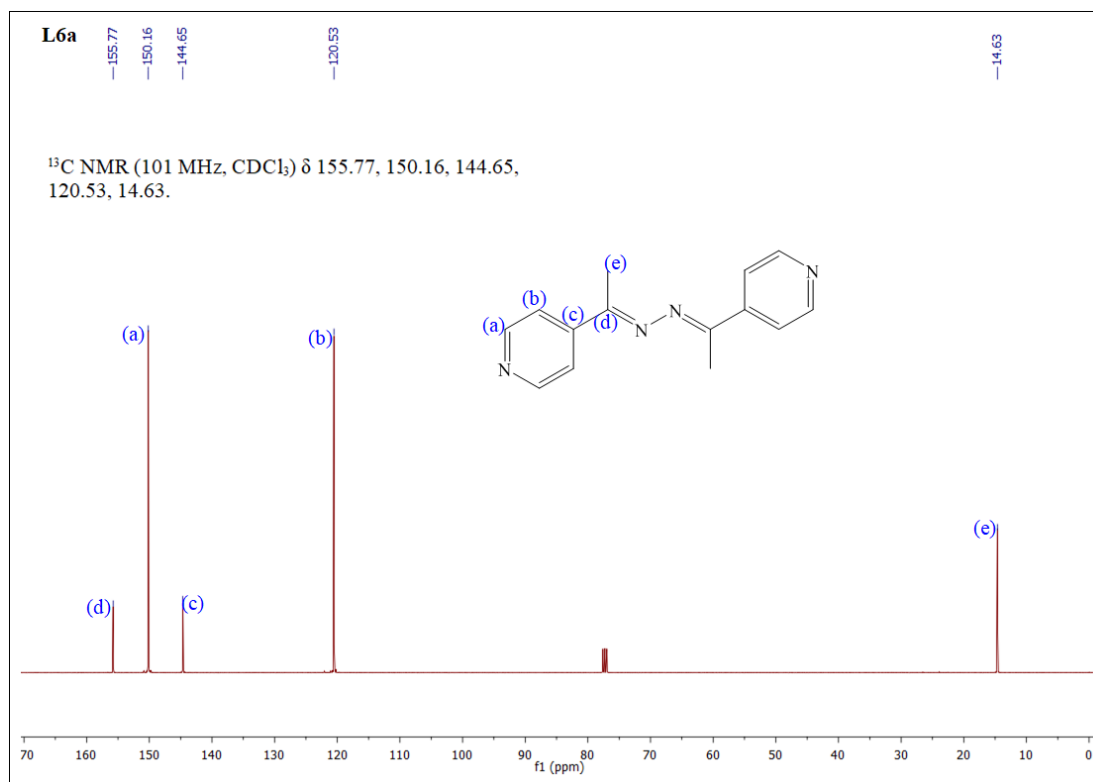
Figure A50: ^1H NMR spectra of **L6a**Figure A51: ^{13}C NMR spectra of **L6a**

Figure A52: Experimental and calculated Powder XRD of L6a

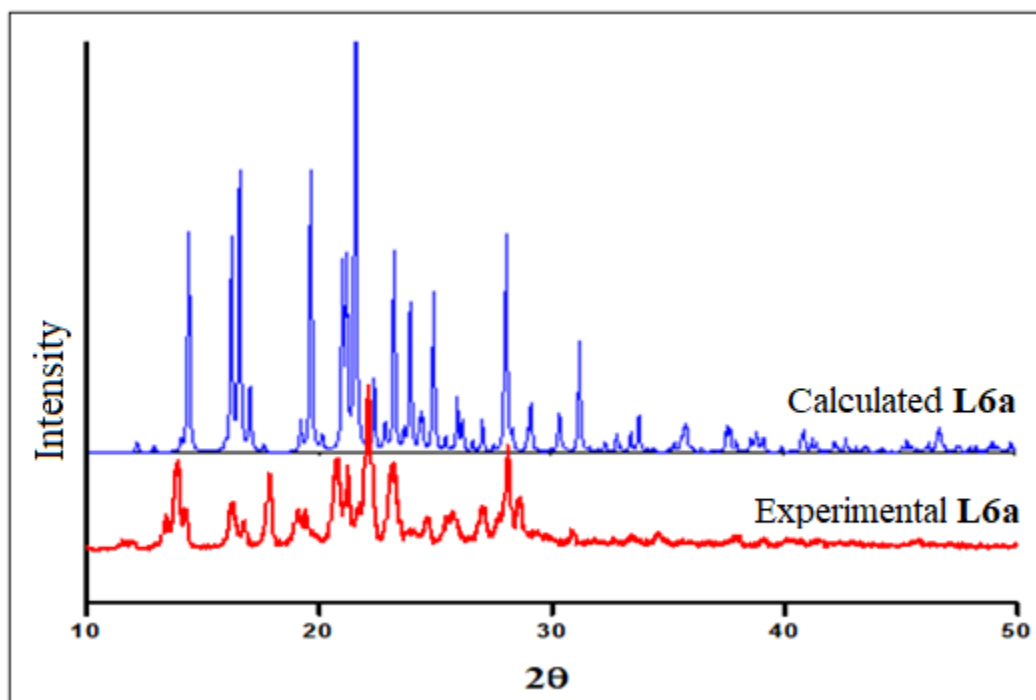


Figure A53: ORTEP of L6a

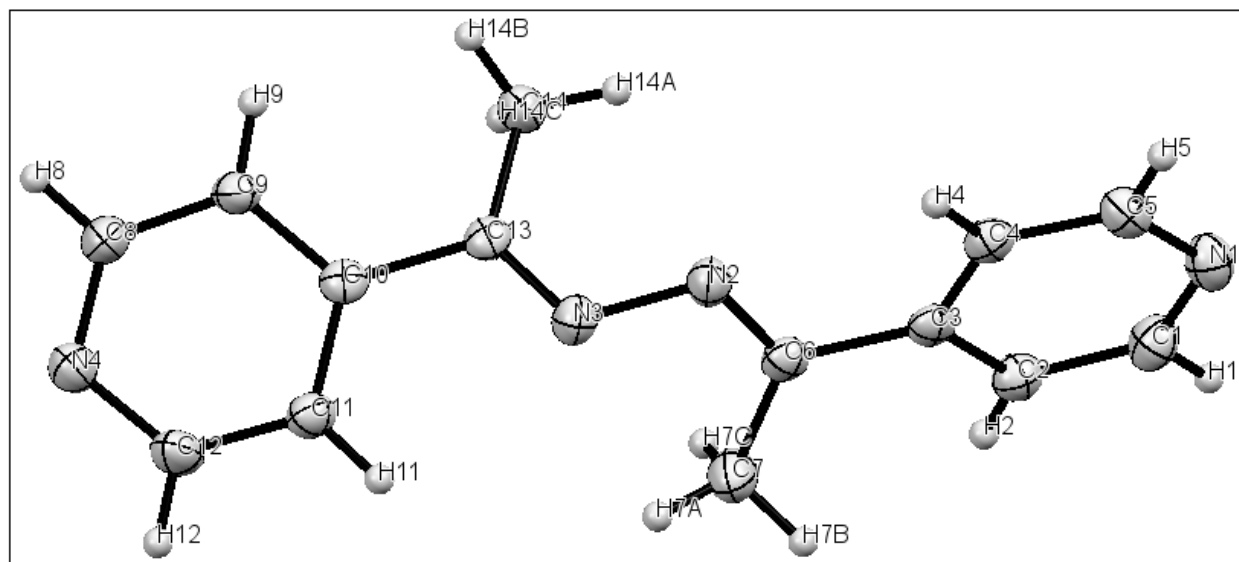


Figure A54: ORTEP of CP1

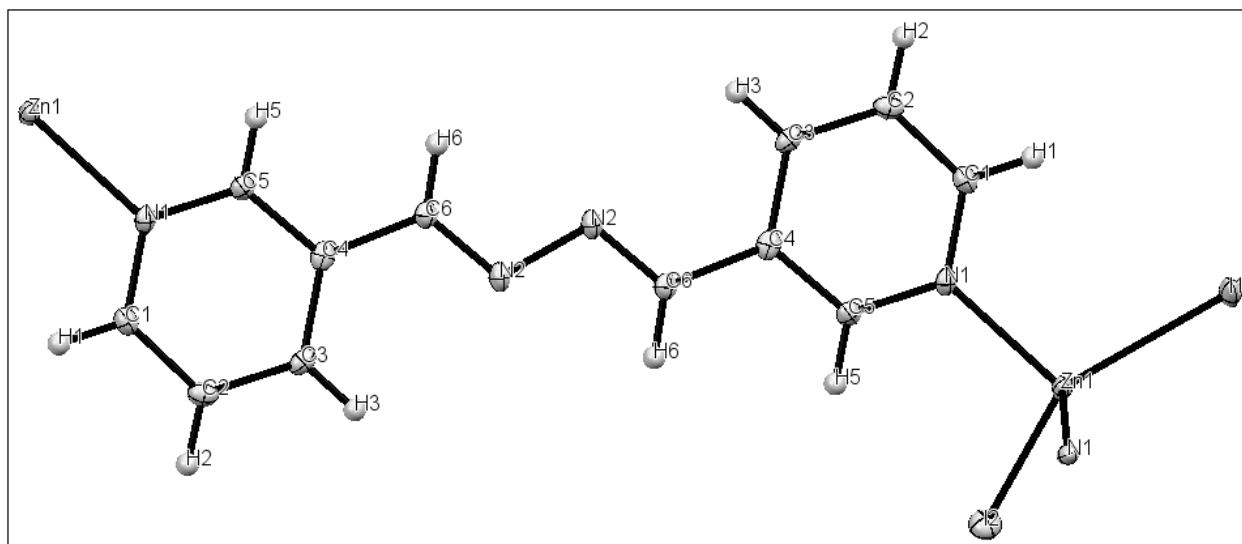


Figure A55: ORTEP of CP2

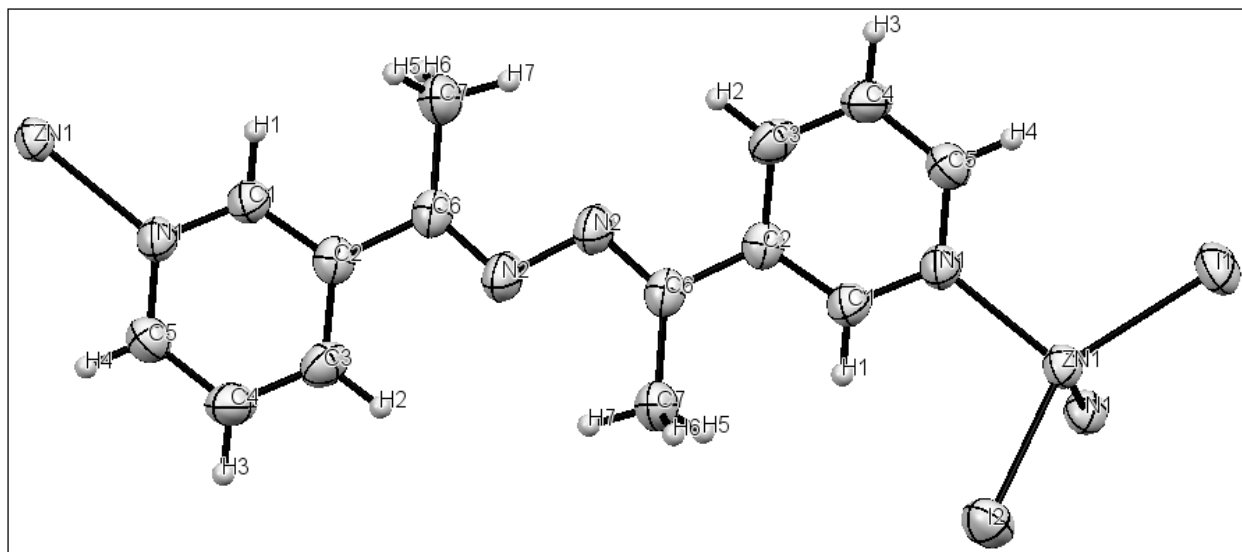


Figure A56: ORTEP of CP3

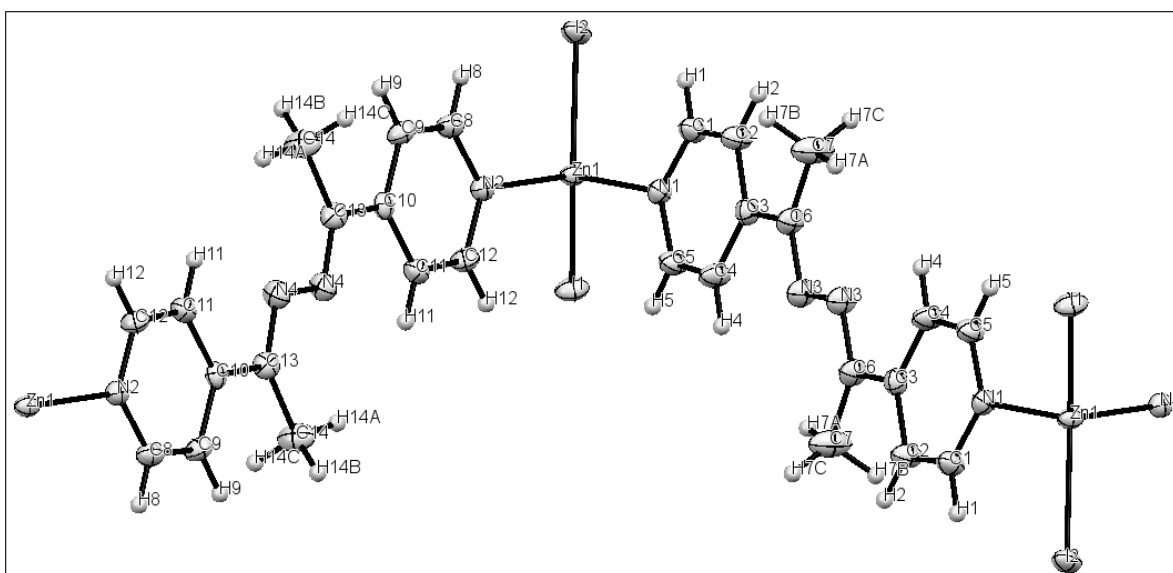


Figure A57: TGA of CP1 and anion exchanged CPs of CP1

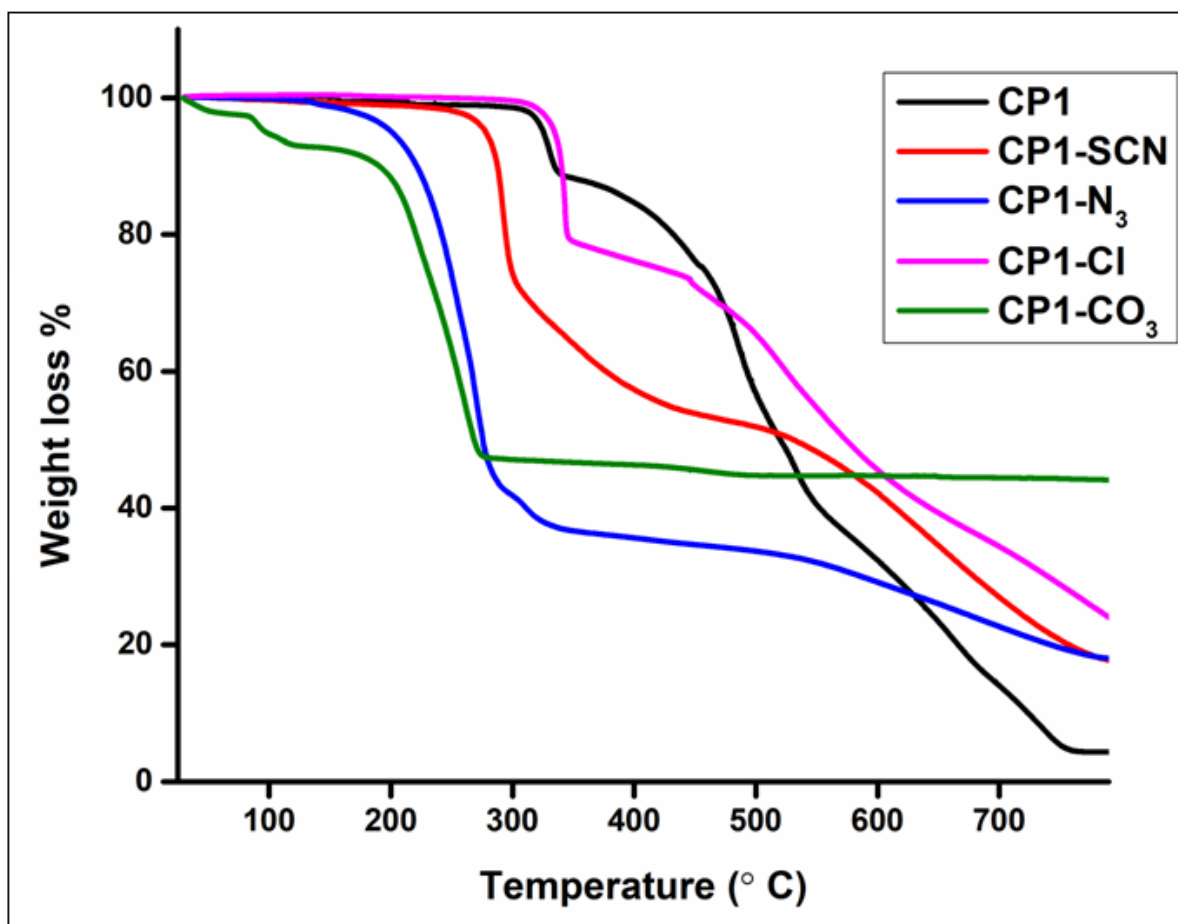


Figure A58: Decomposition of MB dye in presence of CP3

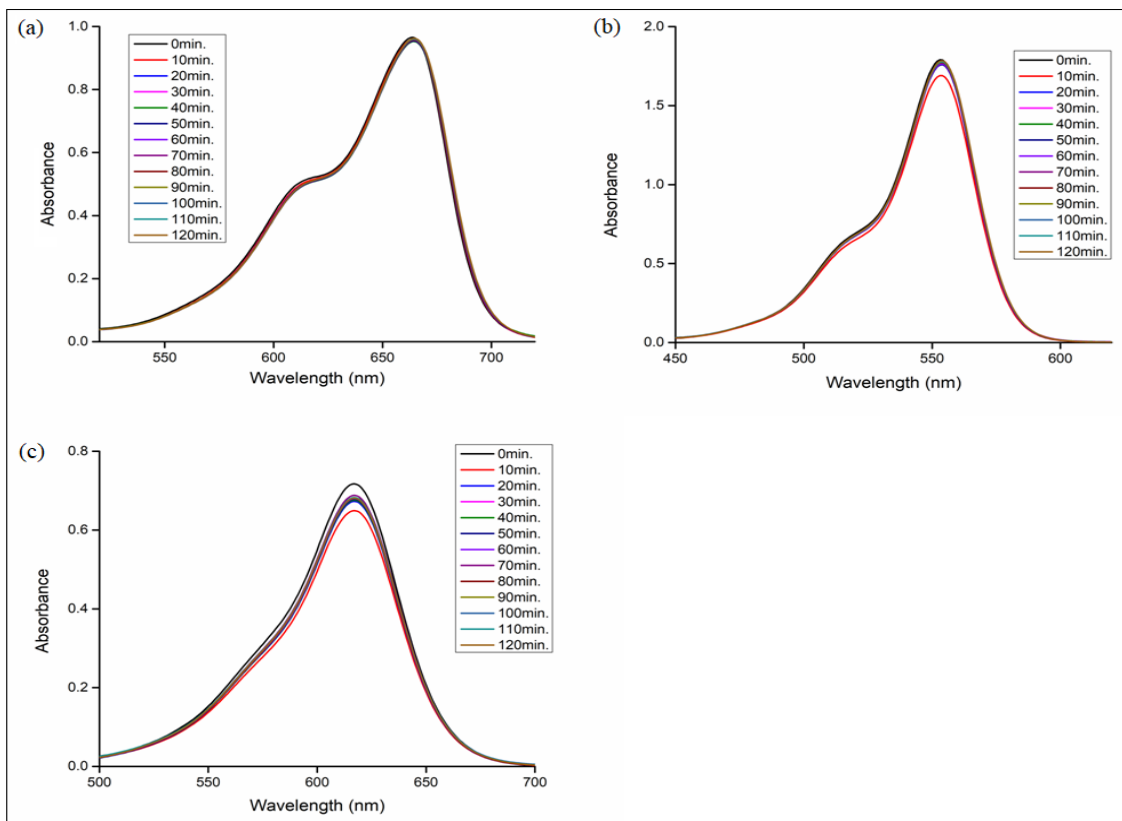


Figure A59: IR spectra of CP4

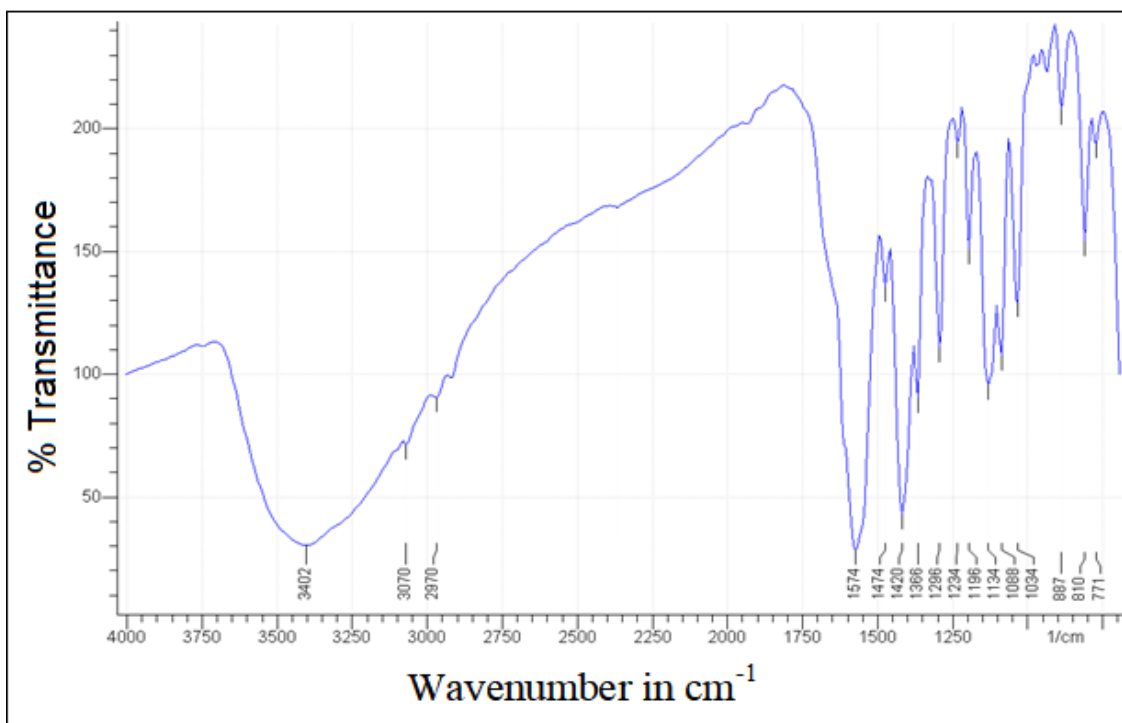


Figure A60: Comparison of calculated and experimental Powder XRD of CP4

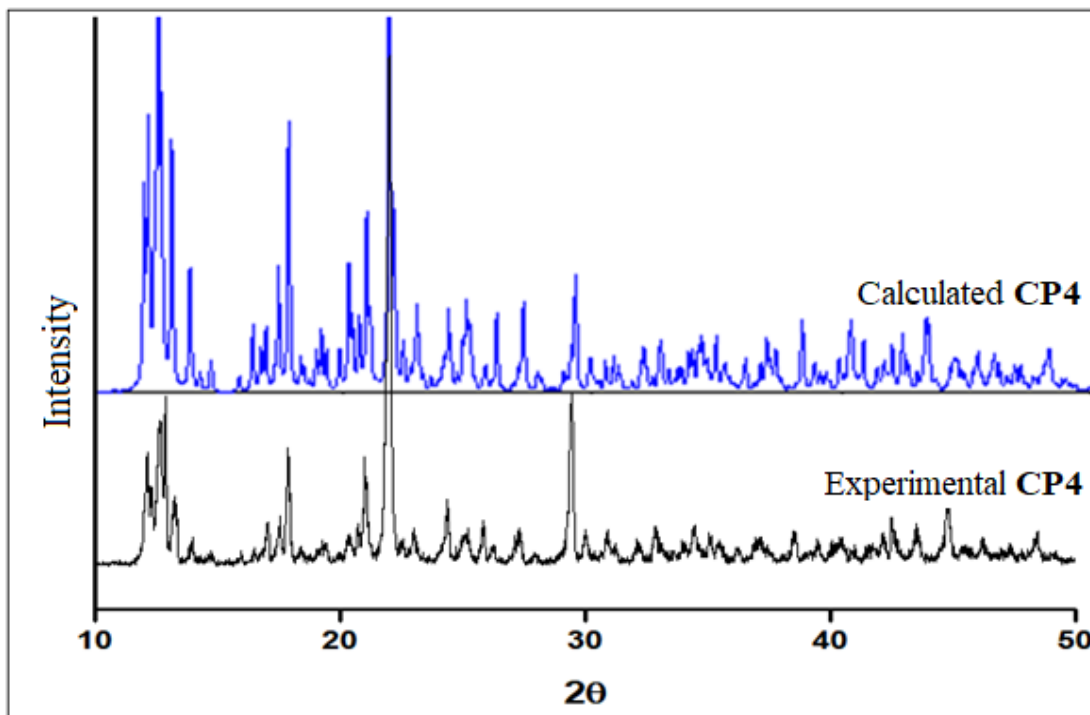


Figure A61: Powder XRD comparison of CP5 with experiment-1 and CP6 with experiment-2

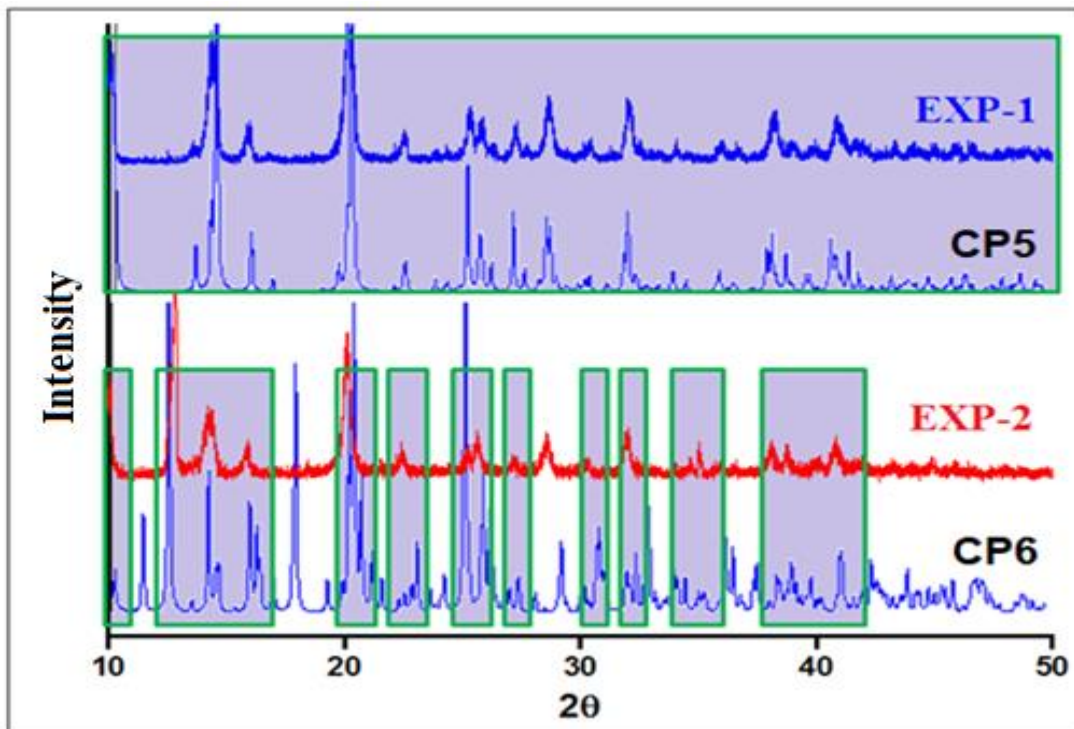


Figure A62: PL spectra of CP4 in different ratio of Acetonitrile-CHCl₃

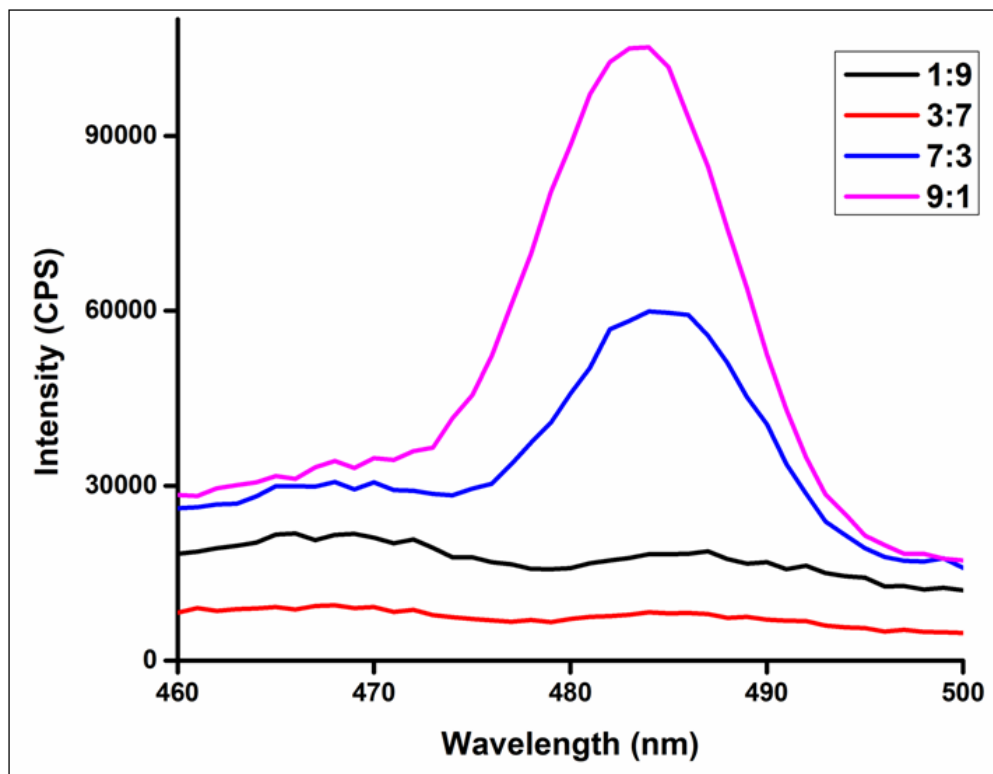


Figure A63: IR spectra of CP7

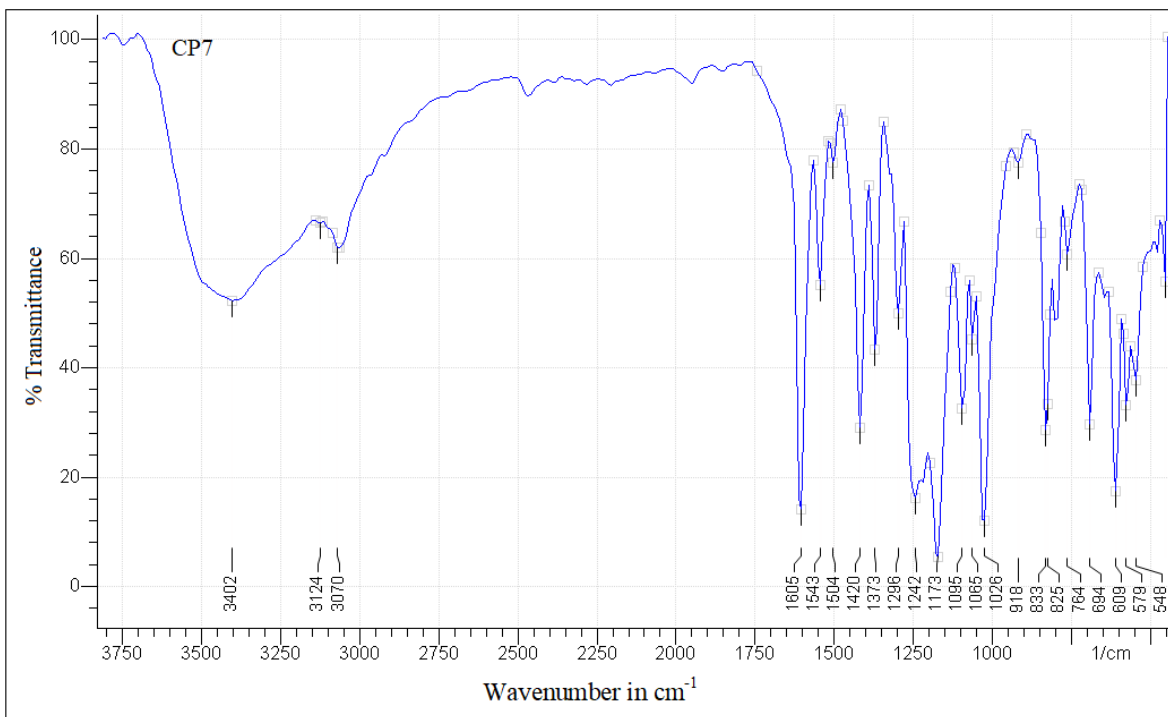
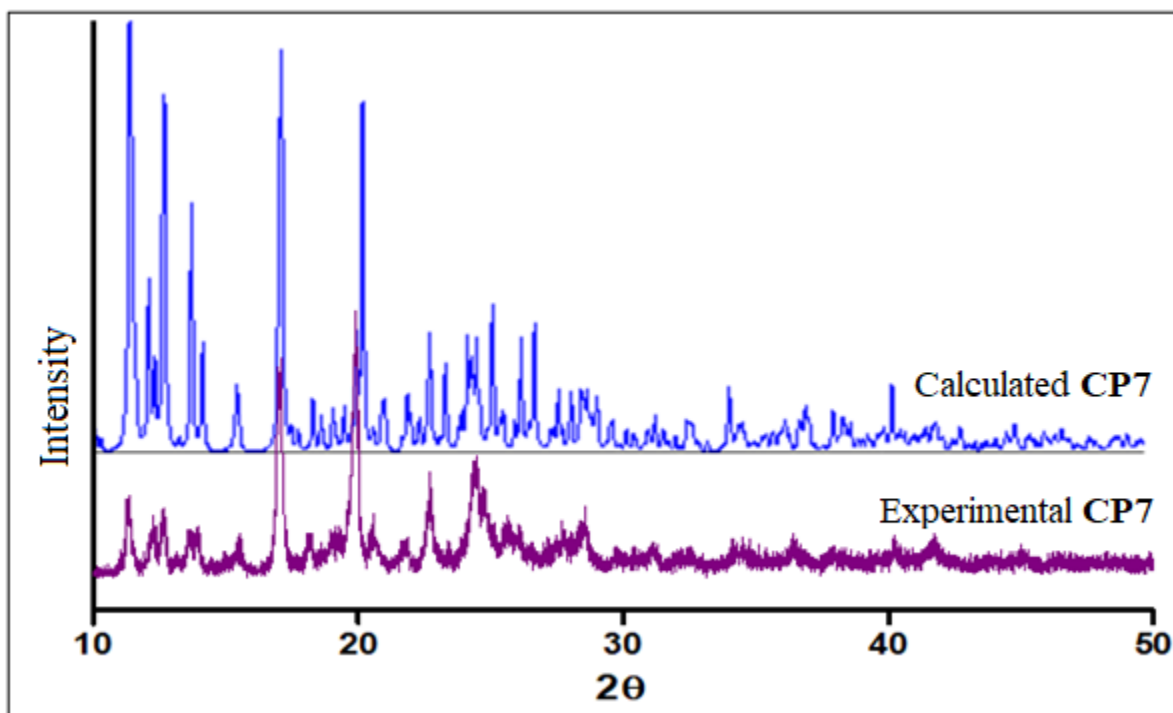


Figure A64: Experimental and calculated Powder XRD of CP7



List of Publications

1. Suman Kumari, **Fayaz Baig**, Rajni Kant, Vivek K. Gupta, Sanjay Mandal and Madhushree Sarkar., Is metal metathesis a framework-templating strategy to synthesize coordination polymers (CPs)? Transmetallation studies involving flexible ligands. *RSC Adv.*, **2014**, **4** (69), **36451-36457**.
2. **Fayaz Baig**, Rajni Kant, Vivek K. Gupta and Madhushree Sarkar., Effects of noncovalent interactions in light emitting properties of *bis*-pyridyl-alkyl-diimines. *RSC Adv.*, **2015**, **5**, **51220–51232**.
3. Moyna Das, **Fayaz Baig** and Madhushree Sarkar., Photophysical properties of di-Schiff bases: Evaluating the synergistic effect of noncovalent interactions and alkyl spacer in enhanced emissions of solids. *RSC Adv.*, **2016**, **6**, **57780–57792**.
4. **Fayaz Baig**, Sadhika Khullar, Sanjay K. Mandal and Madhushree Sarkar., Coordination Polymers comprised of an exobifunctional Schiff base ligand and succinate dianion: Critical analysis of factors affecting the structures and framework dimensionality. *Chemistry Select* **2017**, **2**, **11677 –11685**.
5. **Fayaz Baig**, Sadhika Khullar, Sanjay Mandal, Krishnan Rangan and Madhushree Sarkar., Analysis of supramolecular structure and photophysical properties of a series of Schiff's bases. (**manuscript under preparation**).
6. **Fayaz Baig**, Sadhika Khullar, Sanjay Mandal, Krishnan Rangan and Madhushree Sarkar., 1D Zn(II) coordination polymers of *bis*-pyridyl-diimines: Anion exchange and photo degradation studies. (**manuscript under preparation**).
7. **Fayaz Baig**, Krishnan Rangan and Madhushree Sarkar., Iodine and methyl orange dye adsorption studies on a 3D coordination polymer of Cd(II) with benzene-disulphonate and *bis*-pyridyl-diimines. (**manuscript under preparation**).

List of Papers Presented in Conferences

1. **Fayaz Baig**, Kumari Suman and Madhushree Sarkar. “Is hydrogen bonding along with flexible alkyl chain a way to generate dynamic coordination polymers? A case study on coordination polymers derived from *bis*-pyridyl-diamide ligands” at **National conference on Recent developments in Chemical Sciences (NCRDCS-14)**. (25th – 26th February, **2014**).
2. **Fayaz Baig** and Madhushree Sarkar. “Study of the Structural Features of Di-imine Based Ligands in Order to Correlate the Structure-Property Relationship and a Brief Review on Their Applications” at **National Conference on Nano and Functional Materials 2014 (NFM-2014)**. (7-8 November **2014**).
3. **Fayaz Baig**, Kumari Suman and Madhushree Sarkar. “Post Synthetic Modifications on Coordination Polymers Based on Amide Ligands” at **National Conference on “Frontiers at the Chemistry - Allied sciences Interface (FCASI-2015)**. (13-14 March **2015**).
4. **Fayaz Baig**, Kumari Suman and Madhushree Sarkar. “Post Synthetic Studies on Coordination Polymers Derived from *Bis*-pyridyl-diamide Ligands” at **2nd Indo-German Workshop on Supramolecular Chemistry** (30th March **2015**).
5. **Fayaz Baig** and Madhushree Sarkar. “Analysis of Structure-Optical Property Relationship of *bis*-pyridyl-alkyl-diimines” at **International Conference on Nascent Developments in Chemical Sciences (NDCS-2015)**. (16-18 October **2015**).
6. **Fayaz Baig**, Kumari Suman and Madhushree Sarkar. “Structural Transformations of Coordination Polymers on the Counter Anion Exchange and Metal-metathesis” at **44th National Seminar on Crystallography (NSC-2016)**. (10-13 July **2016**).
7. **Fayaz Baig**, Kumari Suman and Madhushree Sarkar. “Structural Transformations of Coordination Polymers on the Counter Anion Exchange and Metal-metathesis” at **National Conference on Organic Chemistry in Sustainable Development: Recent Advances and Future Challenges**. (29-30 August **2016**).

-
8. **Fayaz Baig**, Kumari Suman and Madhushree Sarkar. “Structural Transformations of Coordination Polymers on the Counter Anion Exchange and Metal-metathesis” at 23rd **ISCB International Conference (ISCBC-2017)**. (8-10 February 2017).
 9. **Fayaz Baig** and Madhushree Sarkar. “Influence of reaction conditions on changing structures of coordination” at **International Conference on Nano and Functional Materials (NFM-2017)**. (16-18 November 2017).
 10. **Fayaz Baig** and Madhushree Sarkar. “Influence of reaction conditions on changing structural features of coordination” at **24th Congress and General Assembly of the International Union of Crystallography (IUCr-2017)**. (21-28 August 2017).

Brief Biography of the Supervisor

Dr. Madhushree Sarkar is an Associate Professor in the Department of Chemistry, Birla Institute of Technology and Science Pilani (BITS Pilani), Pilani Campus. She had done her B.Sc. from Department of Chemistry, St. Stephens College, University of Delhi, India (1997-2000) and M.Sc. from Department of Chemistry, Indian Institute of Technology, Kanpur, India (2000-2002). She received her Ph.D. from Department of Chemistry, Indian Institute of Technology, Kharagpur, India (2003-2007) under the supervision of Prof. Kumar Biradha. During her doctoral studies, she worked on "Supramolecular Chemistry and Crystal Engineering" which involves understanding various Intermolecular Interactions, Molecular Recognitions, "Host-Guest" Chemistry and will ultimately lead to design and synthesize advanced materials for practical purposes (molecular sensing, storage, separation, catalysis).

Dr. **Madhushree Sarkar** joined in BITS Pilani as an Assistant Professor in 2009. She has around eleven years of research experience and eight years of teaching experience. She provided Ph.D to one Ph.D student and currently supervising two Ph.D students, as a result of her research accomplishment she has published 14 research papers in peer-reviewed journals, presented papers and delivered lectures in several national and international conferences. She has completed two research projects as PI funded by BITS Pilani and DST.

Brief Biography of the Candidate

Fayaz Baig completed his B.Sc. from Kavitha Memorial Degree and PG College, Khammam from Kakatiya University, Warangal, India in 2006 and M.Sc. from Periyar University, Salem, India in 2009. For the partial fulfillment of M.Sc. he worked on a project in Aurobindo Pharma Limited on “Synthesis of some related substances of Val-acyclovir Hydrochloride” under the guidance of **Dr. Rama Shankar** in 2008. He worked as an Asst. Prof. in Sree Duttha Engineering College of Science in Hyderabad from 2011-2012. He joined the Department of Chemistry, BITS Pilani, Pilani campus for his doctoral research under the supervision of **Dr. Madhushree Sarkar**. During his doctoral studies, he worked on a project entitled “Crystal Engineering of Metal-Organic Frameworks using Organic Linkers Derived from Template-Controlled Solid-State Reactions” funded by Department of Science and Technology (DST) from 2013-2015. He is a life member in the Indian Crystallographic Association (ICA), India. He published four research articles in peer-reviewed international journals and presented papers in three international and seven national conferences/symposiums. His research interest lies in designing and developing advanced materials (Super-Molecules), that can be used for practical purposes (molecular sensing, storage, separation, and catalysis).